The Dissertation Committee for Okhtay Taghizadeh Dizaj Cheraghi Certifies that this is the approved version of the following dissertation:

Sweep Efficiency for Solvent Injection into Heavy Oil Reservoirs at Grain-scale

Displacement of Extremely Viscous Fluid

Committee:

Kamy Sepehrnoori, Co-Supervisor

Steven L. Bryant, Co-Supervisor

Kenneth E. Gray

Chun Huh

Clint Dawson

Sweep Efficiency for Solvent Injection into Heavy Oil Reservoirs at Grain-scale Displacement of Extremely Viscous Fluid

by

Okhtay Taghizadeh Dizaj Cheraghi, B.S.; M.S.

Dissertation

Presented to the Faculty of the Graduate School of
The University of Texas at Austin
in Partial Fulfillment
of the Requirements
for the Degree of

Doctor of Philosophy

The University of Texas at Austin
December 2007

Dedication

To my parents, my brother, my wife, my beautiful kids and my teachers

Acknowledgements

I would like to take this opportunity to thank my supervising professors, Dr. Kamy Sepehrnoori and Dr. Steven L. Bryant, for their guidance and support throughout the course of this research. I have been grateful for the opportunity of work and learning with them. I would also like to thank and appreciate other supervising committee members, Dr. Kennet E. Gray and Dr. Chun Huh from Department of Petroleum and Geosystems Engineering, and Dr. Clinton N. Dawson from Department of Aerospace Engineering and Engineering Mechanics, for their support and time to evaluate my work and their guidance, time and comments.

National Iranian Oil Company and my supervising professors have made this opportunity possible for me to pass through my PhD studies by their major financial support.

During my academic life of doctorate study in the department of Petroleum and Geo-systems engineering in the University of Texas at Austin and my everyday life in the United States of America, I have met wonderful people from all around the world who have made a difference in my life. I will never forget the memories they made at this stage of my life and their help and support to get me through this step of my life. I hope that I have been able to appreciate their support and return their favor. These friend and colleagues are: Alvaro Barrera, Cleon L. Dunham, Kiomars Eskandary Dalvand, Mohammad Ali Farhadinia, Gholamreza Garmeh, Yousef Ghomian, Cheryl Kruzie, Mayank Malik, Hourshad Mohammady, Reza Navid, Fen Pang, Peyman Porafshari, Ebrahim Saberinia, Aidin Taghizadeh, Gholam-ali Taghizadeh, Arletta Tompkins.

Sweep Efficiency for Solvent Injection into Heavy Oil Reservoirs at Grain-scale

Displacement of Extremely Viscous Fluid

Publication No._____________

Okhtay Taghizadeh Dizaj Cheraghi, Ph.D.
The University of Texas at Austin, 2007

Supervisors: Kamy Sepehrnoori and Steven L. Bryant

The movement of low viscosity fluid through a porous medium containing extremely viscous fluid is emerging as an important phenomenon in several petroleum engineering applications. These include the recovery of heavy oil by solvent injection, the preferential reduction of water flow using polymer gels, and the enhancement of acid fracturing treatments. The displacement of one fluid from a porous medium by a second, immiscible fluid has been extensively studied in two cases: when capillary forces are dominant, and when viscous forces are comparable to capillary forces.

This dissertation research examines a third case: when viscous forces are dominant. The viscosity of the fluid initially present in the porous medium is four or more orders of magnitude greater than the viscosity of the displacing fluid. Consequently, the displacement through an individual pore will be dictated by the hydrodynamic forces required to move the high viscosity fluid. However, very little is known about grain-scale

behavior of such displacements. The research will develop a mathematical model of the viscosity-dominated displacement in a network of conduits.

By neglecting pressure drop within the low viscosity fluid, the model will treat the displacement as a moving boundary problem. The high viscosity fluid will be assumed Newtonian and will move in response to the pressure gradient imposed via the low viscosity fluid. The movement can be treated as pseudo-steady state flow of the high-viscosity fluid. The flow field will be updated whenever the low viscosity fluid advances into a pore previously occupied by high-viscosity fluid. Swept volume will be calculated in each run for comparison and further investigation. We will use classical methods for direct and iterative solutions of large, sparse linear systems to compute these steady states.

Key practical insights to be obtained from the model are the nature of the displacement and effects of geometry and hydraulic conductivities on the sweep efficiency. The model will form the basis for examining additional physical processes, notably mass transfer between fluids, and the possibility that fingering of the low viscosity fluid occurs within individual pore throats.

Table of Contents

Nomenclature

The list of nomenclatures is in the alphabetical order.

A = area, (L^2)

B = boundary vector

g = hydraulic conductivity

i = injected

k = permeability, (L^2)

L = length of bond, (L)

Nc = capillary number (dimensionless)

p = occupancy probability

P = pressure, (m/Lt^2)

Pc = capillary pressure

qi = invading fluid flow rate, (L^3/t)

qd = displaced fluid flow rate, (L^3/t)

r = radius of bond, (L)

x = distance, (L)

α = angle

β = angle

μ = viscosity, ($m.t^3/L^2$)

μ1 = displaced fluid viscosity

μ2 = injecting fluid viscosity

Greek symbols

ξ = correlation length

ν = Darcy velocity, (L/t)

σ = Interfacial Tension, (dyne/L)

Ω = control volume, (L^3)

θ = angle, (degree)

ε = epsilon.

π = Pi number

Superscripts

β = critical Exponent

Subscripts

d = displaced

i = node index

j = node index

k = node index

o = oil

w = water

List of Tables

List of Figures

CHAPTER 1

Introduction

The movement of low viscosity fluid through a porous medium containing extremely viscous fluid is an important phenomenon in several petroleum engineering applications. These include the recovery of heavy oil by solvent injection, the preferential reduction of water flow using polymer gels, and the enhancement of acid fracturing treatments. The displacement of one fluid from a porous medium by a second, immiscible fluid has been studied extensively in two cases: when capillary forces are dominant, and when viscous forces are comparable to capillary forces. In both cases, investigating the behavior at the grain scale provides great insight, because capillary forces are strongly influenced by the geometry of individual pores.

This research examines a third case: when viscous forces are dominant. The viscosity of the fluid initially present in the porous medium is three or more orders of magnitude greater than the viscosity of the displacing fluid. In the limiting case we can assume that the mobility ratio (m) of the displaced fluid and the injecting or displacing fluid will eventually tend to very large values (infinity). Consequently, the displacement through an individual pore will be dictated by the hydrodynamic forces required to move the high viscosity fluid. However, very little is known about grain-scale behavior of such displacements. The sizes, and hence the hydraulic conductances of pore throats varies widely between pores. Moreover, the hydraulic conductances are spatially correlated. Thus, a purely statistical treatment of the displacement cannot capture the essential physics. The research will therefore develop a mathematical model of the viscosity-dominated displacement in a network of conduits. A vital aspect of the research is that unlike traditional pore-scale approaches, the network will not be purely statistical. Rather, it will be taken directly from the known pore space geometry and topology of a physically representative network model porous media. We will perform the simulations on both statistical and physically representative models and discuss the similarities and differences whenever necessary. A simple 3D lattice model is shown in Figure 1.1, which is a 3D cubic lattice consisting of 27 nodes. This network is a 3x3x3 node system, with unit conductivities and zero standard deviation of conductance. All nodes and bonds have the same characteristics, such as size, length, volume, connection, etc.

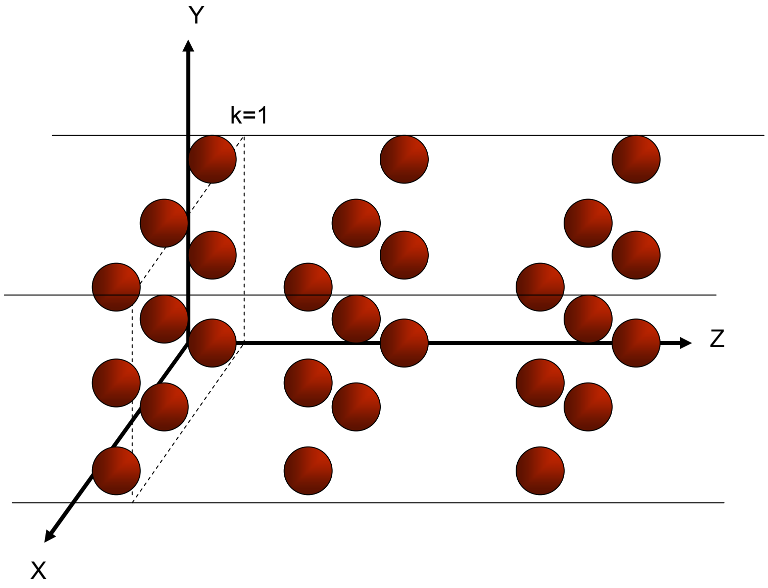

Figure 1.1 A 3D cubic lattice

A real network sample or model is more complicated in terms of size, connectivity, conductivity, geometry, etc. Figure 1.2 shows a real sample of sand particles grouped together that make a network model. It has no specific structure.

Figure 1.2 A real porous media has no structure or regular lattice

Figure 1.3 is a model reproduction of the sand particles sample. It has more realistic geometry than the network in Figure 1.1, but it is still very different from the real sand particles in Figure 1.2. This reproduced sample has a random distribution of particles in space. All the particles have the same size and shape, unlike the real sample in which each particle has its own characteristics, size, orientation, etc.

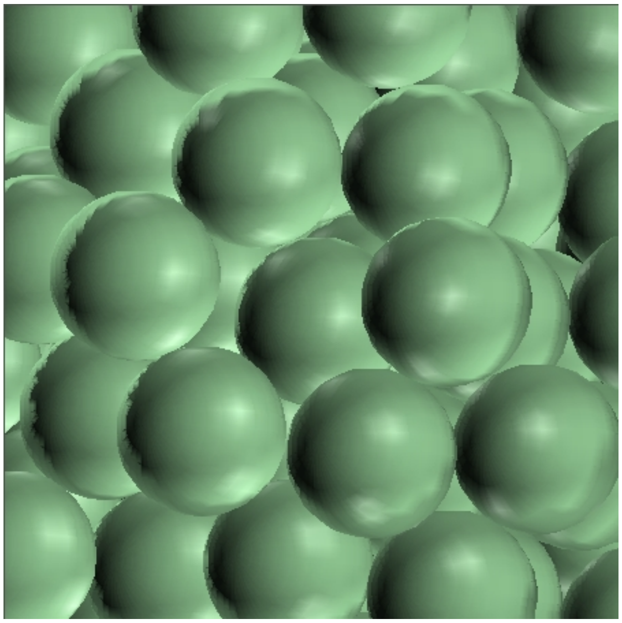

Figure 1.3 Random dense packing of spheres

By neglecting pressure drop within the low viscosity fluid, the model will treat the displacement as a moving boundary problem. The high viscosity fluid will be assumed to be Newtonian and will move in response to the pressure gradient imposed via the low viscosity fluid. The movement can be treated as a pseudo-steady state flow of the high-viscosity fluid. The flow field will be updated whenever the low viscosity fluid advances into a pore previously occupied by high-viscosity fluid.

Note that each node in the network system has x number of surrounding nodes connected to it. A mass balance equation can be written for each node. These equations have to be solved simultaneously for the whole network to find the flow rates in each bond connecting two nodes in the network. As the number of nodes increases in the network, the number of linear equations will increase. Putting all the equations together in a matrix form produces a large sparse matrix. We will use classical methods for direct and iterative solutions of large, sparse linear systems to compute these steady states flows in each bond. We will apply them to large model porous media (10^4 to 10^5 pores), which implies 10^3 to 10^4 updates of the flow field. The possibility of parallelizing the computations has not been tested in this research.

A key practical insight to be obtained from the model is the nature of the displacement, in particular whether the displacing fluid forms a highly ramified, dendritic structure or whether it forms a more compact piston-like front. The former is typical at the pore scale when capillary forces are important and has been observed in laboratory experiments with heavy oil and in the field. The latter will be much more efficient in terms of recovery and sweep efficiency.

CHAPTER 2

Literature Review

In this chapter, we start by defining the keywords used in this dissertation. These definitions are used to explain the static and dynamic properties of structures and behaviors in network systems.

Later we will review the previous research that has been performed in related areas of this work. We will also explain the similarities and differences between our work and others' research and discuss the new ideas and advantages that we have implemented.

2.1 DEFINITIONS

There are several necessary network definitions that are needed before getting into the properties and characteristic behaviors of the systems. Some of these definitions are for explaining the shape and geometry structure of a porous media and others are for defining the behavior of fluids flow in these pore space structures.

Note that some of these definitions might be seen in other documents in different areas such as electronics, computers, etc., but they define similar objectives in a different fashion.

2.1.1. NODE

Node is a physical or imaginary point, surface, or volume that can represent a location where multiple connectors meet. These nodes can be considered as pores in porous media modeling. It is also known as *Vertex* or *Site*. They may have properties such as volume, shape, etc.

2.1.2. BOND

Bond is a connector that connects two nodes together. It is also known as *Edge*. They have properties such as length, radius, shape, roughness, etc. Bonds are the essential parts of any network. Flow cannot happen in a network without bonds. Bonds carry the flow of fluids like oil, water, and gas in petroleum subjects.

2.1.3. NETWORK

Also known as *Graph*, network is any set of nodes (vertex, site) which has been connected by a set of bonds (connections, edge). Networks represent properties like structured or irregular spatial topology. Properties like the degree of connectivity are a result of network structure.

2.1.4. CONNECTIVITY

The number of bonds connecting any node to other nodes in a network is known as the degree of connectivity. This number is also known as the *degree of freedom* for each node. Zero connectivity describes an individual node without any connection.

Connectivity is usually the same value for all the nodes inside a structured network. But in irregular networks, it can vary from node to node.

2.1.5. LATTICE

Lattice is the shape structure of a network. Any lattice has its own characteristic connectivity and shape. Examples of lattice are square, hexagonal, etc. For example, a 3D square lattice has six degrees of connectivity for each node.

Figure 2.1 shows a 3D square lattice. Every node with the '+' sign (red in color prints) in this cubic lattice is connected to six other nodes with the '-'sign (blue in color prints) and vice versa.

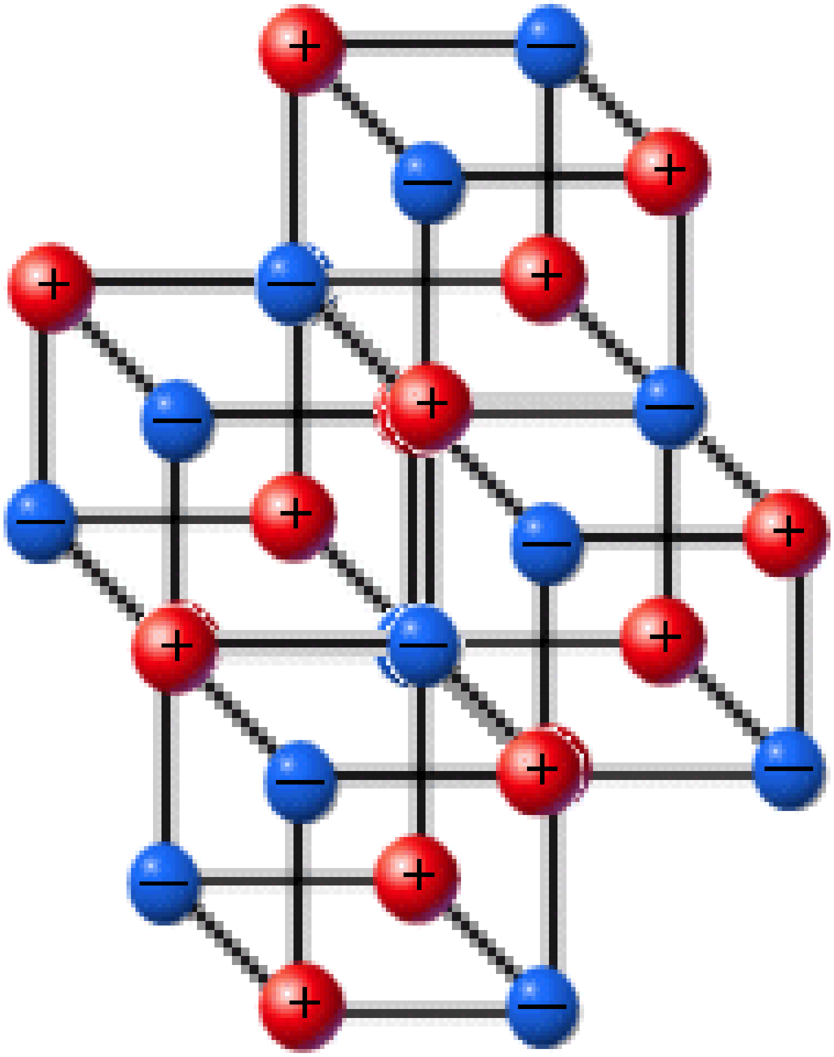

Figure 2.1 3D cubic network with connectivity of six

2.1.6. DIMENSIONLESS

We called our network model a dimensionless network, because the search criterion in our model to find the neighboring nodes for invasion does not follow any regular lattice scheme. This term emphasizes that our network model inside the simulator does not depend on the dimensionality of the network; rather, it depends on the connectivity between nodes, and not the geometrical location of nodes. So, the need to know if the system is 1D, 2D or 3D is waived for the search algorithm. This results in having a regular or irregular network, but without the restriction on nodes connectivity.

Our code is a fully 3D model, but the search algorithm has the advantage of using a connectivity algorithm instead of a lattice location scheme, such as that being used by the regular lattice network models. It is simply a name that we use to define the ability of our simulator, and it only implies that our invasion model is not dependent on the dimensionality of the lattice.

The advantage of this system will be defined in later chapters. For specific examples and further clarification on the dimensionless algorithm, please refer to Chapter-4, Section 4.6' search algorithm.

2.1.7. PERCOLATION

The Percolation Theory is a general mathematical theory of connectivity and transport in geometrically complex networks. Many results can often be encapsulated in a small number of simple algebraic relationships by use of the percolation theory [Buldyrev, 2001].

In simple words, percolation is the connected path from one side or one source in the network to the other side or sink of network, as shown in Figure 2.2.

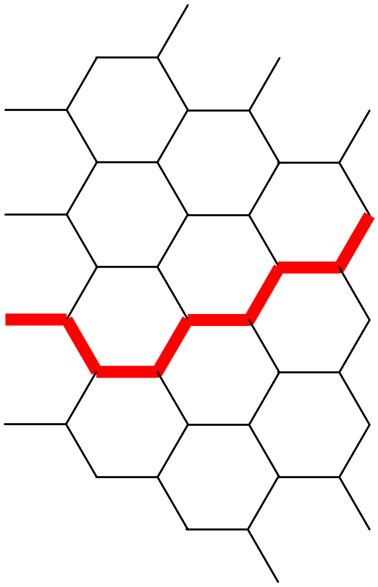

Figure 2.2 Percolation of bonds from onside to the other side of a network

For example, consider a square grid and occupy sites on this grid with a probability, P. For small values of this probability, one can see mostly isolated occupied sites with occasional pairs of neighboring sites that are both occupied.

If neighboring sites are both occupied, we call it a *cluster*. As the occupancy probability increases, we get more isolated clusters, and some clusters grow while others merge together. So, the clusters on the whole get larger (see Figures 2.3 to 2.6).

At a particular value of the occupancy probability, one cluster dominates and becomes (infinitely) large. Above this particular probability, the other clusters become absorbed into this universal cluster until P = 1, the unit probability, every site in the network is occupied.

Note that at one particular value of the occupancy probability a very peculiar thing happens. Suddenly one cluster becomes infinitely large. This is called the spanning cluster, as it spans the entire lattice.

This sudden onset of a spanning cluster occurs at a particular value of the occupancy probability known as the *Percolation Threshold* (*pc*), and is the fundamental characteristic of the percolation theory.

The exact value of this threshold depends on which type of grid or network is used. It is also strongly dependent on the dimensionality of the network grid. A table of approximate values is given in Table 2.1. More accurate values can be found in the book by Stauffer & Aharony [Stauffer and Aharony, 1994].

Figures 2.3 to 2.6 show clusters generation as the probability increases. At a probability of 0.1, individual sites are located all around the lattice and there are also some small clusters of coupled sites. The maximum cluster size in this realization is 5 sites.

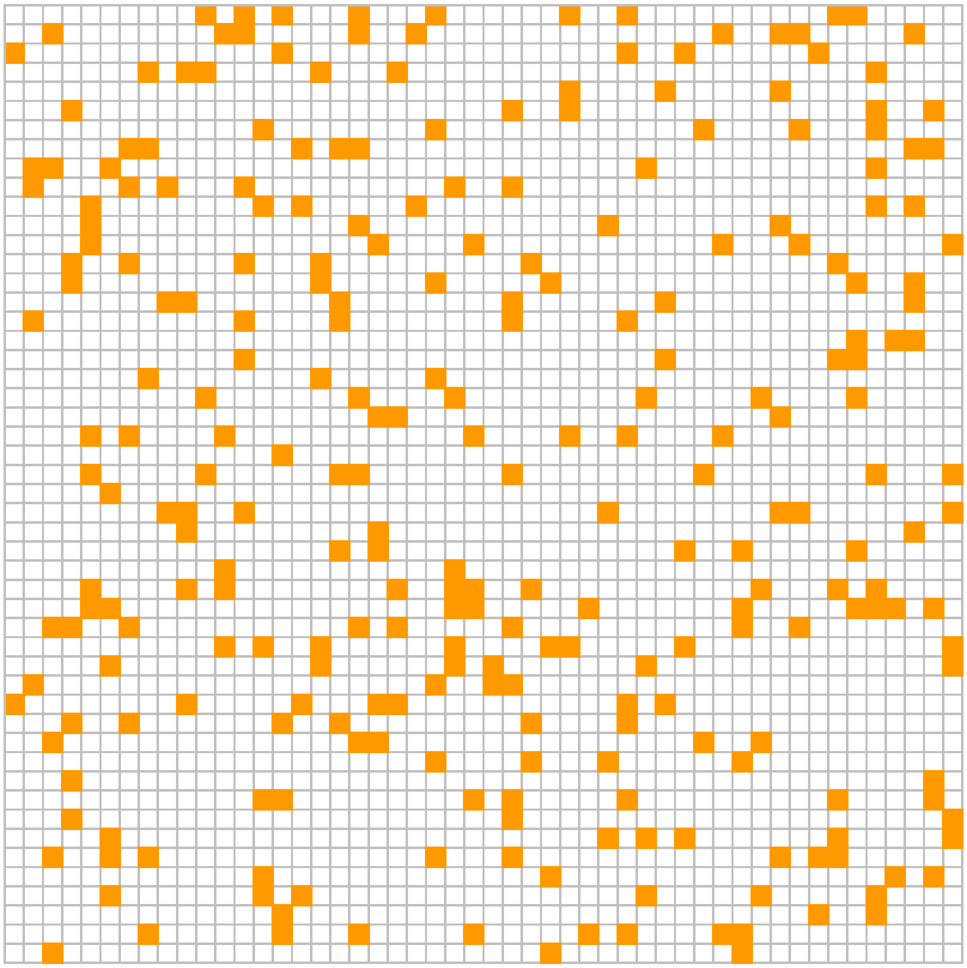

Figure 2.3 Occupancy Probability = 0.1

As shown, the clusters growing larger. One can see clusters that are spanning through several sites. The maximum cluster in this realization is 18 sites, but there is still no connected path through the network from one side to the other. This means that although clusters are growing they are still not large enough to make a spanning path from one side of the network to the other.

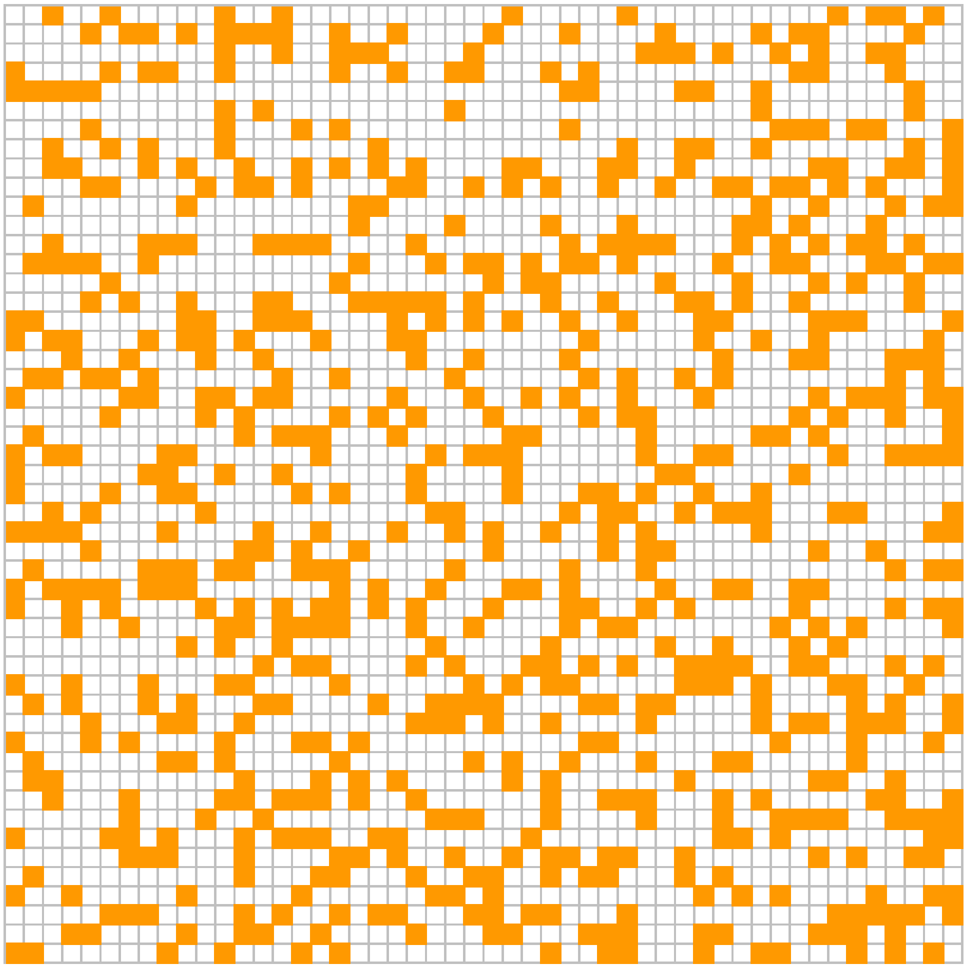

Figure 2.4 Occupancy Probability = 0.3

Increasing the occupancy probability will generate many big clusters. These span a wider space in the network, but there is still no connected path from one side of the lattice to the other.

Figure 2.5 Occupancy Probability = 0.5

As we continue to increase the occupancy threshold, more clusters are generated and they grow larger. The clusters have now made an infinite cluster, which gives a connected path from one side of the network to the other.

Figure 2.6 Occupancy Probability = 0.6

2.1.8. PERCOLATION THRESHOLD

The minimum occupancy probability, as described in Figures 2.3 to 2.6, in which one can obtain a connected path from one side of the network to the other is called the *Percolation Threshold*. The percolation threshold is the exact value of occupancy probability; Below that value, we do not get a connected path through the network.

The percolation threshold depends on lattice degree and dimensionality of the network. There are two different values of threshold in each network: one depends on sites and the other depends on bonds. The site threshold is the occupancy probability in which nodes or sites make a connected path through the network. The bond threshold is the occupancy probability that bonds will make a connected path through the network. Table 2.1 shows some percolation thresholds for different lattices.

Lattice	Degree	Dimension	Site Threshold	Bond Threshold
Hexagonal	3	2D	0.692	0.653
Square	4	2D	0.593	0.500
Tetrahedral	4	3D	0.430	0.388
Triangular	6	2D	0.500	0.347
Simple cubic	6	3D	0.312	0.257
Face-Centered Cubic	12	3D	0.198	0.125
Body-Centered Cubic	12	3D	0.246	0.180
Voronoi	16.27	3D	0.140	0.082

Table 2.1 Percolation threshold values

Note that we have described the connectivity of sites on the lattice as *Site Percolation*. We could have also occupied the edges of the sites (or the bonds). The latter problem is known as *Bond Percolation*. This only affects the percolation threshold, and not the other fundamental properties of the percolation theory.

Not all occupied sites are in the infinite (e.g., spanning) cluster. Below the percolation threshold, the probability that an occupied site falls in the infinite cluster ***P***(p) must be zero, since there is no spanning cluster.

Also, note that lower case p is the occupancy probability, where upper case ***P*** is the fraction of occupied sites belonging to the percolating cluster. This may be slightly confusing, but is the standard nomenclature used throughout percolation literature and, thus is adopted here as well.

2.1.9. CRITICAL COMPONENT AND UNIVERSALITY

Threshold can be described in very simple analytical terms. This analytical form is known as the power or scaling law (see Equation 2.1).

$$P(p) = (p - p_c)^{\beta} \qquad \text{where} \qquad p > p_c \qquad \text{Eq. 2.1}$$

The exponent β is known as a *Critical Exponent*. This has the remarkable feature of being entirely independent of the type of lattice being studied. Whether it is bond or site percolation, it depends only on the dimensionality of space (i.e., 2D or 3D). This is known as "*Universality,*" and is an important aspect of percolation theory and, indeed, critical phenomena in general. In broad terms, it means that the large scale behavior of these systems can be described using relatively simple mathematical relationships, and are entirely independent of the small scale construction. Clearly, this is a very powerful concept as it enables us to study and understand the behavior of a very wide range of systems without needing to worry too much over the details. One key factor which is not universal is the percolation threshold. Note that the scaling laws and critical exponents are universal [Buldyrev, 2001].

Figure 2.7 shows the probability graph of percolation. We do not have any percolation through the network until the occupancy probability reaches a certain threshold value, which varies for each network. At the critical threshold value, percolation occurs. We also have the percolation for higher values of probability than threshold.

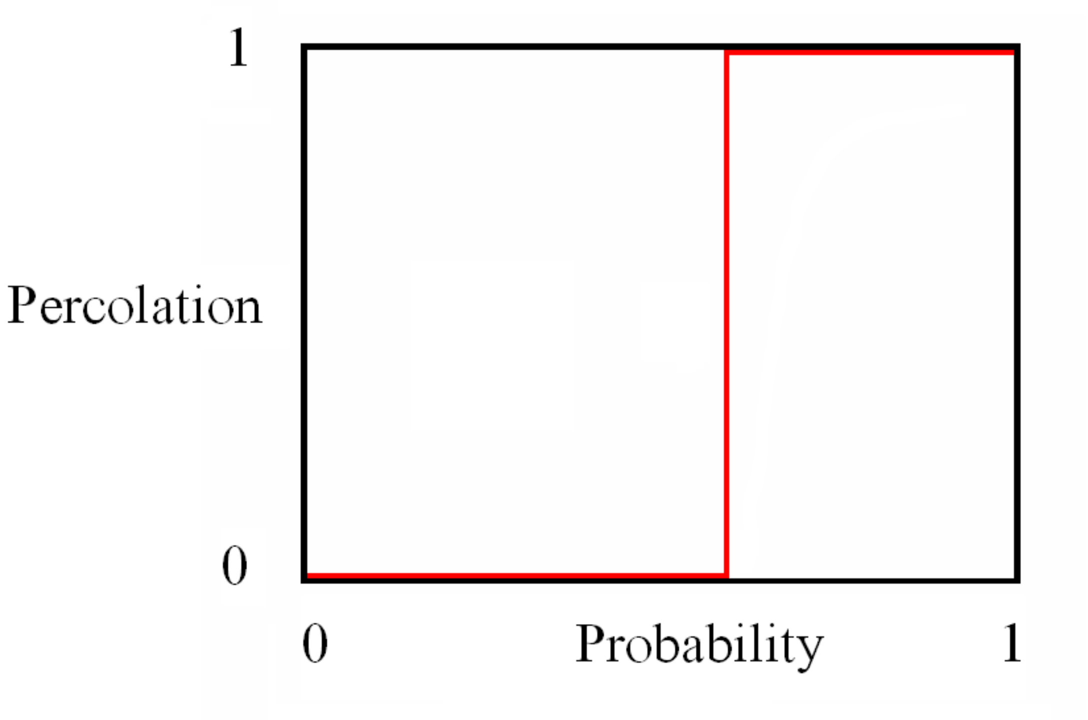

Figure 2.7 Percolation threshold vs. Probability

The critical exponent for a 2D lattice is β = 5/36 and for a 3D lattice is β = 0.41. As realized from the above values, the critical exponent is an exact value for the 2D lattice, but it is an approximate or numerical value for a 3D lattice. This is because, in two dimensions others were able to calculate and determine the exact value, but attempts were not successful for three dimensions. It is not even known if the result should be a rational number in three dimensions [Buldyrev, 2001]. There are also many other critical exponents that can be described near the threshold but they are not in the interests of this research thesis.

2.1.10. CLUSTER SIZE

Consider the two-point correlation function g(r). This function is the probability that if one point is in a cluster, then another point, a distance 'r' away, is in the same clustes (Equation 2.2). This typically has an exponential decay given by a correlation length (ξ).

$$g(r) = e^{-\frac{r}{\xi}} \qquad \text{Eq. 2.2}$$

2.2 NETWORK MODELS

Network models are structures that can be used to define porous media. They are recognized by the number of nodes, location of nodes in space, number of bonds, and property like shapes of bonds. Some networks have more connectivity (i.e., degrees of freedom) than others, depending on the number of connections between pores.

Several definitions and models have been defined, but the major categories are regular and irregular networks or lattices. Some of the regular lattices were defined by Fatt in 1956. These regular lattices were built by repeating each building unit. Connectivity remains constant for this type of network.

Irregular lattices do not have a repeated building block. Instead they are made of random pieces joined together. For these lattices, the degree of connectivity is defined by averaging all the connections on all the nodes. This is why fractional connectivity exists.

2.2.1. FATT'S NETWORK MODELS

In 1956, Fatt presented four different lattices. These models are as follows:

- **SQUARE** lattice
  - Regular graph of degree four
  - Each edge is a cylindrical tube with radius r_i

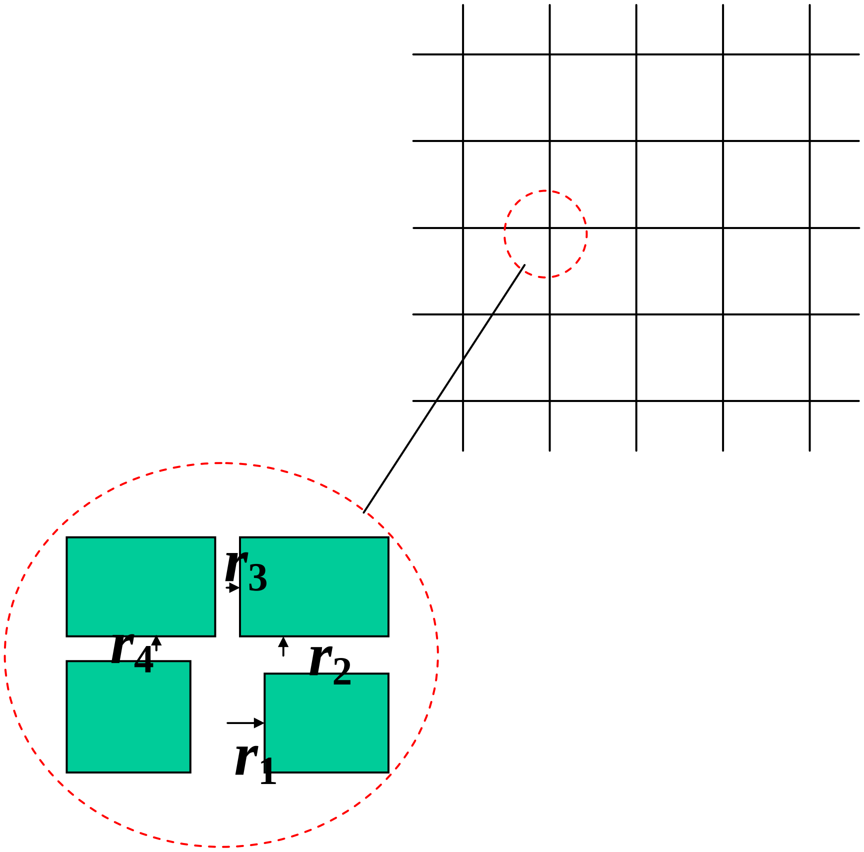

Figure 2.8 Square Lattice with connectivity degree of four [Fatt, 1956]

- **HEXAGONAL** lattice
  - Regular graph of degree three

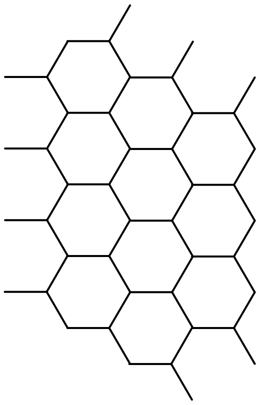

Figure 2.9 Hexagonal lattice, Fatts model [Fatt, 1956]

- **DOUBLE HEXAGONAL** lattice
  - Irregular graph of degree three and six

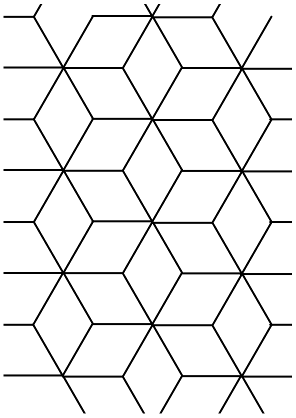

Figure 2.10 Double hexagonal lattice, Fatts model [Fatt, 1956]

- **TRIPLE HEXAGONAL** lattice
  - Regular graph of degree six

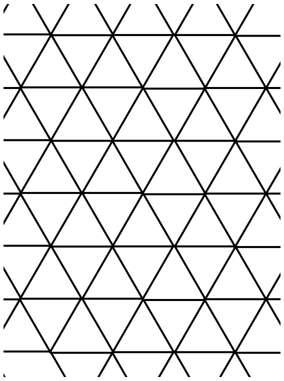

Figure 2.11 Triple hexagonal lattice, Fatts model [Fatt, 1956]

2.2.2. IRREGULAR NETWORK

Figure 2.12 shows a 2D irregular network of nodes and bonds with different degrees of connectivity and characteristic lengths. Some nodes have five connections and others have seven connections.

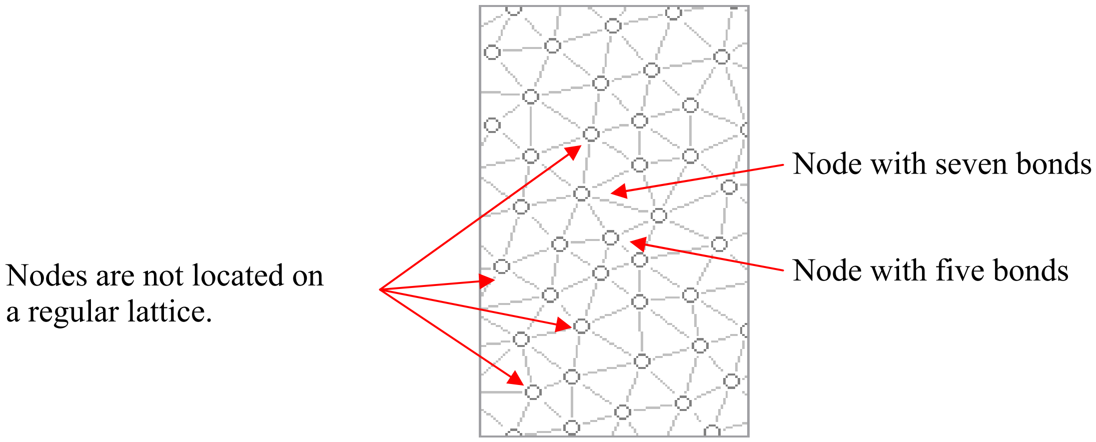

Nodes are not located on
a regular lattice.

Node with seven bonds

Node with five bonds

Figure 2.12 Irregular node locations

Some nodes have five, others have six, and still others have seven degrees of connectivity. Therefore, each node has its own characteristic connectivity. Another important point is that nodes are not located on a regular structure. This is the same for a 1D or 3D irregular network.

The total average connectivity of this sample irregular lattice can be calculated as follows:

Number of nodes = 42

Number of Bonds = $130 \times 2^{*} = 260$

* Each bond has been shared between two nodes, so we have to multiply the number of bonds by two.

$$Connectivity = \frac{Bonds}{Nodes} = \frac{260}{42} = 6.190476.....$$

2.3 PREVIOUS WORKS

There has been much research in the area of pore scale modeling and predicting the petrophysical properties of reservoirs. Most of this research has been done in the areas of permeability and relative permeability curves reconstruction, or predicting the fluid properties of the reservoir and the efforts of matching the results to actual field data.

The interesting physics related to the displacement of a viscous fluid by a less viscous one inside a porous material has been the subject of past and recent years' research, particularly due to its close connections with hydrology and oil recovery [Dullien, 1979 and Sahimi, 1995]. These studies have been fairly successful in describing the complex geometrical features of the displacement structures in terms of statistical mechanical models such as invasion percolation (IP), viscous fingering (VF), and diffusion limited aggregation (DLA) [Chen, and Wilkinson, 1985; Thompson, 1987; Coniglio, 1990; and Oxaal, 1991].

Network models are the most commonly used structure for this type of simulation. Network models typically simulate multiphase flow through an idealized representation of the pore space to calculate average properties, such as relative permeability, capillary pressure, and oil recovery [Bryant and Blunt, 1992; Bakke, 1997; Nilsen et. al., 1996; and Oren et. al., 1997]. The models can only make direct predictions of multiphase properties if both the geometry of the porous medium and the displacement process are precisely known [Fenwick, 1998].

The behavior of the extremely viscous fluid which is attempting to be displaced is still under investigation. Its behavior also depends on the properties of the displacing fluids. These outcomes can vary widely.

Viscous fingering occurs when a high-mobility fluid, such as gas or water, displaces a less mobile fluid, such as oil, in microscopic pore scales. Because the fingers are narrow, they cannot be resolved in conventional macro scale reservoir simulation models. Therefore, empirical models are required that will allow simulators to predict realistic recovery factors [Blunt, 1994]. Viscous fingering is well understood for miscible floods in homogeneous pore systems, where the permeability variations in micro and macro scales are not dominating the displacement, but unstable displacements are still under active research. Blunt et al., also developed a predictive theory which used a fractional flow formulation rather than a dispersive formulation to describe average unstable displacement behavior. According to their paper, the width of the fingered zone is predicted to grow linearly with time [Blunt, 1994]. In this research, we will examine the longitudinal growth of the fingers and determine whether a dominant single finger develops in the invasion process or not.

Most of the earlier research on these topics were based on averaging to obtain a representative value for the large scale field properties. They were also using the capillary control displacement as the engine of these flow rate controls. Vortsos and Satik found that the large scale capillary pressure curve is a non-trivial average of the individual curves [Vortsos, 1991].

Baigorria et al., compared the different approaches for flow in porous media. They compared three methods: 1- Invasion Percolation (IP), which applies where capillary forces are dominant with respect to viscous forces at the fluid interface; 2- Diffusion-Limited Aggregation (DLA) method and 3- The method of Stochastic Networks (SN), which provides both pressure and velocity fields through the simulation process itself. All these methods have been used primarily for assisted and secondary oil recovery, as well as in the contamination of aquifers [Baigorria]. The studies of qualification and quantification of the displacement behavior is still under the scope of research.

The cases of capillary dominant displacement and comparable capillary and viscous forces displacement have been studied to some extent thus far, but the case of viscous dominant displacement has not yet been studied.

Andrade et. al., investigated the dynamics of the viscous penetration in 2D percolation networks at criticality. In their studies, they investigated the case of high ratio of viscosities of displaced fluids and injected fluids. They performed extensive numerical simulations for viscous penetration processes in a typical percolation network of pores. In their study, the driving force was the potential difference between two points. They used constant pressures, applied between two points which are separated by a distance r. They showed that breakthrough times for different distances of r are similar to the case of unit viscosity ratios [Andrade, 2001].

Ambegaokar et. al., found that, in disordered media with broad distribution of conductance values, viscous fingering is dominated by those regions where conductances are larger than some critical values. This value is the largest set of conductances above this threshold that still preserves the global connectivity of the system [Ambegaokar, 1971]. This basically relates to the sweep efficiency of these types of displacement. One of the reasons that sweep efficiency drops dramatically in viscous displacement is because of the problem of traveling through the fast-paced region, instead of forcing fluids inside the more resistant flow paths to displace the in-situ fluids.

It is also important to mention that Murat and Aharony showed, by numerical simulation with two dimensional percolations, that the clusters generated from viscous fingering (VF) and diffusion have the same fractal dimension at the vicinity of the critical point, although many other geometrical differences can be observed between these two processes [Murat and Aharony, 1971].

Andrade et al., also concluded that the viscous displacement through critical percolation networks constitutes a single universality class, independent of the viscosity ration. This critical value is the largest conductance above this threshold that still preserve the global connectivity of the system. They found that distribution of mass and breakthrough time of the invaded clusters have the same scaling form. This is well established in electrical transport of disordered medium with a broad distribution of conductances [Andrade, 2001].

In two recent studies, the dynamics of viscous displacement through percolation porous media were investigated in the limiting condition of unitary viscosity ratio, $M=\mu 2/\mu 1=1$, where $\mu 1$ and $\mu 2$ are the viscosities of the injected and displaced fluids, respectively. In this situation, the displacement front can be approximately modeled by tracer particles that follow the streamlines of the flow. In their study, Andrade et al., were trying to simulate and explain the behavior of the shortest path and minimal traveling time. But these studies have also shown some characteristics of the viscous invasion, which was not intended. Their simulation showed that fingering occurred and reduced sweep efficiency [Lee, 1999; Andrade, 2000].

The findings of Wang et al., in 2006 indicate that, for strongly water-wet systems like the sand packs, the displacing water phase preferentially invades the small pores or narrow flow channels. The higher the oil viscosity, the more viscous fingering, and the more oil will be left in pores in the process of water flooding [Wang et al., 2006].

2.4 NUMERICAL SIMULATIONS

Numerical simulators use a three dimensional confined regular lattice structure, which dictates a certain number for connectivity. This number is constant for all the nodes in that structure. It can only be less if we apply zero conductivity to some of the bonds, but it cannot be higher than the degree of the lattice. For example, a node in a 3D cubic lattice cannot have a degree of connectivity higher than six.

In this research, we are developing a non-dimensional simulator with the ability to accept up to seventeen connections between nodes. This development, which has never been done before, creates the ability to generate connections, even between the nodes that are not physically located near each other (e.g., non-adjacent pores) and have one or more nodes distance in between, even in different directions with different degrees of connectivity. Figure 2.13 shows an example of this development. In Figure 2.13, nodes number 8 and 12 are connected, although there are two nodes (numbers 9 and 10) that physically created a distance between them.

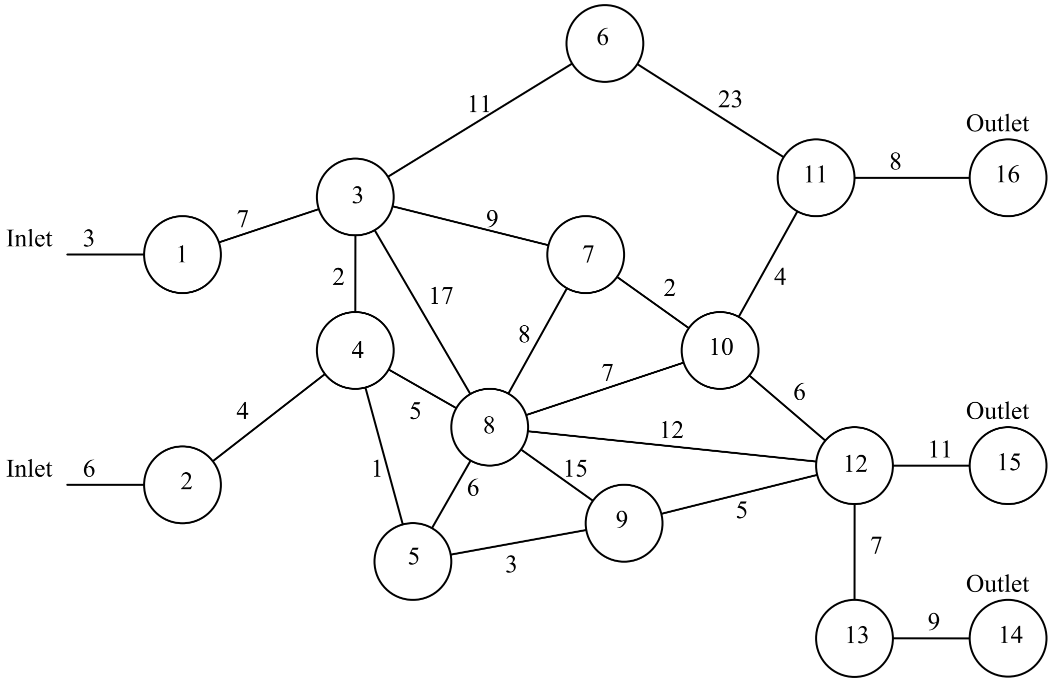

Figure 2.13 Irregular network sample

There are also some other developed simulators which use a digitized sample to make the modeling as realistic as possible, but they don’t have the ability to regenerate the similar samples for multiple realizations [Klov, 2003]. In this approach, we have developed the ability to reconstruct any cumulative distribution of conductances, up to one thousand realizations for each simulation. One can choose any type of conductivities for the network. Examples are; uniform Gaussian random generation of conductivities; a spatially correlated random distribution; a re-sampling of an existing distribution; and reconstruction of a cumulative distribution from that distribution. All these types of distributions and assignment of conductivities can be handled by our code. This ability of conductivity generation, or reading a predefined sample distribution from a file, provides the ability to make multiple realizations on similar distributions, instead of only one network sample and one distribution.

The simulators that have been used in these studies are in the form of regular lattice structures for testing the behaviors of flow, and studying the possible effects and characteristics of flow. These structures include, but are not limited to, square, rectangular, hexagonal, etc. But, the problem of real sample modeling is in the need for a free structure simulator which has not been developed under any previous work. In this research, we have developed a simulator with the ability to obtain a real network sample, and even generate realizations of that real network. Therefore, we have the ability to make realizations of real networks with re-sampling of real conductivities. The other capability that we have implemented in our code is the direct input and construction of networks. One can input a predefined or measured network with both conductivities and topology of bonds and nodes into the simulator and run specific tests.

CHAPTER 3

Problem definition

In this chapter, we explain the viscous dominant problem and the mathematical theories surrounding it. We explain the flow equations, Darcy laws of flow, and the use of these equations to understand movement and behavior of fluids inside the porous medium. We also explain the simplifications that we have implemented to solve the problem.

Ideas like constant potential and moving boundaries are defined here and the use of adjusting boundaries to make more realistic flows inside the porous medium are shown in detail.

3.1 PHYSICAL DESCRIPTION

“The movement of one fluid inside a porous media has been explained by the Navier-Stokes equations. The Navier-Stokes equations, named after Claude-Louis Navier and George Gabriel Stokes, are a set of equations that describe the motion of fluid substances such as liquids and gases. These equations establish that changes in momentum in infinitesimal volumes of fluid are simply the product of changes in pressure and dissipative viscous forces (similar to friction) acting inside the fluid. These forces originate in molecular interactions and dictate how viscous a fluid is. Thus, the Navier-Stokes equations are a dynamical statement of the balance of forces acting at any given region of the fluid” [Polyanin et al., 2002].

The Navier-Stokes equations, unlike algebraic equations, are differential equations which do not seek to establish a relationship among variables such as velocity and pressure. Instead, they make correlations between the rates of change or fluxes of these quantities. In mathematical terms, these are called derivatives. For a simple case of an ideal fluid with zero viscosity, the Navier-Stokes equations state that the rate of change of fluid velocity is proportional to the rate of change (e.g., derivative) of internal pressure [Rhyming, 1991].

This means that solutions for the Navier-Stokes equations of a given physical problem must be sought with the help of calculus. In practical terms, only the simplest cases can be solved in this way and if their exact solution is known. These cases often involve non-turbulent flow in steady state flow - does not change with time - in which the viscosity of the fluid is large or its velocity is small (e.g., small Reynolds number). Otherwise, equations for turbulent flow should instead be used.

Therefore, to solve such complicated problems with no analytical solutions, we have to use computers to implement the numerical calculations. The use of system of equations solver algorithms is both suggested and implemented to solve the potential fields.

Our specific problem is in defining the movement of fluids with orders of magnitude difference in viscosities. The ratios of viscosities, $\frac{\mu_1}{\mu_2}$, are about 10^5, were μ_1 is the displaced fluid and μ_2 is the injecting fluids viscosities, respectively. To find the solution for this problem, we began with some basic assumptions and simplifications.

3.2 BASIC ASSUMPTIONS

The main assumptions applied to our model are as follows:

1. No chemical reaction between fluids;
2. No chemical reaction between fluids and rock;

3. Constant potential at inlet and outlet of the model;
4. Incompressible fluid and rock; and
5. Newtonian fluids.

It is important to show that viscous forces and not capillary forces are dominant in our system. Therefore, we have to calculate the region of capillary numbers for the problem of interest. The capillary numbers are dimensionless values:

$$N_c = \frac{\mu v}{\sigma}, \qquad \text{Eq. 3.1}$$

where N_c is the capillary number (dimensionless), μ is the viscosity of the oil in Newton seconds per square centimeters (N.sec/cm^2), ν is the Darcy velocity in centimeter per seconds (cm/s), and σ is the interfacial tension between the fluids in Newton per centimeters (N/cm), as shown here:

$$N_c = \frac{\frac{N.s}{cm^2} \cdot \frac{cm}{s}}{\frac{N}{cm}} \qquad \text{Eq. 3.2}$$

The common form of units in our industry is centipoises (cp) for viscosity and dynes per centimeter (dyn/cm) for interfacial tension, which does not make the capillary number dimensionless. To change these units to the desired units in the dimensionless form, these variables have to be converted as follows:

$$N_c = \frac{cp.\frac{cm}{s}}{\frac{dyn}{cm}} \qquad \text{Eq. 3.3}$$

$$cp = 10^{-3}Pa.s = 10^{-7}\frac{N.s}{cm^2}$$

$$dyn = 10^{-5}N$$

$$N_c = \frac{cp.\frac{cm}{s}}{\frac{dyn}{cm}} = \frac{cp.10^{-3}\frac{Pa.s}{cp}.\frac{cm}{s}}{\frac{dyn}{cm}10^{-5}\frac{N}{dyn}} = \frac{10^{-3}.10^{-4}\frac{N.s}{cm^2}\frac{cm}{s}}{\frac{dyn}{cm}.10^{-5}\frac{N}{dyn}} = \frac{10^{-7}\frac{N.cm}{cm^2}}{10^{-5}\frac{N}{cm}}$$

$$\Rightarrow N_c = 10^{-2}\frac{\mu(cp).\nu(\frac{cm}{s})}{\sigma(\frac{dyn}{cm})}$$

Eq. 3.4

The Interfacial Tension (IFT) between water and oil (σ_{wo}) is in the range of 24 dyn/cm. Interfacial tension of the injected water can be lowered by adding surfactant to the water. The reduction in the interfacial tension is in the range of 5 to 6 orders of magnitude with the use of surfactant. However using surfactant in heavy oil recoveries has not yet been successfully tested. Please refer to appendix E for the calculated values of water-oil interfacial tensions using Huh's relationship in the presence of surfactants [Huh, 1979].

Heavy oil recovery processes are water and gas injection (which can also have polymer solutions to improve the sweep efficiency), and thermal recoveries such as steam injection. There are also some researches about surfactant injection, which has not yet been successful. We have to calculate the capillary number to understand the process of heavy oil displacement, which can be capillary or viscous dominant displacement or in between. If the capillary number is larger than 0.1, the displacement process is viscous dominant. At a capillary number less than 10^{-4}, capillary forces are dominant; in between 10^{-4} and 0.1 viscous and capillary forces are comparable.

In our cases, the viscosities are in the range of the 10^6 cp, and the Darcy velocities in a heavy oil reservoir are in the range of 1 to 2 feet per day, which is equivalent to $3.5*10^{-4}$ to $7*10^{-4}$ centimeters per seconds, and which we can assume an average of $5*10^{-4}$ velocity.

$$1\frac{ft}{day} = 30.48\frac{cm}{day} = \frac{30.48cm}{86400\sec} = 3.5e10^{-4}\frac{cm}{s}$$

The capillary number for our high viscosity heavy oil displacement with the use of low viscosity fluids will be calculated as

$$N_c = \frac{\mu v}{\sigma} = 10^{-2}\frac{10^6(cp)*5e10^{-4}(\frac{cm}{s})}{24(\frac{dyn}{cm})} = 0.21$$

According to Bryant and Blunt [Bryant et al., 1992], a capillary number above 0.1 is an indication of dominant viscous forces. Therefore, viscous forces are dominant in determining the fluid configuration in this displacement study research.

3.3 FLOW OF TWO FLUIDS

The Navier-Stokes equations are based on the assumption that the fluid, at the scale of interest, is a continuum, i.e., is not made up of discrete particles. Another necessary assumption is that all the fields of interest, like pressure, velocity, density, temperature, and so on, are differentiable (e.g., no phase transitions).

The equations are derived from the basic principles of conservation of mass, momentum, and energy. For that matter, sometimes it is necessary to consider a finite arbitrary volume, called a control volume, over which these principles can be applied. This finite volume is denoted by Ω and its bounding surface. The control volume can remain fixed in space or can move with the fluid.

Navier-Stokes equations indicate that by solving the pressure or potential field inside a network containing incompressible fluids, we can calculate and predict the flow movement.

For more details, equations and their derivations from the Navier-Stokes equations, please refer to Appendix E.

In the porous medium the inlet pressure should overcome the outlet pressure which prevents the fluid from invading the pore.

For any given bond in the porous medium, having incompressible fluid, flow of displaced fluid (index d) is equal to the flow of invading fluid (index i). Therefore

$$q_i = q_d$$

Where q_i is the flow of the invading fluid and q_d is the flow rate of the displaced fluid, respectively. Potential at the interface between the invading and displaced fluids are shown in Figure 3.1.

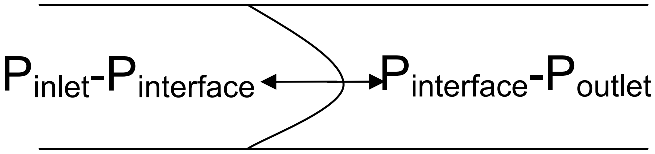

Figure 3.1 Interface potentials

For the invading fluid, the Darcy equation is

$$q_i = \frac{kA}{\mu_i L} \Delta P_i \qquad \text{Eq. 3.5}$$

The potential gradient is $\Delta P_i = P_{inlet} - P_{\text{interface}}$ (Eq. 3.6) and i represents the invading fluid. For displaced fluid we have:

$$q_d = \frac{kA}{\mu_d L} \Delta P_d \qquad \text{Eq. 3.7}$$

With the potential gradient of $\Delta P_d = P_{\text{interface}} - P_{outlet}$ (Eq. 3.8) and d represents the displaced fluid. Since $q_i = q_d$ in a tube:

$$q_d = q_i \Rightarrow \frac{kA}{\mu_d L} \Delta P_d = \frac{kA}{\mu_i L} \Delta P_i \qquad \text{Eq. 3.9}$$

$$q_d = \frac{kA}{\mu_d L} (P_{\text{interface}} - P_{outlet}) = \frac{kA}{\mu_i L} (P_{inlet} - P_{\text{interface}}) = q_i$$

Eq. 3.10

$$\frac{\mu_d}{\mu_i} = \frac{P_{\text{interface}} - P_{DisplacingSideOutlet}}{P_{InvadingSideInlet} - P_{\text{interface}}} \qquad \text{Eq. 3.11}$$

$$\Rightarrow \frac{\mu_d}{\mu_i} = \frac{\Delta P_d}{\Delta P_i} \qquad \text{Eq. 3.12}$$

The only driving force in a viscous displacement is the potential. Considering the large value of the viscosity of in situ fluid and the invading fluid, the viscosity ratio $\frac{\mu_d}{\mu_i} \approx 10^5 to 10^6$, we need a high potential difference to be able to displace the heavy viscous in situ fluid.

Figure 3.2, shows an ideal piston like displacement.

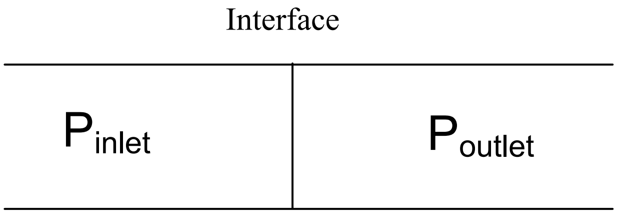

Figure 3.2 Schematic view of interface between invading and displaced fluid, piston like displacement

At the interface, the criterion for the invading fluid to be able to displace the in situ fluid, is

$$P_{InvadingSide} - P_{\mathrm{interface}} - P_{DisplacingSide} > 0 \qquad \text{Eq. 3.13}$$

Therefore, we should have greater inlet potential than the outlet potential plus the interface potential to be able to displace the in situ fluid considering all the other variables equal. The interface potential is the capillary forces between the invading and the displacing fluids. Therefore the force balance has to be

$$P_{InvadingSide} - P_{Capillary} - P_{DisplacingSide} > 0$$

$$\Rightarrow P_{InvadingSide} > P_{Capillary} + P_{DisplacingSide} \qquad \text{Eq. 3.14}$$

The maximum capillary force in this viscous dominant system is in the range of

$$Pc = \frac{2\sigma Cos(\theta)}{r} \qquad \text{Eq. 3.15}$$

$$Pc = \frac{2*24\frac{dyne}{cm}*1}{10^{-2}cm} \approx 5e10^{3}\frac{dyn}{cm^{2}}$$

$$Psi = 6.9e10^{4}\frac{dyn}{cm^{2}}$$

$$therefore$$

$$Pc = \frac{5e10^{3}}{6.9e10^{4}}psi = 0.072psi$$

Where σ, Interfacial tension of the injecting fluid is 24 dyn/cm. Radius of pores (r) in porous medium are usually around 10^{-2} to 10^{-3} centimeters. And the maximum value for Cos(θ) can be 1.

This value is in one bond length. Considering this as a pressure drop in a 10^{-1} cm length in the pore scale, the total drop in a 30 ft well spacing can be calculated as

$$7.2e10^{-2}(\frac{psi}{cm}) = 7.2e10^{-2}(\frac{psi}{cm})*30.48(\frac{cm}{ft})*30 = 65.84psi(\frac{1}{30ft})$$

In a practical engineering project, the inlet and outlet pressures or invading pressure gradients are in the ranges of 10^{3} to 10^{4} psi. Therefore, a pressure drop of 66 psi is 2 to 3 orders of magnitude smaller than the injector pressure and does not have a major affect on the process of displacement.

Therefore, we can express that capillary forces are very small and do not come into calculations in our system and that viscous forces are dominant.

3.4 SIMPLIFICATION OF NETWORK MODEL

The movement of a fluid inside a porous media is a complicated process which has to be modeled to simulate a real flow movement. Imagining a real pore shape which is very complicated (Figure 3.3) and multiply it by millions of pores in a small real sample, it is almost impossible for today’s simulator and computational capacities to calculate all the forces like pressure, gravity, viscosity, chemical reactions between fluids and also rocks and etc., acting on flow inside a pore. Also, the irregular shape of porous media makes it more challenging for us to simulate a real fluid flow inside pores. All these parameters make it very difficult and computationally almost impossible to find the effect of all the physical parameters at once to solve the fluid movement. Therefore simplifying the model is the only way to solve these problems.

Simplifying does not mean that we are not solving the problem, but instead involves disregarding as many parameters as possible in the equations, until we do not lose the reality within a certain acceptable error.

Simplified parameters in our simulation code are the shape of porous media, fluid chemical interactions with each other at the interface and reactions with the pore surface. Because of the scale that we are solving the problem (bigger than micro scale but not macro scale) other important parameters like interfacial tensions are not showing up in equations (as explained earlier).

For example, the shape of a porous medium can be very irregular (see Figure 3.3).

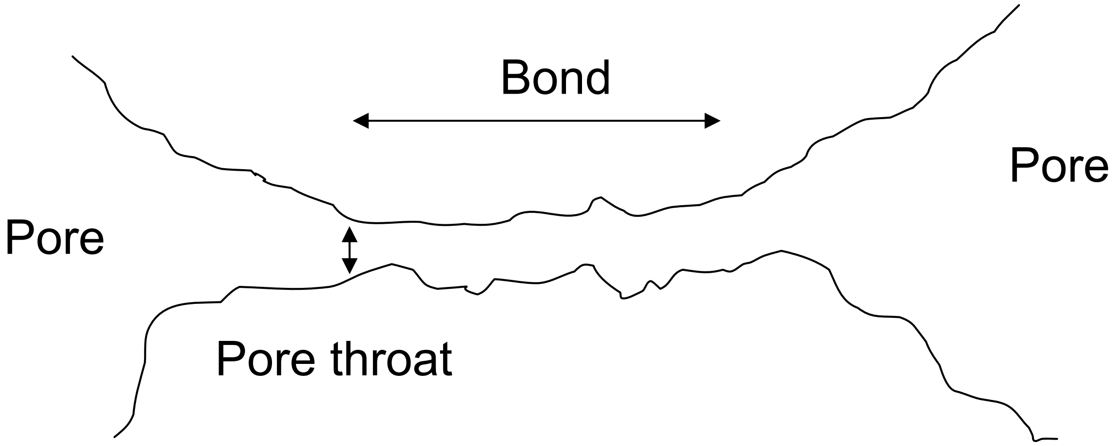

Figure 3.3 Irregular shape of a real pore

As one can see, defining these shapes is not only difficult but can be very time consuming to digitize into a computer model. The other concern is the scale on which we want to simulate such a pore. As we zoom into these pores, shapes continue to change until we get to the molecular scales. We have to go all the way to the molecular scale if we want to have a real pore shape, which is impossible for current computerized calculation capacity.

This makes simulating a 100,000 or 1,000,000 node system completely impossible. So we have to use a simplified model of connectivity between pores, instead of real pore geometry.

To do so one can use a tube model or equivalent conductivity (permeability) instead of simulating a real bond (pore connector) and pore throat. We have used the simplified model of bond conductivity in our model development. We have used radius of each bond and calculated the conductivity of the bond between two pores according to the tube model, which is

$$g_{hydraulic} = \frac{\pi r^4}{8l} \qquad \text{Eq. 3.16}$$

g	Hydraulic conductivity
r	Radius of the bond
μ	Viscosity of the fluid
l	Length of the bond

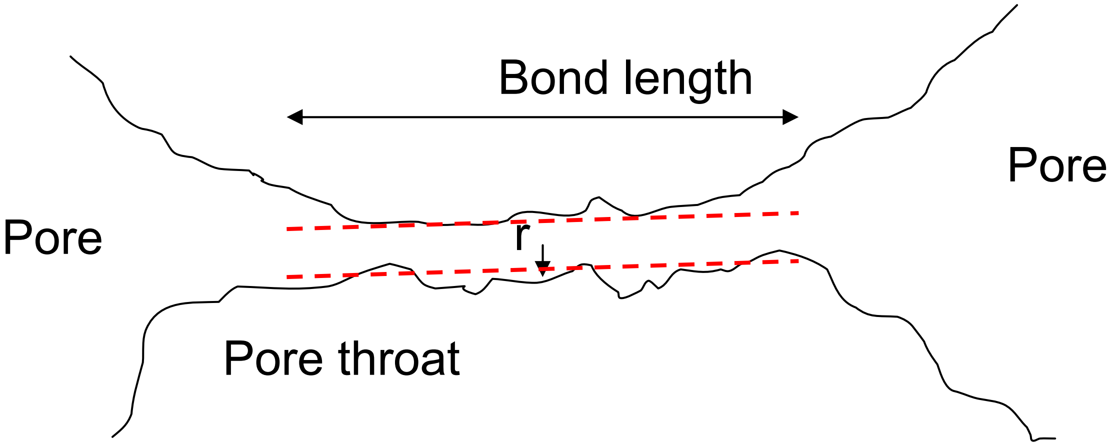

Figure 3.4 Equivalent conductivity of a bond

This calculated conductivity is the one used in equation 3.5 and 3.7. In our simulator one can easily generate random values for the radius of each bond, and the program calculates the conductivity of the bond for each existing bond in the model. But these radii can be read directly from a radius file or even be directly assigned to the bonds from an imported conductivity file.

This is the major simplification in our model, which is same as all other available models, due to the lack of computational and memory capabilities.

The other important simplification in our model is the interface contact between two fluids. We are assuming no miscibility at the interface. This is true for the interface between low viscosity and the heavy viscous in place fluid. This means we have a sharp front at each fluid contact in the bonds. Therefore, there is no need for calculating the miscibility zone and recalculate the whole field for every small moving distance in each bond. It means we do not spend a lot of computer time to calculate the differential fluids movement in each bond if the invading fluid is moving only a small fraction of the bond length in each step.

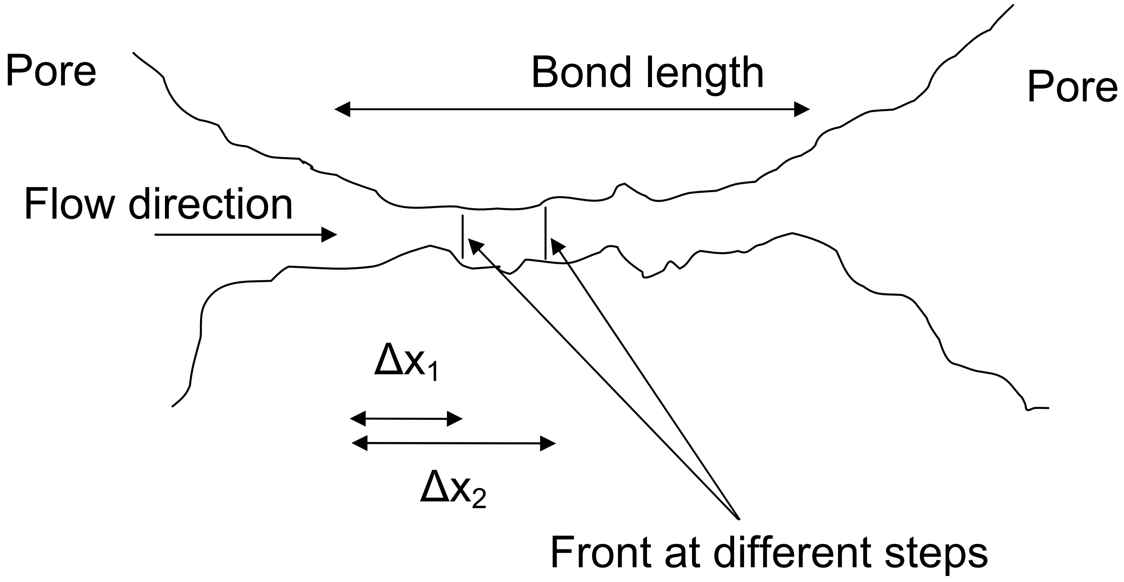

Figure 3.5 Differential movement of fluid inside the pore connecting bond

As shown in Figure 3.5 as flow moves from Δx_1 to Δx_2, potential field in the system changes. This needs a new updating for the potential field which means new calculation. Because any potential has to satisfy the whole network we can not just calculate the potential change for just one bond and two nodes. Therefore we have to calculate the whole potential field for the network for any small movement of flow which is expensive.

To take care of this issue we have made another assumption. If the potential difference between two nodes connected by any given bond in the system (P_1 and P_2), is above seventy percent of the highest potential difference of the ends of any bond in the network at each step of invasion, we assume that the flow has invaded the target pore and passed through the connecting bond. Therefore the potential differences that are thirty percent less than the maximum potential gradient in any given bond cannot pass through the bond and invade the target pore.

Figures 3.6 to 3.12 show the sensitivity study for the choice of seventy percent value. Tests have been performed on a 200 × 100 square lattice with re-sampling of a Finney pack distribution (refer to 5.5 cumulative distribution). All the nodes at the left of the Figures 3.6 to 3.12 are inlet nodes and connected to a potential of 5 units and all the nodes on the right are connected to the outlet with potential of 1 unit. Figure 3.6 shows the case in which only maximum potential passes through the bonds. This figure shows a very thin (one pore thickness) invasion through the network.

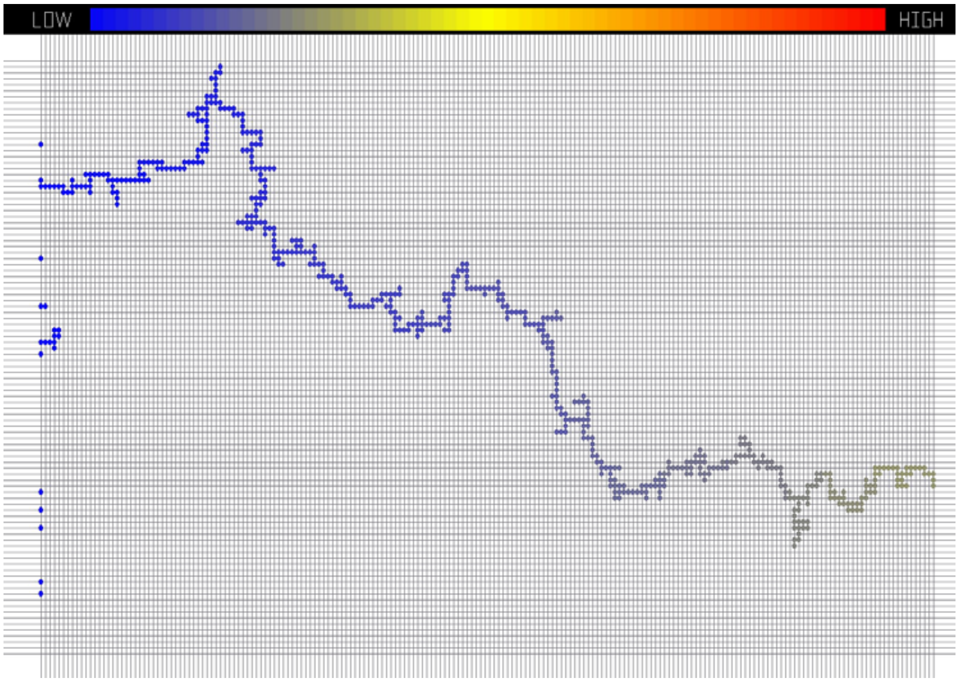

Figure 3.6 Only the maximum potential has been invaded

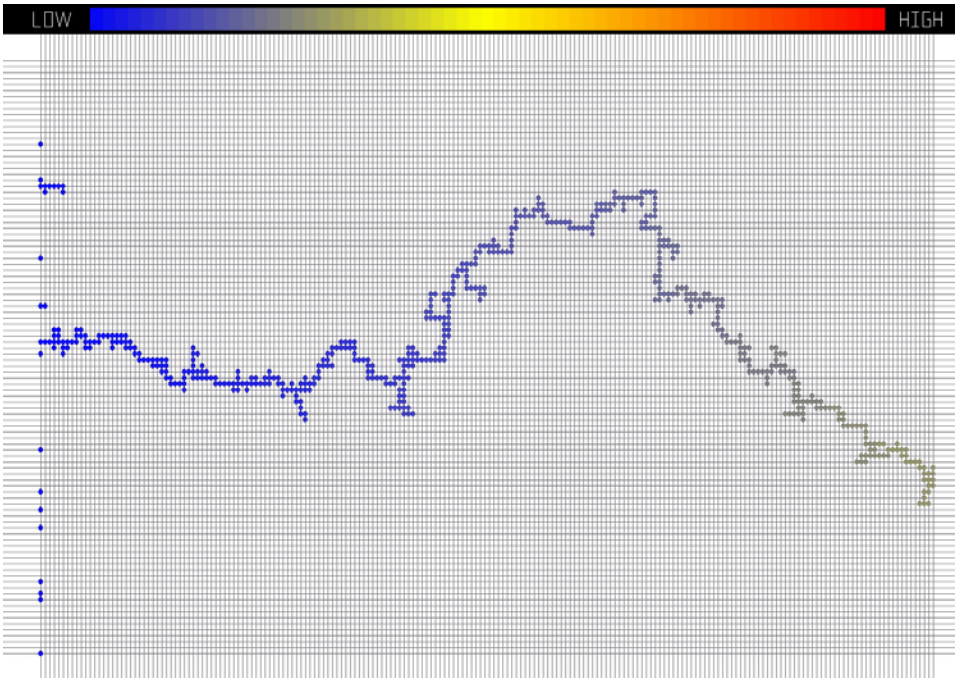

Figure 3.7 Only the top 10 percent of potentials have passed the bond

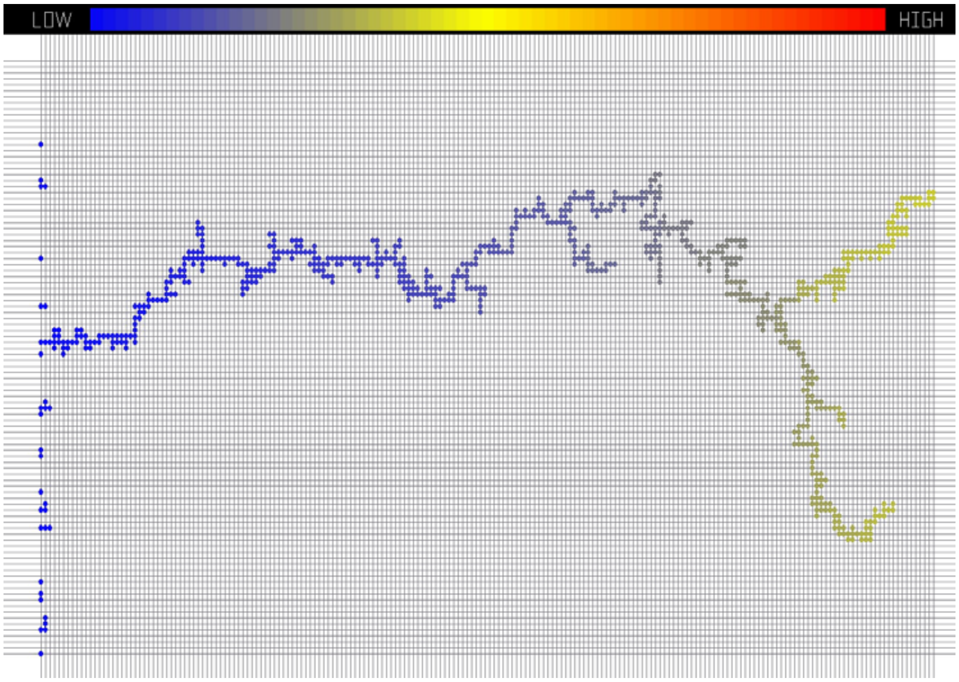

Figure 3.8 Only the top 20 percent of potentials have passed the bond

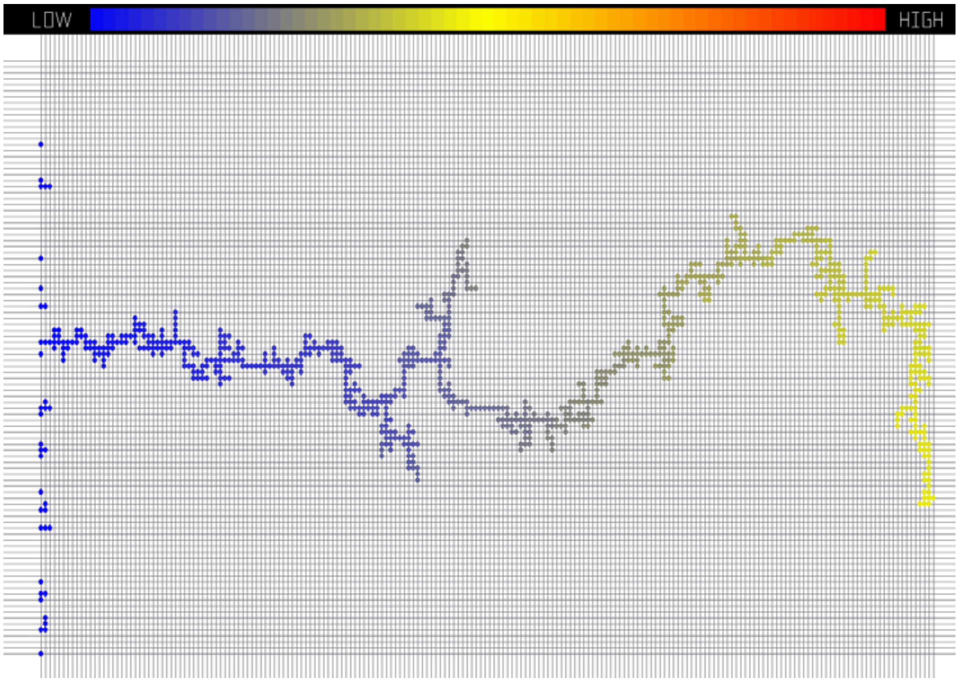

Figure 3.9 Top 30 percent of potentials have passed the bond

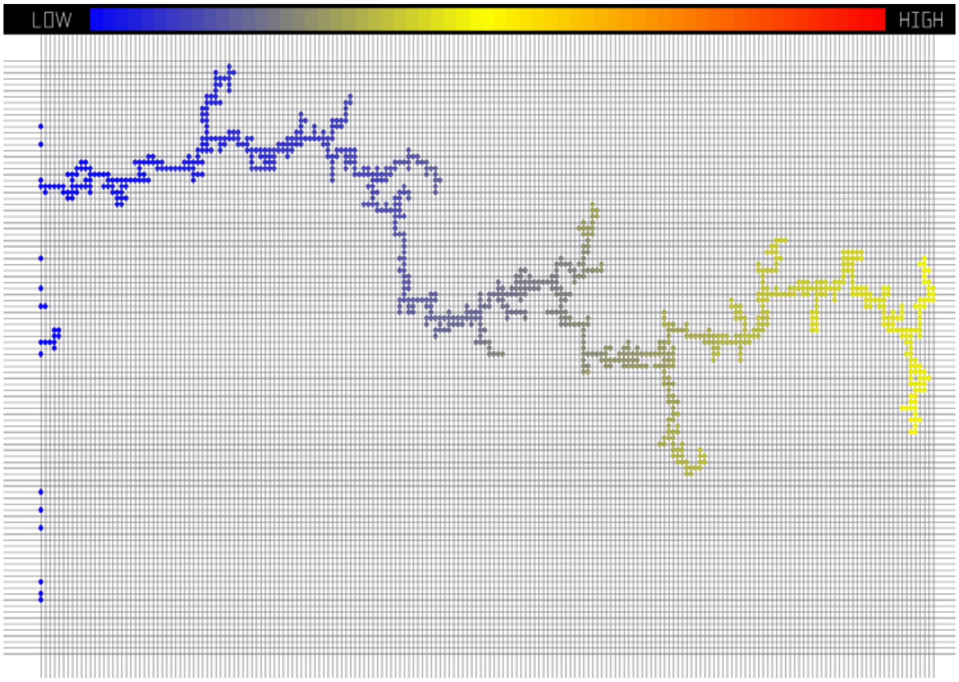

Figure 3.10 Top 40 percent of potentials have passed the bond

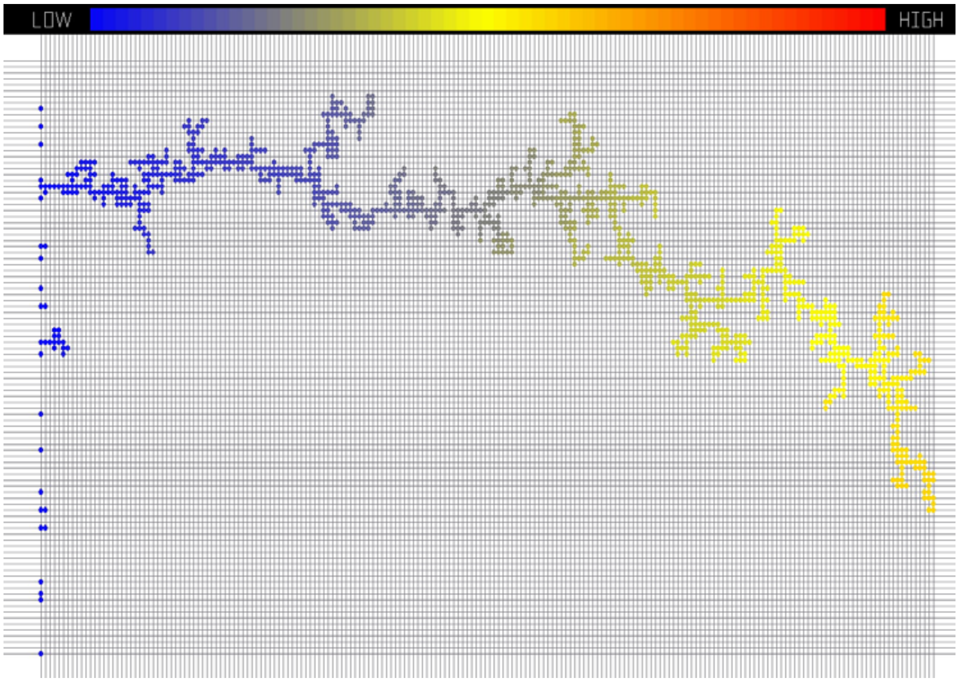

Figure 3.11 Top 50 percent of potentials have passed the bond

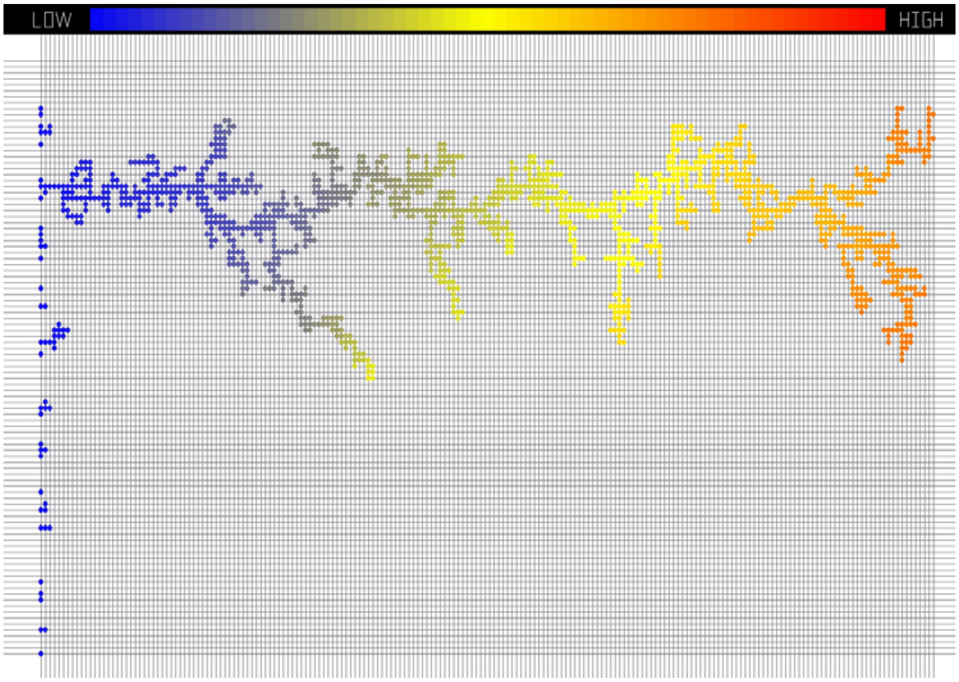

Figure 3.12 Top 60 percent of potentials have passed the bond

Up to 60 percent of the maximum invasion potential difference we still see the one pore or one bond thickness invasion. But Figure 3.13 nodes have made small clusters that are more than one node or bond thick, and at the same time they are not making thick local clusters of invaded nodes. As in Figures 3.14 and 3.15, the 80 and 90 percent invasions show very thick flow path. This 90 percent invasion graph shows the case if a bond has only been invaded 10 percent (which is up to 90 percent less than a bond with maximum potential of invasion).

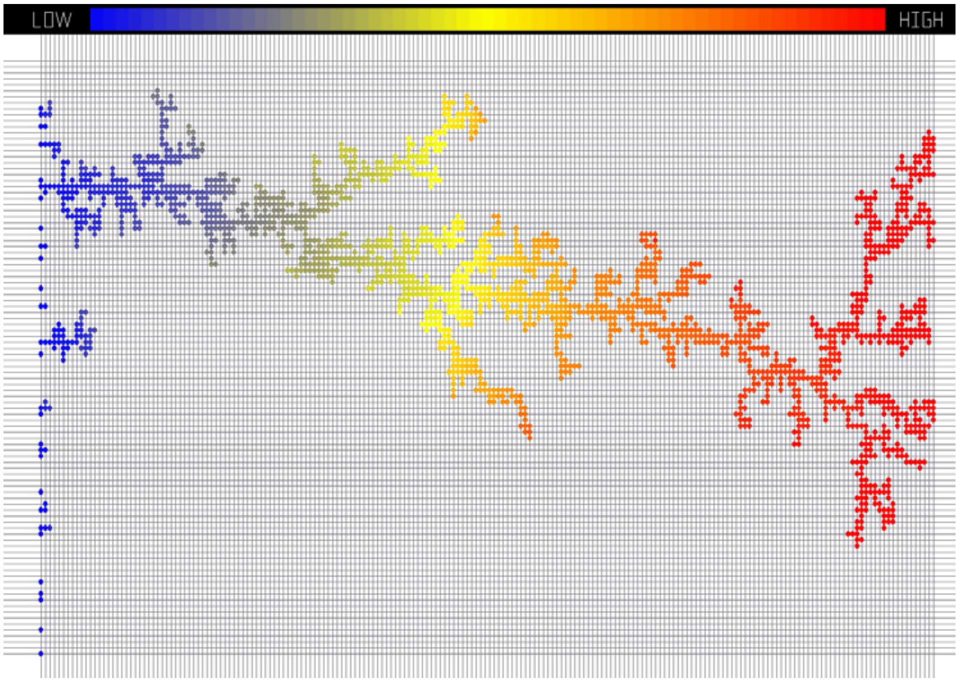

Figure 3.13 All the bonds within the 70 percent of maximum potentials have been invaded

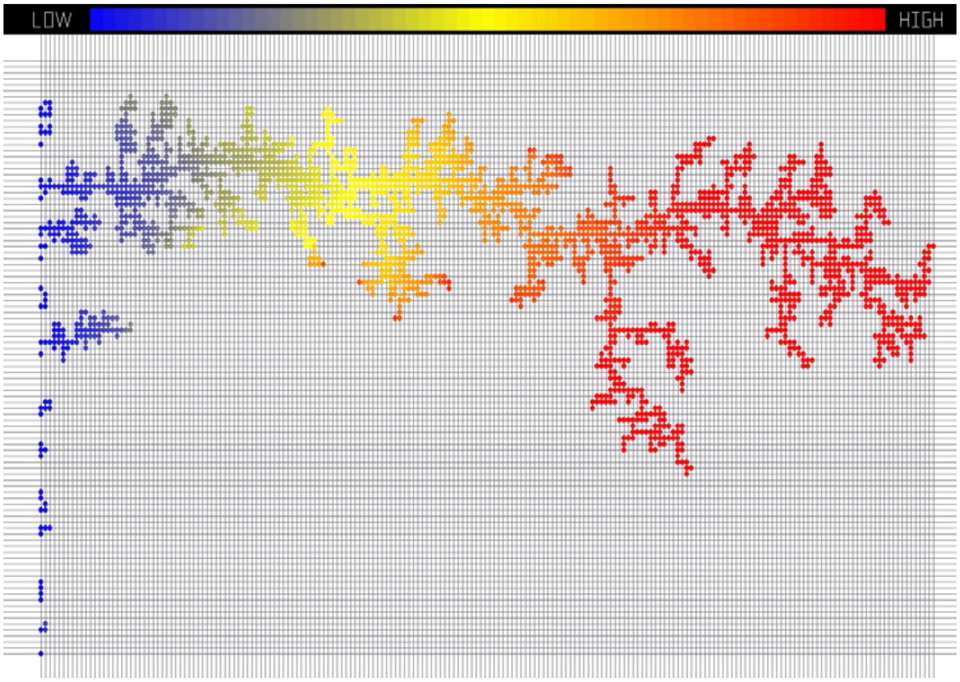

Figure 3.14 All the bonds up to 80 percent of maximum potentials have been invaded

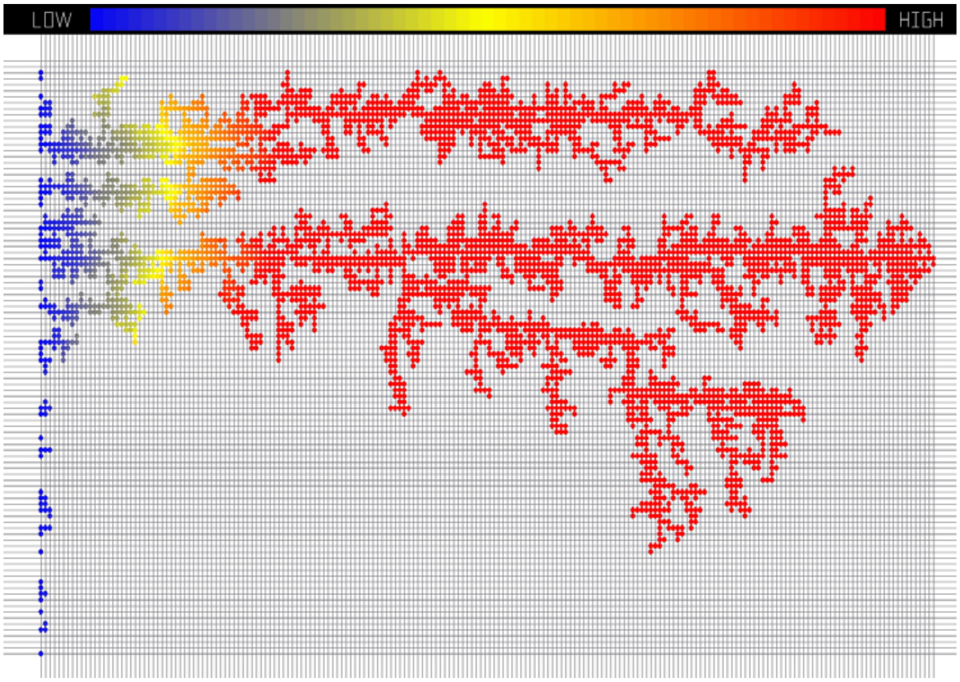

Figure 3.15 All the bonds up to 90 percent of maximum potentials have been invaded

100 percent away from the maximum potential means that all the nodes with any potential have to be invaded. The result of such an invasion is expected to be invasion of all the nodes in the network.

This assumption of seventy percent makes the calculations for the whole network much easier and possible to simulate large network models of 100,000 to 1,000,000 nodes system. We have also added the option of using different percentage bracket from the maximum potential difference in the system.

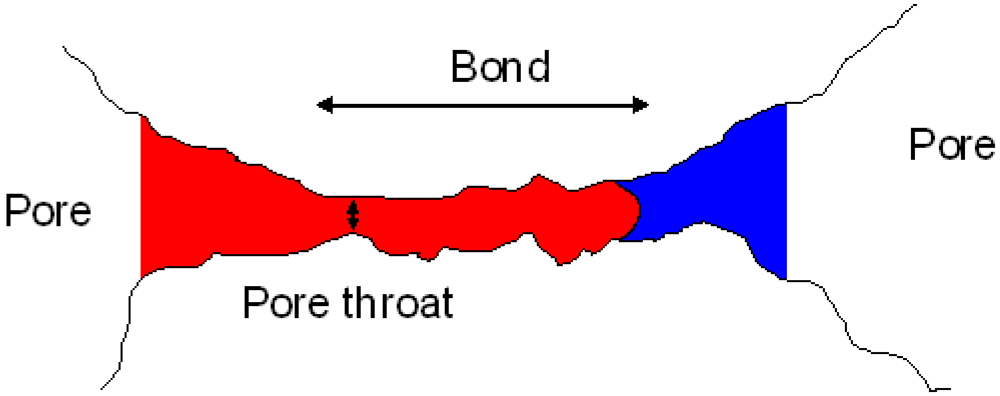

Figure 3.16 Invading fluid has passed the pore throat

Figure 3.16, shows when a bond has been invaded and the invading fluid has passed the pore throat (the point with highest required potential to invade), the rest of the bond can be easily be invaded without any additional potential increase. It takes only time for invading fluid to advance through the rest of the distance in bond and invade the next pore body.

3.5 CONSTANT POTENTIAL

This is one of the most important aspects of our model. Without a constant potential consideration we will not be able to simulate a realistic invasion. The idea has emerged from the characteristics of the invading fluid point of view. Constant potential in the invaded nodes means that in the whole invaded cluster that is connected to the inlet, the potential drop is considered zero, therefore the potential at every point in the invading fluid is equal to the potential or pressure at the inlet.

Figure 3.17 shows the case that invaded fluid has an equal potential in all locations of fluid similar to inlet potential. As one can see, the potential or pressure is constant at all points inside the invaded zone (black dots in the middle of Figure 3.17). It is also equal to the inlet pressure. Boundaries are also no flow boundaries. So the only flow is from inlet with higher potential to the outlet with lower potential. The network is a regular square lattice with connectivity of four. Angle β shows the potential drop in the invading nodes which is zero. The deviation from the horizontal is zero so there is no potential drop. Angle α shows the potential drop in the non invaded zone, which is the overall driving force for the invading fluid to go through the bond and invade the nodes.

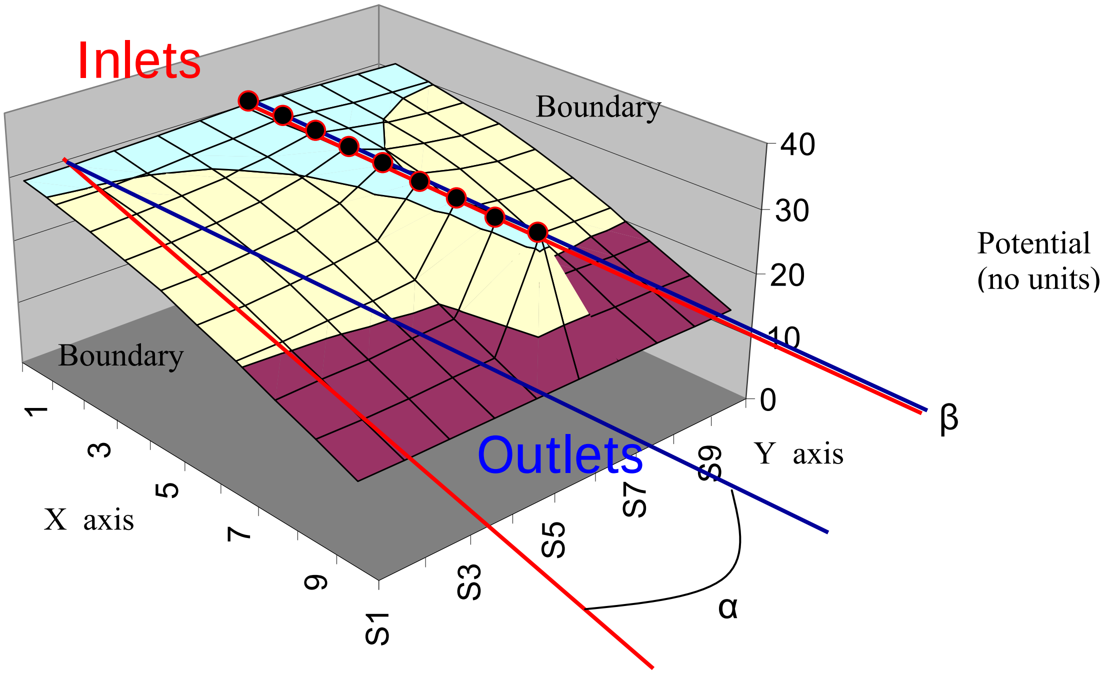

Figure 3.17 Constant potential at all invaded nodes

As is shown in Figure 3.17 there is only a need to calculate the pressure field (potential) at the remaining non-invaded pores. The angle β, the overall pressure gradient in the invaded zone is zero, because the pressure in the invaded pores and inlet is equal. But the overall pressure drop in the non invaded zone (α) is not zero. This $\frac{dP}{dx} = \frac{\Delta P}{\Delta x}$ (Eq.

3.17) is the driving force of invasion. Therefore, we need to calculate this pressure drop and the resulting potential at this part of the network. Constant pressure assumption makes the computational expense much lower since there is only a need to calculate the pressure field in the non-invaded zone.

On the other hand, if we assume that we have pressure drop inside the invading fluid, we need to consider the extra calculation for this additional pressure drop inside the invaded and non-invaded pores. As is shown in Figure 3.18, angle β is not zero any more. This consideration demands much more computational capability. Figure 3.18 shows these two pressure drops that have to be calculated at the same time. All the other assumptions are the same as before.

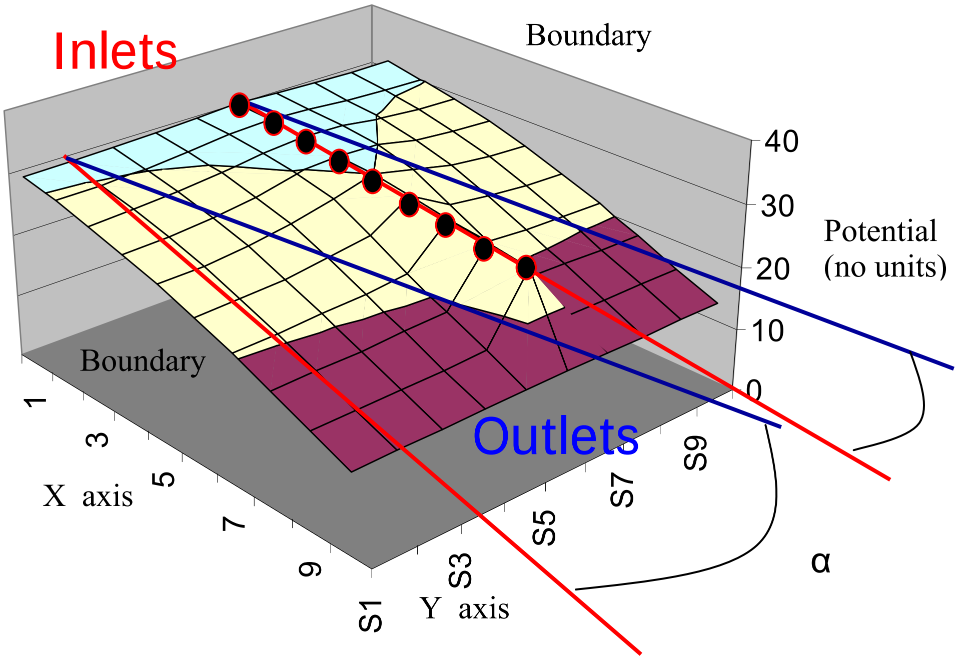

Figure 3.18 Pressure drop inside the invading and displaced fluids at the same time

As shown on Figure3.18, not only we do have a pressure drop in the non-invaded nodes, but also there is an additional pressure drop with a different rate (slope) inside the invaded zone. Therefore, there are additional steps that need to be considered for such a system that makes it computationally very expensive. Angle β, pressure drop inside the invaded region, is not zero. Also, it is different from the pressure drop inside the non-invaded region.

$$\alpha \neq \beta \neq 0 \qquad \text{(Eq. 3.18)}$$

Therefore we have to calculate two delta potential, ΔP_1, inside the non invaded zone and ΔP_2 inside the invaded clusters.

It is important to mention that the assumption of incompressible fluid for the model is very reasonable. Many fluids, unlike gases, have very low to almost zero compress abilities. But this assumption has a huge impact on the computational capabilities to solve problems in the order of 10^5 to 10^6 node system. The reason is as the fluid invades the network and get farther from the inlet potential, the potential at different points inside the fluid becomes different. Different potential has different amount of effect on compressing the volume of invading fluid inside the network. So we have different amount of compression at different points which makes it more difficult computationally. Therefore assuming non compressible fluid will wave the need for extra calculations.

3.6 MOVING BOUNDARY

This objective is the key element in defining the differences in viscosities of the displaced fluid and the invading fluid. The fluid viscosity ratios are assumed to be in the orders of 10^4 and higher. This means the invading fluid has very low viscosity in comparison to the displaced fluid, and since it is assumed to be Newtonian fluid and the pressure drop in the entire injected fluid was zero, therefore the inlet boundary is actually moving with the front of displacement. This consideration will prevent the extra computational efforts needed if the injected fluid was compressible as discussed before.

As the fluid invades more pores in the network, the pressure or potential field is being updated and all the invaded nodes get the same pressure as the inlet. So all of the invaded pores will have a single pressure value the same as the inlet pressure at the beginning of the invasion. Figures to show this effect and updated pressure field for each invaded node in the system. For simplicity, only a sample 2D network has been shown to present this idea (Figures 3.19 to 3.24). The exact similar effect has been implemented in the 3D simulation model.

We have a regular square lattice with connectivity of four, two no flow boundaries, inlet has higher potential than outlet and system is a 2D network. We assume that invaded nodes have the same potential as the inlet.

The following figures show some intermediate steps of the pressure invasion and the resulting pressure field. The first is Figure 3.19 which is the system at the start of an invasion before any invasion takes place. Figure 3.19 shows the pressure field before any invasion. It shows only a linear drop of pressure throughout the field.

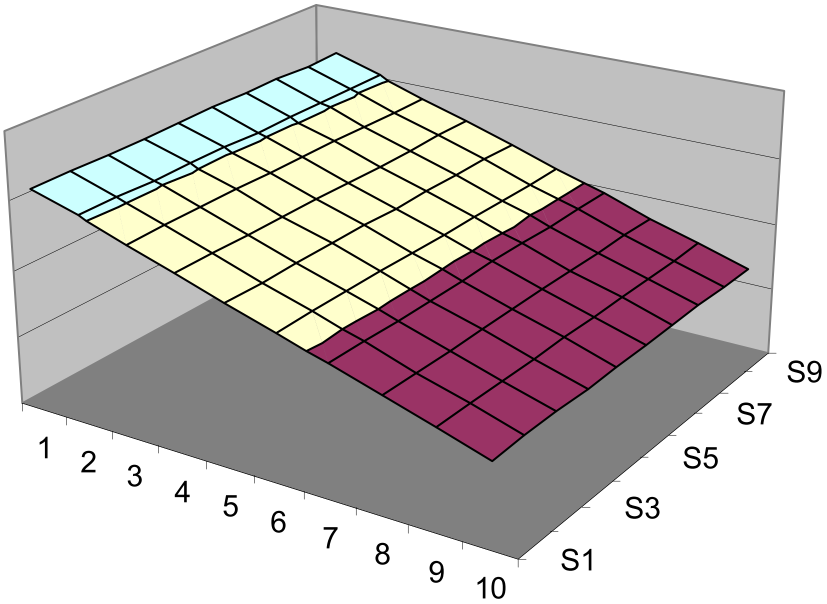

Figure 3.19 Pressure field at rest, before the invasion

Figure 3.19, is a simple invasion where some of the pores are being invaded by fluid. Figure 3.20 shows that invaded nodes made a linear finger in the network. The invaded nodes (marked with red dots on the graph) will get the same potential as the inlet potential, and therefore the resulting pressure field will change. Because it carries a very low viscosity in comparison to the displaced fluid and by our assumption, the pressure will remain constant along the invaded cluster. Updating the pressure field will give a new pressure field for the next invasion step.

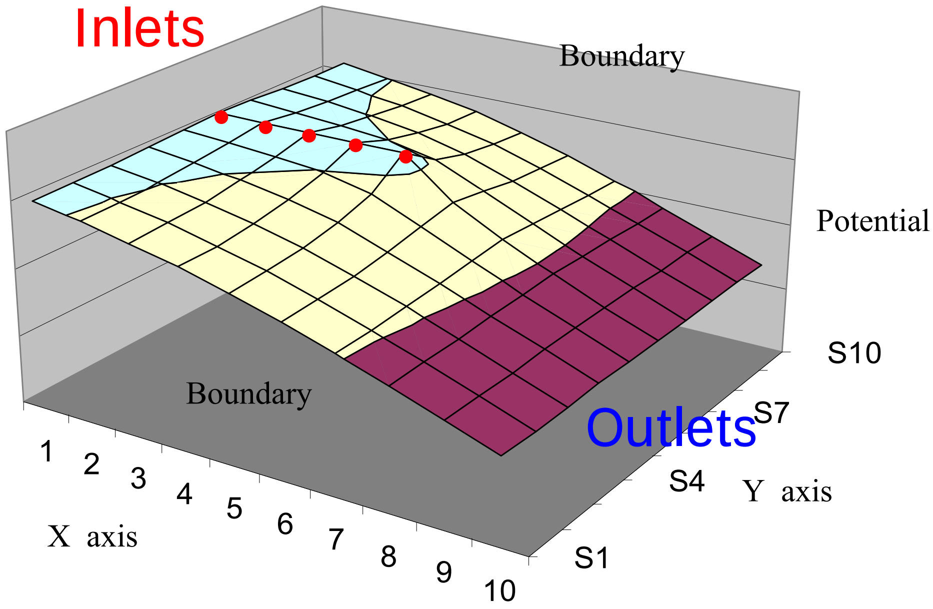

Figure 3.20 Pressure field after five pores being invaded

Figure 3.21 shows another node that has been invaded. This is an imaginary invaded node that has been placed to demonstrate the problem. Comparison of these two last figures shows a big change in the potential field by just one extra node being invaded closer to the outlet. This last invaded node can hugely impact the flow in the nodes behind it by reducing the potential gradient between them and the outlet and preventing them from seeing the potential at the outlet.

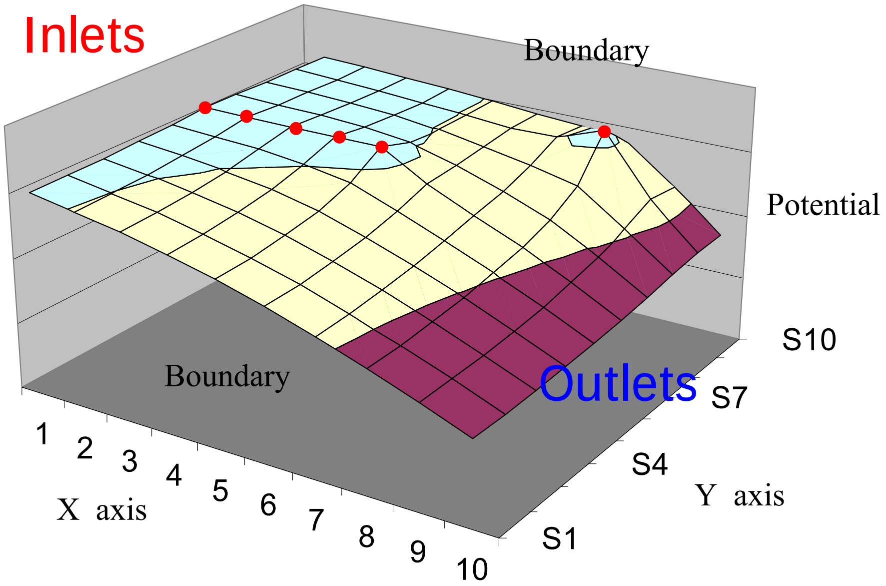

Figure 3.21 Pressure field when an additional node reduces the flow path for some pores behind it

Figure 3.22 shows a couple of extra invaded nodes along the intersection of the two previous invasion paths. This invaded algorithm further changed the potential field distribution. Only the invaded nodes have the same potential as the inlet but because of them a No-Flow region has been developed that changes the potential gradient to zero for the nodes inside that region. This has a huge impact on the recovery of the fluids inside the No-Flow region.

This effect will prevent the flow from going inside the No-Flow region, leaving all the oil behind and reducing the sweep efficiency (This will be discussed later).

Another impact that can be observed from this potential field is the higher gradient between the nodes that are closer to outlet and the outlet potential in comparison to the nodes that have more distance from the outlet. This will force the flow to move along the closer front and again will impact the flow through the nodes with lower potential gradient.

As shown in Figure 3.22 the path between inlet and outlet through S10 has a higher gradient than the path through S1.

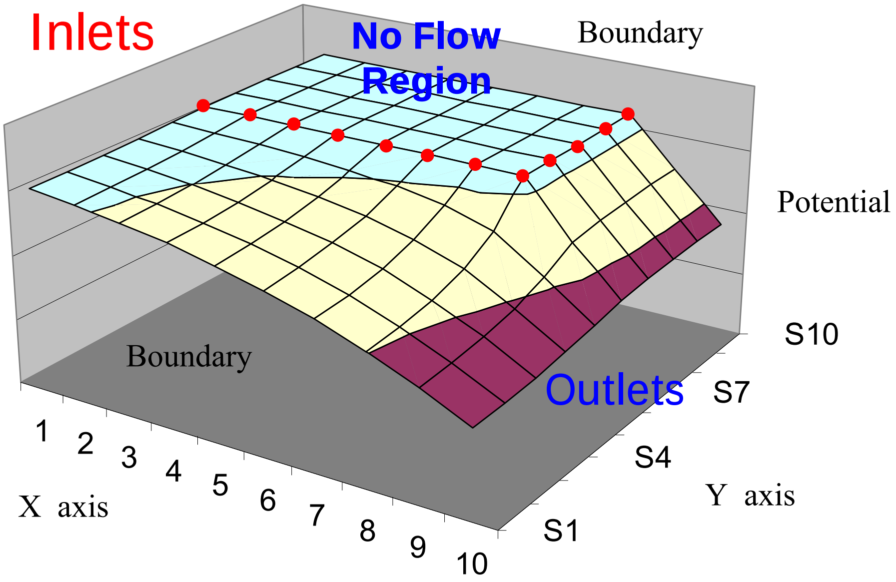

Figure 3.22 No flow region resulted in the pressure field

As can be seen in Figures 3.23 and 3.26 the pores with the highest potential gradient will be invaded. This will cause these nodes to have the highest potential gradient compared to nodes along the path S1 and again for the next invasion step. This process will continue to impact the invasion path until the breakthrough (Figure 3.24).

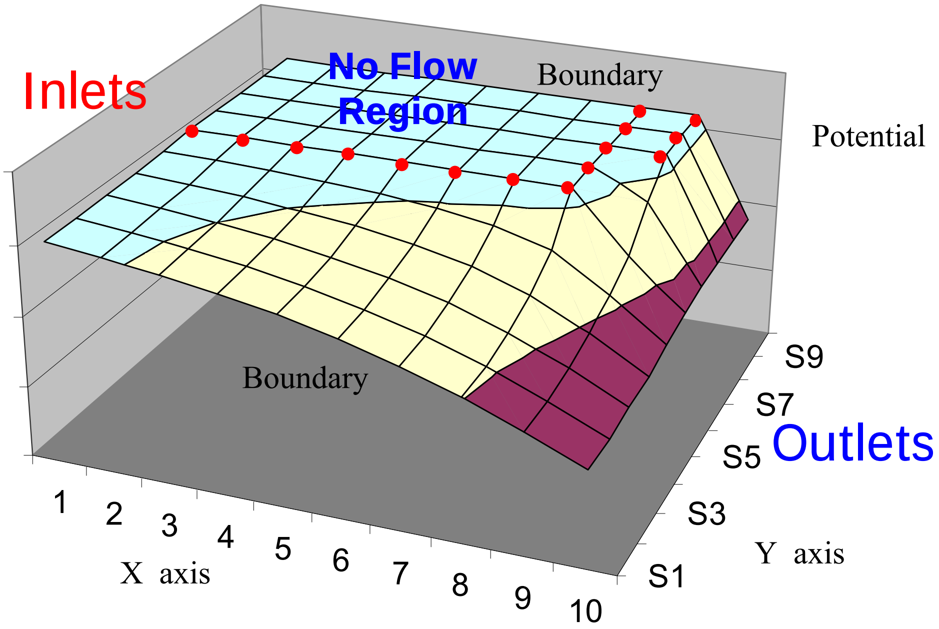

Figure 3.23 Nodes with higher potential gradient will be invaded

The last nodes are making the breakthrough. Figure 3.24 shows the last couple of invaded nodes that are connected to the boundary. This is the moment that the flow path stabilizes. This means that if we don't change the potentials at inlet or outlet the flow rate will not change and therefore no more nodes will be invaded.

To invade more nodes, we either need to change the flow rates (potentials at inlet and outlet) or fluid properties by adding additives like surfactants, solvents and polymer gels. Otherwise, flow will not change its path towards the non-invaded nodes.

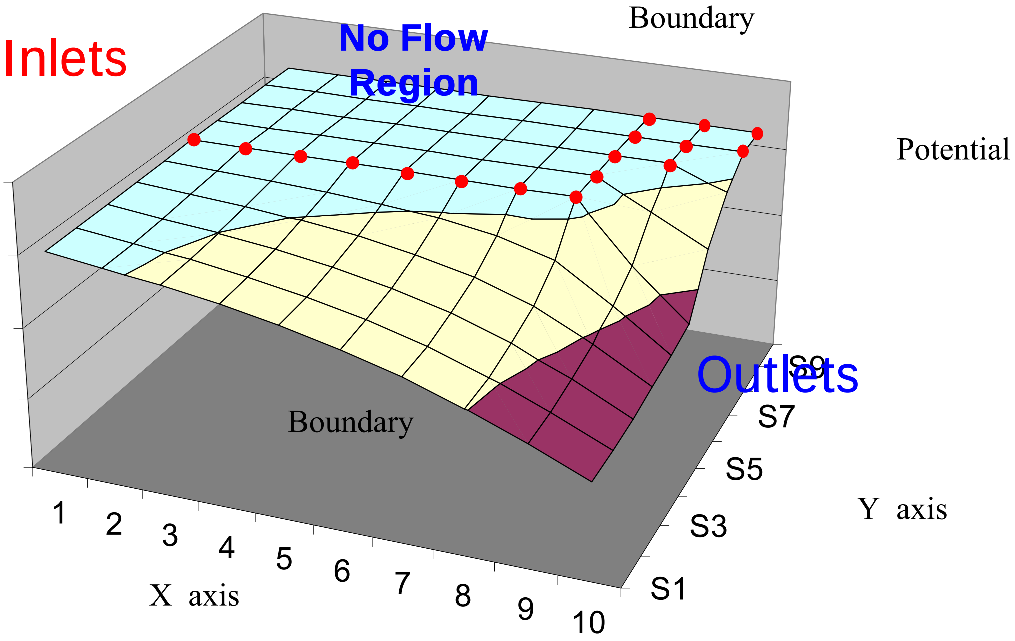

Figure 3.24 Nodes with highest potential gradient at the last step will make the breakthrough

It is very important to consider this effect, otherwise we will not be able to realistically simulate the invasion and make a real model.

3.7 ADJUSTED BOUNDARY

To adjust for the problem of higher potential gradient for the nodes which are closer to the outlet boundary (discussed in the moving boundary section) we have to adjust the potential at the outlet. This adjustment of the outlet boundary will reduce the potential gradient at the nodes which are closer to the outlet and will give more opportunity for the invading fluid to invade all the nodes in the system and move forward towards the outlet and breakthrough.

We have set two different adjustments. One is an adjustment according to the invasion front and the other is an adjustment according to the distance from the inlet. There are some differences in the process of these adjustments but the overall idea is the same, and it is to give similar chances to invading fluid to invade all the nodes. These two adjustments are:

- Front perpendicular plane adjustment.
- Front surface adjustment.

Next we will discuss these two types of boundary pressure (potential) adjustments.

3.7.1. FRONT PERPENDICULAR PLANE ADJUSTMENT

The idea is very simple. We get the fastest invaded node in the system (this node is the closest node to the outlet boundary) and read the potential at all the nodes that are in the perpendicular surface to the flow direction (Figure 3.25). Then according to the potential value in these nodes, we adjust the corresponding outlet node that is in the same linear path. This means increasing the potential at the outlet nodes for those with higher potentials and keeping the outlet potential intact for those that have lower potential. The effect of this process will be a similar potential gradient (for all the nodes that are in same perpendicular surface as the fastest node) between the front and the outlet. This adjustment will also give more chances to all the nodes behind this surface, that have not been invaded, to participate in the invasion process and get the chance to be invaded. Therefore, flow can get through these nodes and move toward the outlet.

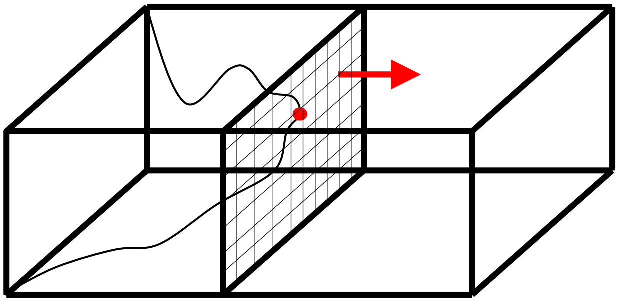

Figure 3.25 Nodes in the same perpendicular surface as the fastest invaded node

Let’s take a look at a 2D example of this process. In this example we start the invasion and in each step we update the outlet boundary with respect to the potential at the front. This is a 20 × 10 node system in x and y directions respectively. The inlet potential is assumed at 5 units and the outlet potential is set to 1 unit. So the potential gradient between the inlet and the outlet is 4 units per total length (Figure 3.26).

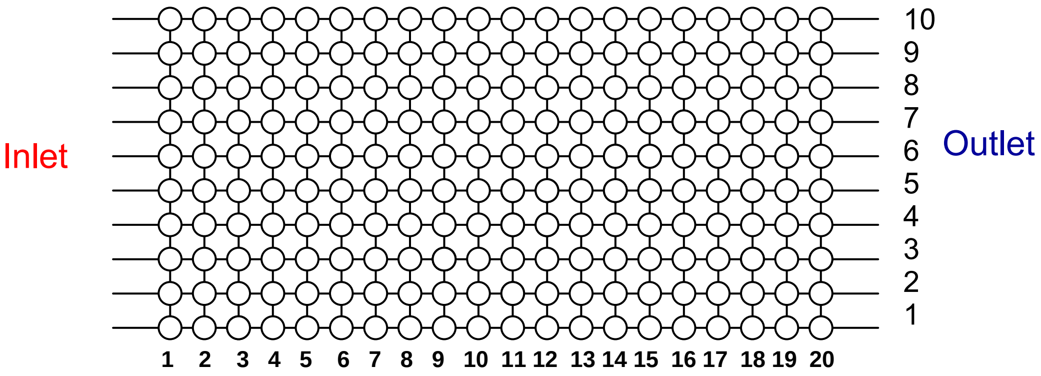

Figure 3.26 The 2D sample node system 20 × 10

After the first invasion step, two nodes have been invaded at the first layer (Figure 3.27). These nodes get the same potential as inlet. The graph of potential at the first layer of invasion is shown in Figure 3.28.

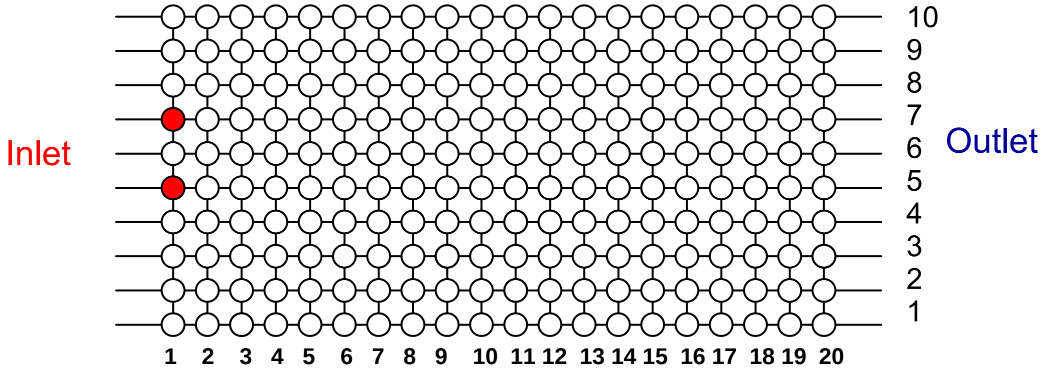

Figure 3.27 The 2D sample node system 20 × 10

The outlet nodes are also being adjusted according to these invaded nodes. As shown on Figure 3.28, the outlet potentials, instead of being one unit, have changed to different values to adjust for the differences between the invaded and the non-invaded nodes.

The procedure is:

First find the minimum potential value on all the nodes with location x of the invaded nodes, which in this case is x = 1. Then calculate the difference with the potential of the invaded node (5 units potential) and apply that difference to the corresponding nodes in the linear path to the outlet, which is a one to one match to the nodes with x = 21 (outlet boundary) .

$$(AdjusteOutletPotential)_i = (V_{inlet} - P_{\min Xplane})_i + PredefincedOutletPotential$$

(Eq. 3.19)

Figure 3.28 shows the potential at the first invaded layer (x = 1). Two nodes have the same potential as the inlet (nodes 5 and 7). Also the outlet nodes have been adjusted to these new potentials with the described procedure. Therefore, nodes 5 and 7 in the outlet boundary (x = 21) have the highest resulting potential and therefore reduced potential gradient. Outlets nodes that are in the same level as the nodes with lower potentials in the front plane, get a lower potential than other outlet nodes, but not less than the assumed outlet potential (1 unit) to have a higher potential gradient in the respected linear path.

This process forces a more balanced potential gradient among all the paths towards the outlet. This process gives a fair chance to all the non invaded nodes in the system to have the opportunity of being invaded without losing communication with the outlet.

It can be seen in Figure 3.28 that almost all the paths towards the outlet will get a similar potential gradient.

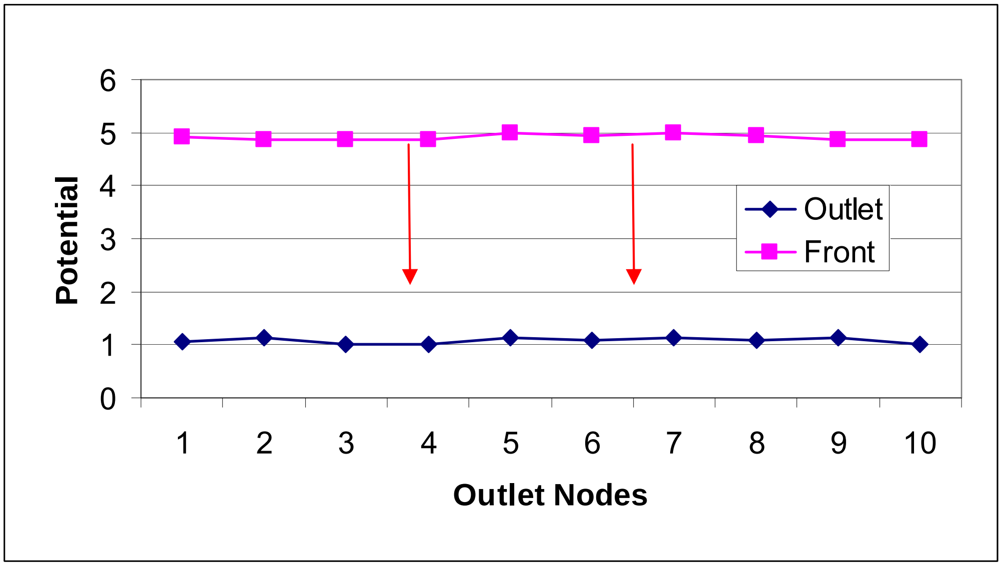

Figure 3.28 Potentials at the first invasion step

After the adjustment process, we start the second invasion step. Every time flow invades one or more predefined number of nodes, the adjustment process re-adjusts the boundary potentials with respect to the predefined outlet potential. Then, recalculate the new pressure or potential field for the next step. This process continues until the breakthrough. Figures and show a couple of middle steps of invasion and the adjusted boundary potential for those steps.

Figure 3.29 shows that the front is now located at the x = 9 and the invaded nodes at the front are in locations 4 and 5. Therefore, the corresponding outlet nodes at the outlet should have the highest adjusted potential for the lowest potential gradient at the outlet boundary.

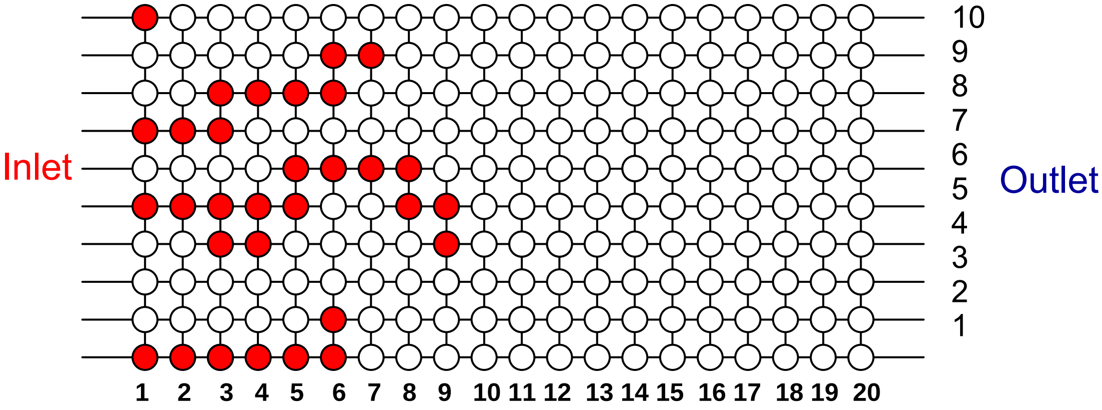

Figure 3.29 More invaded nodes in the 20 × 10, 2D sample node system

Figure 3.30, shows that the outlet nodes located in the same level as front nodes in layers 4 and 5, have the highest potential, equal to inlet.

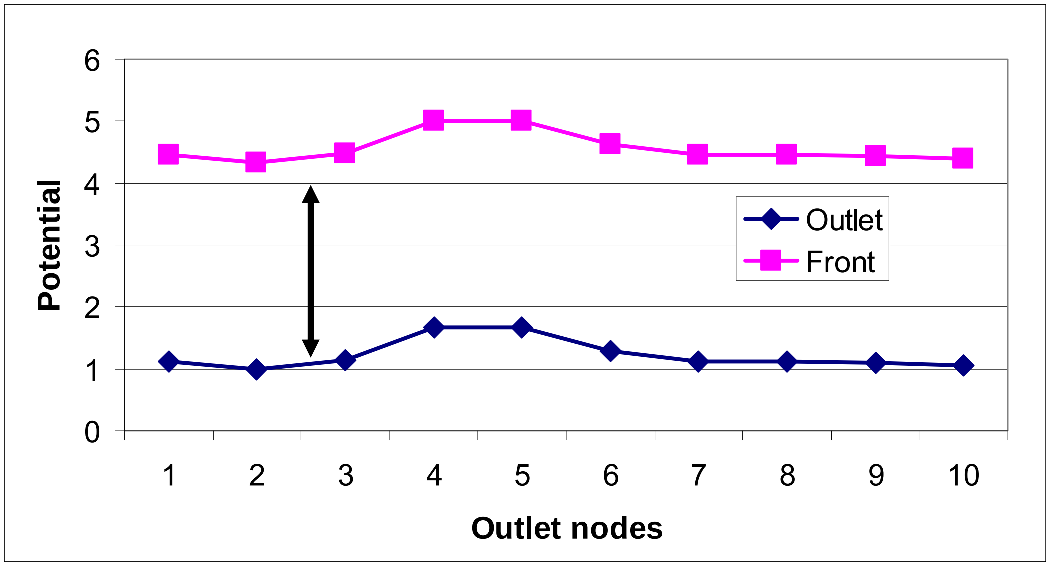

Figure 3.30 Corresponding adjusted potentials at the outlet for the invaded nodes in Figure3.29, middle invasion step

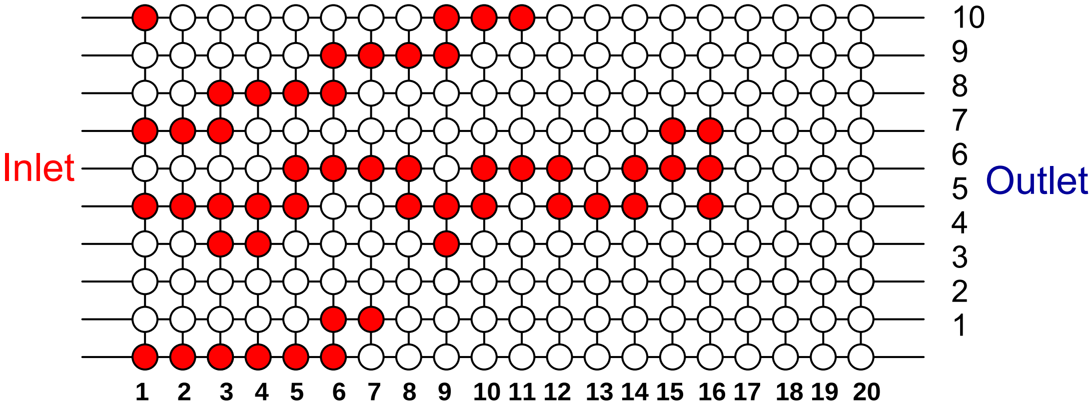

Figure 3.31 More invasions into the sample nodes in the 20 × 10, 2D sample node system.

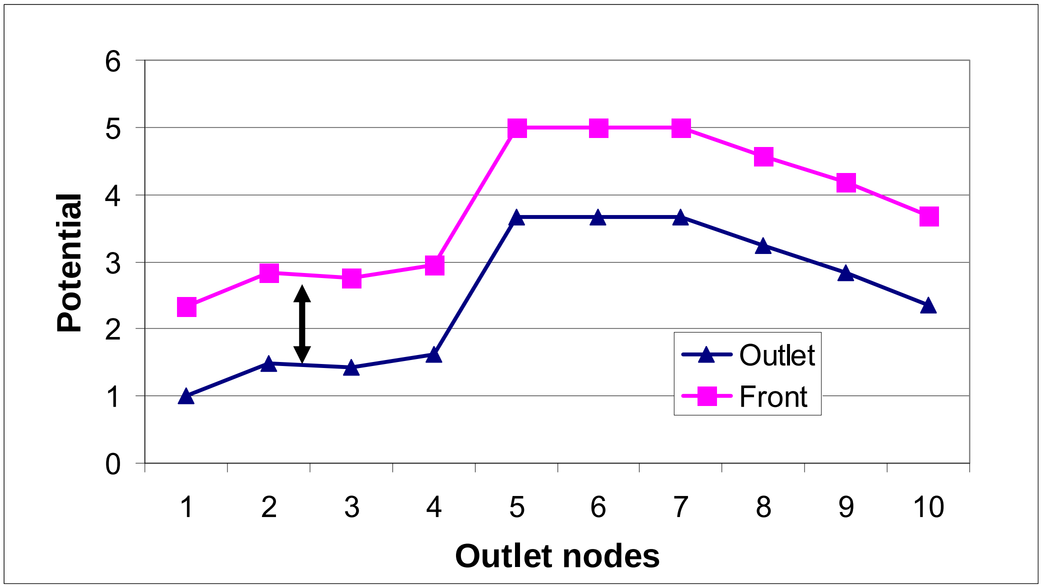

Figure 3.32 Adjusted outlet potentials at some middle invasion step

As Figure 3.31 shows, front is now located at x = 16. Invaded nodes are 5, 6 and 7; therefore we expect the corresponding outlet nodes to have the highest potential for the lowest potential gradient. Figure 3.32 shows the potential at the front layer of invasion and the outlet. As we expected, outlet nodes of 5, 6 and 7 have the highest potential and the other nodes have also been adjusted for an equal invasion chance.

It can be inferred from the figures that as the invasion advances towards the outlet, the outlet potential is adjusted to compensate for the gradient and for lowering the local potential gradient. The key idea is that the potential gradient at all the nodes along the invasion front (perpendicular plane to the flow) has been kept at the same value. Therefore all the nodes along the front plane still have the same chance of invasion if their conductivity allows them to be invaded.

3.7.2. FRONT SURFACE ADJUSTMENT

Front surface adjustment is another way of equalizing the potential gradient. Outlet adjustment according to the distance between the invaded front and the outlet is the same idea as the front perpendicular plane adjustment, which was previously discussed. We have chosen the name "Front Surface Adjustment" to express the idea that in this case the distances are computed from the actual front surface to the outlets and not from the perpendicular plane to the outlet. The difference between front perpendicular plane adjustment and front surface adjustment is that in the latter we are setting the adjustment according to the actual invaded node location in each linear path in the front surface, and not the perpendicular front surface to the path as in the case of the front perpendicular plane adjustment (Figure 3.33).

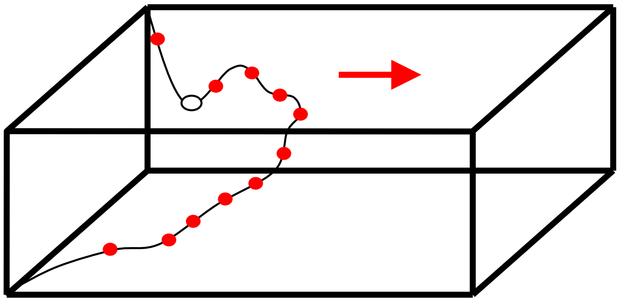

Figure 3.33 Actual front in the process of Front surface adjustment

In the case of the front surface adjustment we can make adjustments for the outlets in which the linear path towards inlet has not even been invaded. In such a case these nodes will get the maximum potential gradients after the adjustment.

Also for the nodes that have been invaded but have some other invaded nodes in front of them, only the most advanced invaded nodes will come to the calculations. An example of such case is the hollow node at the invasion front in the Figure 3.33, which will not come to the calculations; rather the node in front of it in the same line to the outlets will be used for calculations.

The equations and the process of adjustments are the same as the case of front perpendicular plane adjustment and therefore we will not show the process again. The only change between the two cases is the calculation of the distance.

CHAPTER 4

Processes and Mathematical Algorithms

This chapter contains the logic behind each step of the capillary invasion and viscous invasion modeling that has been implemented in this research. The goal is to define the mathematical and logical formulations and strategies behind each part of the model. The computer functions developed by these algorithms have been implemented in the structure of the computer modeling code to simulate a realistic invasion process.

Building the proper structure in developing a computer modeling program is crucial to the future expansions of any model. These structures can dramatically affect the performance of the computer program as the program grows to a larger one. These performances can affect the ability of the software to simulate larger networks in less time.

We have shown in previous chapter that for the movement of fluid inside a porous medium, potentials at both ends of each bond have to be calculated. By knowing these potentials one can calculate the driving force between two nodes (pores). Once ΔP has been calculated, the flow rates for each invasion candidate can be calculated too. Comparing these flow rates or potentials with each other gives us the next invading pore. This pore is the one with the highest potential gradient among all the calculated ΔP's. The criterion for the invasion varies, and depending on the process, can be selected as capillary controlled invasion or viscous controlled invasion.

The developed model in this research is used for the displacement of a high viscosity fluid by a low-viscosity fluid as a moving boundary problem, assuming negligible pressure drop in the displacing fluid and treating P in displaced fluid as steady state problem.

4.1 CAPILLARY INVASION AND VISCOUS INVASION

Invasion percolation was developed for the study of fluid displacement in porous media [Wilkinson et al., 1983]. The theory is based on mapping the threshold pressure of each pore to an occupation probability. In an idealized medium the network of pores and throats may be viewed as a regular lattice in which the sites and the bonds represent the pores and the throats. A random number f_p in the unit interval is assigned to each site and bond to correspond to the threshold pressure. Thus, f_p is the occupation probability indicating that the actual site or bond is filled with the invading fluid at the capillary pressure corresponding to f_p. The invasion percolation process proceeds by letting the displacing fluid grow each time step by occupying the accessible site along the front having the smallest random number. Regions of displaced fluid which become disconnected from the outlet are trapped, and the sites of the trapped cluster can not be invaded. The process is stopped when the invading fluid first percolates, i.e. forms a connected path between the inlet and the outlet. The invasion percolation process is only valid in the limit of extremely slow displacement, that means $Nc \to 0$. In that limit the capillary pressures due to the pore-interfaces are assumed to be in capillary equilibrium and a pore or throat is only invaded by displacing fluid if the capillary pressure is equal to or larger than the corresponding threshold pressure.

In the viscous limit, the principal force is due to viscous forces in the displaced fluid. The process is obtained by injecting a low viscosity fluid into a medium of high viscosity fluid with a high injection pressure or rate. The capillary effects and the pressure drop in the invading fluid are negligible (as mentioned in Chapter 3). The structures typically consist of fingers of invading fluid that propagate through the medium with few trapped clusters of displaced fluid left behind.

Viscous fingering was first studied in a Hele-Shaw channel where one observes fingering patterns when glycerol is displaced by air [Saffman and Taylor, 1958]. A Hele-Shaw cell consists of two transparent plates separated by a given distance and the patterns obtained are fully described by Darcy's equation.

4.2. STEADY STATE FLOW EQUATIONS

In order to simulate the fluid flow inside the porous medium, we have to calculate the potentials and the resulting flow rates at every step of invasion. For every single node on the network model we get a linear mass balance equation. Therefore, we have the same number of equations as the number of nodes in the network.

Let us start with one node and derive the necessary mass balance equation for that node. Figure 4.1 shows a node with four connections.

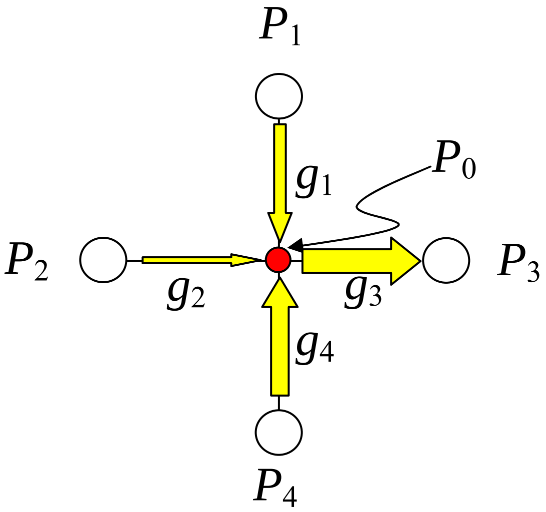

Figure 4.1 Net current in/out of a node

In Figure4.1, the center node has four nodes connected to it and therefore a total of four flow rates into and out of it. We also assume that no mass generation or destruction occurs inside this central node. Each node has its own potential and, depending on the hydraulic conductivity of the bond, has a flow rate. We can write the flow rate in each bond as a function of hydraulic conductivity and the potential gradient between two nodes. Therefore,

$$\begin{aligned} q_1 &= g_1\left(P_1 - P_0\right) \\ q_2 &= g_2\left(P_2 - P_0\right) \\ q_3 &= g_3\left(P_3 - P_0\right) \\ q_4 &= g_4\left(P_4 - P_0\right) \end{aligned} \qquad \text{Eq. 4.1}$$

These rates are shown with arrows in Figure 4.1. The negative value for q means flow out of the node and positive value means flow into the node. According to Kirchoff's law, "Net current into and out of any junction is zero." Therefore, for each node in the network system with M number of connections we can write the general equation of

$$\sum_{j=1}^{M} q_j = 0 \qquad \text{Eq. 4.2}$$

In a network with N number of nodes, this equation will expand to:

$$\sum_{k=1}^{N}\sum_{j=1}^{M} q_{j,k} = 0 \qquad \text{Eq. 4.3}$$

Where $q_{j,k}$ is the flux in jth bond of the kth node. This equation is the sum of all flow conservation parameters in a given network is called the Global Flow Conservation equation. For example, 2D, N by N network, consisting of M bonds per node, has $M*N^2$

number of flow conservation parameters, and a 3D, N by N by N network with M bonds per node, has MxN^3 parameters. All such global flow conservation equations can be written in a matrix form, if we write each flow equation for each node, separately.

To do so, we have to make an adjacency matrix for the node locations to make the connected nodes map of all the nodes in the network. Figure 4.2 shows a 3 by 3 square lattice network example. Circles indicate a node and lines indicate a connecting bond.

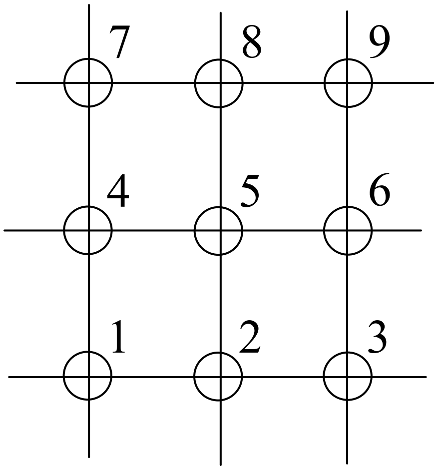

Figure 4.2 2D, 3×3 network

Table 4.1 shows the corresponding adjacency matrix for this 2D network system with 9 nodes. If the value of the matrix is 1, this means the corresponding row and column nodes are connected.

In the adjacency matrix each row number corresponds to the node number in the network. Therefore, the first row belongs to node number 1 and the 9th row belongs to node number 9. The adjacency matrix also shows that in the first row which belongs to first node, nodes number 2 and 4 are connected to node number 1. And similarly in row number 5, nodes number 2, 4, 6 and 8 are connected to that node.

	1	2	3	4	5	6	7	8	9
1	1	1		1					
2	1	1	1		1				
3		1	1			1			
4	1			1	1		1		
5		1		1	1	1		1	
6			1		1	1			1
7				1			1	1	
8					1		1	1	1
9						1		1	1

Table 4.1 Adjacency matrix for the 9 node system example

To build a conductivity matrix, another step, would be to enter the bond conductivity properties at the same locations in the adjacency matrix. This way we will have one table with both the locations of connected nodes and the corresponding property of the connecting bond. Figure 4.3 shows the same 3 by 3 network with the bonds hydraulic conductivities, and Table 4.2 shows the same adjacency matrix filled with the corresponding bond information, which is now called conductivity matrix instead of the adjacency matrix.

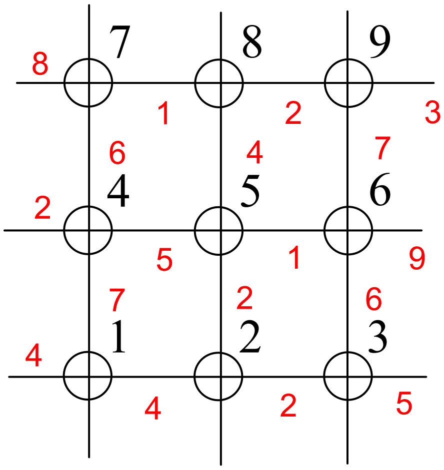

Figure 4.3 3 by 3 square lattice with bond hydraulic conductivities shown

	1	2	3	4	5	6	7	8	9
1	11	4		7					
2	4	8	2		2				
3		2	8			6			
4	7			18	5		6		
5		2		5	12	1		4	
6			6		1	14			7
7				6			7	1	
8					4		1	7	2
9						7		2	9

Table 4.2 Adjacency matrix filled with bond hydraulic conductivities; is now called conductivity matrix

The values in the main diagonal of the matrix shown in Table 4.2 are the sum of all the conductivities in that row, the reason for this sum in the main diagonal will be explained later when we derive the general form of flow equations.

If a cell in Table 4.2 is not empty (zero), this means that the nodes in the corresponding row and column are connected, and the cell value shows the hydraulic conductivity of the connecting bond between the two nodes. For example, in the first row, values in columns 2 and 4 are not zero, which means node number 1 is connected to nodes number 2 and 4. The hydraulic conductivity of the bonds connecting nodes number 2 and 4 to node number 1, are 4 and 7 units, respectively. This is shown in both Figure 4.3 and Table 4.2.

The adjacency and conductivity matrices are similar in occupied cells. Values are all either 1 for occupied cells or zero or empty for non occupied cells in the adjacency matrix. But in conductivity matrix they are some other values depending on the bond properties.

The next step is to fill the adjacency matrix with the conductivity of the bonds in the network to make a system of equations. Later, this system of equations will be solved using numerical methods, to get the potentials and the flow rates corresponding to each node and bond in the network. Figure 4.4 shows the notation for writing the general form of the flow equations honoring the Kirchoff's law.

In Figure4.4, NBR(k,m) means the neighbor m of the center node number k. for example in the figure, P_k has 4 neighbor nodes 1 through 4. And g_j is the flux from the neighbor m to the k^{th} node, j changes from 1 to M (number of connected nodes to the center node).

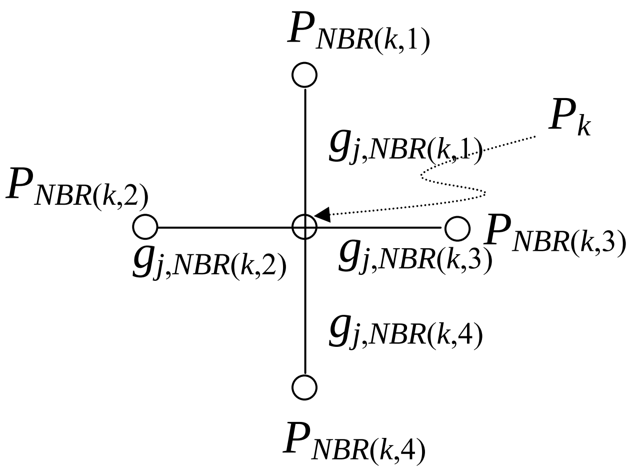

Figure 4.4 General form of flow equations

Therefore, the general form of flow equation for each node in the network can be written as:

$$\sum_{j=1}^{M}\left(g_{j,NBR(j,k)}P_{NBR(j,k)}\right)-\sum_{j=1}^{M}g_{j,NBR(j,k)}P_k=0 \qquad \text{Eq. 4.4}$$

Therefore for every node in the network we can say:

$$\forall k\in\{sites\}:P_k-\frac{\sum_{j=1}^{M}\left(g_{j,NBR(j,k)}P_{NBR(j,k)}\right)}{\sum_{j=1}^{M}g_{j,NBR(j,k)}}=0 \qquad \text{Eq. 4.5}$$

The hydraulic conductivity matrix for all the equations together will result in the general form of the conductivity matrix. For example, we write the general conductivity matrix for the 3 by 3 node system, as a system of equations in the form of a $\bar{G}$ matrix, as follows:

$$\begin{bmatrix}
\sum_{j=1}^{M} g_{j,NBR(j,1)} & -g_{2,NBR(2,1)} & 0 & -g_{4,NBR(4,1)} & 0 & 0 & 0 & 0 & 0 \\
-g_{1,NBR(1,2)} & \sum_{j=1}^{M} g_{j,NBR(j,2)} & -g_{3,NBR(3,2)} & 0 & -g_{5,NBR(5,2)} & 0 & 0 & 0 & 0 \\
0 & -g_{2,NBR(2,3)} & \sum_{j=1}^{M} g_{j,NBR(j,3)} & 0 & 0 & -g_{6,NBR(6,3)} & 0 & 0 & 0 \\
-g_{1,NBR(1,4)} & 0 & 0 & \sum_{j=1}^{M} g_{j,NBR(j,4)} & -g_{5,NBR(5,4)} & 0 & -g_{7,NBR(7,4)} & 0 & 0 \\
0 & -g_{2,NBR(2,5)} & 0 & -g_{4,NBR(4,5)} & \sum_{j=1}^{M} g_{j,NBR(j,5)} & -g_{6,NBR(6,5)} & 0 & -g_{8,NBR(8,5)} & 0 \\
0 & 0 & -g_{3,NBR(3,6)} & 0 & -g_{5,NBR(5,6)} & \sum_{j=1}^{M} g_{j,NBR(j,6)} & 0 & 0 & -g_{9,NBR(9,6)} \\
0 & 0 & 0 & -g_{4,NBR(4,7)} & 0 & 0 & \sum_{j=1}^{M} g_{j,NBR(j,7)} & -g_{8,NBR(8,7)} & 0 \\
0 & 0 & 0 & 0 & -g_{5,NBR(5,8)} & 0 & -g_{7,NBR(7,8)} & \sum_{j=1}^{M} g_{j,NBR(j,8)} & -g_{9,NBR(9,8)} \\
0 & 0 & 0 & 0 & 0 & -g_{6,NBR(6,9)} & 0 & -g_{8,NBR(8,9)} & \sum_{j=1}^{M} g_{j,NBR(j,9)}
\end{bmatrix}
\begin{bmatrix} P_1 \\ P_2 \\ P_3 \\ P_4 \\ P_5 \\ P_6 \\ P_7 \\ P_8 \\ P_9 \end{bmatrix} = 0$$

This is equivalent to:

$$\bar{G}P = 0$$

This general matrix of linear system of equations does not have the boundary condition. Therefore, the right hand side (RHS) of the equation is zero.

Let us assume that there are two no flow boundaries on the top and bottom and the left side is connected to the inlet and the right side is connected to the outlet, as shown in Figure4.5.

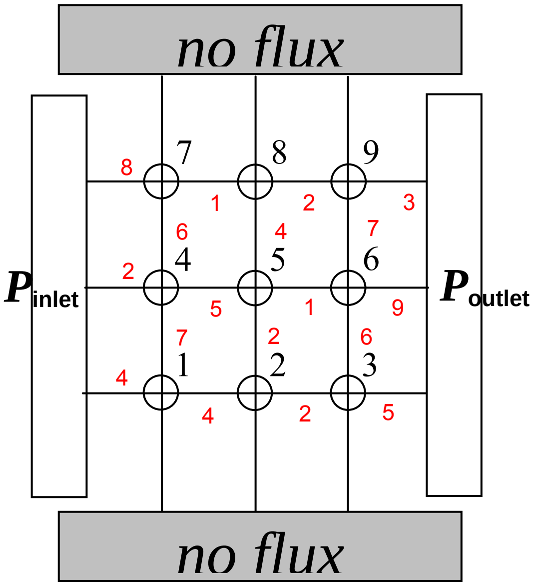

Figure 4.5 Inlet, outlet and no flow boundaries

Nodes number 1, 4 and 7 are connected to the inlet and nodes number 3, 6 and 9 are connected to the outlet. As the equation 4.4 suggests, the flow conservation equation for node number 1 should be in the form of:

$$\left(\sum_{j=1}^{3} g_{j,NBR(j,1)}\right)P_1 - g_{2,NBR(2,1)}P_2 - g_{4,NBR(4,1)}P_4 = g_{inlet,NBR(inlet,1)}P_{inlet} \qquad \text{Eq. 4.6}$$

The right side of this equation is the flow into the node number 1 from inlet. Similarly, all the other nodes connected to the inlet (4 and 7) will have a positive flow equal to the conductivity of the connecting bond between them and inlet multiply by the inlet potential. The nodes connected to the outlet, will have a negative flow equal to the conductivity of the connecting bond between that node and the outlet multiply by the outlet potential. Negative sign is an indication of flow out of the node. Therefore, the RHS vector will be:

$$\begin{bmatrix} g_{(1,inlet)}P_{inlet} \\ 0 \\ -g_{(3,oulet)}P_{outlet} \\ g_{(4,inlet)}P_{inlet} \\ 0 \\ -g_{(6,oulet)}P_{outlet} \\ g_{(7,inlet)}P_{inlet} \\ 0 \\ -g_{(9,oulet)}P_{outlet} \end{bmatrix}$$

And the resulting system of equations will be as follows:

$$\begin{bmatrix}
\sum_{j=1}^{M} g_{j,NBR(j,1)} & -g_{2,NBR(2,1)} & 0 & -g_{4,NBR(4,1)} & 0 & 0 & 0 & 0 & 0 \\
-g_{1,NBR(1,2)} & \sum_{j=1}^{M} g_{j,NBR(j,2)} & -g_{3,NBR(3,2)} & 0 & -g_{5,NBR(5,2)} & 0 & 0 & 0 & 0 \\
0 & -g_{2,NBR(2,3)} & \sum_{j=1}^{M} g_{j,NBR(j,3)} & 0 & 0 & -g_{6,NBR(6,3)} & 0 & 0 & 0 \\
-g_{1,NBR(1,4)} & 0 & 0 & \sum_{j=1}^{M} g_{j,NBR(j,4)} & -g_{5,NBR(5,4)} & 0 & -g_{7,NBR(7,4)} & 0 & 0 \\
0 & -g_{2,NBR(2,5)} & 0 & -g_{4,NBR(4,5)} & \sum_{j=1}^{M} g_{j,NBR(j,5)} & -g_{6,NBR(6,5)} & 0 & -g_{8,NBR(8,5)} & 0 \\
0 & 0 & -g_{3,NBR(3,6)} & 0 & -g_{5,NBR(5,6)} & \sum_{j=1}^{M} g_{j,NBR(j,6)} & 0 & 0 & -g_{9,NBR(9,6)} \\
0 & 0 & 0 & -g_{4,NBR(4,7)} & 0 & 0 & \sum_{j=1}^{M} g_{j,NBR(j,7)} & -g_{8,NBR(8,7)} & 0 \\
0 & 0 & 0 & 0 & -g_{5,NBR(5,8)} & 0 & -g_{7,NBR(7,8)} & \sum_{j=1}^{M} g_{j,NBR(j,8)} & -g_{9,NBR(9,8)} \\
0 & 0 & 0 & 0 & 0 & -g_{6,NBR(6,9)} & 0 & -g_{8,NBR(8,9)} & \sum_{j=1}^{M} g_{j,NBR(j,9)}
\end{bmatrix} \times \begin{bmatrix} P_1 \\ P_2 \\ P_3 \\ P_4 \\ P_5 \\ P_6 \\ P_7 \\ P_8 \\ P_9 \end{bmatrix} = \begin{bmatrix} g_{(1,inlet)}P_{inlet} \\ 0 \\ -g_{(3,oulet)}P_{outlet} \\ g_{(4,inlet)}P_{inlet} \\ 0 \\ -g_{(6,oulet)}P_{outlet} \\ g_{(7,inlet)}P_{inlet} \\ 0 \\ -g_{(9,oulet)}P_{outlet} \end{bmatrix}$$

This is equivalent to

$$\bar{G}P = F$$

Where G is the hydraulic conductivity matrix, P is the potentials vector of the nodes and F is the flow boundaries vector.

This matrix has the form of LIU which is a combination of a lower triangular matrix L, a diagonal matrix, I, and an upper triangular matrix U, as M=L.I.U. This is shown as:

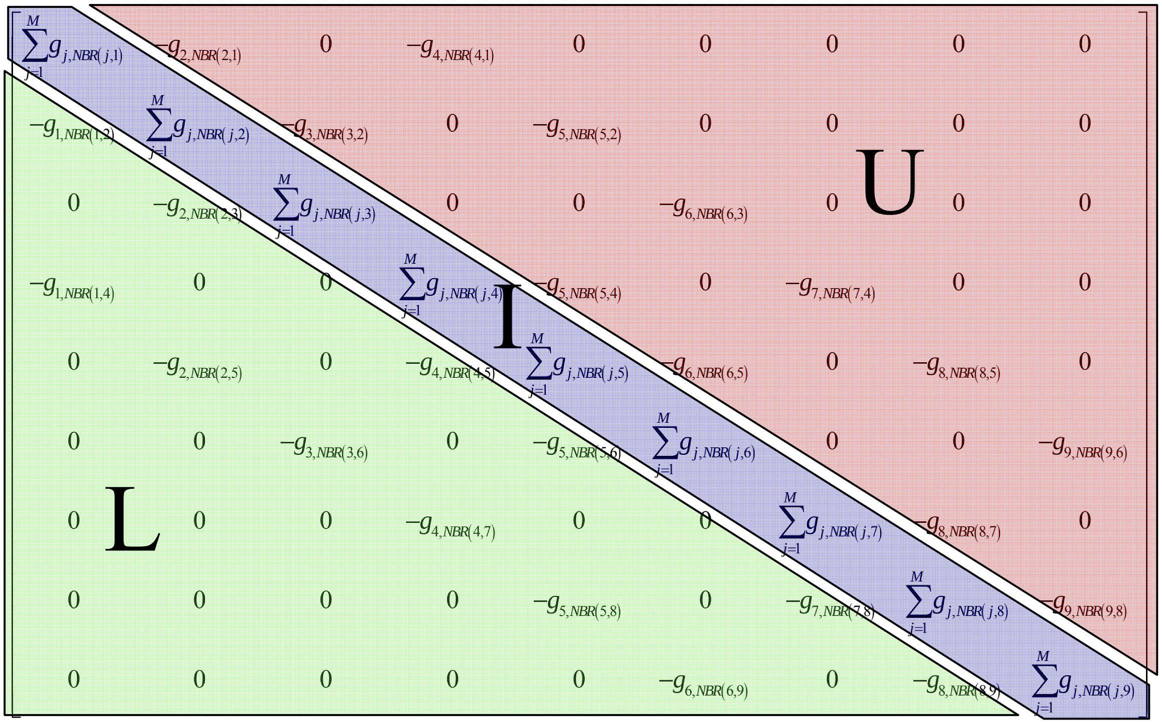

$$\begin{bmatrix}
\sum_{j=1}^{M} g_{j,NBR(j,1)} & -g_{2,NBR(2,1)} & 0 & -g_{4,NBR(4,1)} & 0 & 0 & 0 & 0 & 0 \\
-g_{1,NBR(1,2)} & \sum_{j=1}^{M} g_{j,NBR(j,2)} & -g_{3,NBR(3,2)} & 0 & -g_{5,NBR(5,2)} & 0 & 0 & 0 & 0 \\
0 & -g_{2,NBR(2,3)} & \sum_{j=1}^{M} g_{j,NBR(j,3)} & 0 & 0 & -g_{6,NBR(6,3)} & 0 & 0 & 0 \\
-g_{1,NBR(1,4)} & 0 & 0 & \sum_{j=1}^{M} g_{j,NBR(j,4)} & -g_{5,NBR(5,4)} & 0 & -g_{7,NBR(7,4)} & 0 & 0 \\
0 & -g_{2,NBR(2,5)} & 0 & -g_{4,NBR(4,5)} & \sum_{j=1}^{M} g_{j,NBR(j,5)} & -g_{6,NBR(6,5)} & 0 & -g_{8,NBR(8,5)} & 0 \\
0 & 0 & -g_{3,NBR(3,6)} & 0 & -g_{5,NBR(5,6)} & \sum_{j=1}^{M} g_{j,NBR(j,6)} & 0 & 0 & -g_{9,NBR(9,6)} \\
0 & 0 & 0 & -g_{4,NBR(4,7)} & 0 & 0 & \sum_{j=1}^{M} g_{j,NBR(j,7)} & -g_{8,NBR(8,7)} & 0 \\
0 & 0 & 0 & 0 & -g_{5,NBR(5,8)} & 0 & -g_{7,NBR(7,8)} & \sum_{j=1}^{M} g_{j,NBR(j,8)} & -g_{9,NBR(9,8)} \\
0 & 0 & 0 & 0 & 0 & -g_{6,NBR(6,9)} & 0 & -g_{8,NBR(8,9)} & \sum_{j=1}^{M} g_{j,NBR(j,9)}
\end{bmatrix}$$

The resulting system of equations has the following properties:

1. Sparse
2. Banded for regular crystalline lattices
3. Will not have banded structure for irregular lattices
4. Is a positive definite matrix

5. Can be decomposed to lower and upper triangular matrices and an I matrix in the format of LIU = G.
6. Can be solved by iterative solutions
7. Will converge to the solution because of positive definite property

A 3D network model is shown as another example of such a conductivity matrix. The network is a 3 by 3 by 3 equal to 27 nodes. The network is a regular cubic lattice and all the bonds have the unit hydraulic conductivities. Figure 4.6 shows a 3D view of such a network model.

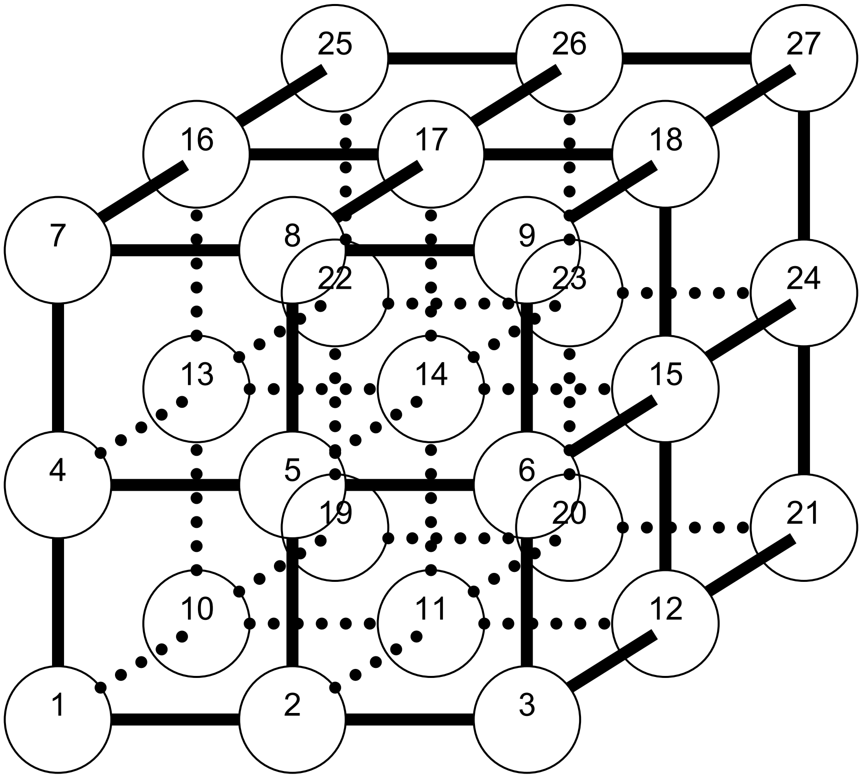

Figure 4.6 3D square lattice consisting of 27 nodes

The corresponding conductivity matrix for such a cubic lattice with unit bond conductivities is shown in Table 4.3. The diagonal values are calculated using the general form of flow equations (Eq. 4.4). Positive sign means flow into a node and negative sign as stated before, means flow out of a node.

	1	2	3	4	5	6	7	8	9	10	11	12	13	14	15	16	17	18	19	20	21	22	23	24	25	26	27
1	4	-1	0	-1	0	0	0	0	0	-1	0	0	0	0	0	0	0	0	0	0	0	0	0	0	0	0	0
2	-1	4	-1	0	-1	0	0	0	0	0	-1	0	0	0	0	0	0	0	0	0	0	0	0	0	0	0	0
3	0	-1	4	0	0	-1	0	0	0	0	0	-1	0	0	0	0	0	0	0	0	0	0	0	0	0	0	0
4	-1	0	0	5	-1	0	-1	0	0	0	0	0	-1	0	0	0	0	0	0	0	0	0	0	0	0	0	0
5	0	-1	0	-1	5	-1	0	-1	0	0	0	0	0	-1	0	0	0	0	0	0	0	0	0	0	0	0	0
6	0	0	-1	0	-1	5	0	0	-1	0	0	0	0	0	-1	0	0	0	0	0	0	0	0	0	0	0	0
7	0	0	0	-1	0	0	4	-1	0	0	0	0	0	0	0	-1	0	0	0	0	0	0	0	0	0	0	0
8	0	0	0	0	-1	0	-1	4	-1	0	0	0	0	0	0	0	-1	0	0	0	0	0	0	0	0	0	0
9	0	0	0	0	0	-1	0	-1	4	0	0	0	0	0	0	0	0	-1	0	0	0	0	0	0	0	0	0
10	-1	0	0	0	0	0	0	0	0	5	-1	0	-1	0	0	0	0	0	-1	0	0	0	0	0	0	0	0
11	0	-1	0	0	0	0	0	0	0	-1	5	-1	0	-1	0	0	0	0	0	-1	0	0	0	0	0	0	0
12	0	0	-1	0	0	0	0	0	0	0	-1	5	0	0	-1	0	0	0	0	0	-1	0	0	0	0	0	0
13	0	0	0	-1	0	0	0	0	0	-1	0	0	6	-1	0	-1	0	0	0	0	0	-1	0	0	0	0	0
14	0	0	0	0	-1	0	0	0	0	0	-1	0	-1	6	-1	0	-1	0	0	0	0	0	-1	0	0	0	0
15	0	0	0	0	0	-1	0	0	0	0	0	-1	0	-1	6	0	0	-1	0	0	0	0	0	-1	0	0	0
16	0	0	0	0	0	0	-1	0	0	0	0	0	-1	0	0	5	-1	0	0	0	0	0	0	0	-1	0	0
17	0	0	0	0	0	0	0	-1	0	0	0	0	0	-1	0	-1	5	-1	0	0	0	0	0	0	0	-1	0
18	0	0	0	0	0	0	0	0	-1	0	0	0	0	0	-1	0	-1	5	0	0	0	0	0	0	0	0	-1
19	0	0	0	0	0	0	0	0	0	-1	0	0	0	0	0	0	0	0	4	-1	0	-1	0	0	0	0	0
20	0	0	0	0	0	0	0	0	0	0	-1	0	0	0	0	0	0	0	-1	4	-1	0	-1	0	0	0	0
21	0	0	0	0	0	0	0	0	0	0	0	-1	0	0	0	0	0	0	0	-1	4	0	0	-1	0	0	0
22	0	0	0	0	0	0	0	0	0	0	0	0	-1	0	0	0	0	0	-1	0	0	5	-1	0	-1	0	0
23	0	0	0	0	0	0	0	0	0	0	0	0	0	-1	0	0	0	0	0	-1	0	-1	5	-1	0	-1	0
24	0	0	0	0	0	0	0	0	0	0	0	0	0	0	-1	0	0	0	0	0	-1	0	-1	5	0	0	-1
25	0	0	0	0	0	0	0	0	0	0	0	0	0	0	0	-1	0	0	0	0	0	-1	0	0	4	-1	0
26	0	0	0	0	0	0	0	0	0	0	0	0	0	0	0	0	-1	0	0	0	0	0	-1	0	-1	4	-1
27	0	0	0	0	0	0	0	0	0	0	0	0	0	0	0	0	0	-1	0	0	0	0	0	-1	0	-1	4

Table 4.3 Conductivity matrix for the sample 3D network in Figure 4.6

4.3. NUMERICAL SOLVER FOR STEADY STATE FLOW CALCULATIONS

Since the resulting system of equations can be solved by iterative methods, we used the Gauss-Seidel method with updating as our solver, which is in the form of:

$$\begin{aligned} &\bar{G}P = F \\ &AX = B \\ &A = I - L - U \\ &(I - L - U)X = B \\ &X^{n+1} = B + LX^{n+1} + UX^{n} \end{aligned} \qquad \text{Eq. 4.7}$$

Applying the Gauss-Seidel iterative method we get:

$$\begin{aligned} &X^{n+1} = X^{n} + B + LX^{n+1} + UX^{n} - X^{n} \\ &X^{n+1} = X^{n} + \Delta X \end{aligned} \qquad \text{Eq. 4.8}$$

X^{n+1}, is the potential solution. The stopping criterion for the iterative solver is a relative error of potential difference between two iterations less than a ε that can be defined as:

$$\max\left(\frac{X_i^{n+1} - X_i^{n}}{X_i^{n}}\right) < \varepsilon \qquad \text{Eq. 4.9}$$

If we use a very large number of nodes, in the orders of 10^5 or 10^6, the resulting system of equations will be in the size of $10^6 \text{x} 10^6 = 10^{12} + 2\text{x}10^6$ (for boundaries) spaces. This amount of computer memory is a large value to hold all the information in the matrix which is not quite achievable. Therefore, we must compress the data without losing the integrity. A compressed matrix algorithm was developed in order to keep all the information and at the same time allow the iterative solutions. Since the structure of our model will not be based on regular network models, we cannot use the ordinary banded matrix solvers (please refer to Section 4.6, irregular multi dimension structure). Therefore, there is a need to develop another type of compression. The designed method for our solver is to save only the non zero values of the L.I.U matrix. We have assumed the maximum number of 27 connectivities in our model.

Thus, to hold all the necessary information of conductivities and connections we only need 10^6x27+2x10^6 blocks of memory, which is almost 5 orders of magnitude smaller than the previous form without compression. This makes it possible to hold the information for about one million nodes network for every two Gigabytes of memory.

An example of a node with 26 connectivities would be a center node in a cube with connections to all the nodes at the corners, middle of the surfaces and middle of the connecting lines between two corners, as shown in Figure 4.7. Node number 14 in the middle of cube has 26 connections.

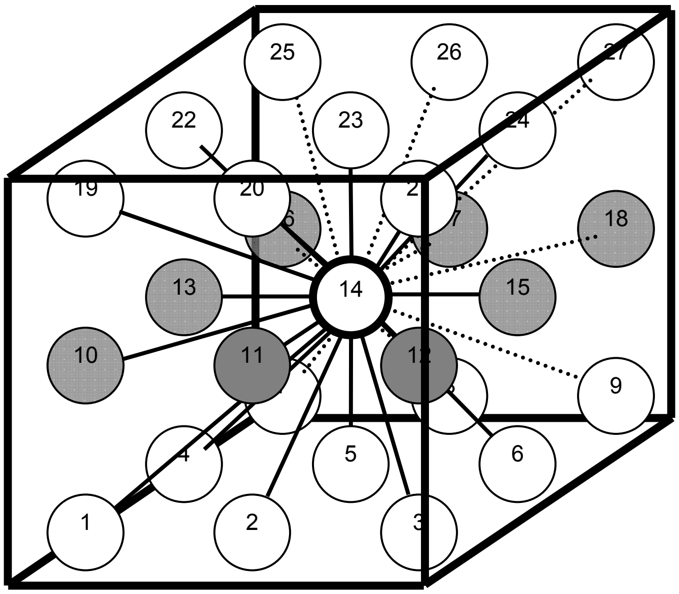

Figure 4.7 A center node in a cube with 26 connections

In the compressed format, each row will corresponds to the node ID, same as before, and the information for each connected node will be filled in the next columns in each row. For example the previous 27 nodes network adjacency matrix (in Table 4.3) will look like Table 4.4 in compressed format.

	1	2	3	4	5	6	7
1	4	-1	-1	-1			
2	-1	4	-1	-1	-1		
3	-1	4	-1	-1			
4	-1	5	-1	-1	-1		
5	-1	-1	5	-1	-1		
6	-1	-1	5	-1	-1		
7	-1	4	-1	-1			
8	-1	-1	4	-1	-1		
9	-1	-1	4	-1			
10	-1	5	-1	-1	-1		
11	-1	-1	5	-1	-1	-1	
12	-1	-1	5	-1	-1		
13	-1	-1	6	-1	-1	-1	
14	-1	-1	-1	6	-1	-1	-1
15	-1	-1	-1	6	-1	-1	
16	-1	-1	5	-1	-1		
17	-1	-1	-1	5	-1	-1	
18	-1	-1	-1	5	-1		
19	-1	4	-1	-1			
20	-1	-1	4	-1	-1		
21	-1	-1	4	-1			
22	-1	-1	5	-1	-1		
23	-1	-1	-1	5	-1	-1	
24	-1	-1	-1	5	-1		
25	-1	-1	4	-1			
26	-1	-1	-1	4	-1		
27	-1	-1	-1	4			

Table 4.4 Compressed adjacency matrix

Another matrix same as Table 4.4 is necessary to hold the locations information. Table 4.5 shows such a matrix.

	1	2	3	4	5	6	7
1	1	2	4	10			
2	1	2	3	5	11		
3	2	3	6	12			
4	1	4	5	7	13		
5	2	4	5	6	8	14	
6	3	5	6	9	15		
7	4	7	8	16			
8	5	7	8	9	17		
9	6	8	9	18			
10	1	10	11	13	19		
11	2	10	11	12	14	20	
12	3	11	12	15	21		
13	4	10	13	14	16	22	
14	5	11	13	14	15	17	23
15	6	12	14	15	18	24	
16	7	13	16	17	25		
17	8	14	16	17	18	26	
18	9	15	17	18	27		
19	10	19	20	22			
20	11	19	20	21	23		
21	12	20	21	24			
22	13	19	22	23	25		
23	14	20	22	23	24	26	
24	15	21	23	24	27		
25	16	22	25	26			
26	17	23	25	26	27		
27	18	24	26	27			

Table 4.5 Data locations in the adjacency matrix

Please note that all the rows in Table 4.5 have been compressed to the first 7 columns. These are the only necessary cells to save in the memory. Table 4.5 has compressed into two tables with same number of 27 rows but 7 columns; the 27 columns ahs been compressed into 14 columns, in the compressed format. This is an improvement of 200 percent on a 27 node system over the previous expanded format. As the matrix gets larger and the number of nodes in the network increases to 10^6 or larger, this improvement increases to 4 or 5 orders of magnitude and more, over the regular format.

We can also fill the adjacency matrix with the bonds information such as radius or hydraulic conductivities, etc. This adjacency matrix with conductivity information will be called conductivity matrix.

Two test examples are shown here to verify our model. The test network is a 40 × 40, 2D square lattice node system with unit hydraulic conductivities for all the bonds in the network. The inlet has 5 units of potential and the outlet is set to be zero. The solution to such a system is expected to be a smooth decreasing potential surface from the inlet to the outlet. Figure 4.8 shows the results of such a solution, which is exactly as we expect. It is also accurate within the error tolerance.

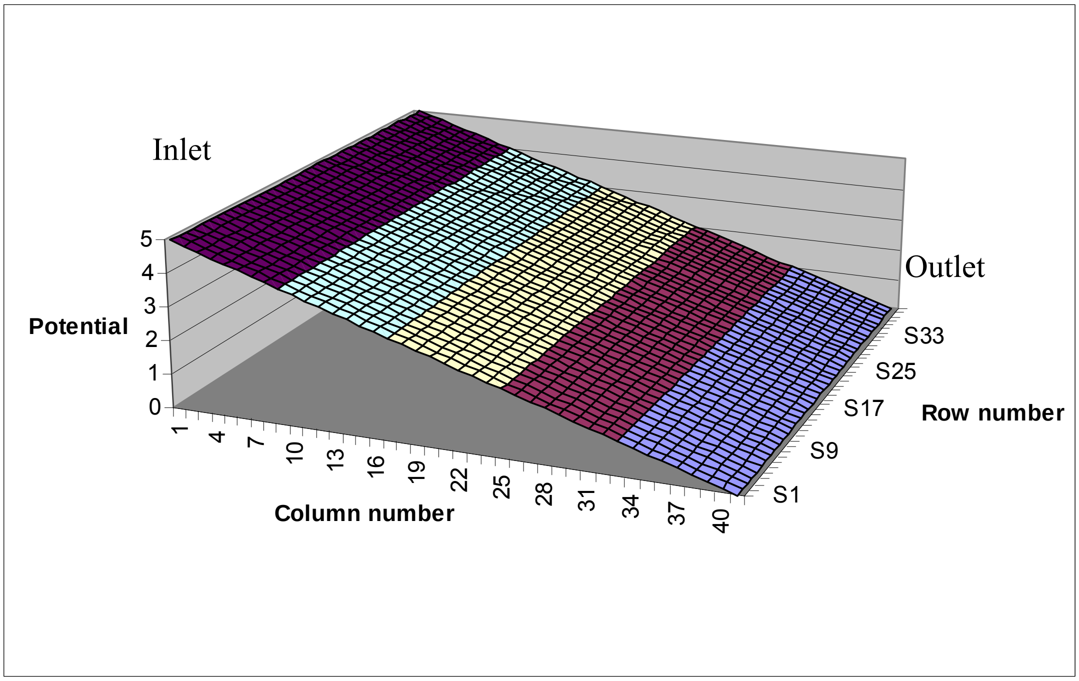

Figure 4.8 Potential solution for a unit conductivity network

Another example is the same 2D square network of 40 × 40 nodes. In this example however the conductivities vary and they have been sampled from a Gaussian random distribution. The range of conductivities is now between 1 and 100 units. As before, we expect the solution of potentials to be a general trend of decreasing values from inlet to outlet. This means that the values of potential have to be different in each grid from inlet to outlet, but the general decreasing trend from inlet to outlet has to be honored (Figure 4.9).

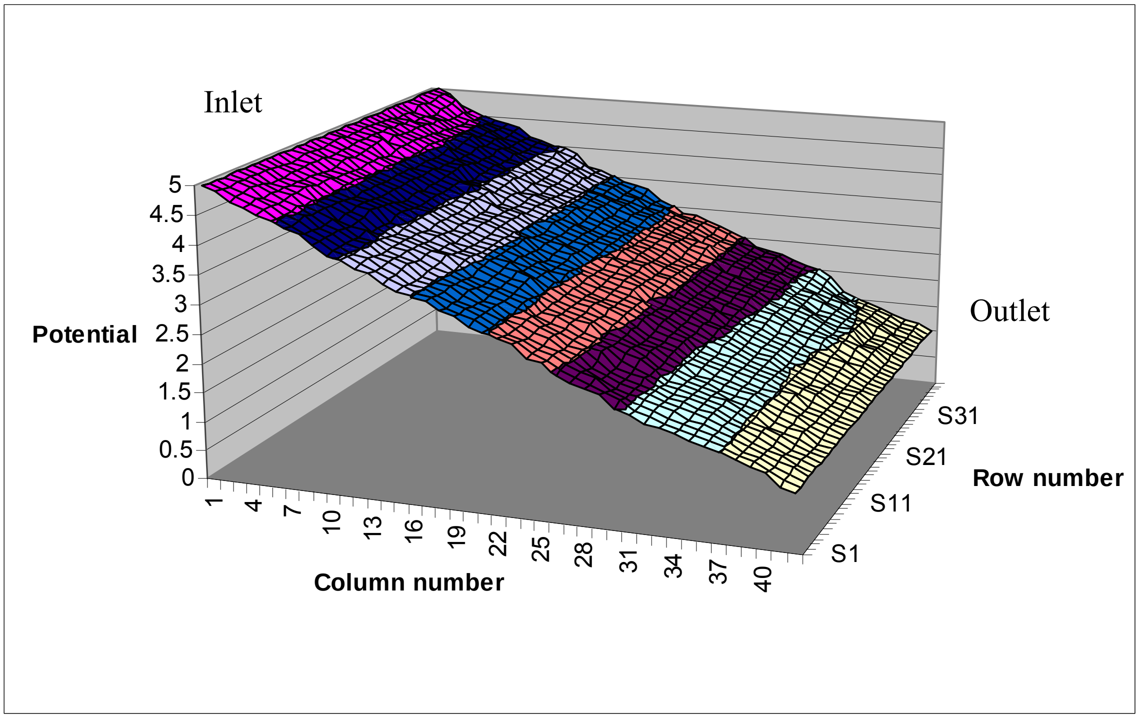

Figure 4.9 Potential solution for random conductivities

The solution potential shown in Figure 4.9, has the general trend from inlet to outlet, as we expected with in the error tolerance.

4.4. CAPILLARY CONTROLLED DISPLACEMENT

For the capillary controlled invasion process we calculate the flow path by comparing the conductivity of the bonds, and determining whether the invasion potential can invade the bond or not. However, we do not update the potential field in every step for invasion.

The first step in the process of capillary controlled invasion is to determine the hydraulic conductivity of each connecting bond between two pores. Hydraulic conductivities can be calculated in different ways. Therefore we have implemented different ways to either import the conductivities directly from a file or read a specific property of bonds to calculate the hydraulic conductivity for each bond. We have discussed all the different ways to import these conductivities in the Appendix A.

We then start with a small invasion potential at the inlet nodes. We will increase this potential in small steps later. Imposing this starting invasion potential on the nodes that are connected to the inlet boundary, we determine the first candidate of the invasion. All the nodes that are connected to the inlet nodes will be exposed to this invasion potential. If the invasion potential is greater than the minimum potential necessary to invade a bond and reach the neighbor connected pore, the node will be invaded. This invaded node will be added to the list of invaded nodes and the invasion potential and the invaded bond will be recorded. This process of comparison between the minimum necessary potential to invade a bond with the imposed invasion potential continues until all the possible nodes, which can be invaded with this invasion potential, are being invaded. At the end of this step we will have a list of all the connected nodes to the inlet that could be invaded with the first step invasion potential.

Figure 4.10 shows a sample network for showing the percolation test. The network is a 3 by 3 node system on a regular square lattice of degree 4. Each bond's minimum invasion potential is shown by a number representing the magnitude of minimum necessary potential to invade through that bond. Smaller values mean flow can pass more easily through the bond and reach the next pore (node), therefore bonds with lower shown value on the graph have higher conductivities and flow can invade them with lower invasion potential. Each pore (node) is also marked with a number in the middle as the node ID. The nodes marked as number 10, 11 and 12 are the outlet nodes.

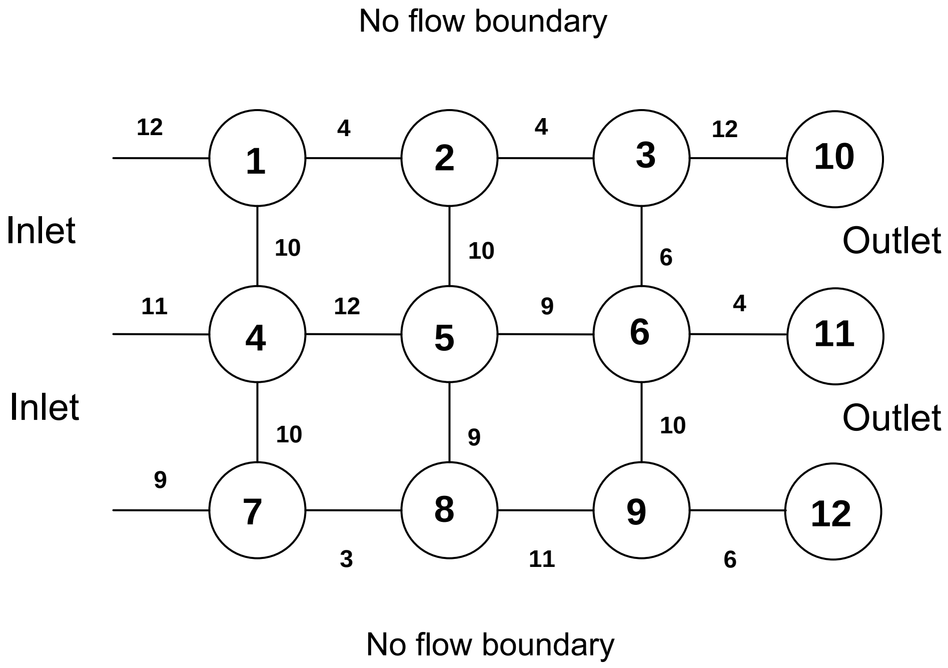

Figure 4.10 A 3 × 3 square lattice network

Let the first invasion potential be 1 unit. This is less than the minimum potential necessary to invade the three nodes, 1, 4 and 7 that are connected to the inlet. The minimum invasion potential for invading these connected nodes to the inlet boundary is 9 units of potential, corresponding to node number 7, connected to the inlet. Therefore, no invasion will occur until we reach this minimum necessary invasion potential. As we increase the invasion potential we will eventually reach potential of 9 units. At this invasion potential, node number 7 will be invaded because the capillary pressure of the connecting bond is less or equal to the necessary invasion potential imposed by the inlet. Thus, node number 7 will be invaded (Figure 4.11).

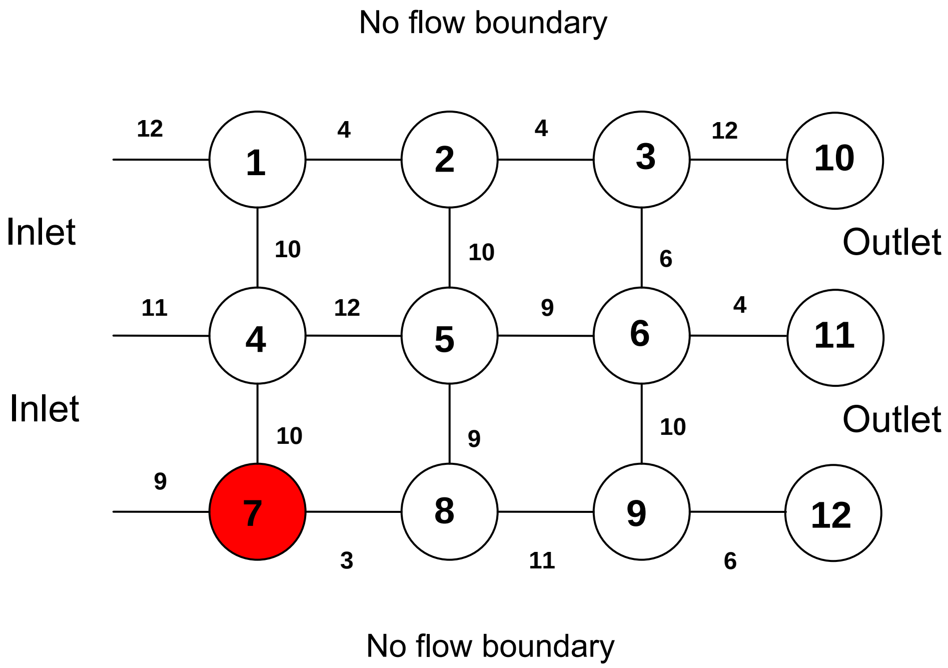

Figure 4.11 The first node has been invaded in an invasion percolation process

Now that node number 7 has been invaded from inlet, its potential will be same as the inlet potential (No potential drop in the invaded cluster, moving boundary). In this case, it will be 9 units of potential at the first step of invasion. The two other nodes connected to node number 7 are nodes number 4 and 8, with the necessary invasion potential of 10 and 3 units respectively, as shown on Figure 4.11. Because the invasion potential in node number 7 is 9 units and is higher than the potential needed to invade node number 8, node number 8 will also be invaded. But node number 4 will not be invaded. Because the minimum necessary potential to pass through the connecting bond between nodes number 7 and 4 is 10 units (as shown on Figure 4.11) and therefore is higher than the invading potential of 9 units. So the next invaded node will be node number 8. It is important to mention that we are still in the first step of invasion without increasing the invasion potential.

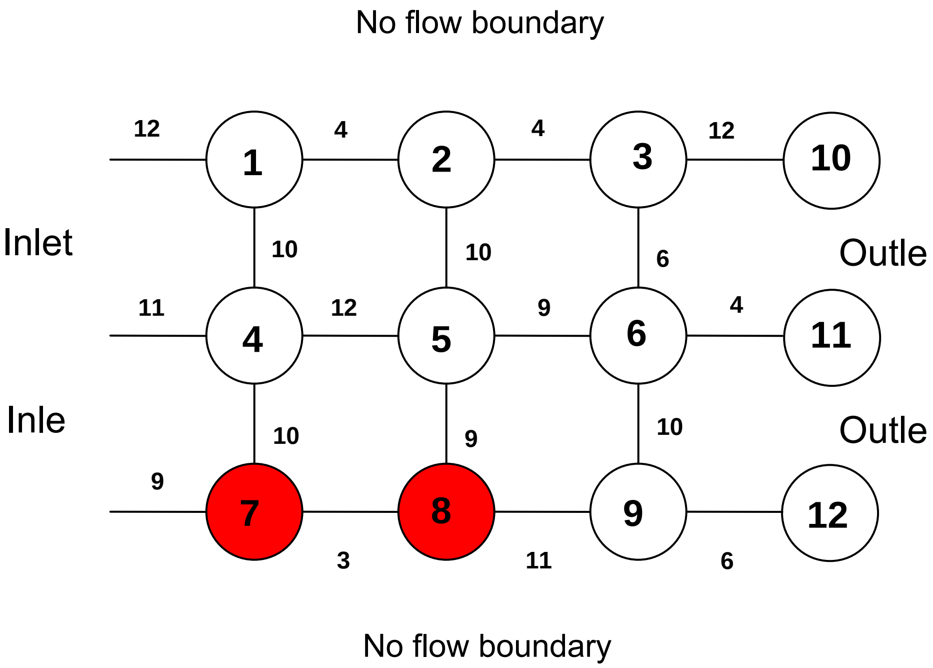

Figure 4.12 Second node has been invaded in the percolation process. Invasion potential is 9 units

The resulting table so far will look like Table 4.6. This table shows the invaded nodes, the stage at which they have been invaded, and the invasion potential.

Node	Stage	Invasion Potential
7	1	9
8	1	9

Table 4.6 Table of invaded nodes in the invasion percolation process

The same process will choose node number 5 to be invaded through node number 8, because the necessary invading potential is less than or equal to the imposed potential through node number 8. But node number 9 cannot be invaded since 11 units of potential are needed to invade the bond connecting them through node number 8 (Figure 4.13).

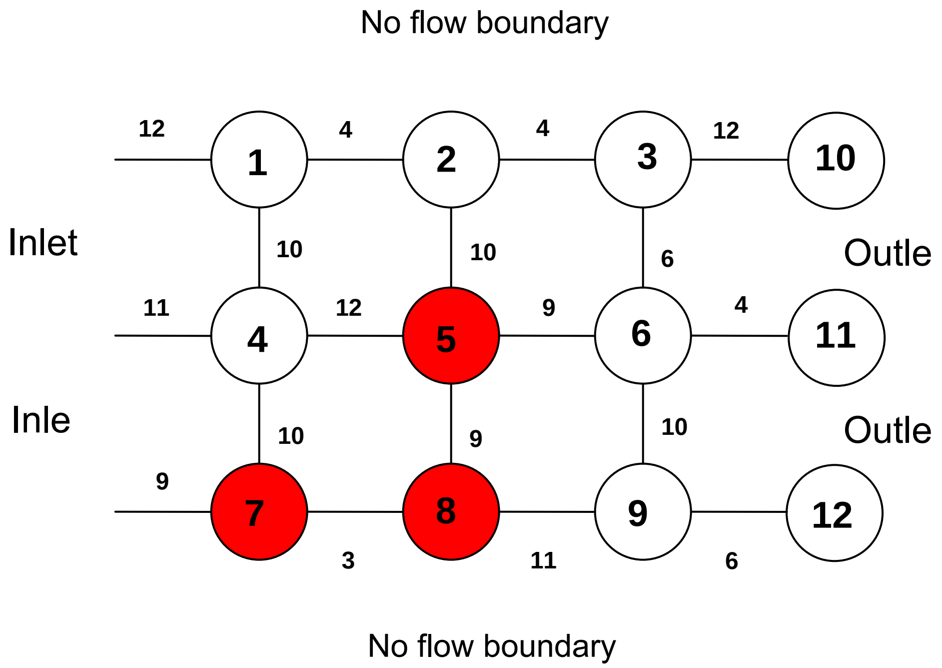

Figure 4.13 Invasion continues through the network. Invasion potential is 9 units

Continuing the process of invasion percolation, we see that the candidates for invasion connected to node number 5 are nodes 4, 6, and 2. From these nodes, the node number 6 can be invaded with the current invasion potential. The same process will then show that nodes number 3, and then number 2 will also be invaded and the last node of invasion will be node number 1. As we continue this process by invading the new possible candidates, add the invaded nodes to the invaded nodes table, and check the connected nodes to the invaded ones in every step, we will have the first invasion step completed as shown in Table 4.7.

Node	Stage	Invasion Potential
7	1	9
8	1	9
5	1	9
6	1	9
3	1	9
11	1	9
2	1	9
1	1	9

Table 4.7 Table of invaded nodes in the first step of invasion percolation process

Node number 11 in table 4.7 is the corresponding outlet node connecting node number 6 to the outlet. This is equivalent to a breakthrough from node number 6. Figure 4.14 shows the completed invaded nodes for the first step of invasion in the process of percolation.

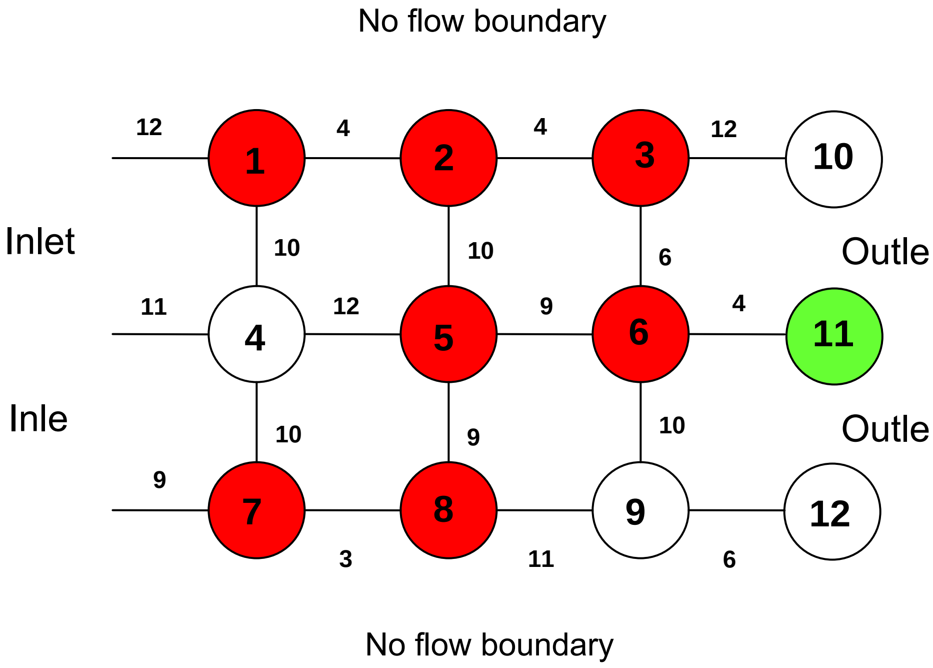

Figure 4.14 First invasion step has been completed. Invasion potential is 9 units

For the next step we will increase the invasion potential by a predefined value. This predefined value can be very small or very large and it depends on the minimum difference between the necessary invading potential needed to pass through the connecting bonds. In this case, the minimum is one unit of potential. So for the next step, we will continue the same process by adding that delta unit of invasion potential to the previous value and continuing the process; first by checking the remaining connected nodes to the inlet and then checking nodes that are connected to the invaded nodes from the previous step of percolation.

It should be mention that, if two nodes are connected to a third node and the connecting bonds to the third node have the same necessary minimum invading potential, the node that have been invaded first in the table of invaded nodes, will invade the third node. In this example, at the second step of invasion with 10 units of invasion potential, node number 4 has not been invaded through the inlet. Because the minimum necessary invasion potential to invade the connecting bond from the inlet is at least 11 units of potential. But at this stage of invasion, node number 4 is a candidate for invasion from nodes number 1 or 7. The necessary invasion potential from either node 1 or 7 is 10 units. But node number 7 has been invaded first. Therefore, node number 4 will be invaded through node number 7, not node number 1. It will also be added to the table of invaded nodes for the second step of the capillary controlled invasion.

Continuing the process, other invaded nodes with a minimum necessary invasion potential of 10 will be nodes number 9 and 12. Node number 12 is the outlet node corresponding to node number 9. This means, that through node number 9 a breakthrough can happen. The resulting table of invasion will be Table 4.8.

Node	Stage	Invasion Potential
7	1	9
8	1	9
5	1	9
6	1	9
3	1	9
11	1	9
2	1	9
1	1	9
4	2	10
9	2	10
12	2	10

Table 4.8 Table of invaded nodes, Step two of invasion percolation

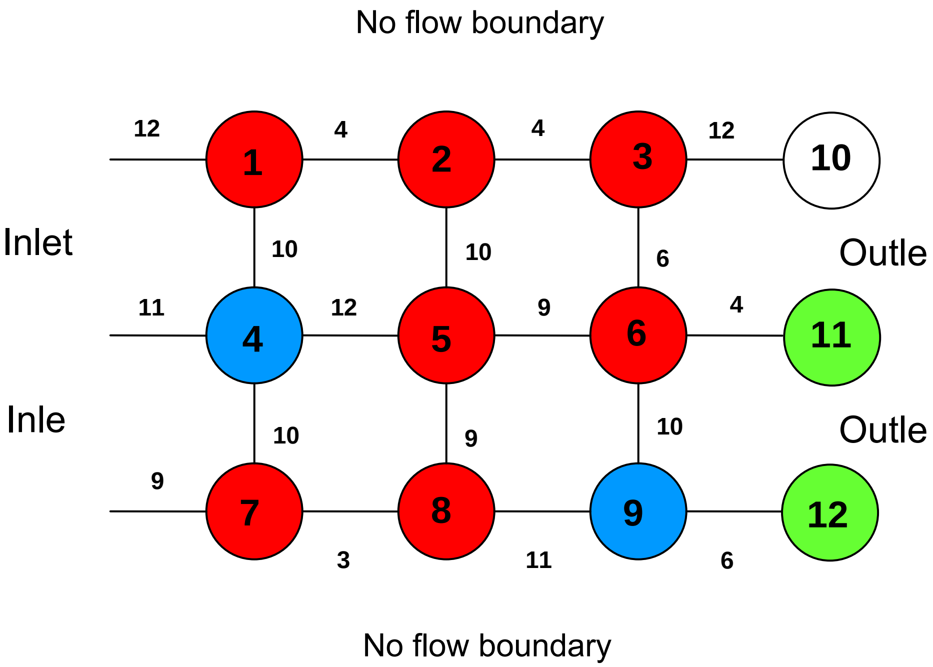

Figure 4.15 Second step of invasion percolation with 10 units of invasion potential

At this stage of the example, all the internal nodes, which are nodes number 1 through 9, have been invaded. The only remaining node is the outlet connection to node number 3, which is node number 10. The necessary invasion potential for invading the connecting bond to this outlet node is 12 units of potential. Therefore the next step of invasion, which will be invasion potential of 11, cannot invade the connecting bond. So invasion step 3 will be processed but will not have any invading nodes. The next step, which will be invasion potential of 12, is capable of flooding node number 10 with the minimum required potential of 12.

The final table of invasion will look like Table 4.9, which has all the nodes in the network and the invaded boundary nodes.

Node	Stage	Invasion Potential
7	1	9
8	1	9
5	1	9
6	1	9
3	1	9
11	1	9
2	1	9
1	1	9
4	2	10
9	2	10
12	2	10
10	4	12

Table 4.9 Last step of invasion percolation

Now that the process has been explained, we can take a look at another example with many more nodes. A large network of 40,000 nodes in XY plane has been tested. The network is a 200 × 200 node system on a square lattice of degree 4. Throats have been re-sampled from a Finney pack distribution. The Finney pack is a random dense packing of spheres. The spheres can be mono size or different size. A schematic of a random dense packing of mono size spheres is shown in Figure 4.16 [Devarajan, 2006].

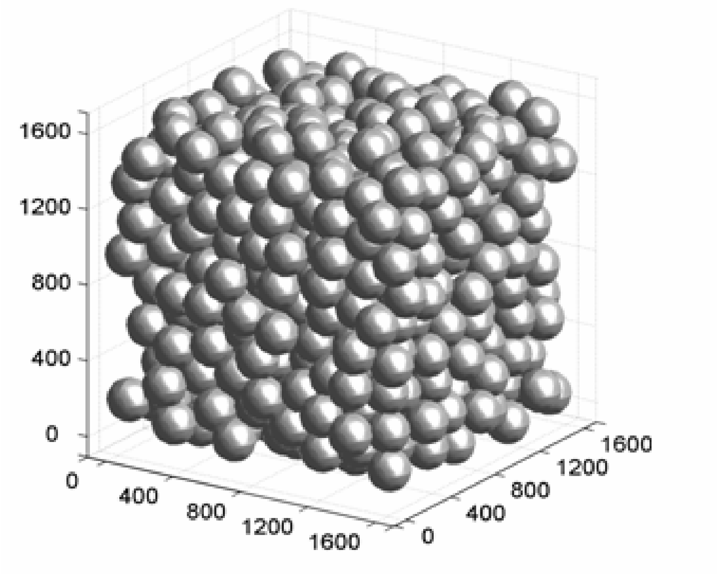

Figure 4.16 Schematic description of a "Finney" pack with mono-sized grains. All dimensions are given in μm

The distribution of pore throats radii from Finney dense packing has been used in many drainage or invasion tests and simulations. Figure 4.17 shows the histogram of these Finney radii. There are two major anomalies of drainage curvatures, one in the lower end of the graph and the other on the upper end of the graph. Therefore, it is a bi-modal distribution. Figure 4.18 shows the Finney pack bond radii frequency and the corresponding cumulative distribution.

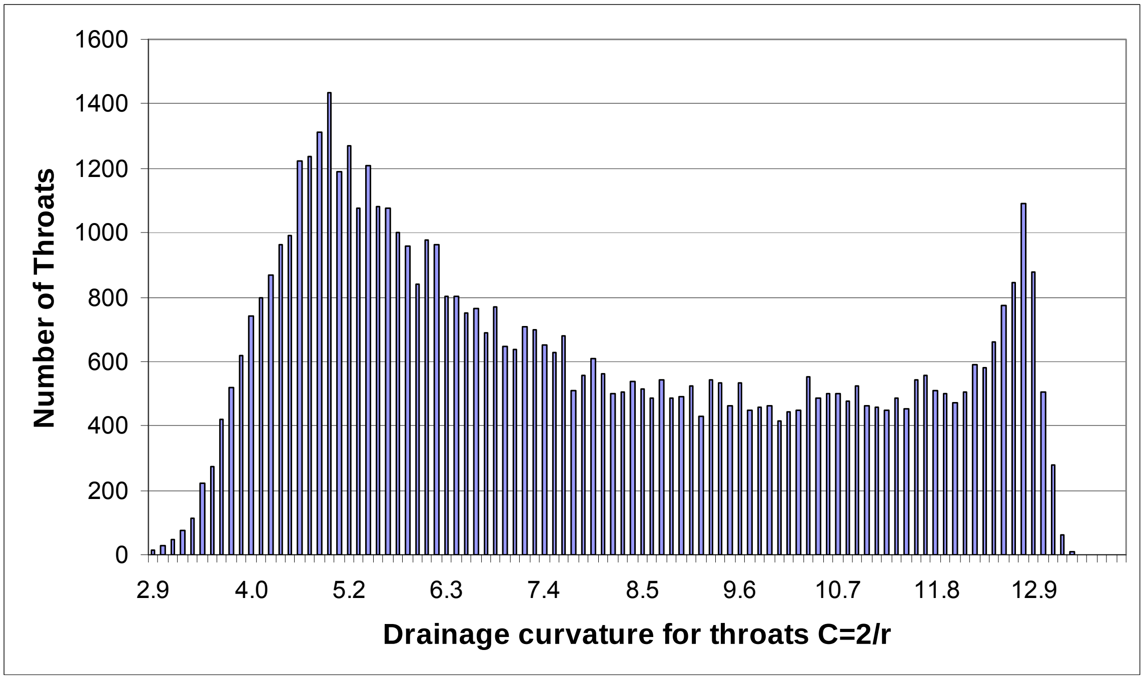

Figure 4.17 Histogram of throats drainage curvature

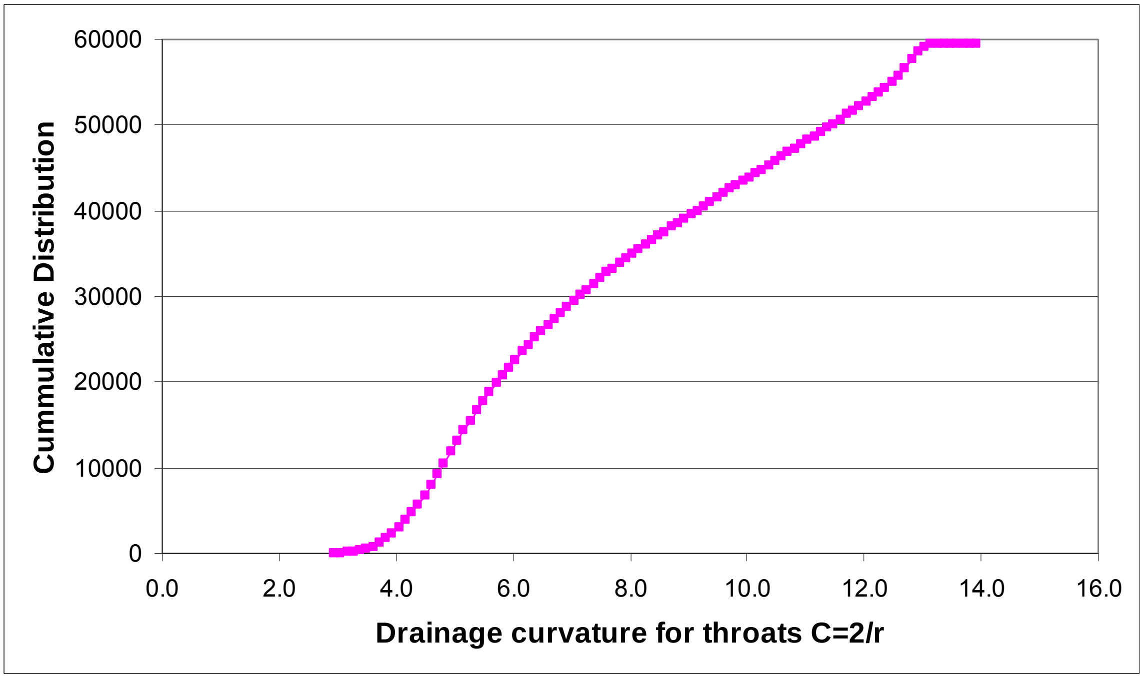

Figure 4.18 Finney packs throats drainage curvature distribution

We have 200 nodes connected to the inlet on the left and 200 nodes connected to the outlet on the right of the graphs. Figures 4.19 to 4.25 show the invasion percolation test on the above mentioned network. Flow is from left to right on the graphs. Top and bottom boundaries are no flow boundaries. We start the invasion percolation process with low potentials and gradually increase the potentials. These potentials from low to high are shown with a color spectrum from blue to red on color prints. Blue represents low potentials and red represents high potentials. On black and white (B&W) prints this spectrum from low to high potential is shown from dark gray to light gray.

Figure 4.19 shows the very first stages of invasion percolation. Nodes shown in black (on B&W print) or blue (on color prints) represent the pores that have been invaded with low potential gradients.

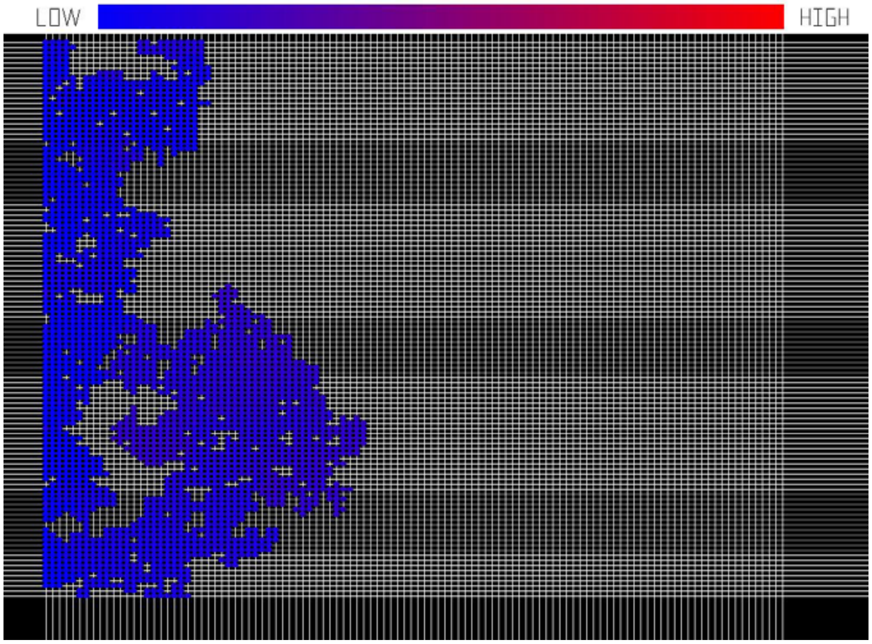

Figure 4.19 First stages of invasion percolation with low potential gradients

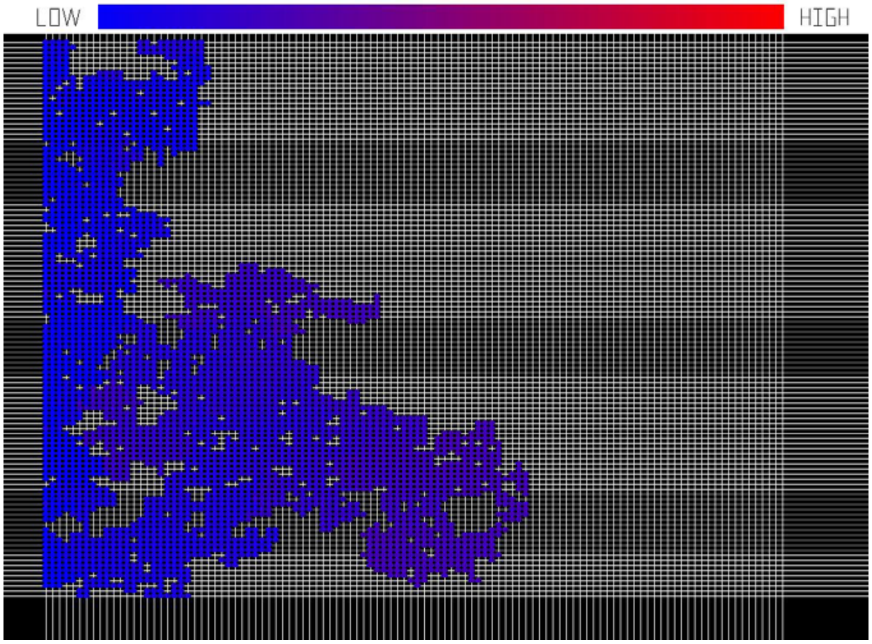

Figure 4.20 Invasion advances more into the network

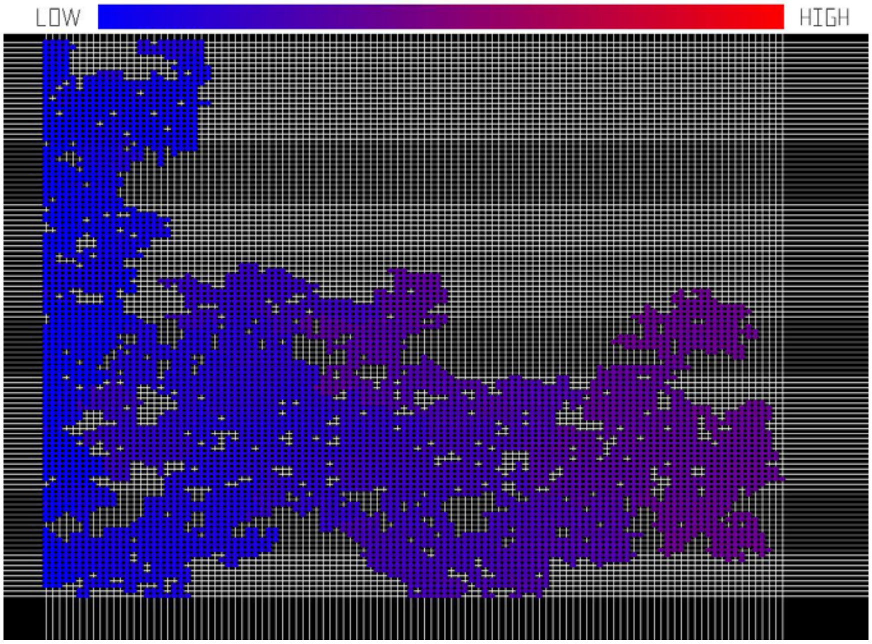

Figure 4.21 Breakthrough has happened

Color changes toward the red spectrum (light gray on B&W prints) means higher invasion potentials. In Figure 4.21, which shows the occurrence of breakthrough, only about one third of the nodes have been invaded and about two thirds of the nodes remain.

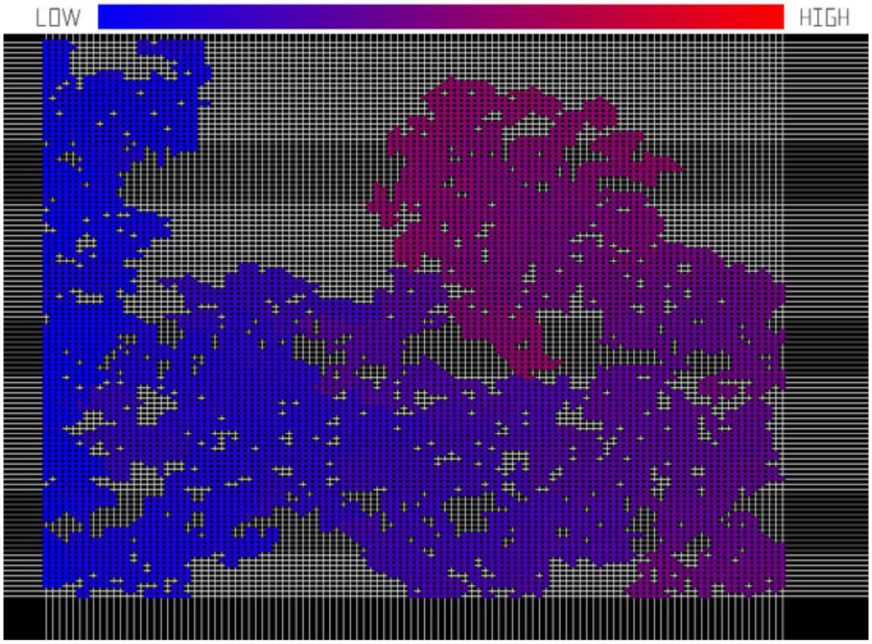

Figure 4.22 Increasing the potential above the breakthrough

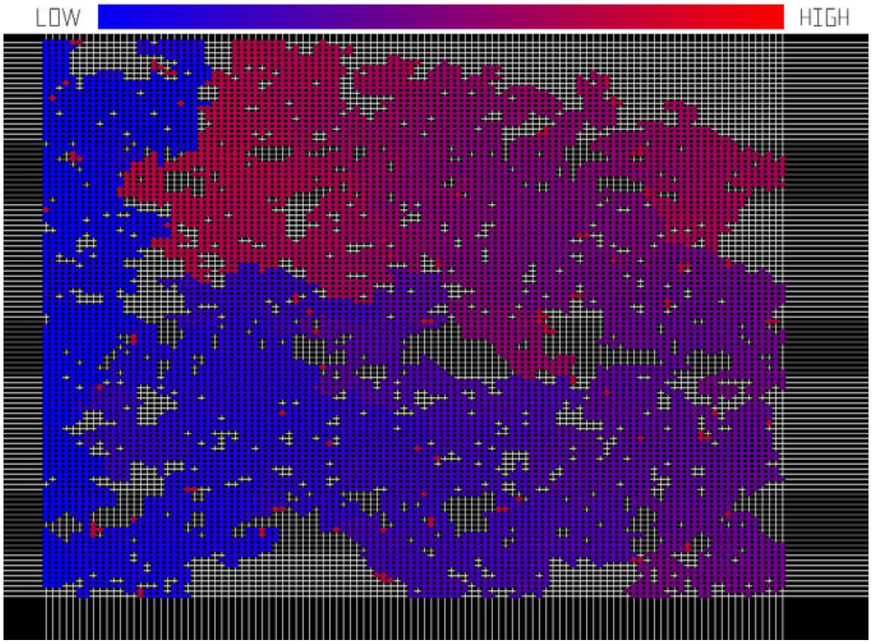

Figure 4.23 Higher potentials needed to invade the remaining nodes from previous stages of invasion

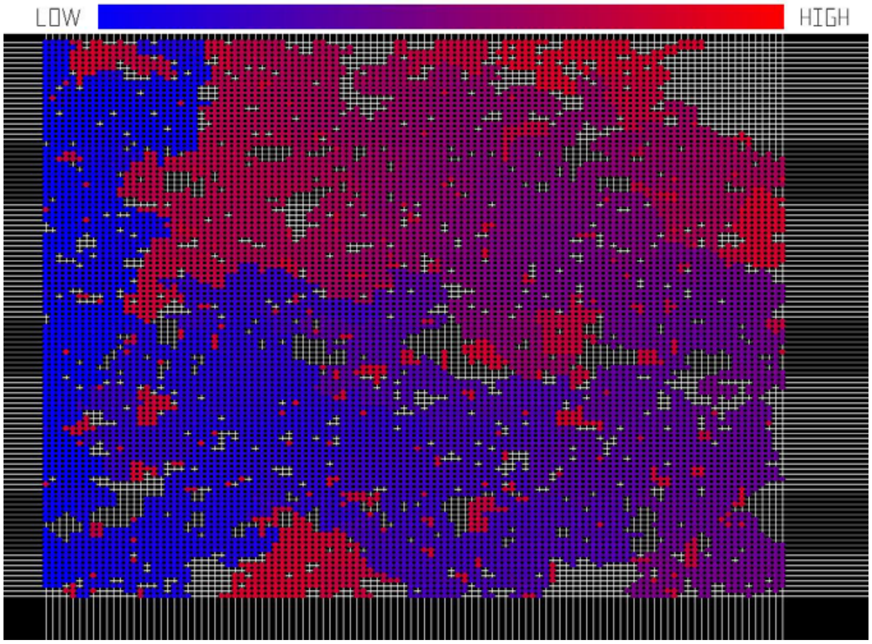

Figure 4.24 Some remaining nodes from previous stages are being invaded with very high potential gradients

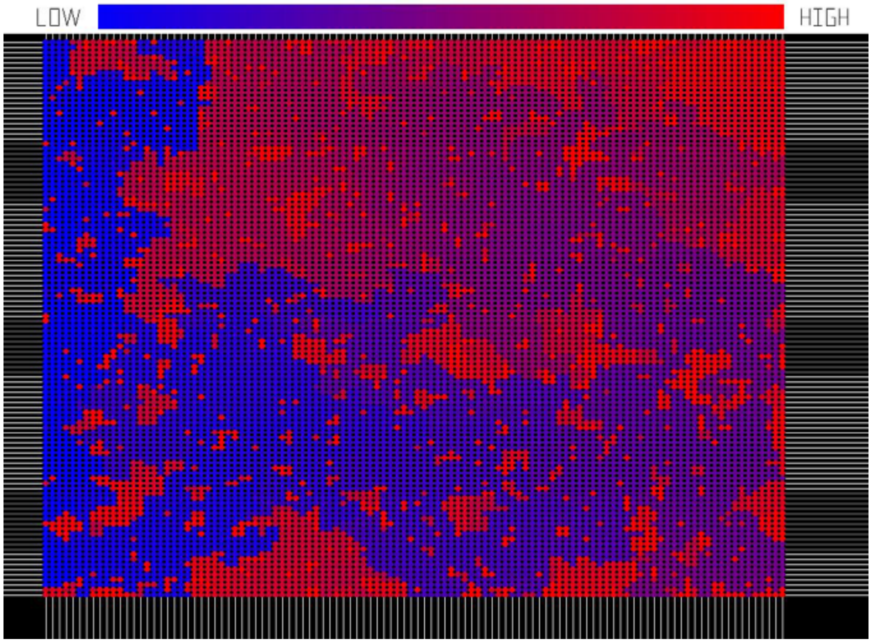

Figure 4.25 Last stage of invasion percolation until the last node is invaded

The last stage of invasion percolation is shown in Figure 4.25. All the nodes in the network have been invaded. There are many nodes in the network that have been invaded only with very high potential. These nodes are shown in red in Figure 4.25 (light gray in B&W prints).

4.5. VISCOUS INVASION

As we have shown in the physical description of our model in Chapter three, in order to simulate the viscous invasion we need to have the potential at both ends of a bond to calculate whether or not invading fluid can advance to the next pore. Capillary pressure is important but as we shown in Chapter 3, it has less effect on the fluid flow in a viscous displacement case when capillary number is higher than 0.1. It is important to mention, for a viscous displacement, potentials at all the network grids (nodes) must be updated each time a pore is invaded.

Fluid flow advancement criterion is the rate of flow in each bond. First we calculate the potential field in the network. Then we calculate the potential difference, ΔP, between every two connected nodes in the network. With the potential difference, we calculate the flow rate in every bond in the network system. Then, we sort the flow rates for the entire connected nodes to the inlet or the invading fluid front, which ever has more advanced in the network, from highest to the lowest rate. Having the sorted flow rates in every bond, depending on our choice we can invade all or percentage of the nodes that have the highest flow rates in the network. For example we can choose from all the flow rates, only the top 70 percent rates, invade their targeted node which is connected.

An example of this process has been setup. The example network is a 4 by 4 node system located on a regular square lattice of degree four. Conductivities have been uniformly sampled from a Gaussian random generator. Node numbers are shown in the middle of each node. Left and right nodes are connected to inlets and outlets, respectively. For this example test we chose that only the maximum rate of flow in the candidate bonds invade the next pore and advances. The Inlet has 5 units potential and the outlet is set to 1 unit. The error tolerance for the solver has been set to 10^{-15}. Figure 4.26 shows this test network for the 16 nodes system.

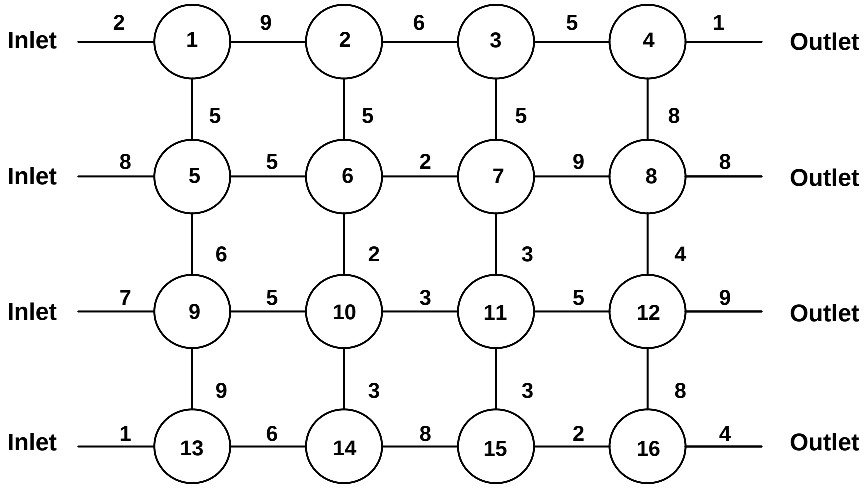

Figure 4.26 4x4 network for viscous invasion test

The first step, as mentioned before, is to calculate the flow field potential. Using the developed matrix solver with updating as explained before in Section 4.2, we get the first potentials solution for each node in the system. Table 4.10 shows the resulting solution for the 4 by 4 network system.

Inlets					Outlets
5	3.89564	3.43857	2.63339	2.01636	1
5	4.27661	3.58208	2.2842	1.75776	1
5	4.20834	3.50241	2.41624	1.57163	1
5	3.93928	3.3589	2.8698	1.59376	1

Table 4.10 Potentials for each node in the system at the beginning of viscous invasion test.

Checking the mass balance error for each node shows the error is below the set value, which was 10^{-15}. Table 4.11 shows the mass balance error calculation for the first step.

	Y1	Y2	Y3	Y4
X1	-3.38E-14	-2.84E-14	-1.82E-14	-6.66E-15
X2	-1.87E-14	5.33E-15	-1.87E-14	-8.88E-16
X3	-1.69E-14	-6.22E-15	-6.22E-15	-8.88E-16
X4	0	1.78E-15	-4.44E-15	-2.66E-15

Table 4.11 Mass balance error calculated for each node

Now we have to calculate the flow rates in each bond in the network. The criterion for invasion has been chosen to be the highest flow rate among all the possible candidates, as mentioned previously. Table 4.12 shows the calculated flow rates for all the candidate bonds in the test example. Each node has at least three bonds connecting it to other nodes in this example network system, as shown in Figure 4.26 and therefore has to have at least three flow rates calculated. But for simplicity, we only show the highest flow rate calculated for each node. Table 4.12 shows these flow rates for only the front of flow in the candidate nodes. For the first step of invasion, the moving front candidates are made up of nodes number 1, 5, 9 and 13.

Highest Flow rates @ node number
0.552181 @ 1
0.090424 @ 5
0.113094 @ 9
1.060720 @ 13

Table 4.12 Highest flow rates calculated at the front

As shown in Table 4.12, the flow rate in node number 13 of this front is the highest. Therefore, this node will be invaded from the inlet. Figure 4.27 shows the invaded nodes in the first step of viscous invasion.

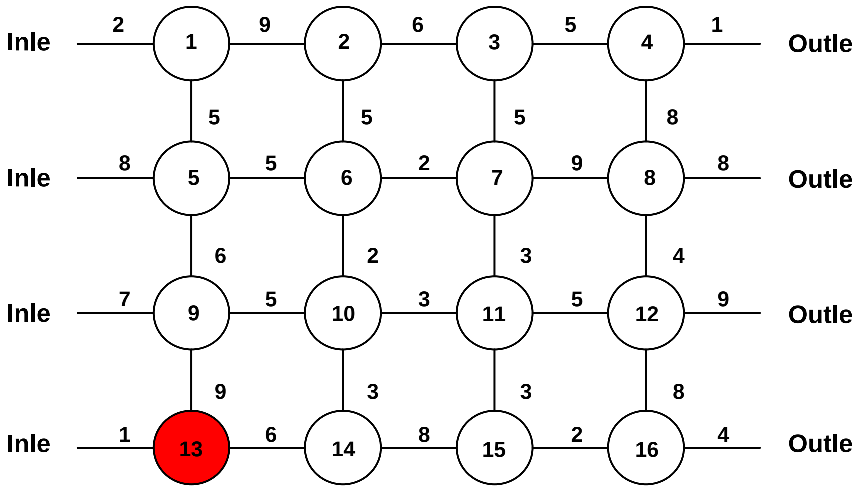

Figure 4.27 First invaded node in 4x4 viscous invasion test

Now that one node in the system has been invaded, the potential field will change, and therefore we need to update the flow field. The reason is, if the flow front advances to another location in the network and we assign the inlet potential to the corresponding invaded node in that advancing front (moving boundary criterion), the potential field with the current solution, will not satisfy the general form of flow equations (Eq. 4.4). Therefore, we have to update the potentials in our system of equations which consists of the L.I.U. matrix and the boundary rates. Then solve the system of equations again to get the new potentials that satisfy the new resulted field.

The invaded node, as mentioned before will have the same potential as inlet potential (neglecting the potential drop in the invaded zone) and the new flow front will be made up of nodes number 1, 5, 9 and 14. After updating the potentials at the front and solving the resulted potential field, we will get the new solution for the potential, as shown in Table 4.13.

Inlets					Outlets
5	4.04681	3.59921	2.76754	2.11267	1
5	4.47122	3.79153	2.42439	1.84247	1
5	4.68625	3.94027	2.68683	1.67767	1
5	5	4.04959	3.37777	1.72692	1

Table 4.13 Potentials for each node in the system at the second step of viscous invasion test

The mass balance error calculated for this new potential field shows that we are in the predefined range of accuracy (Table 4.14).

	Y1	Y2	Y3	Y4
X1	-3.38E-14	-2.84E-14	-1.82E-14	-6.66E-15
X2	-1.87E-14	5.33E-15	-1.87E-14	-8.88E-16
X3	-1.69E-14	-6.22E-15	-6.22E-15	-8.88E-16
X4	0	1.78E-15	-4.44E-15	-2.66E-15

Table 4.14 Mass balance error calculated for the second step of the viscous invasion test

With this new potential field we can calculate the flow rates for each bond in the system. Again, only the highest flow rates have been shown in table 4.15, for simplicity.

Highest flow rates @ node number	
0.476595 @ 1	0
0.066098 @ 5	0
0.044822 @ 9	0
0	0.158402 @ 14

Table 4.15 Highest flow rates calculated at the front

Node number 1 has the highest flow rate from the inlet and will therefore be invaded. Figure 4.28, shows the new invaded node in the network.

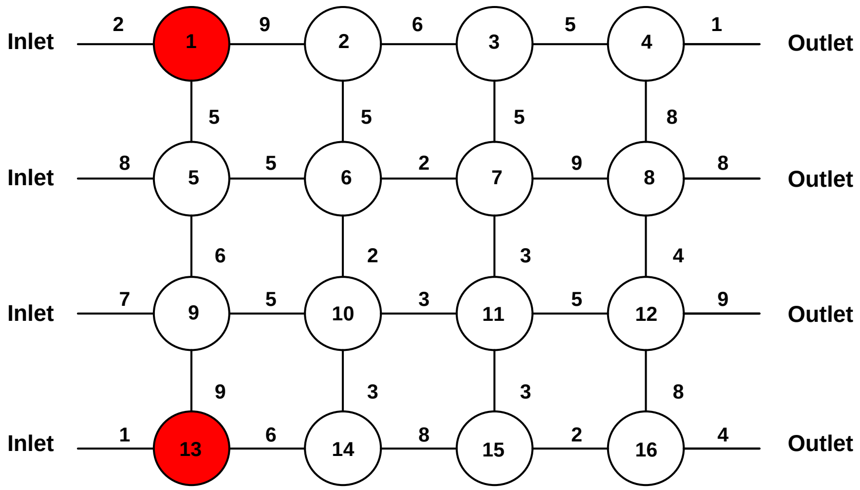

Figure 4.28 Second invaded node in 4x4 viscous invasion test

Continuing with the same process, we will advance to node number 14. Potential field, mass balance calculation errors and the resulted calculated flow rates are shown in Tables 4.16 to 4.18, Figure 4.29, shows the new invaded node.

Inlets					**Outlets**
5	5	4.23617	3.13992	2.32153	1
5	4.7729	4.17676	2.64282	1.97522	1
5	4.77765	4.07181	2.7945	1.73097	1
5	5	4.10275	3.44142	1.76647	1

Table 4.16 Potentials field in the system at the third viscous invasion step

	Y1	**Y2**	**Y3**	**Y4**
X1	0	-2.13E-14	-2.71E-14	-1.02E-14
X2	-8.88E-15	-9.77E-15	-2.18E-14	0
X3	-1.07E-14	4.44E-15	-9.77E-15	-5.33E-15
X4	0	-1.42E-14	1.78E-15	4.44E-16

Table 4.17 Mass balance error calculated for the third step of the viscous invasion test.

Highest flow rates @ node number	
0	0.08487 @ 2
0.028387 @ 5	0
0.031765 @ 9	0
0	0.149541 @ 14

Table 4.18 Highest flow rates calculated at the front

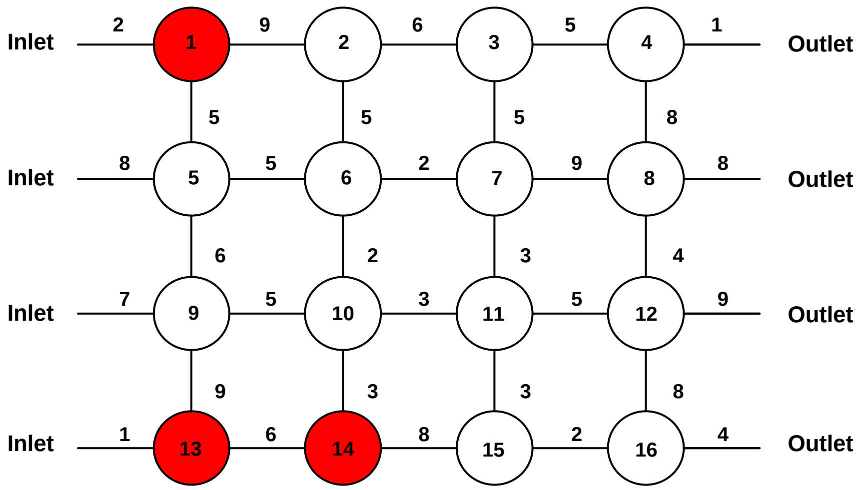

Figure 4.29 Third invaded node in 4x4 viscous invasion test

Step four of invasion. Potential field, mass balance errors and flow rates are shown in Tables 4.19 to 4.21 and Figure 4.30. Node number 10 has been invaded from node number 14.

Inlets					Outlets
5	5	4.27516	3.20112	2.37702	1
5	4.80601	4.2593	2.73637	2.03408	1
5	4.8413	4.37578	3.05337	1.83623	1
5	5	5	4.07652	1.91735	1

Table 4.19 Potential field for viscous invasion test, step 4

	Y1	Y2	Y3	Y4
X1	0	-2.66E-14	-1.78E-14	-1.82E-14
X2	-8.88E-15	-9.77E-15	-2.44E-14	1.78E-15
X3	1.15E-14	4.88E-15	-4.00E-15	4.44E-15
X4	0	0	-1.78E-15	-1.78E-15

Table 4.20 Mass balance error calculated for viscous invasion test, step 4

Highest flow rates @ node number		
0	0.080538 @ 2	0
0.024249 @ 5	0	0
0.022672 @ 9	0.208072 @ 10	0
0	0	0.115435 @ 15

Table 4.21 Highest flow rates calculated at the front, step 4

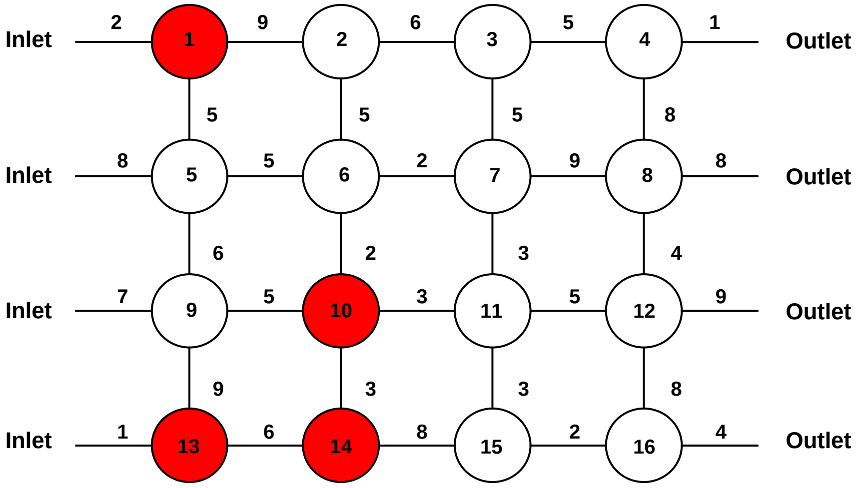

Figure 4.30 Invaded nodes in viscous invasion test, step 4

Step five of invasion. Potential field, mass balance errors and flow rates are shown in Tables 4.22 to 4.24 and Figure 4.31. Node number 11 has been invaded from node number 10.

Inlets					Outlets
5	5	4.32868	3.26125	2.42448	1
5	4.86792	4.40123	2.81712	2.07955	1
5	4.97065	5	3.23351	1.88927	1
5	5	5	4.1238	1.95441	1

Table 4.22 Potential field for viscous invasion test, step 5

	Y1	Y2	Y3	Y4
X1	0	-2.49E-14	-1.64E-14	-4.88E-15
X2	-9.77E-15	-7.99E-15	-1.51E-14	0
X3	-1.33E-14	0	0	-3.55E-15
X4	0	0	3.55E-15	8.88E-16

Table 4.23 Mass balance error calculated for viscous invasion test, step 5

Highest flow rates @ node number		
0	0.074591 @ 2	0
0.016510 @ 5	0.299384 @ 6	0
0.004193 @ 9	0	0.588831 @ 11
0	0	0.109526 @ 15

Table 4.24 Highest flow rates calculated at the front, step 5

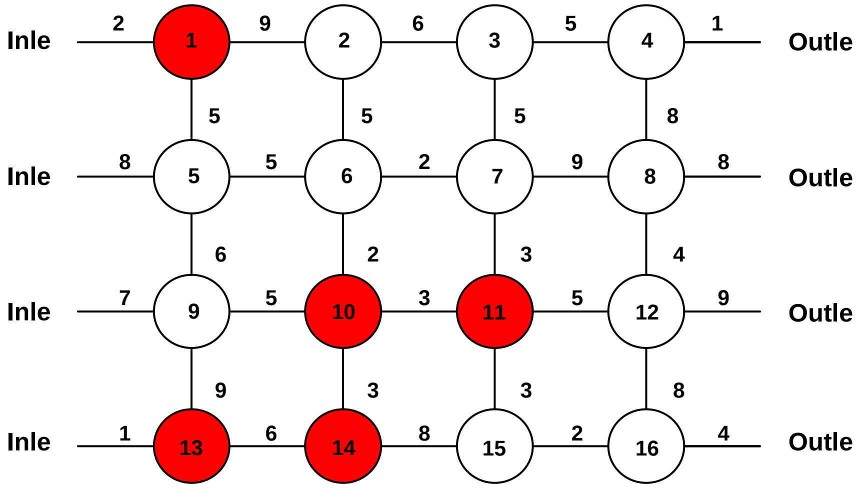

Figure 4.31 Invaded nodes in viscous invasion test, step 5

Step six of invasion. Potential field, mass balance errors and flow rates are shown in Tables 4.25 to 4.27 and Figure 4.32. Node number 7 has been invaded from node number 11.

Inlets					Outlets
5	5	4.44759	3.55291	2.70227	1
5	4.89563	4.52686	3.32994	2.3834	1
5	4.97681	5	5	2.38277	1
5	5	5	4.58497	2.30229	1

Table 4.25 Potential field for viscous invasion test, step 6

	Y1	Y2	Y3	Y4
X1	0	-2.31E-14	-1.47E-14	-1.02E-14
X2	-4.44E-15	-1.07E-14	-1.87E-14	5.33E-15
X3	-2.66E-15	0	0	-3.55E-15
X4	0	0	0	1.78E-15

Table 4.26 Mass balance error calculated for viscous invasion test, step 6

Highest flow rates @ node number			
0	0.061379 @ 2	0	0
0.013046 @ 5	0.236572 @ 6	0.556686 @ 7	0
0.003313 @ 9	0	0	0.523447 @ 12
0	0	0.051879 @ 15	0

Table 4.27 Highest flow rates calculated at the front, step 6

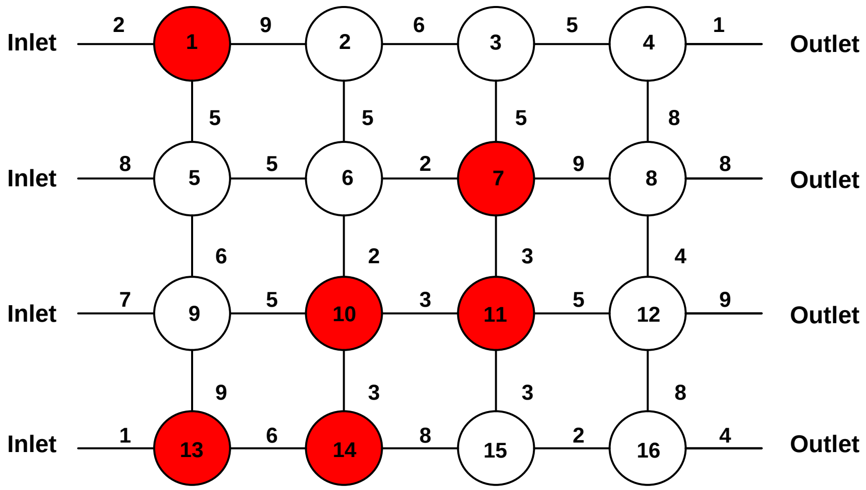

Figure 4.32 Invaded nodes in viscous invasion test, step 6

Step seven of invasion. Potential field, mass balance errors and flow rates are shown in Tables 4.28 to 4.30 and Figure 4.33. Node number 12 has been invaded from node number 11.

Inlets					Outlets
5	5	4.81561	4.44495	3.44509	1
5	4.98423	4.92852	5	3.12582	1
5	4.9965	5	5	2.52202	1
5	5	5	4.59748	2.38365	1

Table 4.28 Potential field for viscous invasion test, step 7

	Y1	Y2	Y3	Y4
X1	0	-3.82E-14	-7.11E-15	-9.33E-15
X2	-1.33E-14	1.15E-14	0	-7.11E-15
X3	0	0	0	7.11E-15
X4	0	0	0	0

Table 4.29 Mass balance error calculated for viscous invasion test, step 7

Highest flow rates @ node number			
0	0.020488 @ 2	0.111011 @ 3	0
0.001971 @ 5	0.035742 @ 6	0	0.208242 @ 8
0.000501 @ 9	0	0	0.495596 @ 12
0	0	0.050314 @ 15	0

Table 4.30 Highest flow rates calculated at the front, step 7

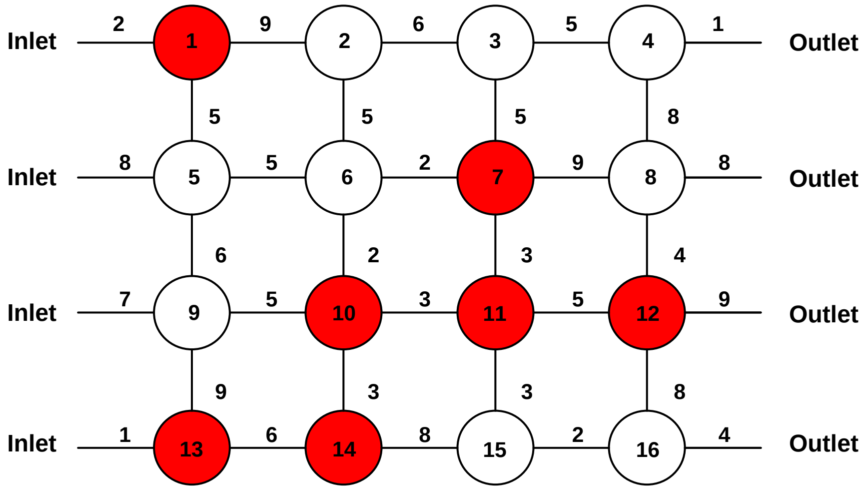

Figure 4.33 Invaded nodes in viscous invasion test, step 7

This is the last step of invasion where breakthrough occurred. Potential field, mass balance errors and flow rates are shown in Tables 4.31 to 4.33 and Figure 4.34. Outlet node number 19 has been invaded from node number 12.

Inlets					Outlets
5	5	4.84801	4.54247	3.7183	1
5	4.987	4.94108	5	3.54298	1
5	4.99711	5	5	5	1
5	5	5	4.82022	3.83146	1

Table 4.31 Potential field for viscous invasion test, breakthrough

	Y1	Y2	Y3	Y4
X1	0	-4.17E-14	-1.33E-14	4.44E-16
X2	-2.75E-14	5.33E-15	0	-7.11E-15
X3	-1.33E-14	0	0	0
X4	0	0	-5.33E-15	-1.78E-15

Table 4.32 Mass balance error calculated for viscous invasion test, breakthrough

Highest flow rates @ node number			
0	0.016888 @ 2	0.091505 @ 3	0
0.001625 @ 5	0.029462 @ 6	0	0.161891 @ 8
0.000413 @ 9	0	0	0
0	0	0.022472 @ 15	0.146067 @ 16

Table 4.33 Highest flow rates calculated at the front, breakthrough

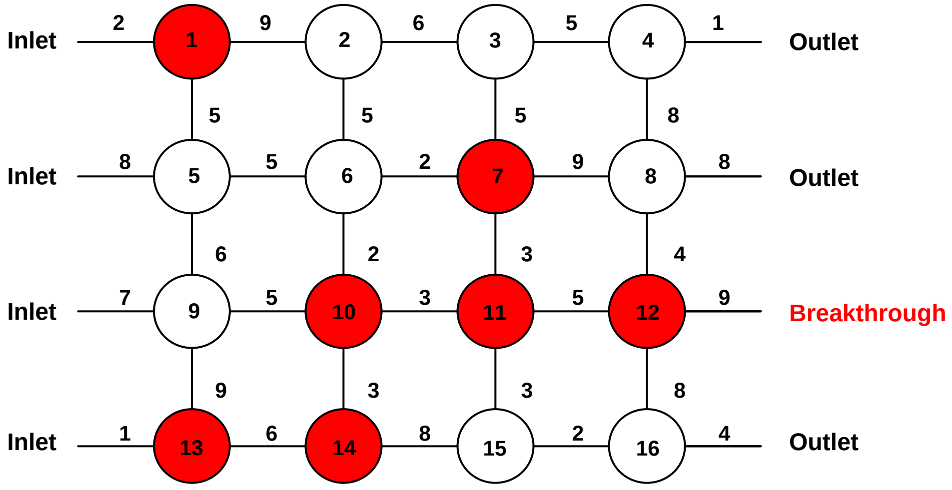

Figure 4.34 Invaded nodes in viscous invasion test, breakthrough.

Some examples of the viscous invasion test with different choice of flow rates for viscous invasion and larger networks of 20,000 nodes have been shown in Figures 3.6 through 3.15 in chapter 3. Therefore we don’t show more example tests for viscous invasion on networks with higher number of nodes, in this section.

4.6. SEARCH ALGORITHM

One of the issues in network modeling that makes it expensive in terms of computer time is finding the best way to search the connected nodes.

In regular lattices, since the degree of freedom and the locations are known for each node, it is very easy to define internal loops in the computer code to search for adjacent neighbors. For example, in a regular cubic lattice checking the upper and lower or left and right neighbors or even the two other neighbors located in the adjacent layers in 3D is simple and can be done with just three search loops for i, j and k in computer code. Figure 4.35 shows these neighbors in a 3D cubic regular lattice.

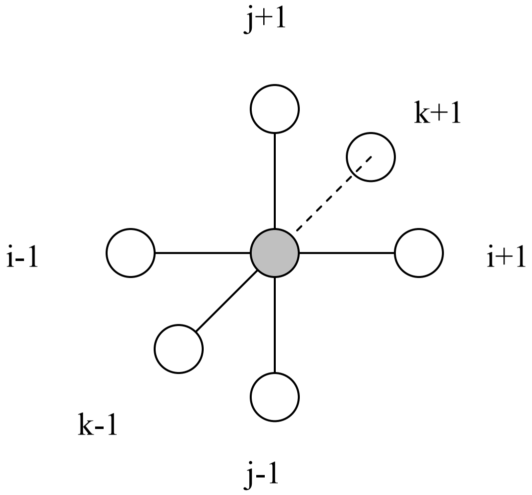

Figure 4.35 Neighboring nodes indices in a 3D cubic lattice

Also, there is no need to store these neighbors in the memory since they are all on a fixed predefined location. But in a real sample, the number of connections and the locations do not obey a regular format, although there is a maximum or minimum number of connectivity involved. This fact imposes a need for a structure capable of locating all nodes in three dimensions and also of keeping track of neighbor nodes, and at the same time being able to address the properties of the bonds in between these nodes for calculations.

This problem forces us to use a new structure that is capable of addressing all these issues at the same time. The major importance of this structure is its ability to fit into any lattice. It is called irregular multi dimension structure, and we will discuss it in more detail in the next section.

In our code we have implemented two search algorithms. One algorithm is for regular lattices, with integrated search loops, and the other for irregular lattices.

4.7. IRREGULAR MULTI-DIMENSION STRUCTURE

A node in a regular 3D lattice can only be connected to nodes that are in the adjacent layers of i±1, j±1 and k±1 (Figure 4.35). But in irregular lattices, a node can be connected to another node without any pattern.

The most important part of this model is the irregular multi dimensional structure that we have implemented into the modeling software. This gives us the ability to define any kind of structure, regular or irregular lattices, and with different numbers of connections between nodes (for irregular lattices). For example, one can define a Voronoi space, which has up to 17 degree of connectivity in its structure. Figure 4.36 shows an example of such an irregular structure. As shown in Figure 4.36, there is no specific i, j or k indexing, like the regular three dimensional lattices. Instead there will be a table containing all the neighboring nodes, locations and the properties of the bonds connecting nodes.

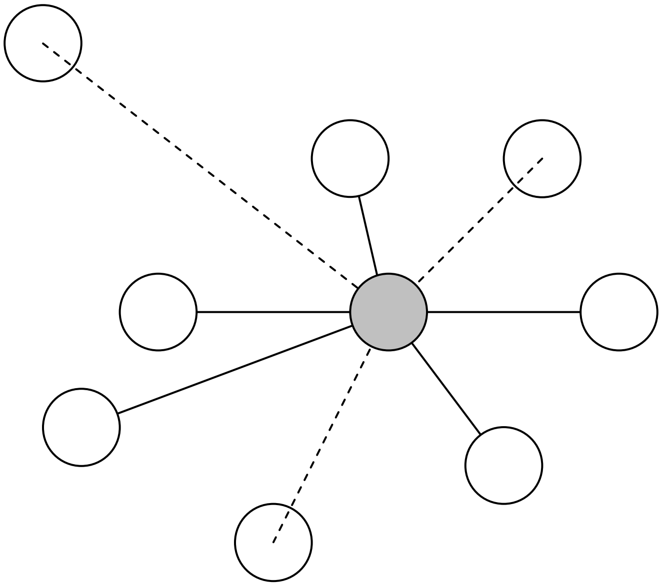

Figure 4.36 Node with irregular 3D connections have the capability to be connected to nodes that are in random distances

To explain the structure of this method we need to look at an example. Figure 4.37 shows a test example irregular network. We have 8 nodes with different numbers of connectivity and which are irregularly numbered. We have nodes from one degree of connectivity to nodes with six degrees. To be able to track all connectivities and locations we need a connectivity table as follows.

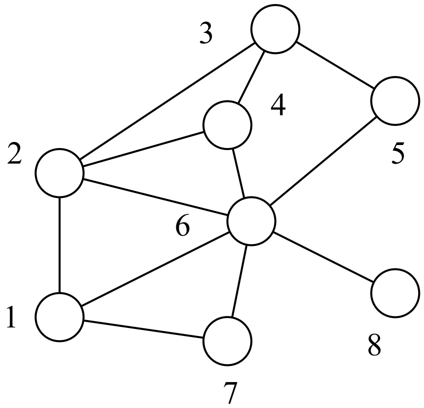

Figure 4.37 Irregular network connectivity example

The first column of the table will be the number of nodes connected to each node, which can range from one to any integer number depending on the connectivity of that node (pore). The maximum of this connectivity may be set by a variable that can also allow the size of the array. The rest of the table will contain the connected nodes' ID numbers (assigned number to each node). Another table is needed to carry the bonds' information, such as length, radius, shape or any other property that may be of interest. These properties can be radii, wettabilities, and etc. The row number would also be equal to the ID of the node.

As can be inferred from the Table 4.34, row one is for node number one, which has three connected nodes; and the connected nodes ID's are two, six and seven, as shown in Figure 4.37. The second row corresponds to second node, which has four neighbors with IDs one, three, four and six. The same rule applies for nodes three to eight. By this procedure we fill the irregular lattice information in each row in the table. Please note that the first column is only the number of connected neighbors, not the neighbors' ID. The row number corresponds to the nodes' ID. This means row number one hold information for node number one, which has three connected nodes. This irregular lattice has connectivities from one to six. Therefore, the table of cells should have seven columns. Table 4.34 shows the resulting information table for the sample irregular network shown in Figure 4.37.

The main benefit of this structure is its simplicity. One can input each node, the number of nodes connected to this node (connectivity) and the ID's of these nodes from any other source, and generates this structure. If the imported information is from a regular lattice, this table will show a regular pattern in it, like Table 4.3, and if you have an irregular lattice it can handle that structure too.

Number of connections	Connected to Nodes					
3	2	6	7			
4	1	3	4	6		
3	2	4	5			
3	2	3	6			
2	3	6				
6	1	2	4	5	7	8
2	1	6				
1	6					

Table 4.34 Connectivity of the nodes in the sample irregular network

Also, to check the validity of the table, each node ID should be repeated as the number of its connectivity in the connected nodes part of the table. For example node number six in the above example has been repeated six times in rows one, two, four, five, seven and eight for the connected nodes.

In this fashion, the process of finding the neighbors is a bit different from the regular lattice neighbor finding internal loops. For each node the program code reads the ID number of nodes and then checks the corresponding row. It then reads the connected nodes IDs one by one.

As mentioned before, another table is needed to hold the information of the bonds connecting these nodes together. Therefore, we defined the same structured table, which is the same as the connectivity table, for bonds information. This table will hold the bonds conductivity corresponding to each Node couple.

Figure 4.38 shows a more complicated example, with nodes and the bonds' conductivities between them. Using the rules mentioned before, we can generate the connectivity table, as shown in Table 4.35. Also, the bond conductivity table, which holds information about the bonds, is presented in Table 4.36, with a similar structure to Table 4.34.

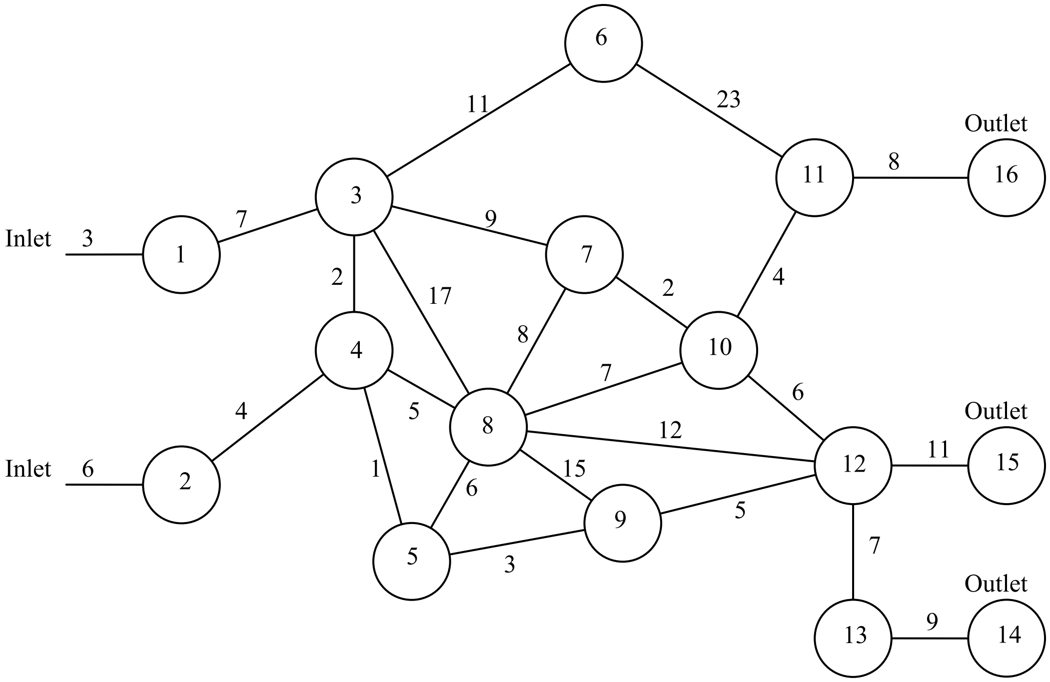

Figure 4.38 Irregular 2D network example

Number of connections	Connected to Nodes						
2	**Inlet**	3					
2	**Inlet**	4					
5	1	4	8	7	6		
4	3	2	5	8			
3	9	8	4				
2	3	11					
3	3	8	10				
7	4	5	9	12	10	7	3
3	5	12	8				
4	7	11	12	8			
3	6	10	**16**				
5	10	9	13	8	**15**		
2	12	**14**					
1	13						
1	12						
1	11						

Table 4.35 Connectivity matrix

	Conductivity Table						
Middle Nodes	3	7					
	6	4					
	7	2	17	9	11		
	2	4	1	5			
	3	6	1				
	11	23					
	9	8	2				
	5	6	15	12	7	8	17
	3	5	15				
	2	4	6	7			
	23	4	8				
	6	5	7	12	11		
	7	9					
Outlets	9						
	11						
	8						

Table 4.36 Bonds conductivity matrix

CHAPTER 5

Testing and Verifications

INTRODUCTION

This chapter consists of verifications of some the important objects in the developed code. We start with simple cases that we know what would be range or behavior of the results to the test each function in the code. These tests will help us to verify the accuracy of the model.

Functions like conductance generators or re-samplers will be tested and verified. Tests will be done on unit conductivity networks or networks with a single dominant channel. Structure like equal potentials or middle spot injectors will also be tested. We will also run some simple test on 2D and 3D regular lattices and compare the results with the known or expected values to check the accuracy of the simulator.

After verification, we can perform complicated tests on irregular networks for the purpose of this research.

5.1. UNIFORM RANDOM DISTRIBUTION OF CONDUCTANCE

The developed software has a function capable of generating uniform random values. This function uses the direct random generator of the C++ computer language. The C++ function rand( ) generates random integers in the range of 0 to RAND_MAX which is usually 2147483647 (equal to 2^{31}-1). These values are uniformly distributed. That is, if you called "**rand()**" many times, a histogram of the values would appear flat, signifying each integer is equally likely to be generated.

Figure 5.1 shows a sample generated uniform random values for conductance between 1 and 100 unit of conductivity for a two dimensional 100 × 100 square lattice. The number of generated random conductivities should be $2N^2$ for an N by N square network, which are 20,000 bond conductivities.

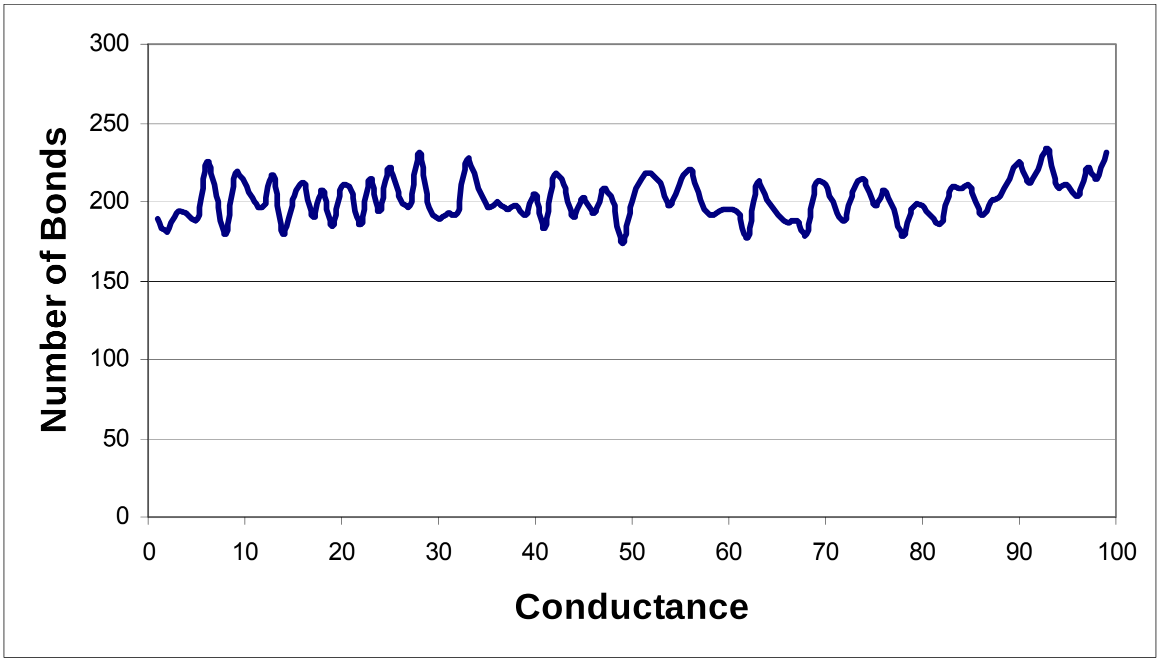

Figure 5.1 Distribution of bond conductivities for 20,000 uniform random values, between 1 and 100

For the limiting case this histogram should become a flat line, if the number of conductivity samples approaches infinity.

5.2. NORMAL DISTRIBUTION OF CONDUCTANCE

Computer generated random numbers are uniformly distributed. There is a neat and efficient trick for turning uniformly distributed numbers into normally distributed ones. Suppose x1 and x2 are random numbers chosen from a uniformly distributed random variable in the interval (0, 1). Then

$$y = Cos(2\pi x_2)\sqrt{-2\log(x_1)} \qquad \text{Eq. 5.1}$$

is normally distributed with mean 0 and standard deviation 1. There are many ways to perform this transformation. Some people use this direct transformation and some others use more complicated algorithms to make sure that they get the normal Gaussian distribution with the desire mean and standard deviation. These more complicated ones can be used but they are much more time consuming.

One these methods is called the Box-Muller method, Which uses two sine and cosine for generating the normal random numbers from a uniform distribution but it takes around 10 times more time, although it might be less than a 0.01% more accurate than the usual quick method for generating 100,000 random numbers.

The quick method that has been used in this research uses the following transformation which is very fast and efficient. It can generate 1,000,000 random numbers with a 400 MHz. CPU on a personal computer in less than 10 seconds.

$$y = Mean + \sqrt{-2\log(\frac{x_1 + 1}{RAND\_MAX})} \times Sin(\frac{2\pi x_2}{RAND\_MAX}) \times STD$$

Eq. 5.2

X1 and X2 are random numbers taken from a uniform distribution. Figure 5.2, shows a comparison between the quick and Box-Muller methods for 100,000 random numbers.

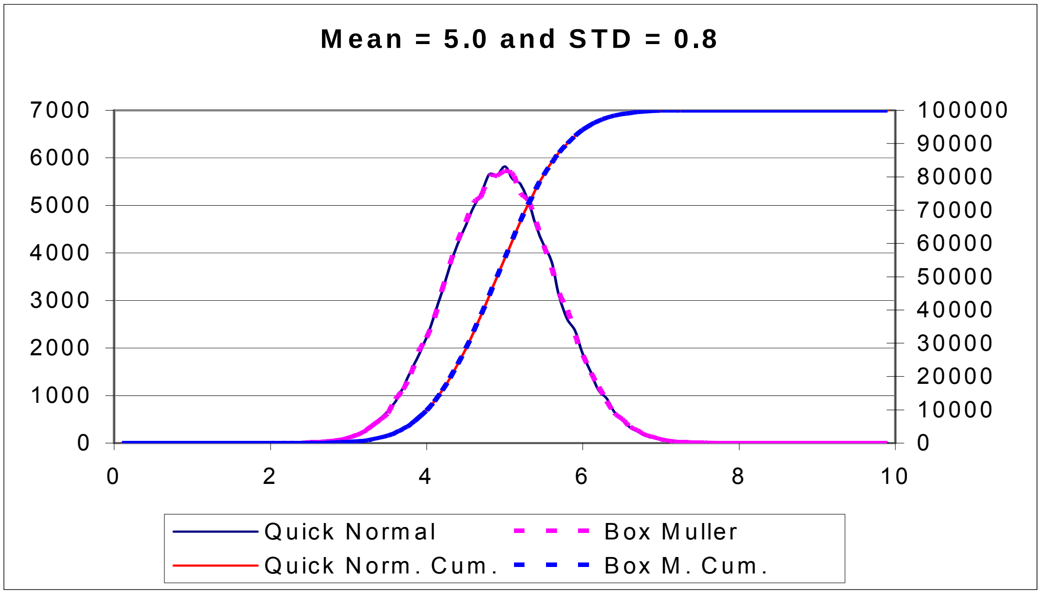

Figure 5.2 Comparison between Box-Muller and Quick method

5.3. BI-MODAL GAUSSIAN NORMAL RANDOM DISTRIBUTION OF CONDUCTANCE

It is very easy to generate a bi-modal normal distribution when you can generate the normal ones. Just generate any normal distribution that you want and then add the two distributions together. Supper position principal can be use for these distributions. You can super impose them together and generate any distributions. Next graphs show two Gaussian normal distributions with standard deviations (STD) of 0.7 but different means equal to 3 and 7. Using supper position we get a bi-modal distribution of these two. Each has 100,000 random numbers normally distributed (sampled from a uniform distribution by the quick method), Figures 5.3 and 5.5.

In this example we chose similar number of random points for each distribution but it is not important. Different distributions with different number of points can be superimposed.

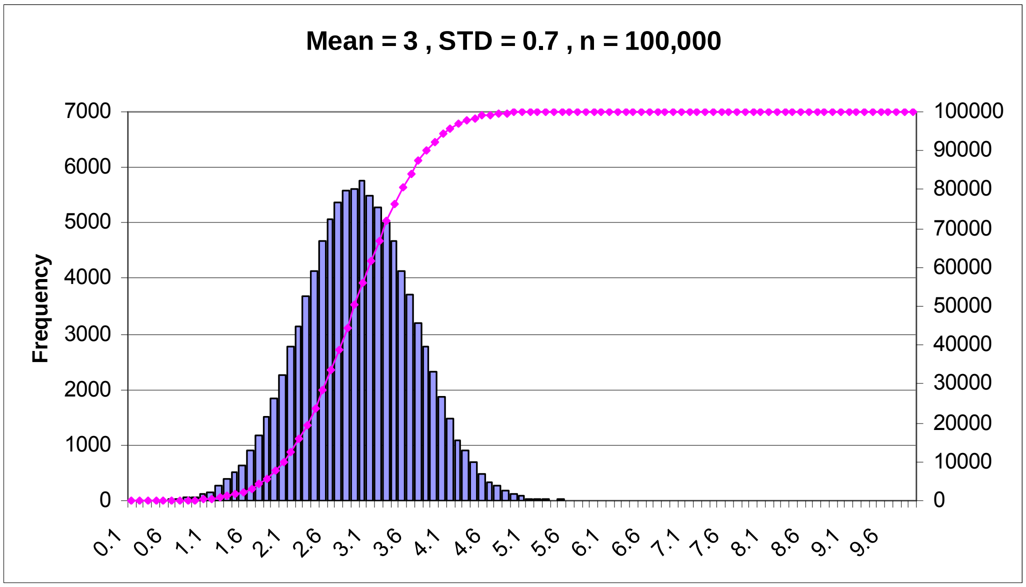

Figure 5.3 Normal distribution with mean of 3 and STD 0.7

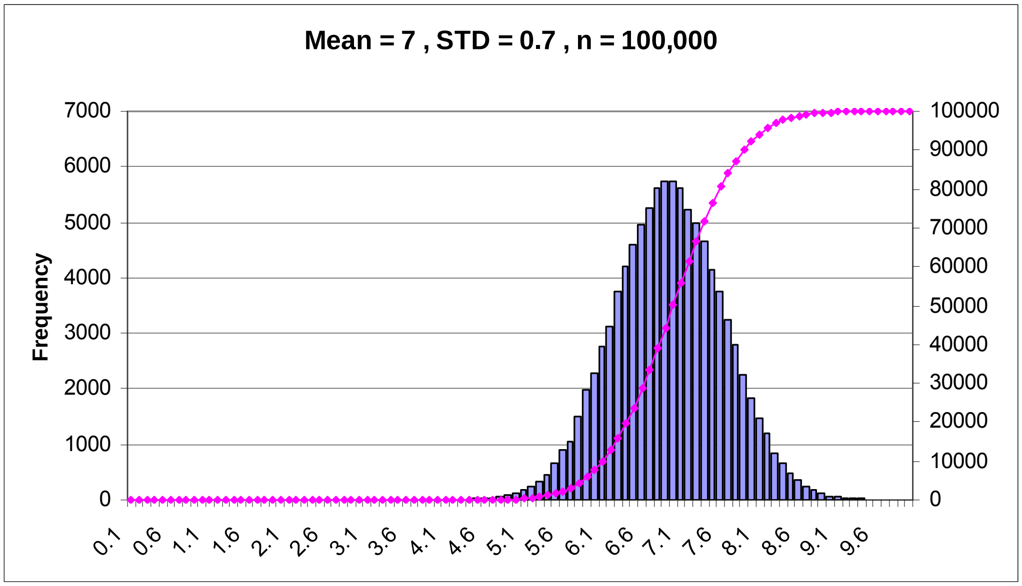

Figure 5.4 Normal distribution with mean of 7 and STD 0.7

Adding these two distributions together, we get the distribution shown in Figure 5.5. The resulted distribution has the characteristics of both normal distributions.

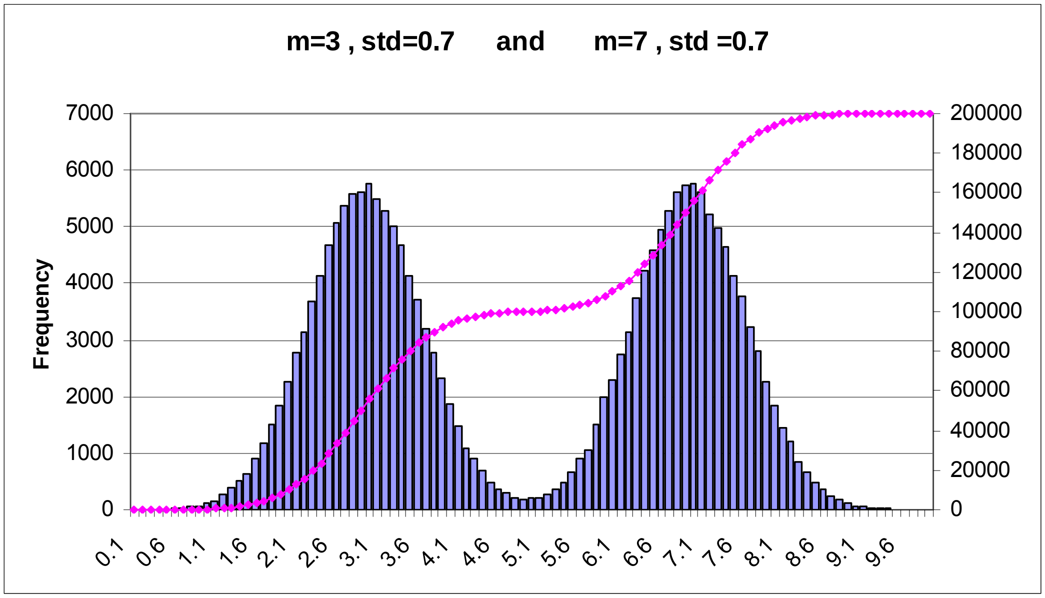

Figure 5.5 Bi-Modal distribution with its cumulative distribution

The cumulative distribution of these two normal ones is the addition of the two normal distributions, which has total of 200,000 random numbers.

5.4. UNIFORM RE-SAMPLING OF AN ARBITRARY DISTRIBUTION OF CONDUCTANCE

One of the important internal functions of the developed software in this research dissertation is the ability to read any arbitrary distribution and generate either a denser more refined similar distribution or just uniformly re-sample the distribution. This function gives us the ability to read any distribution of conductance or bond radii for a real or artificially generated sample and make as many as realizations as necessary for the necessary invasion tests.

The reason for uniform re-sampling is that we want to keep the shape of the distribution intact even if we make hundreds of realizations. Therefore, all the random realizations of this distribution will have the similar distribution.

A test has been set to verify the accuracy of the function. We feed a cumulative distribution of conductivities with 100 conductivity values from a cumulative distribution function (CDF). We then generated the same distribution with a denser sampling of 200 values. Figure 5.6, shows the original CDF and the generated denser CDF.

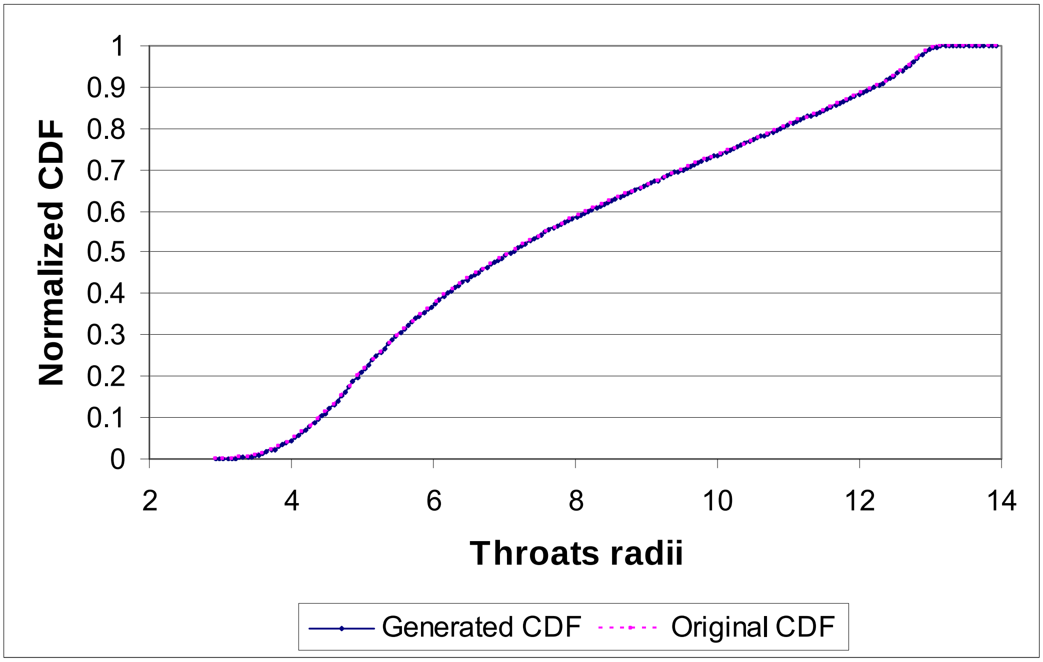

Figure 5.6 Original and generated CDF’s

As shown on Figure 5.6, the normalized generated CDF has exactly fitted the original cumulative distribution.

As an example of direct re-sampling, if we take the Finney pack distributions presented in Chapter 4 in Figure 4.18, and resample the original 60,000 sample for only 20,000 bond radii, the cumulative distribution and histogram of the re-sampled values should be similar. Figures 5.7 and 5.8, show CDF and histogram of such an under sampling.

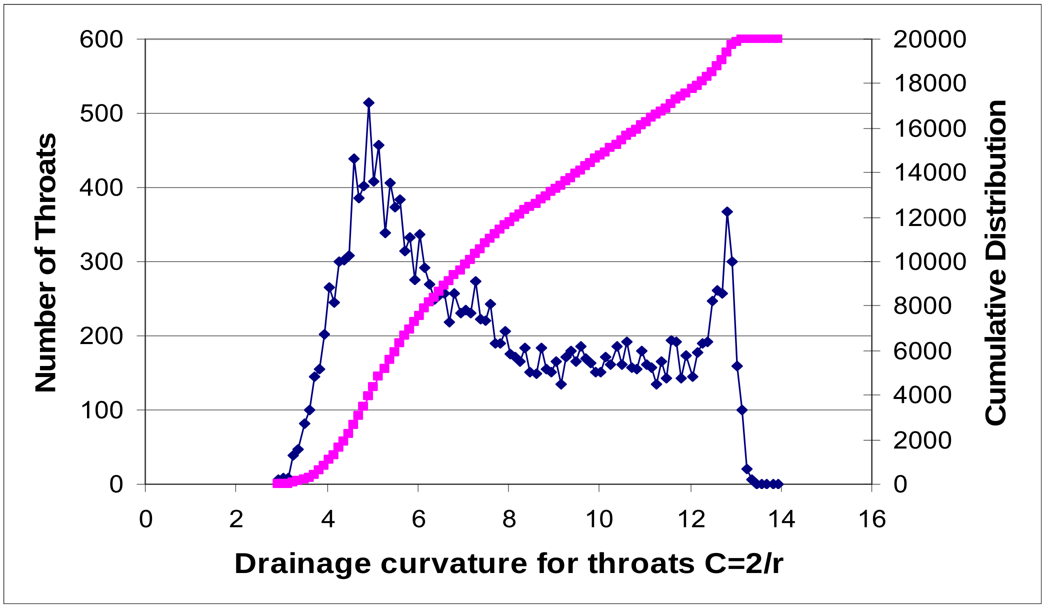

Figure 5.7 CDF of the 20,000 re-sampled values

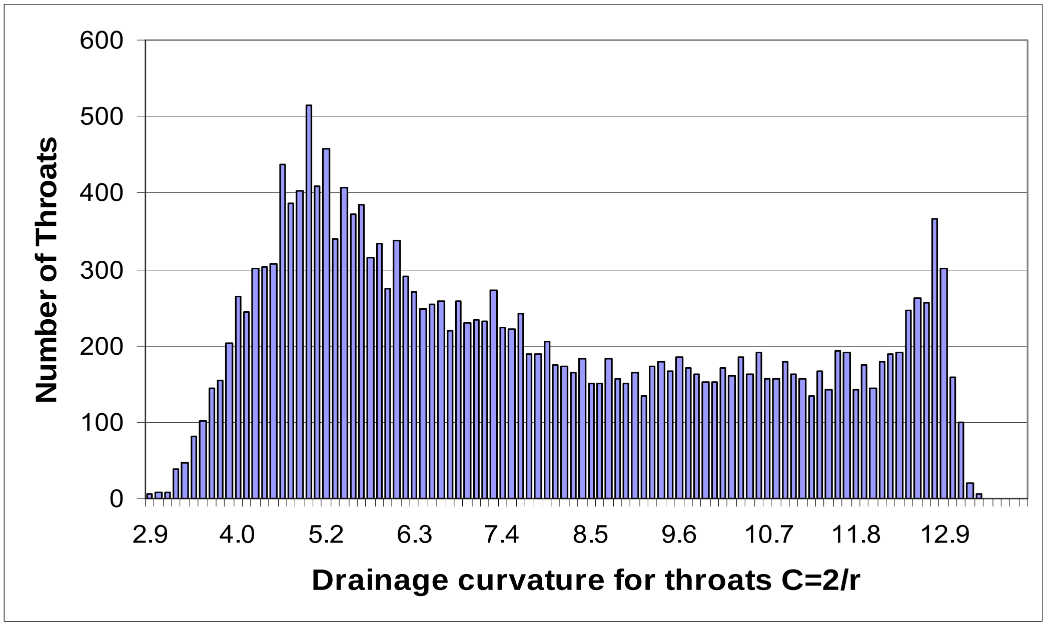

Figure 5.8 Histogram of the 20,000 re-sampled drainage curvature for throats

5.5. DIRECT DATA INPUT

This feature allows to directly reading all the information of a network, such as nodes connectivity, bond properties like throats radii and length, 3D locations of nodes, location of injectors and producers, and etc.

This feature allows performing tests on any irregular or imaginary network structure. It will also makes the user capable of finely changing even a single node or bond property in a network and repeats the simulations. For details of how to perform these changes please refer to Appendix A.1, data entry.

5.6. NUMERICAL SOLVER

In this section we test the developed numerical solver to verify that the solution for the system of equations is correct. An example of 9 nodes on a 3 by 3 square lattice has been set for the test. The bond conductivities have randomly chosen and are shown on Figure 5.9.

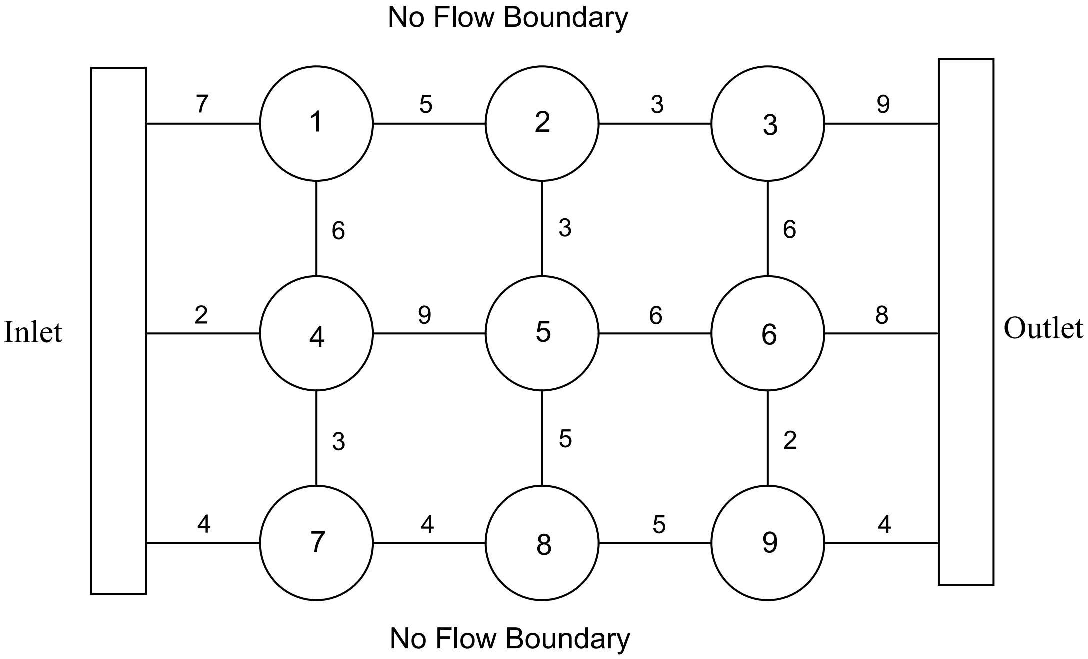

Figure 5.9 3 by 3 test square network

Up and bottom are no flow boundaries. Inlet has 5 unit potential and outlet has 1 unit potential. The overall potential gradient is $\Delta P = P_{in} - P_{out} = 5 - 1 = 4$ units. The resulted system of equations for this network with the conductivity of each bond is

$$\begin{bmatrix} 18 & -5 & 0 & -6 & 0 & 0 & 0 & 0 & 0 \\ -5 & 11 & -3 & 0 & -3 & 0 & 0 & 0 & 0 \\ 0 & -3 & 18 & 0 & 0 & -6 & 0 & 0 & 0 \\ -6 & 0 & 0 & 14 & -9 & 0 & -3 & 0 & 0 \\ 0 & -3 & 0 & -9 & 23 & -6 & 0 & -5 & 0 \\ 0 & 0 & -6 & 0 & -6 & 22 & 0 & 0 & -2 \\ 0 & 0 & 0 & -3 & 0 & 0 & 11 & -4 & 0 \\ 0 & 0 & 0 & 0 & -5 & 0 & -4 & 14 & -5 \\ 0 & 0 & 0 & 0 & 0 & -2 & 0 & -5 & 11 \end{bmatrix} \times \begin{bmatrix} P_1 \\ P_2 \\ P_3 \\ P_4 \\ P_5 \\ P_6 \\ P_7 \\ P_8 \\ P_9 \end{bmatrix} = \begin{bmatrix} 7P_{Inlet} \\ 0 \\ 9P_{Outlet} \\ 2P_{Inlet} \\ 0 \\ 8P_{Outlet} \\ 4P_{Inlet} \\ 0 \\ 4P_{Outlet} \end{bmatrix}$$

Substituting the inlet and outlet potentials will generate the system of equations with the boundary conditions as

$$\begin{bmatrix} 18 & -5 & 0 & -6 & 0 & 0 & 0 & 0 & 0 \\ -5 & 11 & -3 & 0 & -3 & 0 & 0 & 0 & 0 \\ 0 & -3 & 18 & 0 & 0 & -6 & 0 & 0 & 0 \\ -6 & 0 & 0 & 14 & -9 & 0 & -3 & 0 & 0 \\ 0 & -3 & 0 & -9 & 23 & -6 & 0 & -5 & 0 \\ 0 & 0 & -6 & 0 & -6 & 22 & 0 & 0 & -2 \\ 0 & 0 & 0 & -3 & 0 & 0 & 11 & -4 & 0 \\ 0 & 0 & 0 & 0 & -5 & 0 & -4 & 14 & -5 \\ 0 & 0 & 0 & 0 & 0 & -2 & 0 & -5 & 11 \end{bmatrix} \times \begin{bmatrix} P_1 \\ P_2 \\ P_3 \\ P_4 \\ P_5 \\ P_6 \\ P_7 \\ P_8 \\ P_9 \end{bmatrix} = \begin{bmatrix} 35 \\ 0 \\ 9 \\ 10 \\ 0 \\ 8 \\ 20 \\ 0 \\ 4 \end{bmatrix}$$

This system of equations with the boundary values is ready to be exported into the L.I.U. solver. The solution for this system is

$$\begin{bmatrix} P_1 \\ P_2 \\ P_3 \\ P_4 \\ P_5 \\ P_6 \\ P_7 \\ P_8 \\ P_9 \end{bmatrix} = \begin{bmatrix} 3.95721 \\ 3.00467 \\ 1.58314 \\ 3.53441 \\ 2.83864 \\ 1.74707 \\ 3.79904 \\ 2.79654 \\ 1.95244 \end{bmatrix}$$

The error tolerance is 10^{-14} but only the first 5 digits for the solution are shown. To verify the accuracy of the solver we picked three nodes and plug the values in their equations. Nodes number 1, 5 and 9 were shown for this verification. The equations will be as follows:

For node number 1

$$
\begin{aligned}
&18P_1 - 5P_2 - 6P_4 = 7P_{inlet} \\
&\Rightarrow 18*3.95721 - 5*3.00467 - 6*3.53441 = 7*5 \\
&\Rightarrow 71.22978 - 15.02335 - 21.20646 = 35 \\
&\Rightarrow 71.22978 - 15.02335 - 21.20646 - 35 = 0 \\
&\Rightarrow 71.22978 - 71.22981 = -0.00003
\end{aligned}
$$

For node number 5

$$
\begin{aligned}
&23P_5 - 3P_2 - 9P_4 - 6P_6 - 5P_8 = 0 \\
&\Rightarrow 23*2.83864 - 3*3.00467 - 9*3.53441 - 6*1.74707 - 5*2.79654 = 0 \\
&\Rightarrow 62.45008 - 9.01401 - 31.80969 - 10.48242 - 13.9827 = 0 \\
&\Rightarrow 65.28872 - 65.28882 = -0.0001
\end{aligned}
$$

For node number 9

$$
\begin{aligned}
&11P_9 - 2P_6 - 5P_8 = 4P_{outlet} \\
&\Rightarrow 11*1.95244 - 2*1.74707 - 5*2.79654 = 4*1 \\
&\Rightarrow 21.47684 - 3.49414 - 13.9827 = 4 \\
&\Rightarrow 21.47684 - 3.49414 - 13.9827 - 4 = 0 \\
&\Rightarrow 21.47684 - 21.47684 = 0
\end{aligned}
$$

The reason that the answers are not accurate up to 10^{-14} is because we only show the first 5 digits after the decimal point. If we do the hand calculations up to the 14th decimal points, the results would be less than the error tolerance.

Plugging the numerical solution into the equations shows that solution is accurate within the error tolerance. So we can confidently use the developed numerical solver with compressed memory, defined in Chapter 4.

5.7. CUMULATIVE DISTRIBUTION GENERATION

Cumulative distributions functions can be read from a file. In this case a Cumulative Probability Distribution table is loaded from the specified location in input file and it should include in the first line, the number of rows in the table, and the table should include the minimum and maximum values corresponding to the probabilities 0 and 1 respectively.

The program reads the original table and uses 3-point polynomial interpolation to generate a bigger table with 100 rows. The polynomial interpolation uses the average between the 3-point upwards and 3-point downwards to ensure that the probability values monotonically increase as required in a proper CDF.

As an example we use a test CDF with only 25 sample probability values from a Finney pack distribution. Figure 5.10, shows the CDF graph of this distribution.

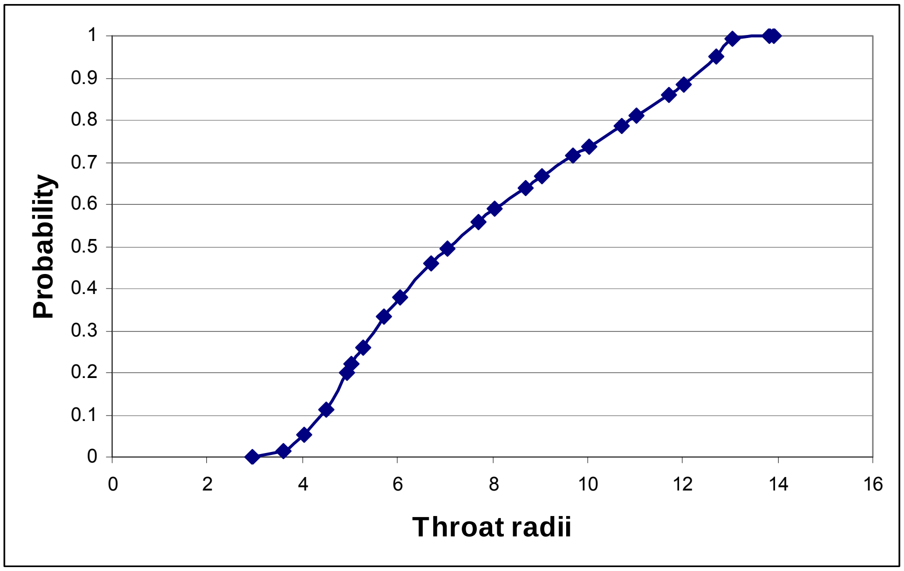

Figure 5.10 CDF with only 25 sample values

Then we use the CDF generator of the code to make a denser cumulative distribution with 100 sample values. The generated denser CDF is shown in Figure5.11, which matches the original CDF.

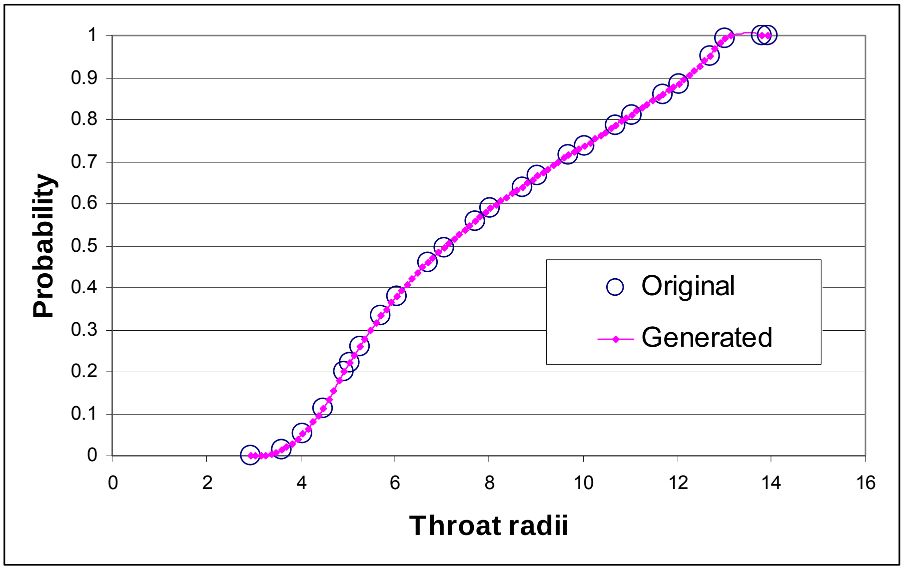

Figure 5.11 Original and generated CDF's

The parameter values for simulations are sampled from the big table with 100 rows using linear interpolation. A uniform random generator is used for the sampling as explained previously. This random generator also has a seed number that allows the reproduction of random sequences when desired.

5.8. VISCOUS INVASION TESTS

This section consists of test with the viscous invasion modeling to better understand the behavior of viscous displacement. In these tests we implement different types of throat radii distributions for bonds. We impose faults in the networks and put injectors in different locations on 2D square and 3D cubic lattices networks to investigate the movement of high viscosity fluid inside the porous media.

First we start with two dimensional networks. We make tests with unit throat sizes or tests with dominant single channels.

5.8.1. UNIT CONDUCTIVITY – 2D

This test is to check the situation that we have an artificially homogeneous system. This means all the bonds in the system have an equal hydraulic conductivity. The reason to verify this test is to validate the code search criterion in 2D and check if all the nodes are getting invaded or not. The expected result of this test should be a network of nodes, all invaded systematically column by column from inlet to outlet. No node should be left behind.

The test is a 50 × 50 square lattice network, unit bond hydraulic conductivity for all bonds, 50 inlet nodes at the left with 5 units of potential and 50 outlet nodes on the right with 1 unit of potential. The potential gradient will be 4 units per 50 nodes distance. Upper and lower nodes are connected to no flow boundaries.

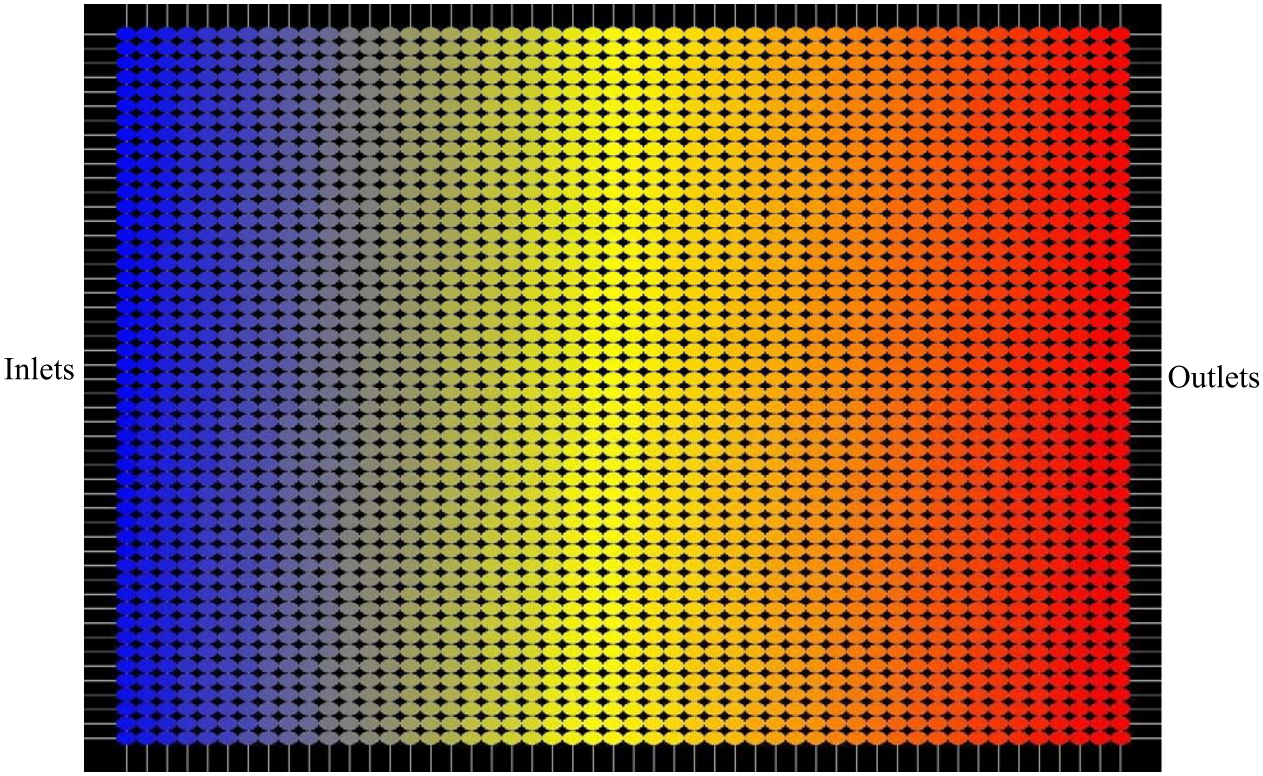

Figure 5.12 Unit hydraulic conductivity, viscous invasion test

This test agrees with the expected results. Each column of nodes was invaded at the same time (Figure 5.12). We used different shades for the columns to show which group of nodes have been invaded together.

5.8.2. DOMINANT SINGLE CHANNEL – 2D

In this test we actually set the situation that one specific path in the network has more hydraulic conductivity than other paths. To do so, we choose couple of nodes and put a large pore throat radius for the connecting bond between them. Other bonds radii were being sampled from a random generator. The system is a 2D 50 × 50 square lattice. Inlet and outlets are on the left and right with 5 and 1 unit of potential respectively. Upper and lower nodes are connected to no flow boundaries.

The ID's of the nodes with high bond radii are shown in Table 5.1. Figure 5.13 also shows the location of this high flow path in the network.

Nodes ID				
451	458	515	769	876
452	509	566	820	877
453	560	616	871	878
454	511	666	872	879
405	462	716	873	880
356	413	717	874	881
407	464	718	875	882

Table 5.1 ID of the nodes with high throats radii

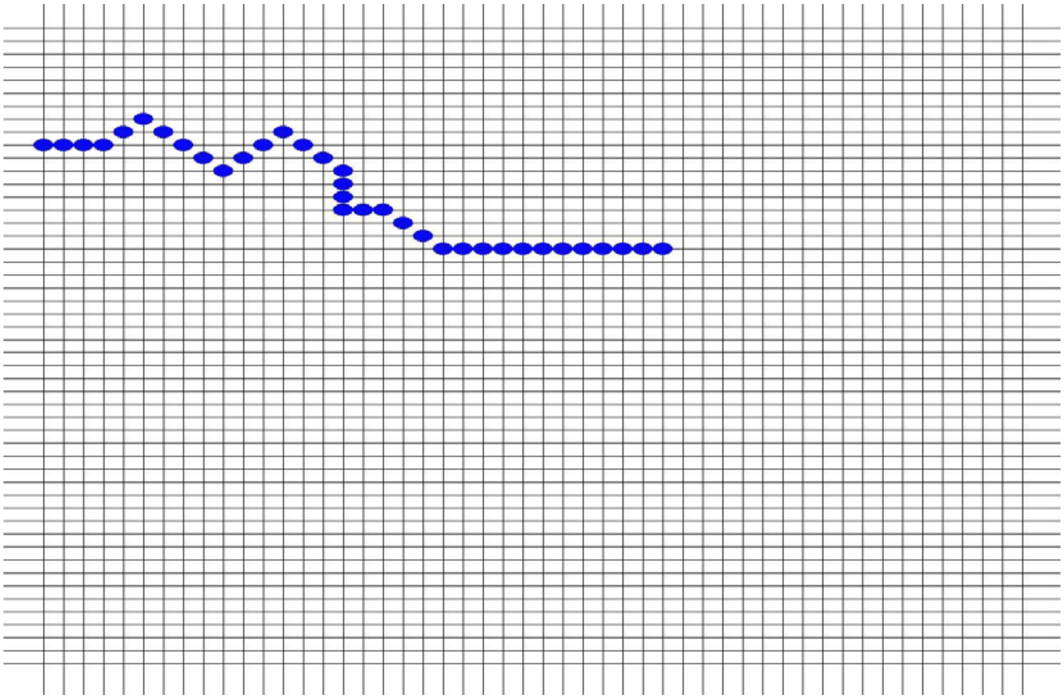

Figure 5.13 Location of nodes with the high flow connected path in the network

The common sense is that the flow of fluid should choose this high conductivity path in the network as the dominant flow. Since the rest of the bonds in the network have random conductivities, it is possible to have other invaded nodes in the network. There is a very low chance of having another dominant path but because we have a uniform random choice of throats radii, cluster of high flow paths should not happen. Viscous invasion simulation has been performed on this system. Two tests have been done, one with only the maximum flow rate to advance, and the second with top 30 percent of flow rates to advance for the invasion. These tests have been shown in Figures 5.14 and 5.15.

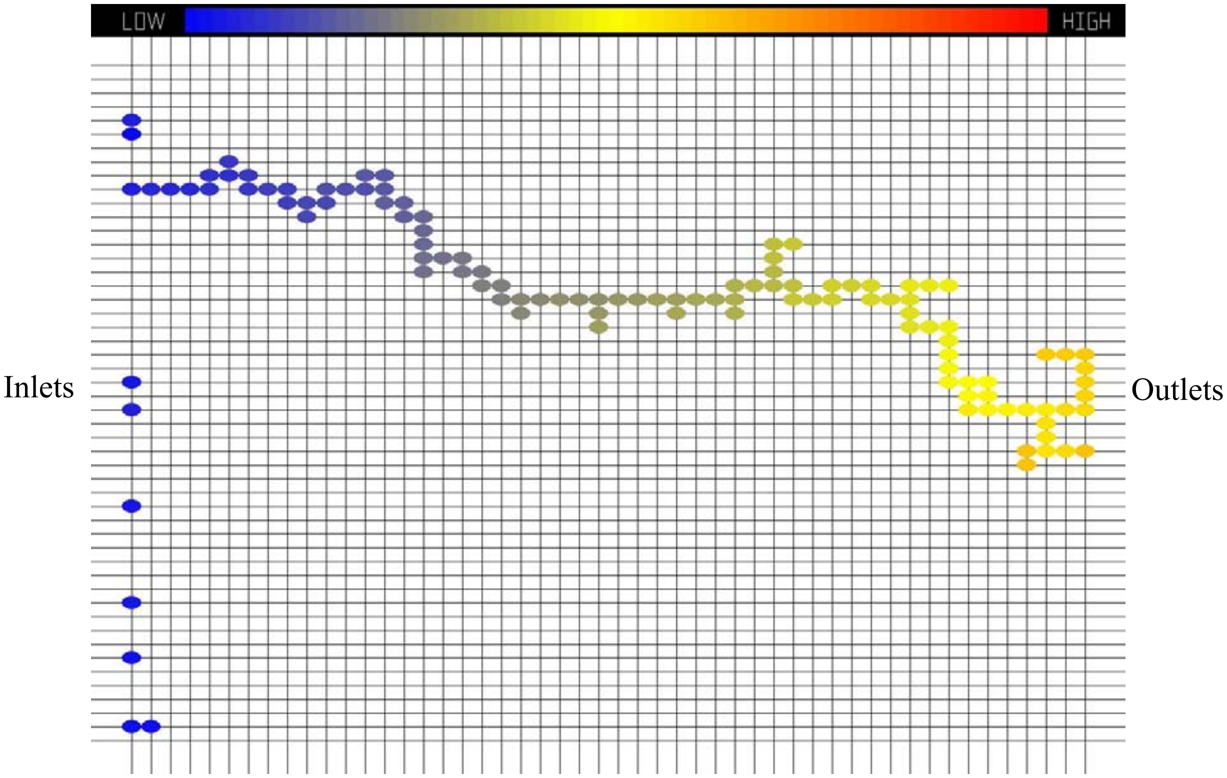

Figure 5.14 Viscous invasion for the case with dominant single channel, the maximum flow rate advancement

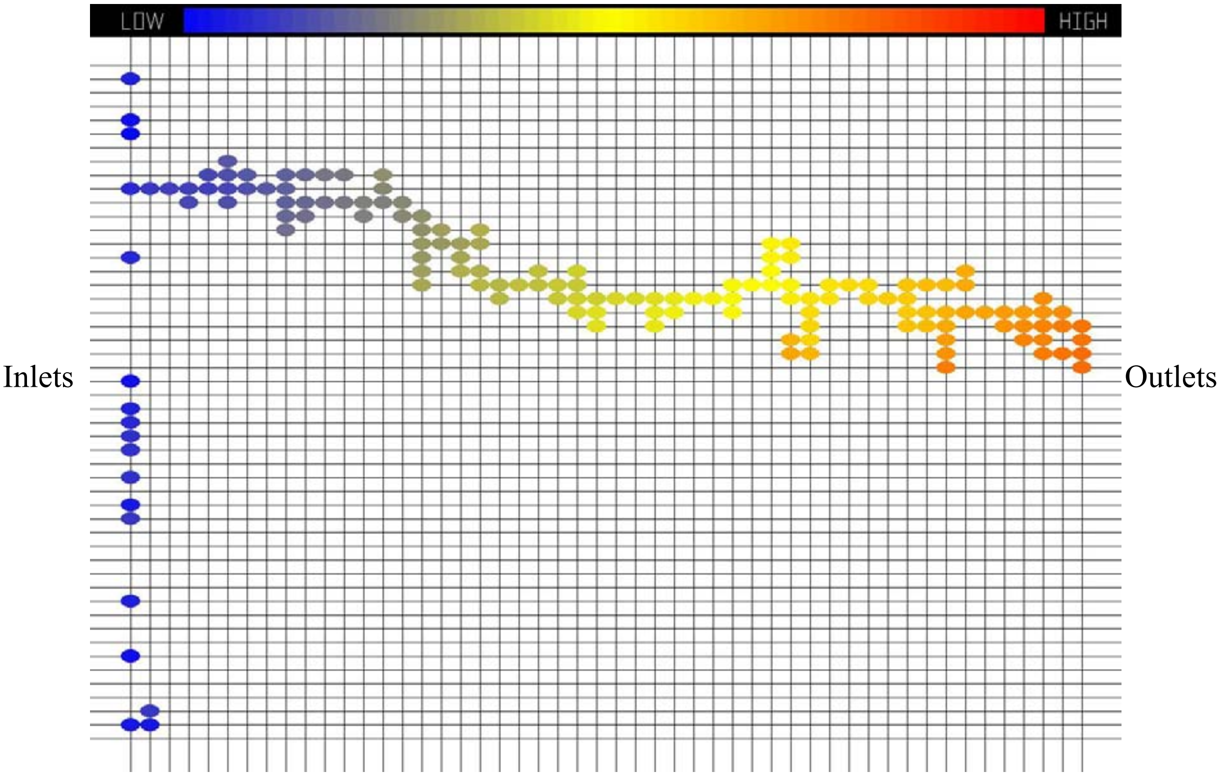

Figure 5.15 Viscous invasion for the case with dominant single channel, the top 30 percent of flow rate advancement

In Both cases, flow has passed through the dominant channel, even though there were some peripheral invasions. The general trend of invasion has been dictated by the dominant channel until the last node with high flow path. After the last node of dominant channel, the invasion got into the random distribution and finds the dominant flow afterward.

5.8.3. FRACTURE – 2D

Fractures are very important in study of fluids flow in porous media. They are high conductivity paths for the injected fluids. Fractures have very high hydraulic conductivities and their permeability is much higher than the surrounding matrix. Therefore, being able to accurately simulate the high velocity flow path of a fracture in this viscous displacement is important.

In this part we simulate the case of viscous invasion with a fracture inside the sample. The fracture is assumed to be connected to the inlet and extends into the network. The same 50 × 50, 2D square lattice has been used, inlet with 5 units of potential and outlets with 1 unit of potential are in the left and right side of the network. Top and bottom are no flow boundaries. The bond radii's are sampled from a uniform random distribution. For this invasion test we have chosen the top 30 percent of flow rates to advance in the network.

The fracture location and extents is in Table 5.2 and a visual of the fracture shape is shown in Figure 5.16.

Nodes ID	
1251	
1252	
1253	
1254	
1255	
1306	1206
1357	1157
1408	1108
1459	1059
1510	1010
1561	961
1612	912
1663	863
1714	814
1765	765

Table 5.2 Fracture IDs

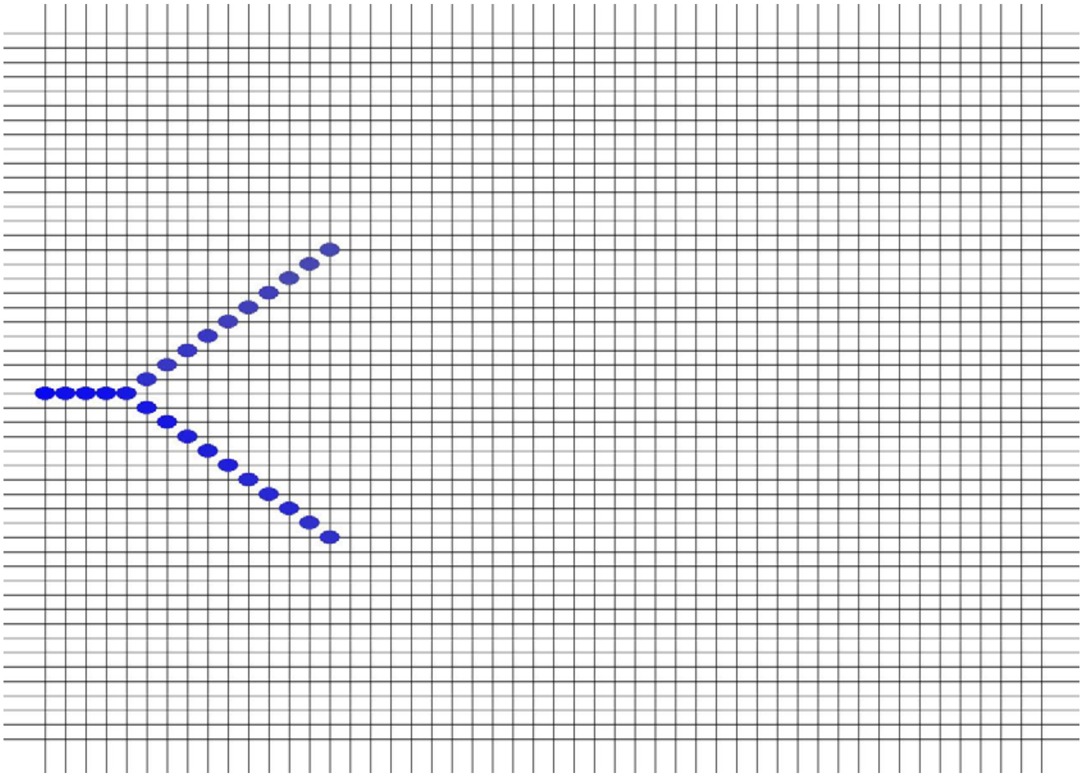

Figure 5.16 Fracture shape in the network

We expect that the fluid flows into the network and easily pass through the fracture inside the medium. After reaching the end of the fractures, flow expected to spread into the system and invasion continues until the breakthrough happens. Viscous invasion test results are shown in Figure 5.17.

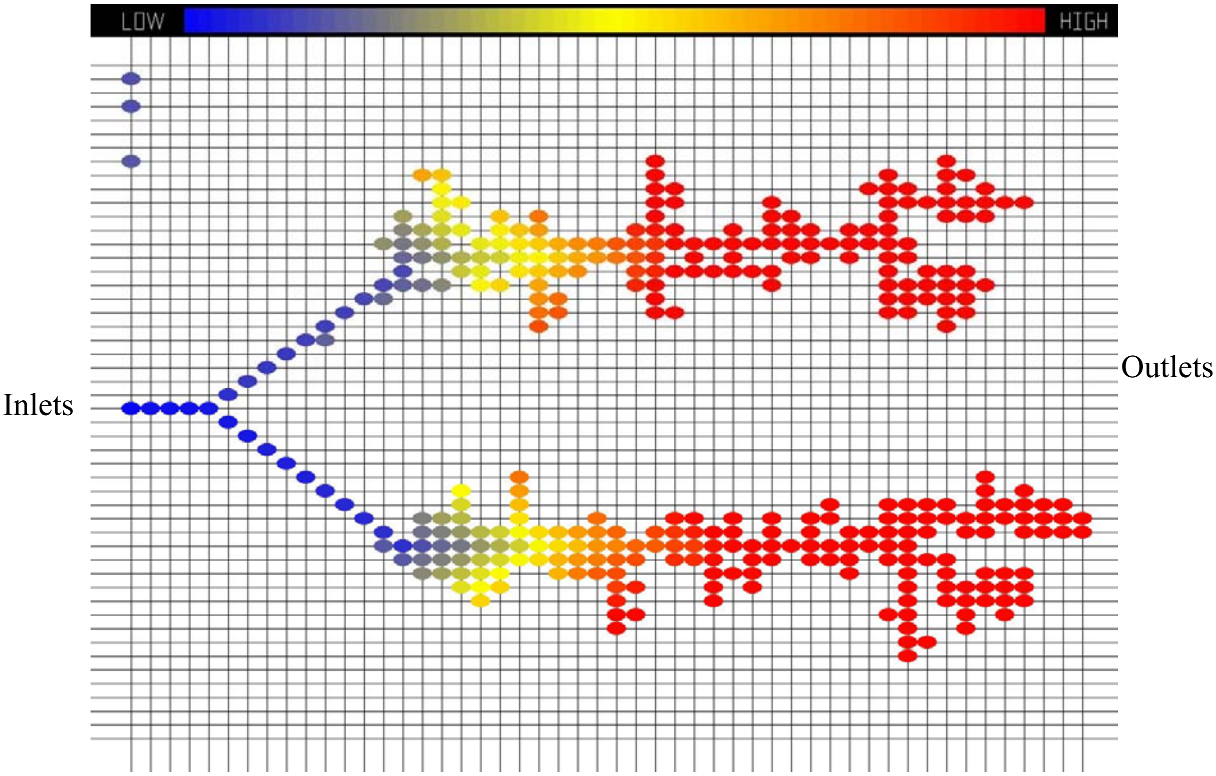

Figure 5.17 Viscous invasion in the case of fractures

As expected, flow quickly passes through the fractures and from the end of fractures spreads in the medium.

5.8.4. MIDDLE SPOT INJECTOR – 2D

This test is to verify the presence of injectors somewhere in the middle of the network. It is like having injector wells in a reservoir which is surrounded by no flow boundaries on all three sides. The outlet boundary is only one side of the network. The point here is to verify that the flow of injectors should be independent from each other. The only driving force that dictates the fluid flow should be the potential gradient and the hydraulic conductivity of the connecting bonds between injectors and outlet.

The system is a 50 × 50 2D square network lattice. Three sides are no flow boundaries, one side is outlet. Three injectors have been placed in the medium as indicated in Table 5.3 and shown in Figure 5.18. Injectors have 5 units of potential and outlets have 1 unit of potential. All the bonds radii have been uniformly sampled from a random generator.

Injectors ID
510
1260
2010

Table 5.3 Location of injectors

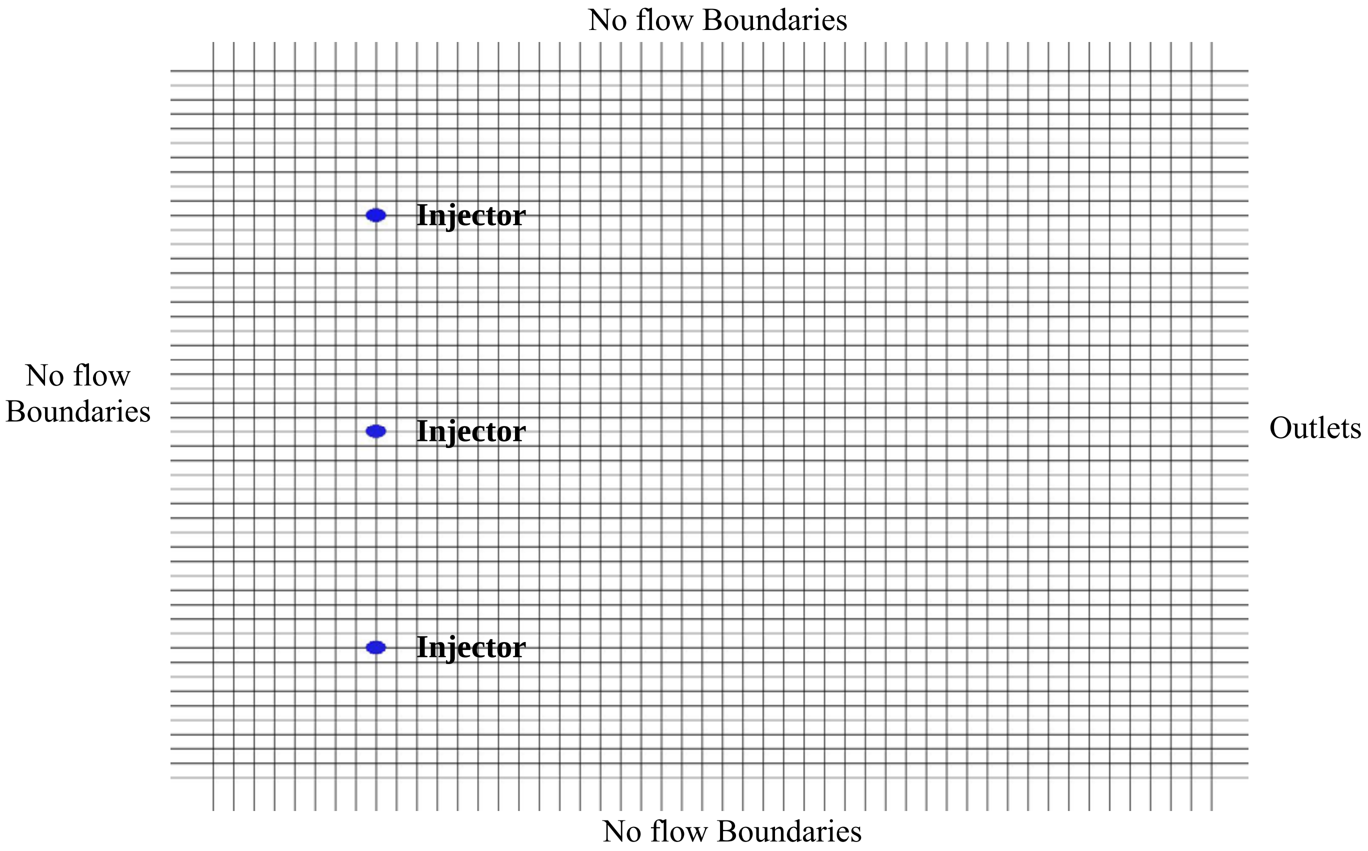

Figure 5.18 Location of the injectors in the medium

Result of fluid flow from injectors toward the outlets by executing the viscous invasion on this injection scheme is shown in Figure5.19. The three injectors are independent from each other.

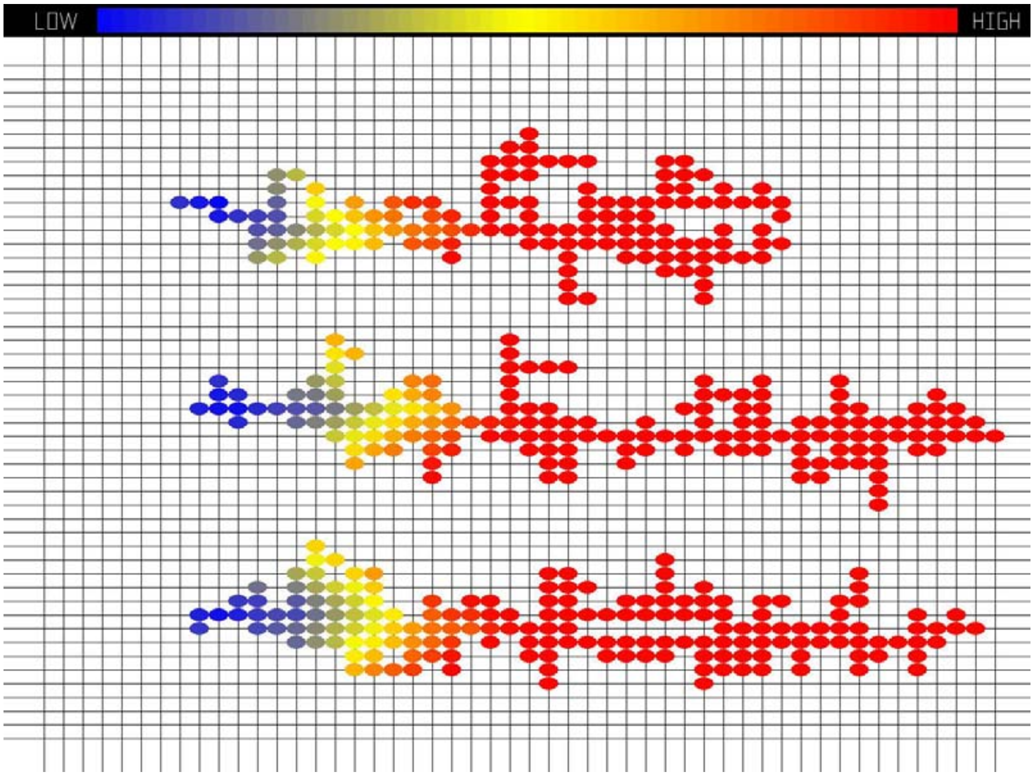

Figure 5.19 Three injectors in the medium

5.8.5. UNIT CONDUCTIVITY – 3D

This viscous invasion test is to check the validity of unit conductivity on a 3D network. The lattice is a 3D cubic lattice with connectivity of six. All bonds have equal throat radii, and the size of the network is 50 × 50 × 50, which is a total of 125,000 nodes. The inlet has 5 units of potential and the outlet has 1 unit. All four sides of the cube are no flow boundaries. Flow is from bottom to top of the cube. All the 2,500 nodes in the first level (bottom of the cube) are connected to the inlet and all the 2,500 nodes on top are connected to the outlet. We chose only the top 1 percent of flow rates in the bonds advance just to take care of the error tolerance. Otherwise, only one of the nodes in each step of invasion will be invaded.

We expect the results to be the invasion of all the nodes, layer by layer, perpendicular to the flow direction, similar to the case of unit hydraulic conductivity for the 2D case (Section 5.8.1.). Figure 5.20 illustrates the invaded network system in 3D.

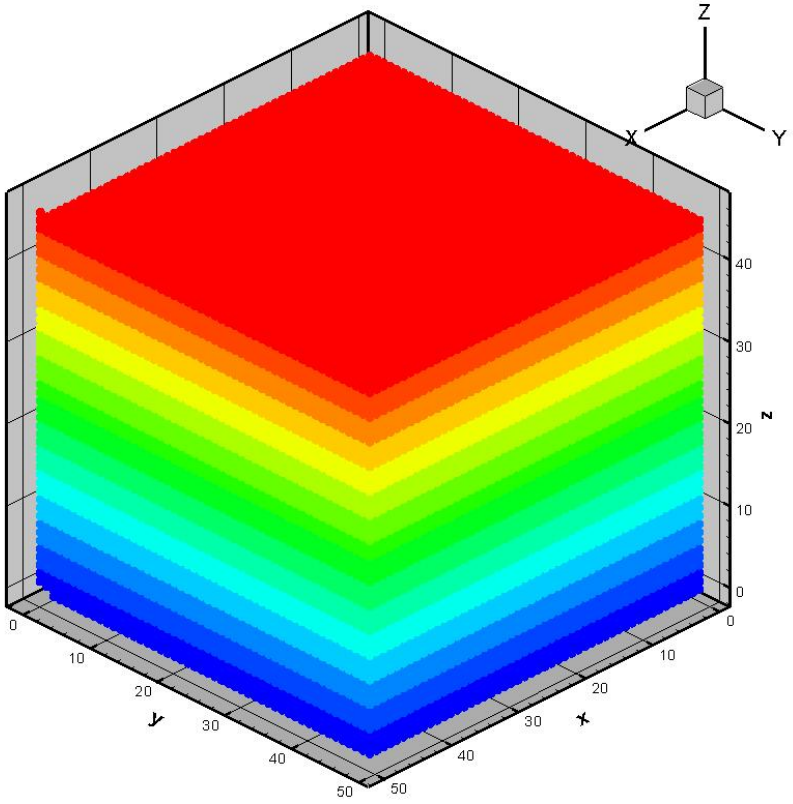

Figure 5.20 Viscous invasion, 3D cubic lattice with unit bond throat sizes

On the Figure 5.20, all the nodes that have been invaded at a same time step have same colors. Each layer perpendicular to the fluid flow direction is a distinct layer as we expected, since all the nodes in that layer have been invaded at the same time.

5.8.6. DOMINANT SINGLE CHANNEL – 3D

This is a test when one single channel has more hydraulic conductivity (higher throat radius) than other possible paths in the network. We have set the throats radii in one path to be significantly higher than the other throats radii, so this path becomes a dominant channel in the network.

Network is a 50 × 50 × 50 cubic lattice. All the throats radii have been uniformly sampled from a random generator. The sides are no flow boundaries and 2500 nodes at the bottom are connected to the inlets and 2500 nodes at the top are connected to the outlets. The nodes ID's for the dominant channel are shown in Table 5.4 and Figure 5.21 shows the 3D view of this dominant channel.

Nodes ID			
1275	18775	36275	53775
3775	21275	38775	56275
6275	23775	41275	58775
8775	26275	43775	61275
11275	28775	46275	
13775	31275	48775	
16275	33775	51275	

Table 5.4 IDs of the single dominant channel in the 3D cubic lattice

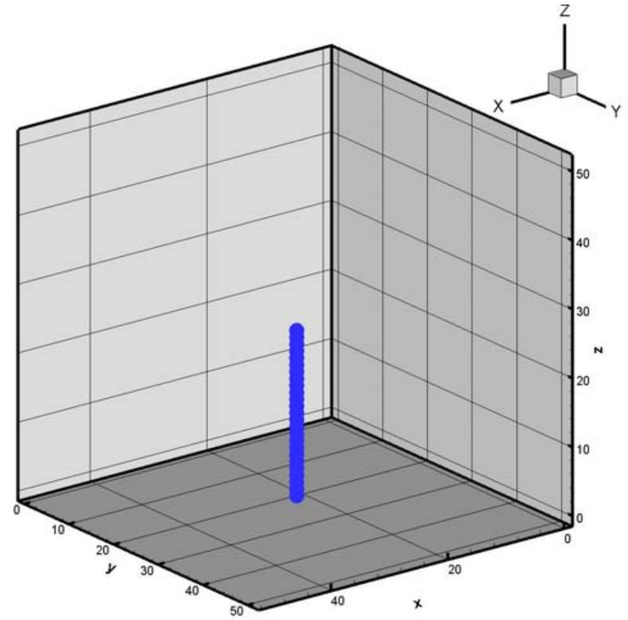

Figure 5.21 Dominant single channel 3D view

Figures 5.22 and 5.23 show the viscous invasion performed on this system with dominant single channel. The path with high throat radii is the lower part up to the z = 20 nodes. Although it was just one single path but some other surrounding nodes have also got invaded. All these surrounding nodes got invaded because of local effects of the high flow dominant channel which provided them with a high potential node just adjacent to them.

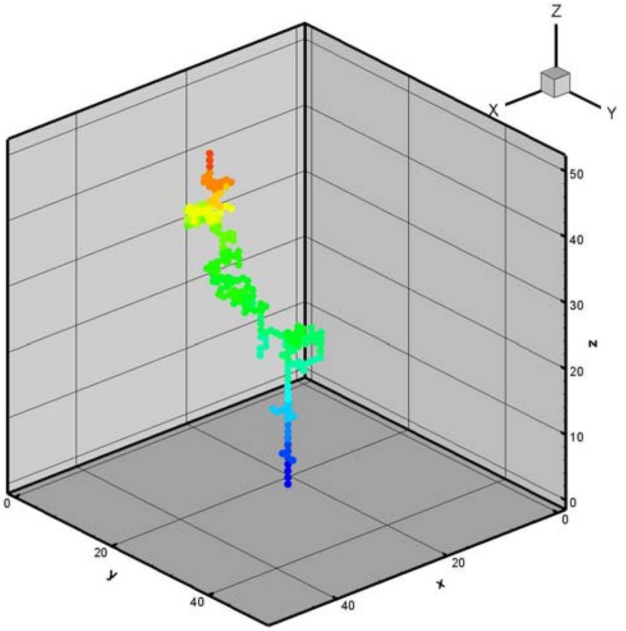

Figure 5.22 Invaded nodes in a network with one dominant channel, view 1

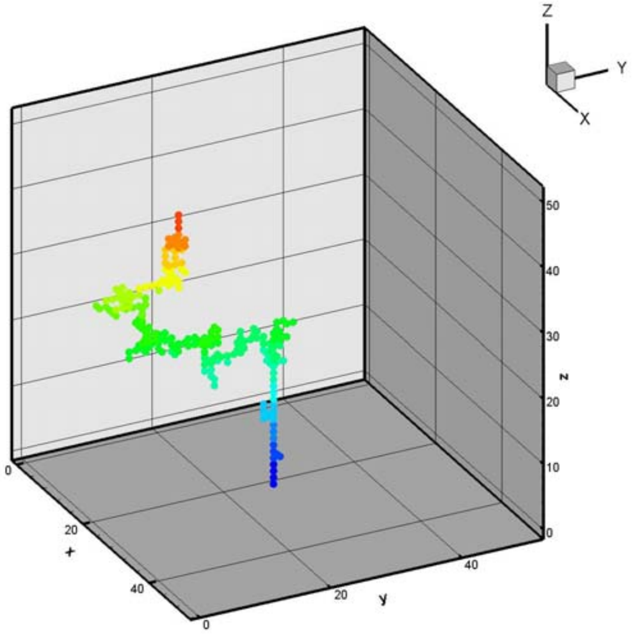

Figure 5.23 Invaded nodes in a network with one dominant channel, view 2

As expected the invasion followed the path of dominant channel until the last node in the high flow path and then followed the available high flow path in the network.

5.8.7. FRACTURE – 3D

This is a test with a 3D fracture in the network. A 45 degree plane with a high hydraulic conductivity has been defined in the 3D network. The same 50 × 50 × 50 cubic lattice network has been used. Same as previous tests, all for surrounding cube planes are no flow boundaries and the inlet and outlets are located at the bottom and top of the cube respectively. Inlets have 5 units of potential and outlets have 1 unit. Throats radii have been uniformly sampled from a random generator.

Fracture extends are shown in Table 5.5 and Figure 5.24 to 5.25 illustrate the shape of the fracture inside the three dimensional cubic network.

Node IDs for the fracture										
520	521	522	523	524	525	526	527	528	529	530
3070	3071	3072	3073	3074	3075	3076	3077	3078	3079	3080
5620	5621	5622	5623	5624	5625	5626	5627	5628	5629	5630
8170	8171	8172	8173	8174	8175	8176	8177	8178	8179	8180
10720	10721	10722	10723	10724	10725	10726	10727	10728	10729	10730
13270	13271	13272	13273	13274	13275	13276	13277	13278	13279	13280
15820	15821	15822	15823	15824	15825	15826	15827	15828	15829	15830
18370	18371	18372	18373	18374	18375	18376	18377	18378	18379	18380
20920	20921	20922	20923	20924	20925	20926	20927	20928	20929	20930
23470	23471	23472	23473	23474	23475	23476	23477	23478	23479	23480
26020	26021	26022	26023	26024	26025	26026	26027	26028	26029	26030
28570	28571	28572	28573	28574	28575	28576	28577	28578	28579	28580
31120	31121	31122	31123	31124	31125	31126	31127	31128	31129	31130
33670	33671	33672	33673	33674	33675	33676	33677	33678	33679	33680
36220	36221	36222	36223	36224	36225	36226	36227	36228	36229	36230
38770	38771	38772	38773	38774	38775	38776	38777	38778	38779	38780
41320	41321	41322	41323	41324	41325	41326	41327	41328	41329	41330
43870	43871	43872	43873	43874	43875	43876	43877	43878	43879	43880
46420	46421	46422	46423	46424	46425	46426	46427	46428	46429	46430
48970	48971	48972	48973	48974	48975	48976	48977	48978	48979	48980

Table 5.5 IDs of the nodes of a three dimensional fracture.

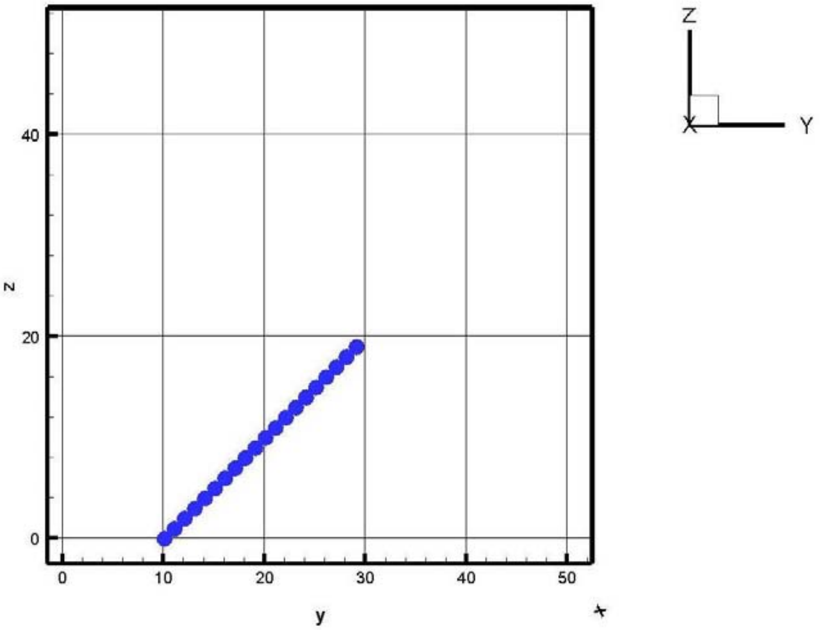

Figure 5.24 2D, YZ plane view of the 3D fracture in the cubic lattice

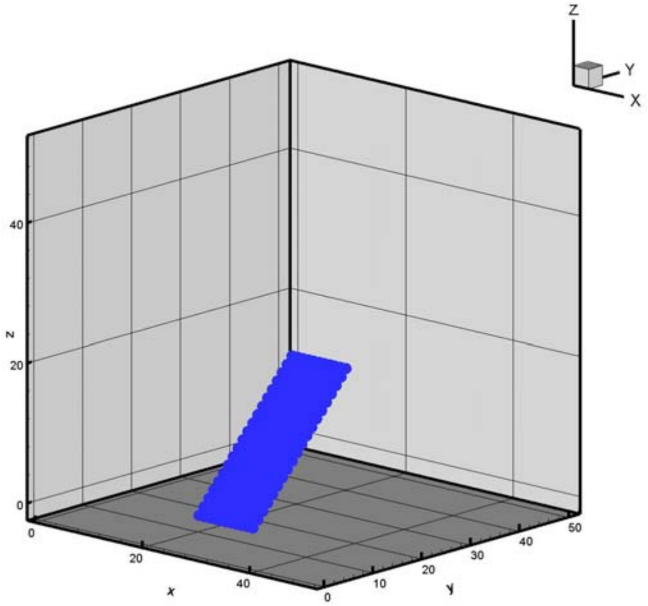

Figure 5.25 3D view of the fracture in the cubic lattice

The viscous invasion through such a fracture might be complicated, but the trend is expected to be through the fracture and then scatter into the network. Since the fracture is a wider object in the model in comparison to a dominant single channel, we should also see some spills of fluid into the network from the surface of fracture. Figures 5.26 and 5.27 illustrate two views of viscous invasion of fluid into the network with a fracture.

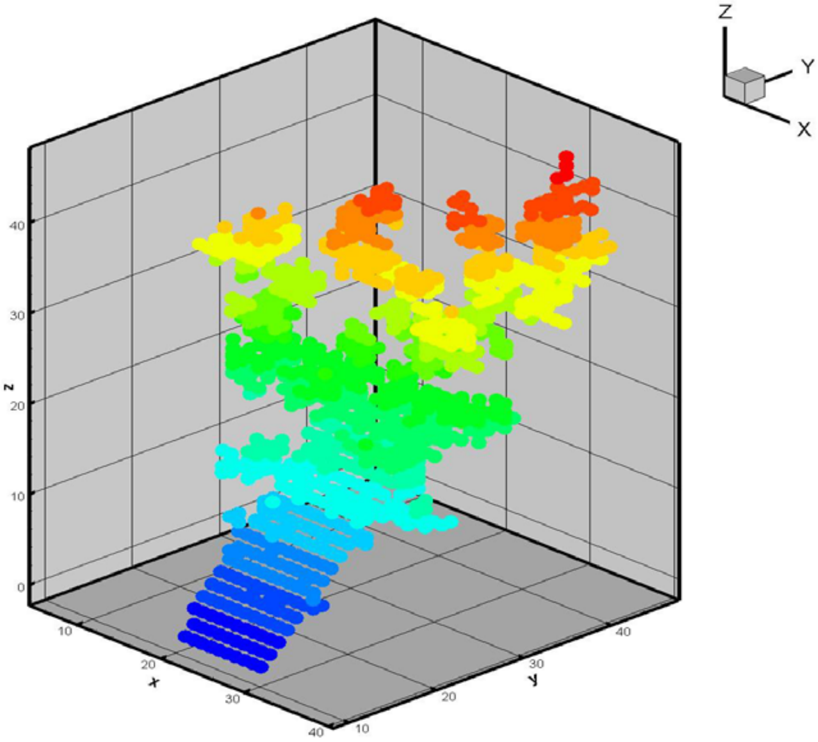

Figure 5.26 Viscous invasion in the case of fracture, view 1

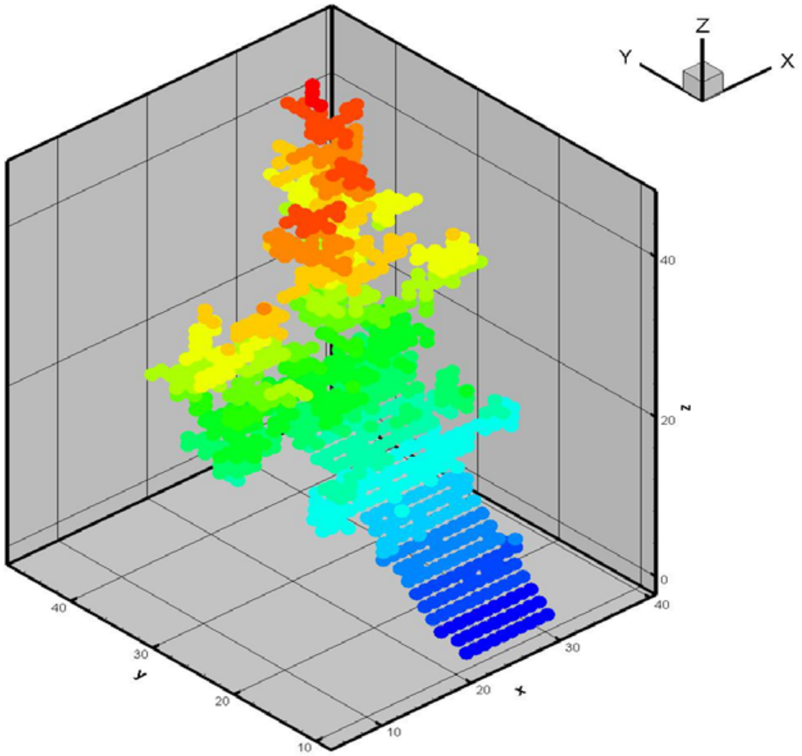

Figure 5.27 Viscous invasion in the case of fracture, view 2

As expected before, viscous invasion mainly passed through the fracture up to the end of fracture but there were some small channels coming out of the fracture too. From the end of the fracture the main streams of viscous flow starts spreading into the random space of throats radii.

5.8.8. FOUR SPOT INJECTOR – 3D

In this case we test and verify the 4 spot injector schemes. The same 50 × 50 × 50 cubic lattice have been set with the no flow boundaries of the four sides. General fluid flow gradient is from bottom to top. The top nodes are connected to outlets. Locations of the four injectors are shown in Table 5.6 and the three dimensional view to the location of the injectors in the network is shown in Figure 5.28. Throats radii are uniformly sampled from a random generator.

X	Y	Z
9	9	20
39	9	20
9	39	20
39	39	20

Table 5.6 XYZ location of the injectors

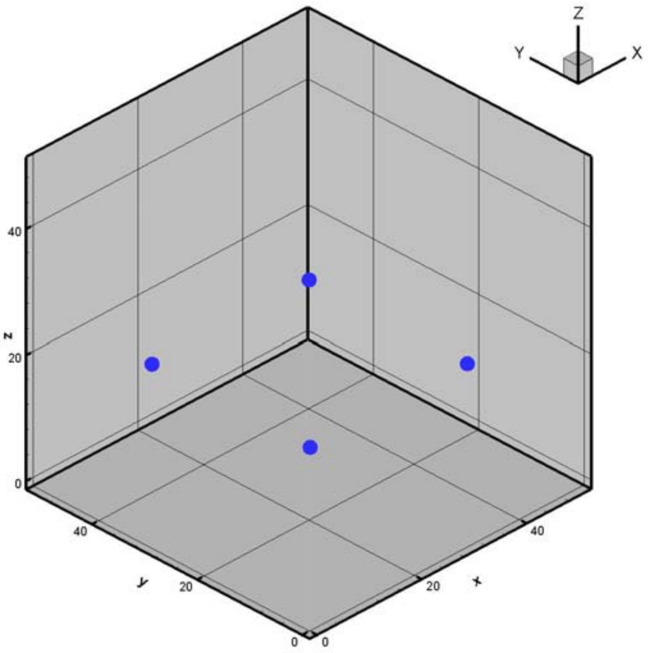

Figure 5.28 3D view of the 4 spot injectors

Performing the viscous invasion on this 4 spot injector scheme should probably show the same behavior as the two dimensional injectors result in Section 5.8.4. Figure 5.29 and 5.30 show two views of the viscous invasion of fluid inside the network

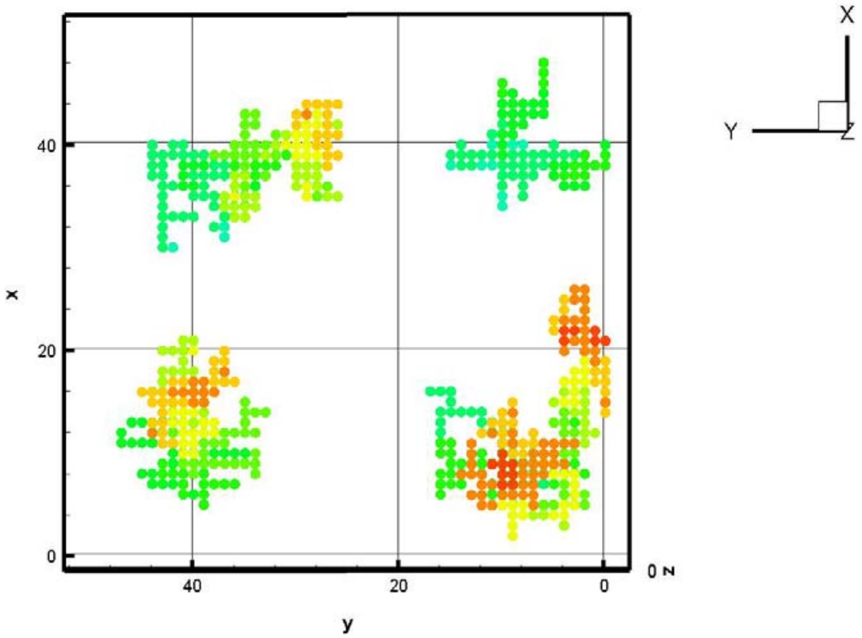

Figure 5.29 Top view to the viscous invasion, case of 4 spot injectors

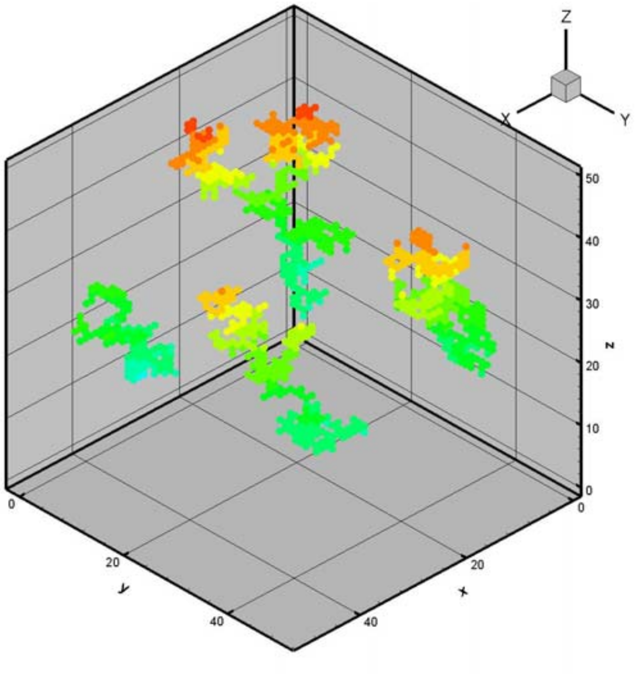

Figure 5.30 3D view of viscous invasion case of 4 spot injectors

5.9. FRONT PERPENDICULAR PLANE ADJUSTMENT

Figure 5.31 shows a bigger two-dimensional network on a regular square lattice of 20,000 nodes (200 × 100 node system) that has been invaded with the front plane adjustment.

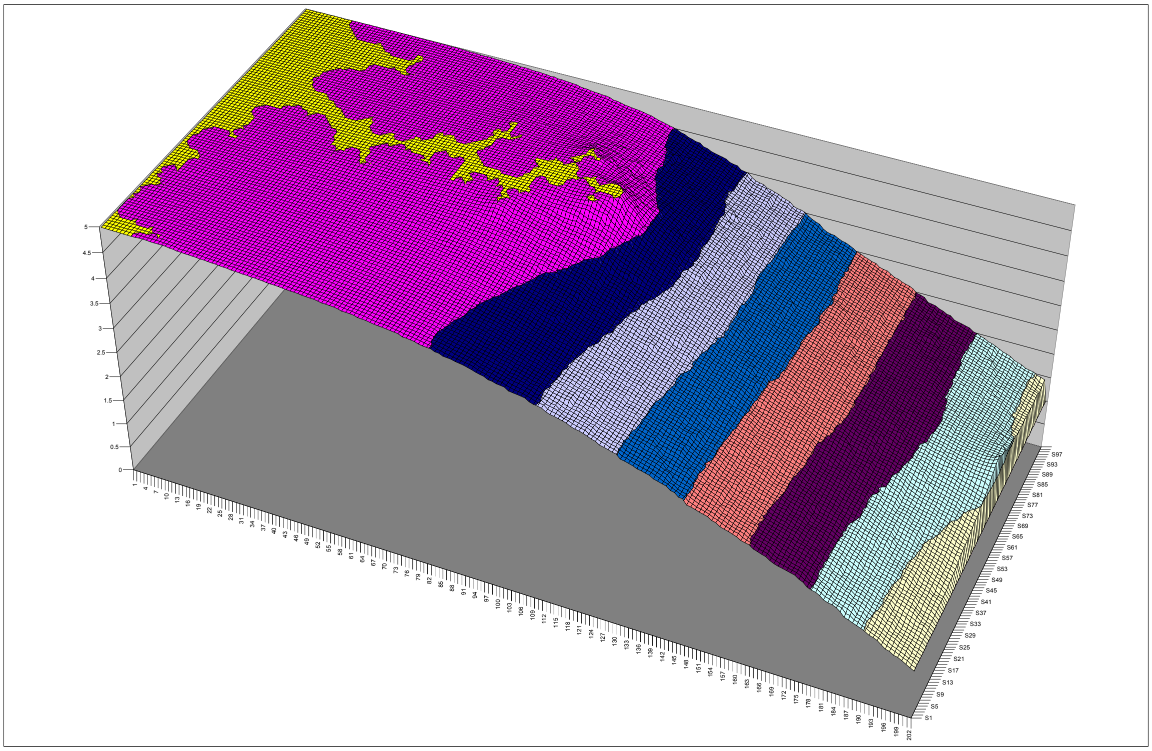

Figure 5.31 Potential distribution in the network at a middle invasion step

On this regular square lattice of 20,000 nodes, 100 nodes are connected to the inlet, with potential of 5 units, and 100 nodes are connected to the outlet, with 1 unit potential. Figure 5.32 shows the potentials at the front plane and the outlet if we take the potential at the front plane in the network and compare it to the adjusted potential at the outlet.

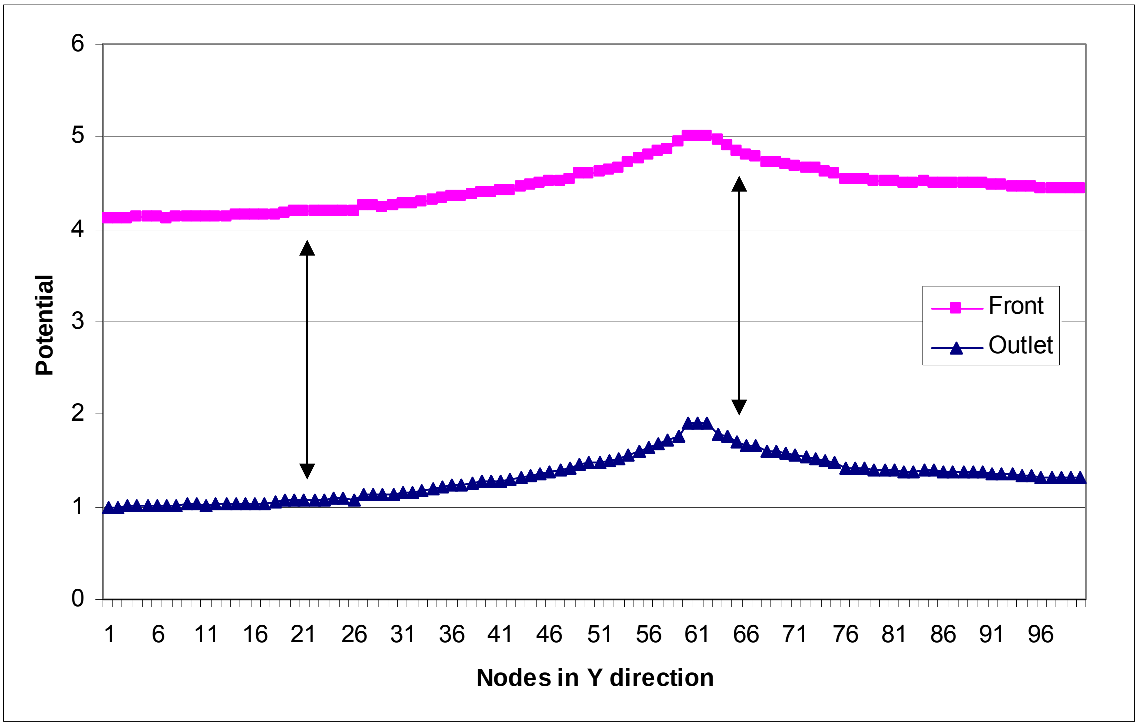

Figure 5.32 Comparison of the potentials at the front plane and the adjusted outlet

As shown on Figure 5.32, the potential gradient is equal for all the paths inside the network. This means there is an equal opportunity for all the nodes to be invaded.

At the breakthrough (end of the invasion), the potentials at the front, which is the last plane in x direction and the outlet potential, will be very similar. Therefore the potential gradient will be very small as shown in figure 5.33, it also shows the invaded nodes at the breakthrough. Figure 5.34 illustrates the corresponding adjusted potentials just at the breakthrough and the last plane in the x direction. Again the potential gradient for all the nodes is the same, meaning there is an equal opportunity for the fluids to invade all the nodes equally. Only the nodes with higher conductivity to the invading fluids will be invaded.

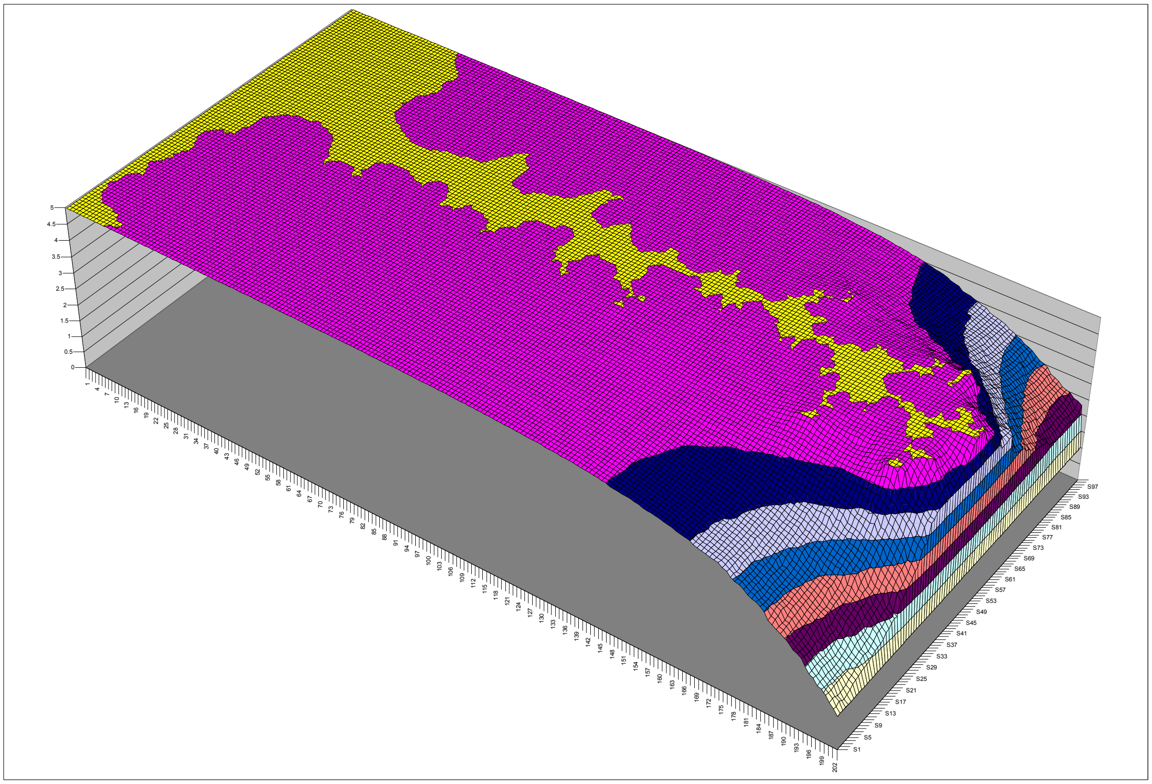

Figure 5.33 Potential distribution in the network at breakthrough time

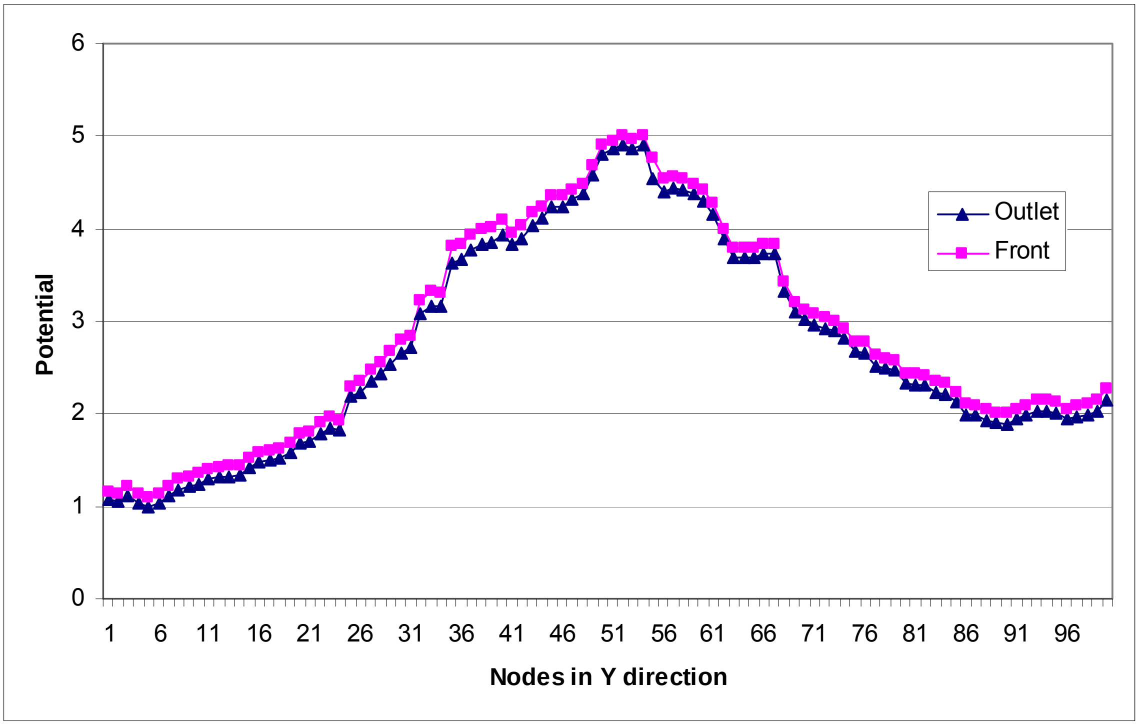

Figure 5.34 Potentials at the front plane and the outlets at the breakthrough time

Again, potential gradient has been kept equal for all the nodes at the front, even at the last step before the breakthrough.

Figure 5.35 shows a comparison of some middle steps of invasion potentials just to see how the front potentials are changing while the fluids invade the network of nodes. The corresponding adjusted potentials at the outlets are also shown in Figure 5.36.

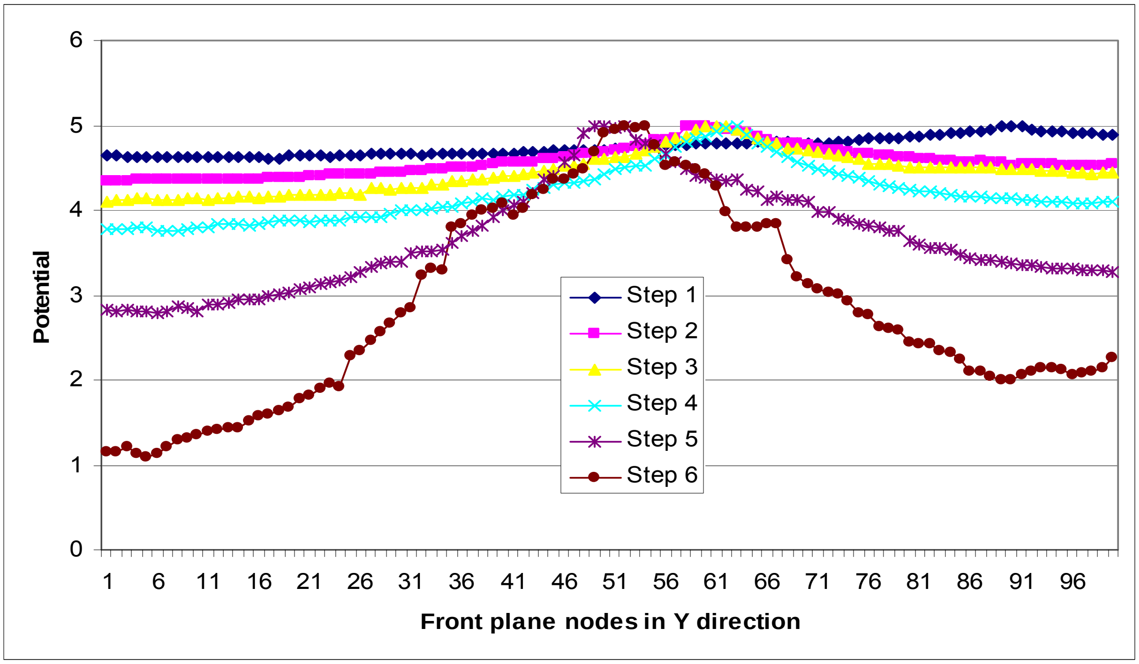

Figure 5.35 Potentials at the front during the invasion

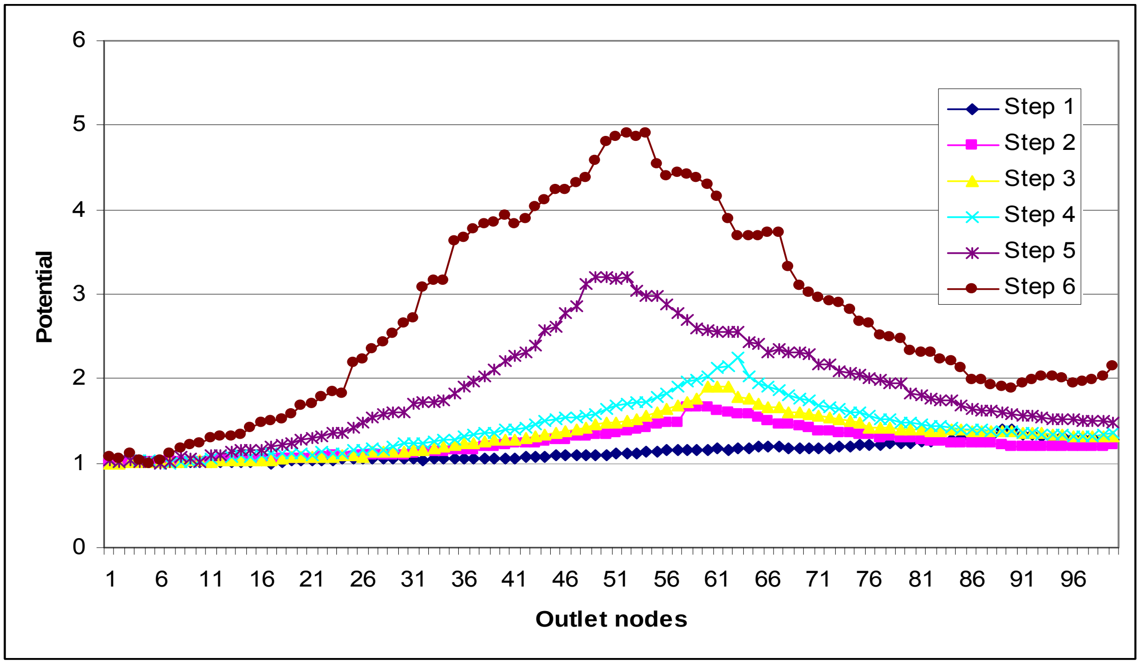

Figure 5.36 Adjusted potentials at the outlets

If you pick any pair, the potential gradients at all the invasion paths throughout the network, for every invasion step, are equal. A one to one match exists, between the potentials at the invasion front and the adjusted outlets according to the front. This shows the correct application of the invasion model adjusted boundary section, throughout the invasion modeling.

Figures 5.37 to 5.42 show the invasions as they happened for each of the steps mentioned in the Figures 5.35 and 5.36.

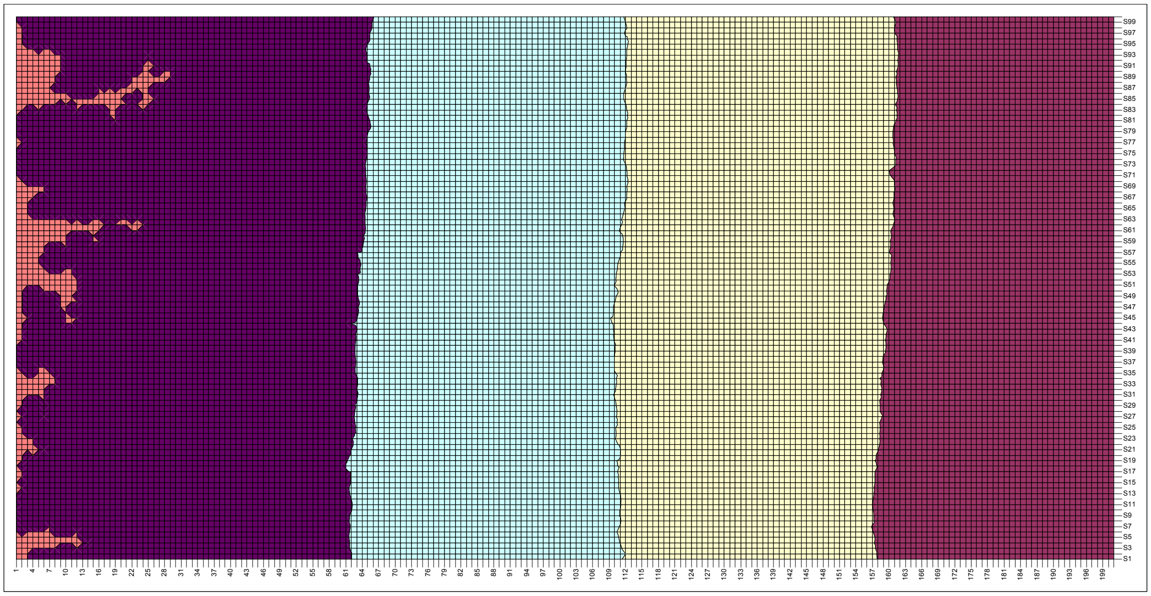

Figure 5.37 Step 1 of invasion, using Front Perpendicular Plane Adjustment

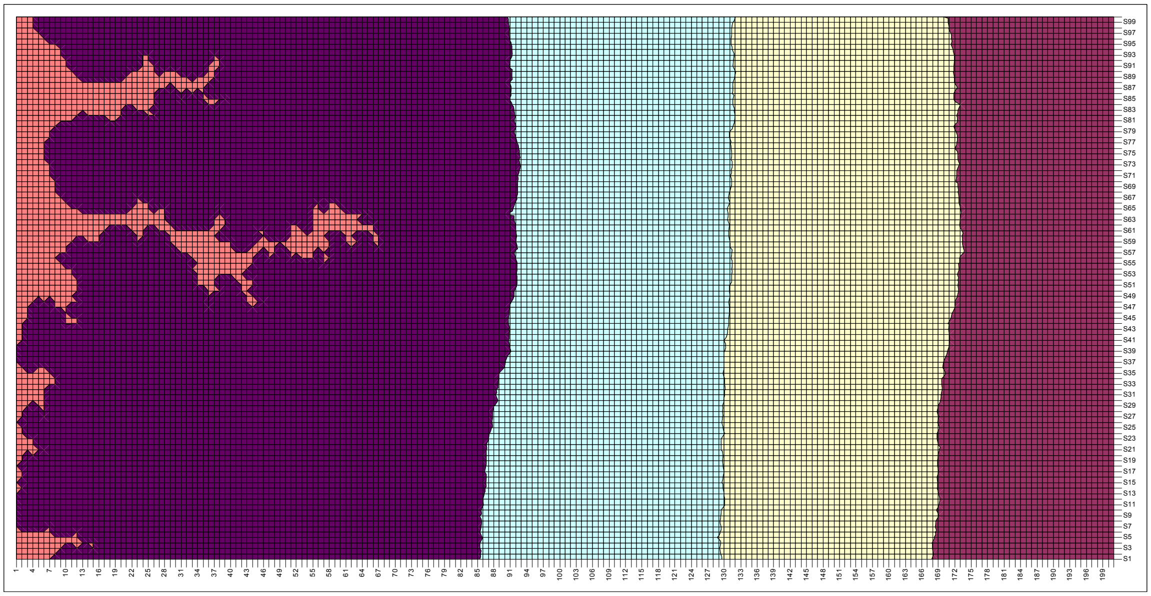

Figure 5.38 Step 2 of invasion, using Front Perpendicular Plane Adjustment

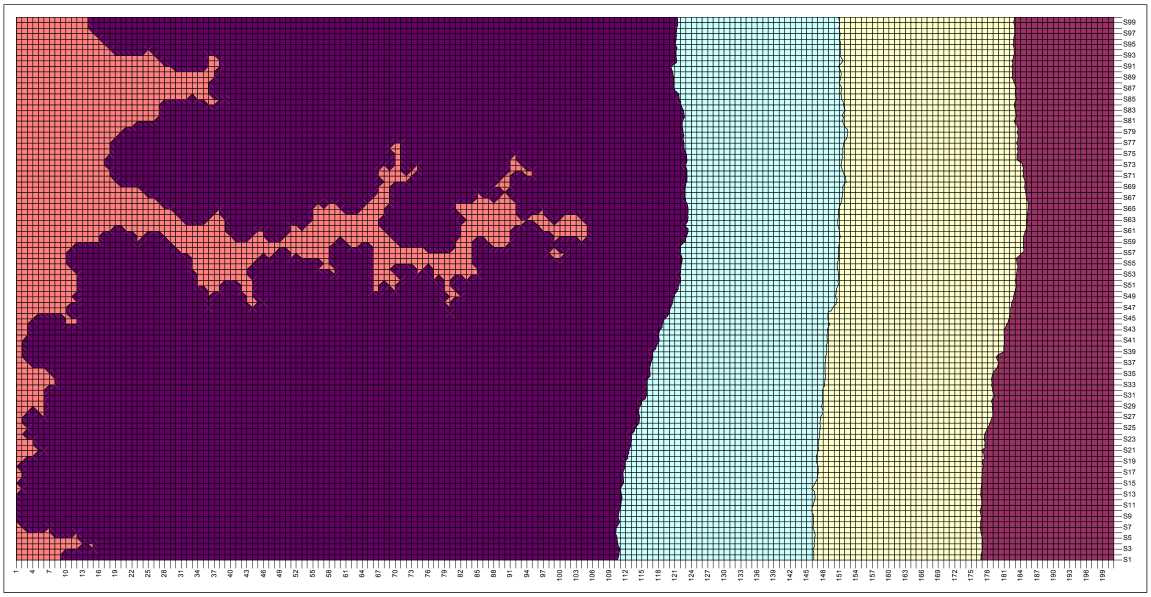

Figure 5.39 Step 3 of invasion, using Front Perpendicular Plane Adjustment

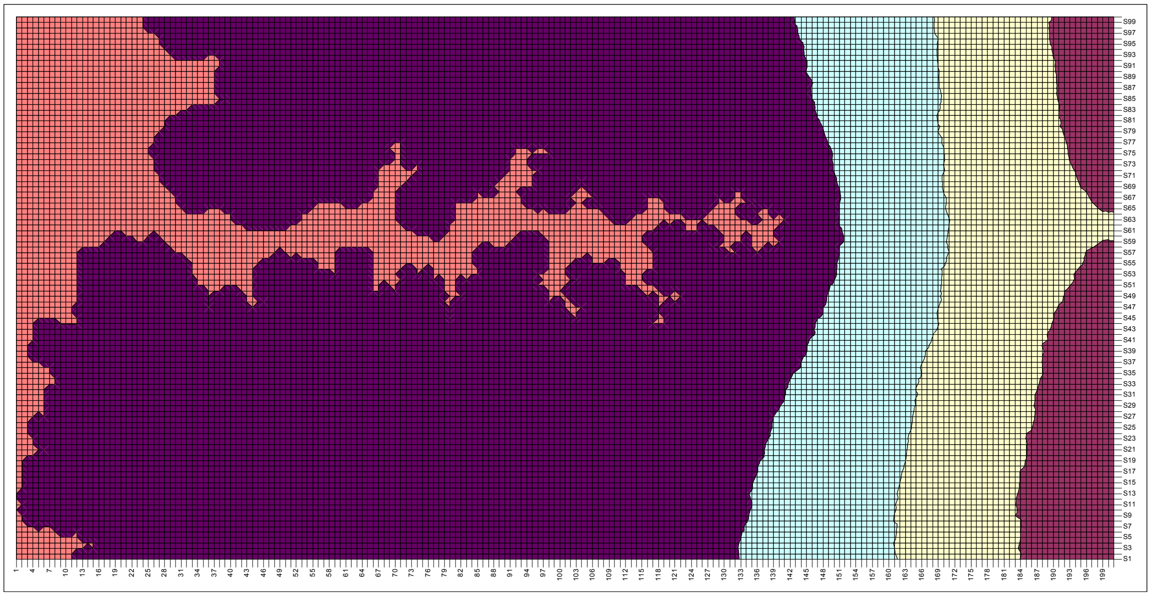

Figure 5.40   Step 4 of invasion, using Front Perpendicular Plane Adjustment

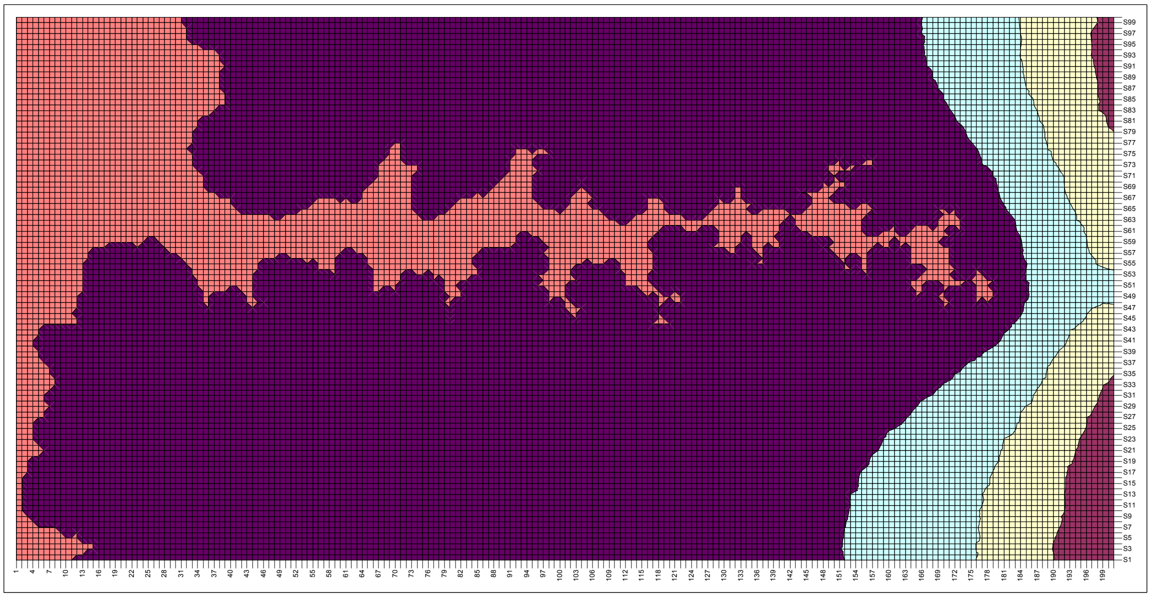

Figure 5.41   Step 5 of invasion, using Front Perpendicular Plane Adjustment

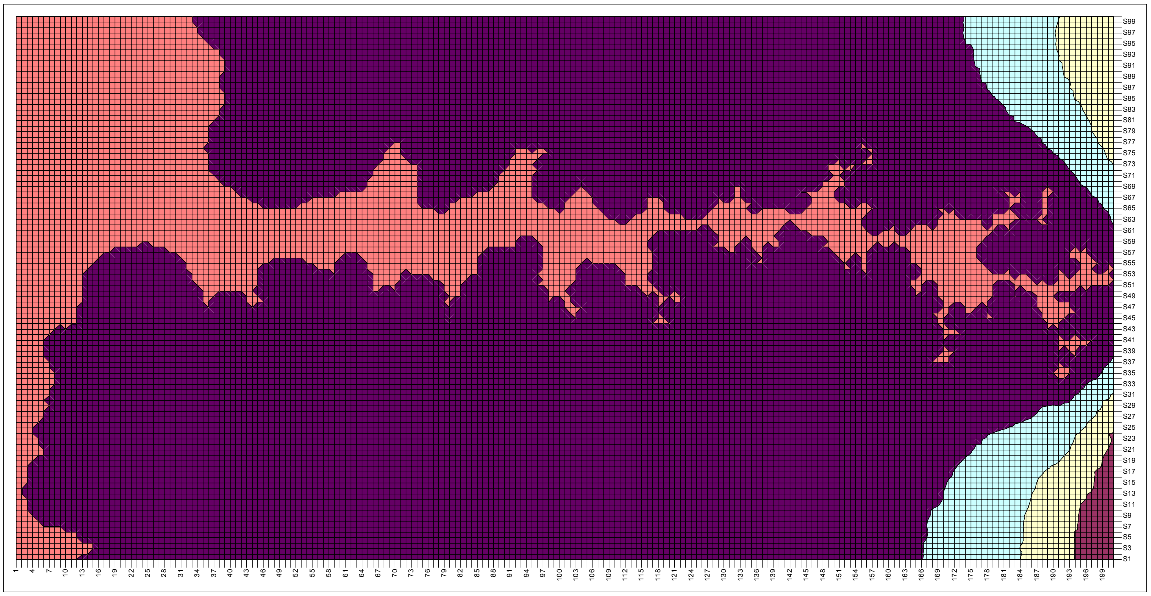

Figure 5.42 Step 6 of invasion, using Front Perpendicular Plane Adjustment

5.10. FRONT SURFACE ADJUSTMENT

The test network is same as the last test, a 2D model, and 200 nodes in X direction and 100 nodes in Y direction. The flow is in the X direction. All the nodes with x = 1 are connected to the inlet and all the nodes with x = 200 are connected to the outlet. Both inlet and outlet have a constant potential. All the nodes along the y = 1 and y = 100 are assumed to be connected to a no flow boundary. Imposing the potential of 5 units at the inlet and 1 unit on the outlet, makes a 4 unit potential gradient on a distance of 200 nodes. Running the invasion percolation test shows some differences between these two types of boundary adjustment schemes. First let us take a look at the invasion and the adjusted boundaries according to the front surface potentials. Figure 5.43 shows a slide of a middle of the network invasion simulation using Front surface adjustment.

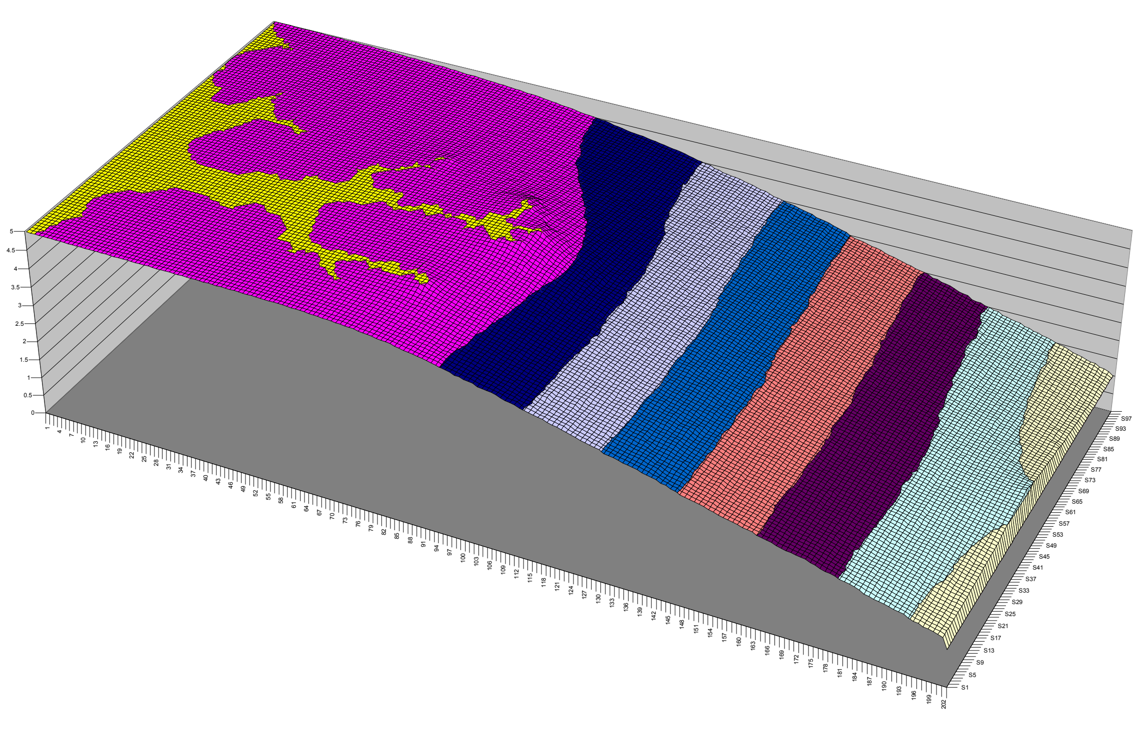

Figure 5.43 Potential distribution in the network at a middle invasion step

The potentials at this front are shown in Figure 5.44. The adjusted potentials at the outlet for this step of invasion are also shown in that figure. By comparing these two graphs we can see that the potential gradient has been kept equal for all the flow paths towards the outlet, meaning there is an equal chance for flow to invade all the nodes if their bonds conductivity allows.

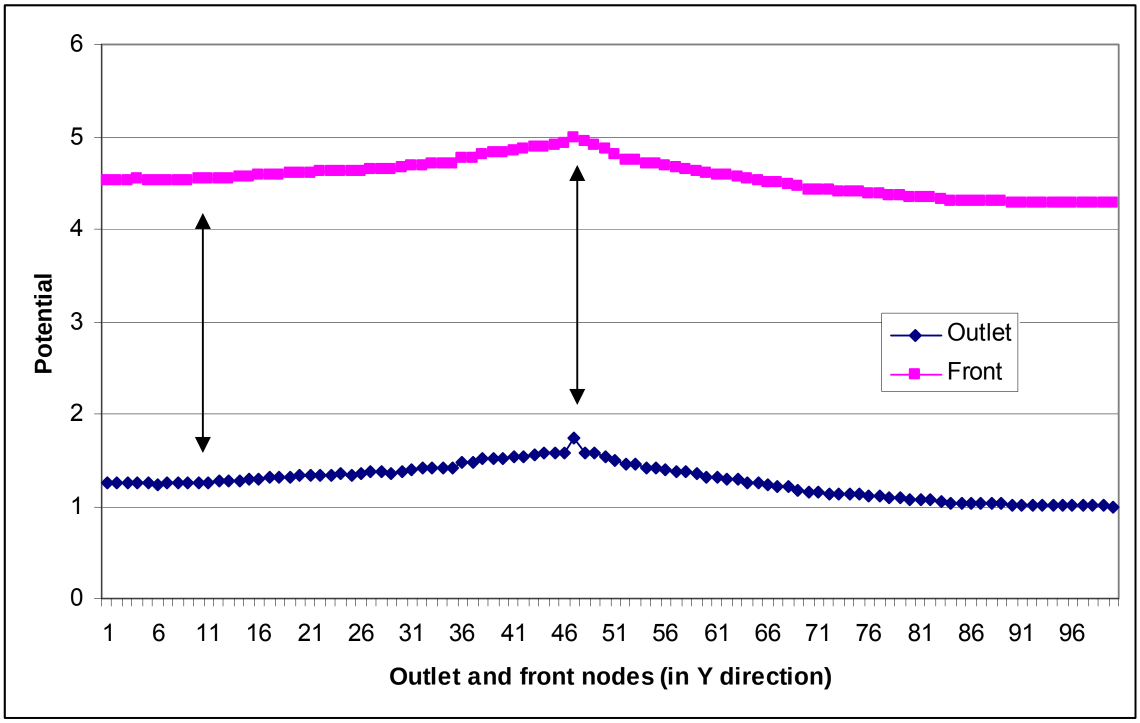

Figure 5.44 Front and outlet potentials for the invasion in Figure 5.43 using front surface adjustment

Figures 5.45 and 5.46 demonstrate the same network invasion at the breakthrough and the adjusted outlet potentials according to the front surface. Figure 5.47 illustrate the change in the front potentials in some middle steps of the invasion and Figure 5.48 shows the adjusted potentials at the outlet for the same steps of invasion. These two latter graphs give a brief view of the potential changes inside the network at the front and outlet nodes.

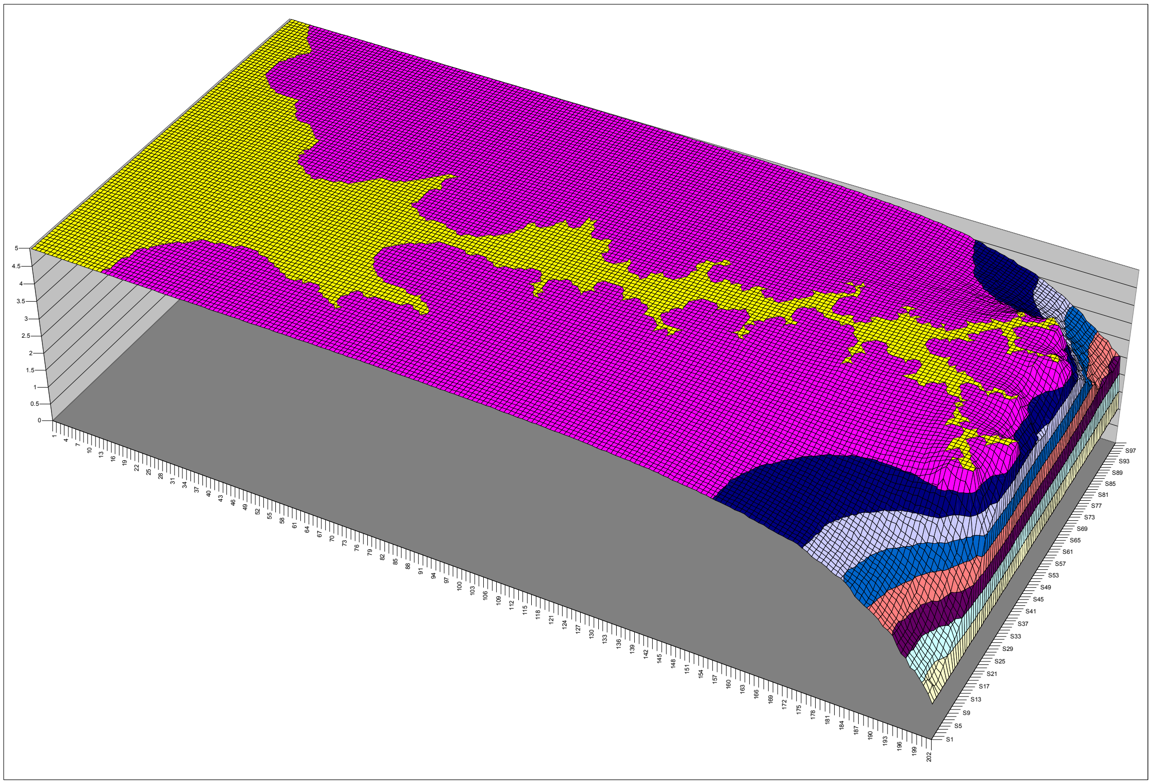

Figure 5.45 Potential distribution in the network at breakthrough using front surface adjustment

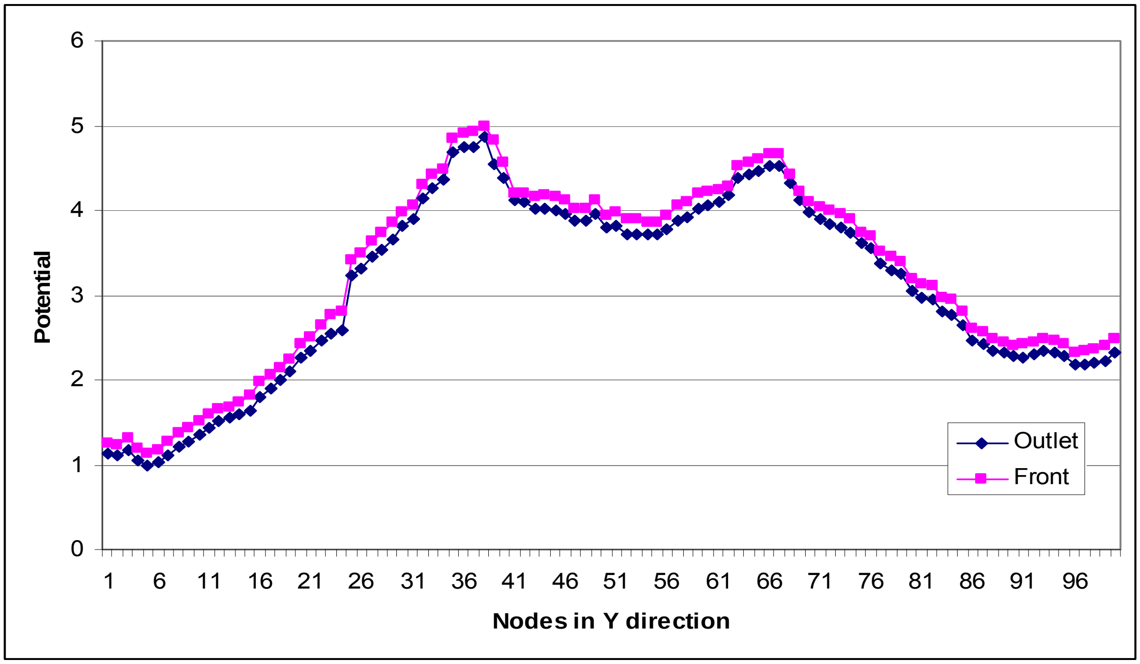

Figure 5.46 Adjusted outlet and the last invasion front surface potentials

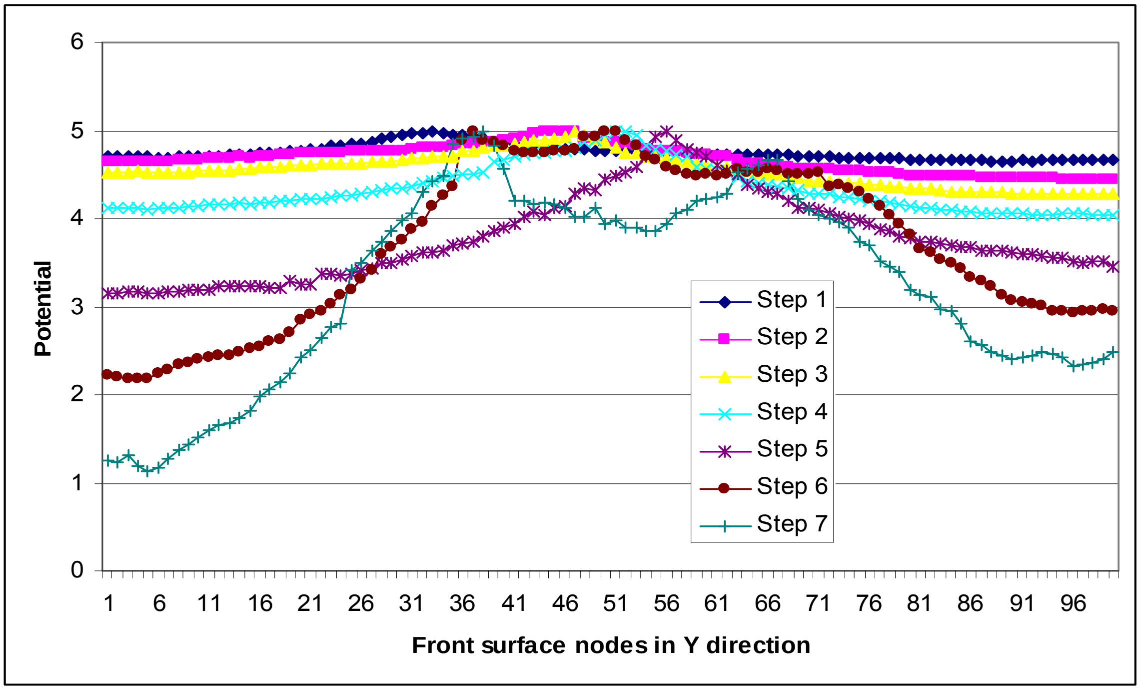

Figure 5.47 Front surface potentials at some middle steps of invasion, using front surface adjustment method

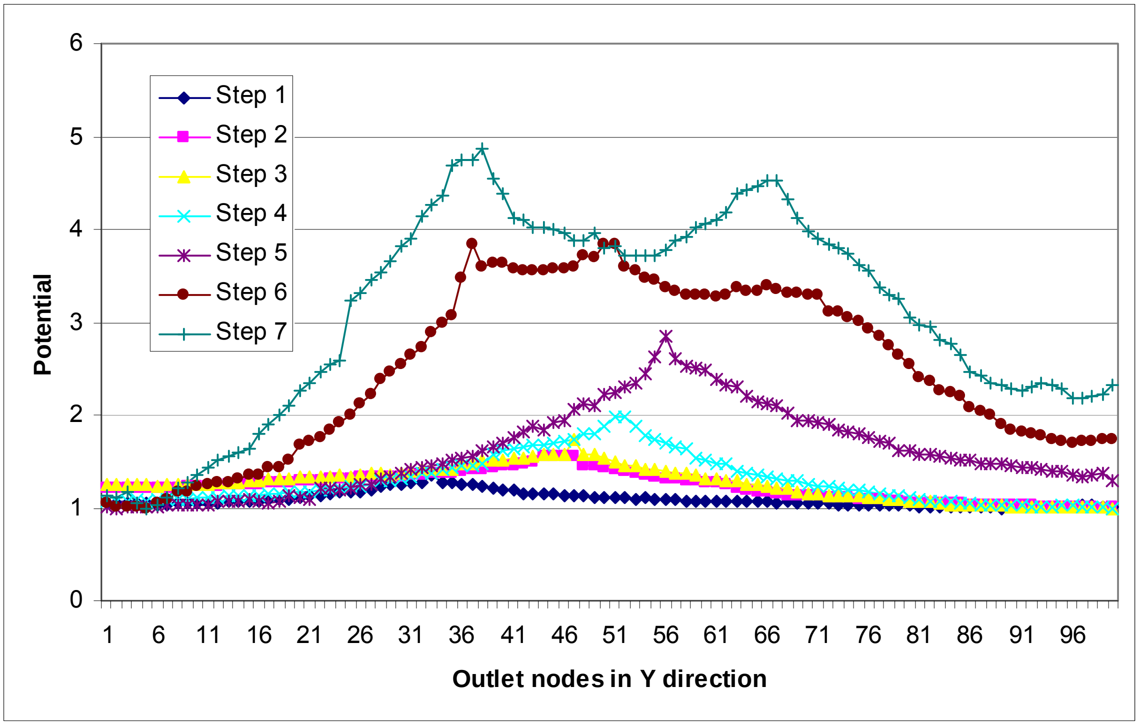

Figure 5.48 Outlet adjusted potentials for the middle steps of invasion, using front surface adjustment method

Figures 5.49 to 5.55 illustrate the invasions as it happened at each of the steps mentioned in the Figures 5.47 and 5.48. All the nodes on the left (x = 1) of the slide from y = 1 to y = 100 are connected to the inlet with the potential of 5 units and the ones on the right (x = 200) are connected to the outlet with the potential of 1 unit. The invasion in the network model flows from left to right, where we have a positive potential gradient of 4 units.

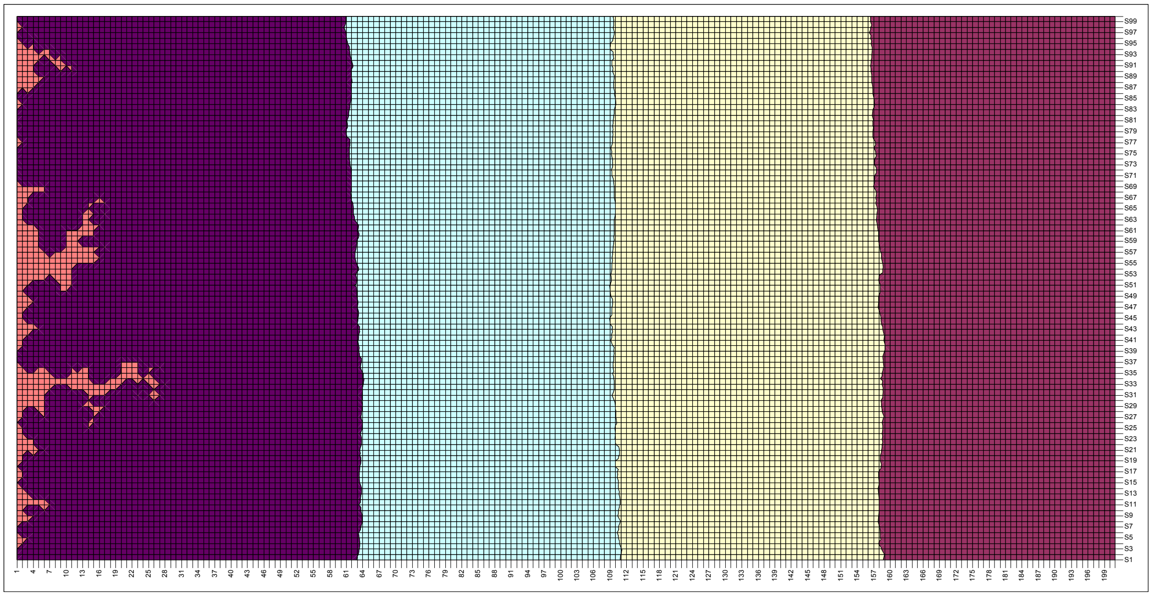

Figure 5.49 Step 1 of invasion, using Front surface Adjustment method

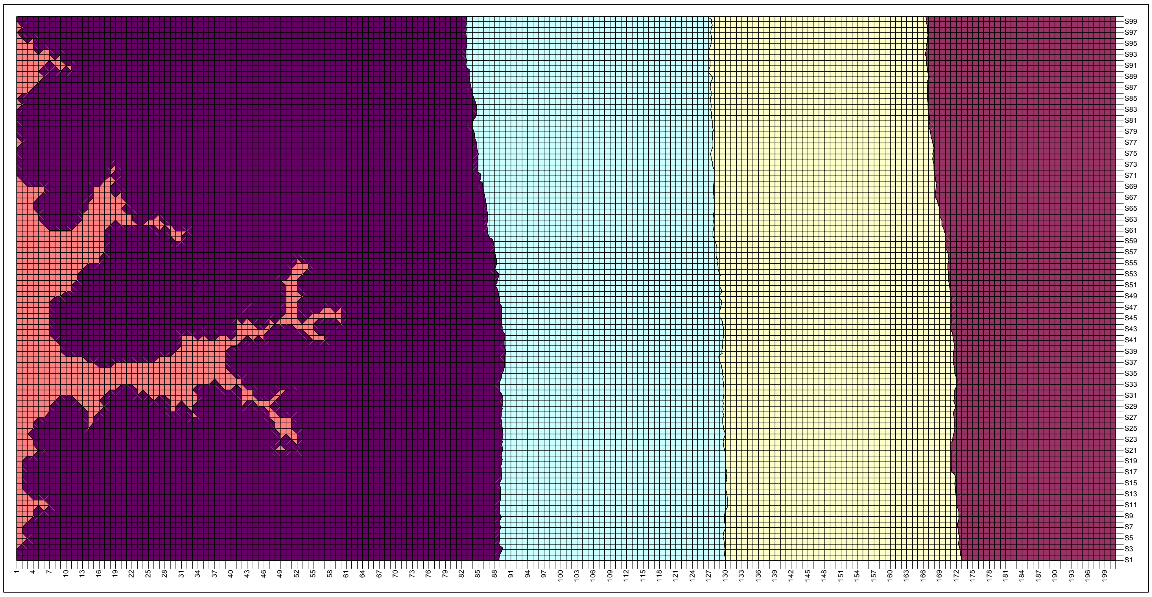

Figure 5.50 Step 2 of invasion, using Front surface Adjustment method

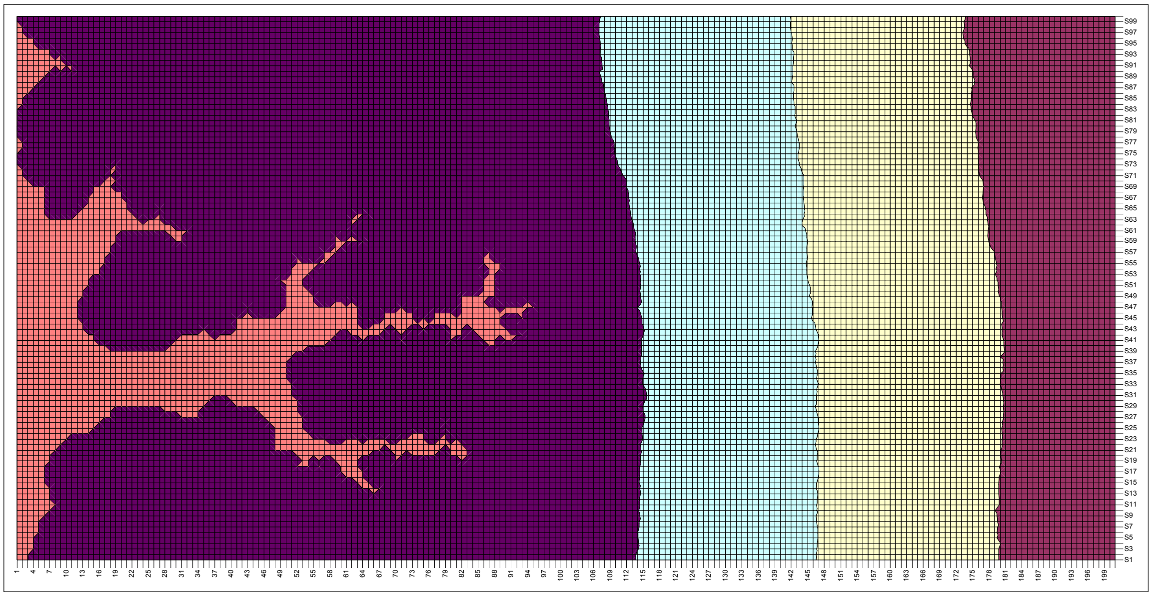

Figure 5.51 Step 3 of invasion, using Front surface Adjustment method

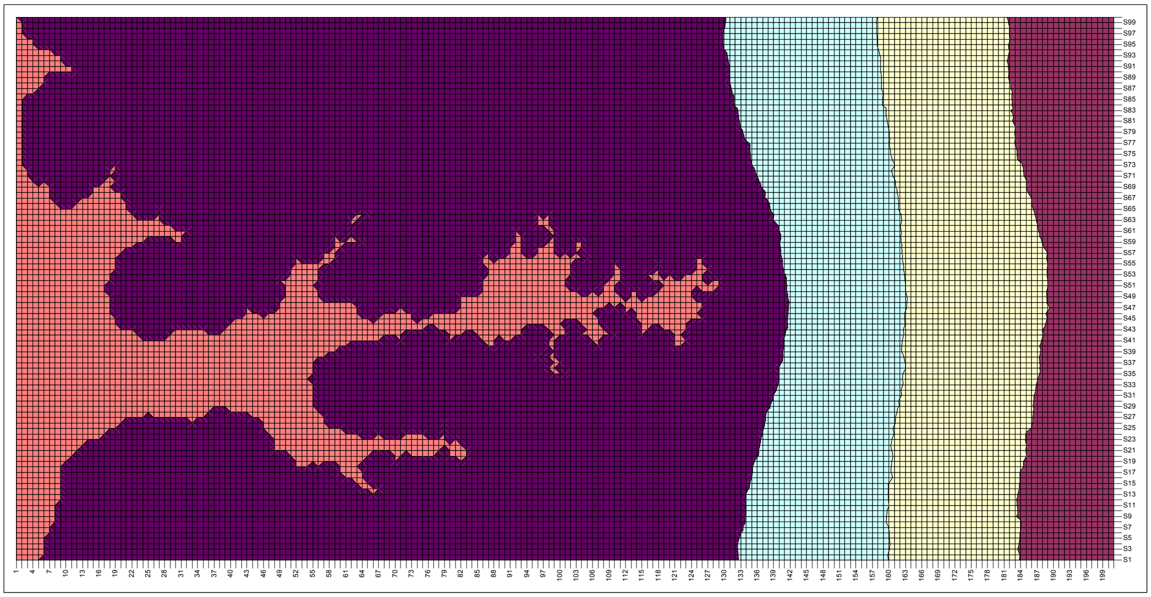

Figure 5.52 Step 4 of invasion, using Front surface Adjustment method

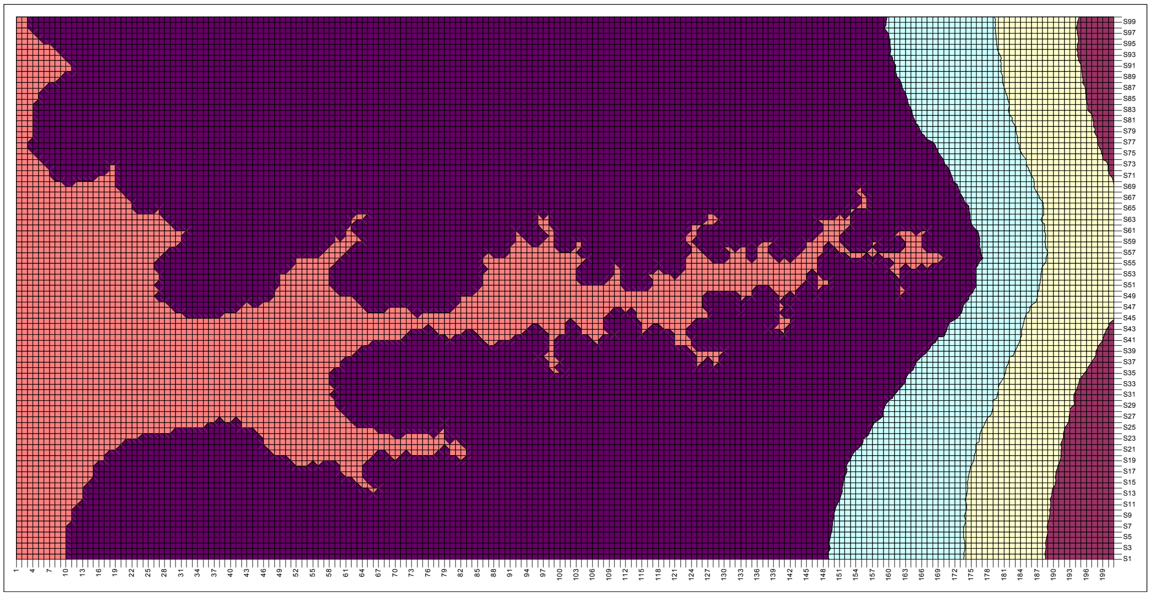

Figure 5.53 Step 5 of invasion, using Front surface Adjustment method

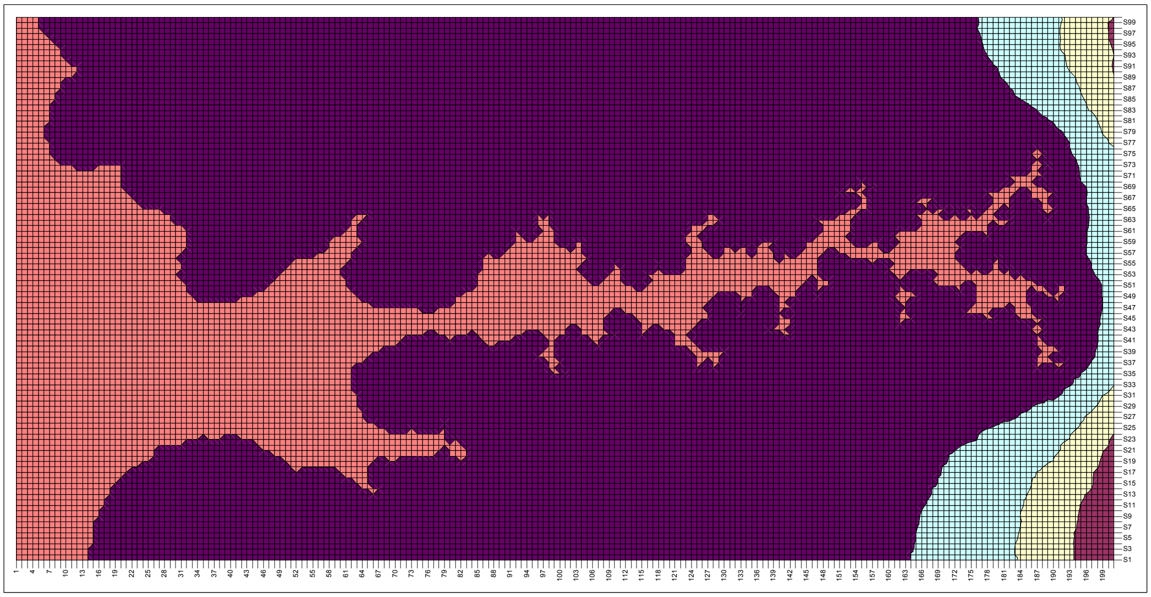

Figure 5.54 Step 6 of invasion, using Front surface Adjustment method

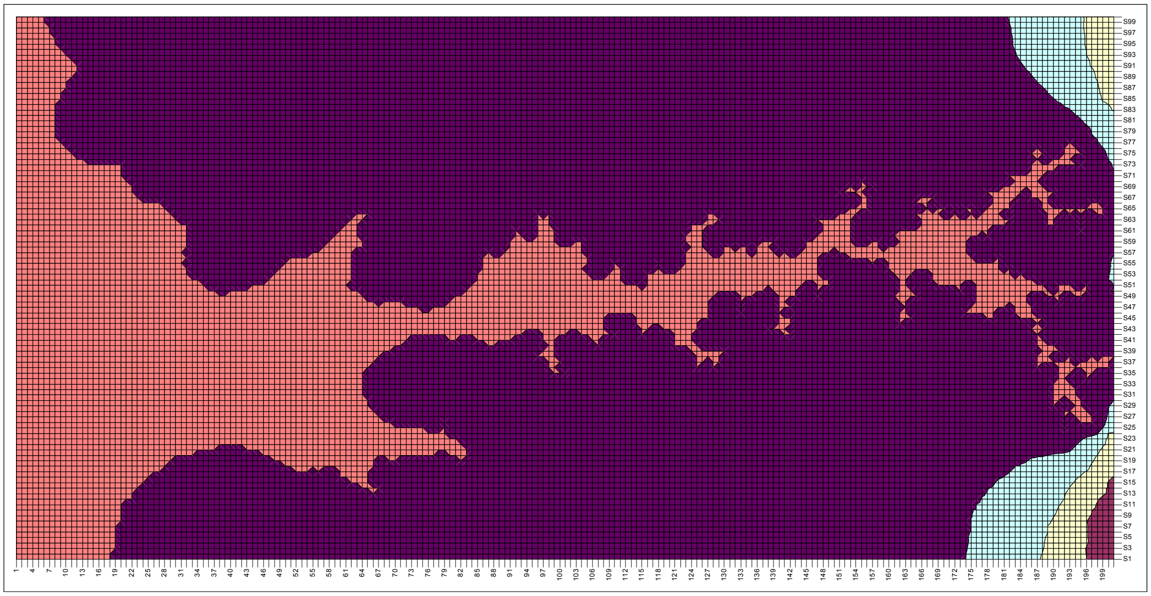

Figure 5.55 Step 7 of invasion, using Front surface Adjustment method

Comparing the total number of invaded nodes in the two method of adjusting boundaries shows a difference. In the case of front perpendicular plane adjustment, we have a total of 3,044 invaded nodes from the 20,000 nodes in the network. In the case of the front surface adjusted boundaries invasion method we have a total of 3389 invaded nodes. It is a difference of about 10% over the number of invaded nodes which is because, in the case of front surface adjustment method, we impose a little higher potential gradient to compensate for the nodes that are further behind the most advanced invaded nodes.

The front surface adjustment method gives more opportunity to the invasion potential candidates that are right at the criticality to advance than the front perpendicular plane adjustment method.

We have done another test to confirm the results. This time we are using the same 20,000 node system with 200 nodes in X direction and 100 nodes in Y direction, except here we are invading the network in the y direction. Flow direction is in the y axis direction (from bottom to top). Figures 5.56 to 5.57 show a two dimensional invasion test without any outlet boundary adjustment and with two types of adjustments. The first one is invasion with no adjustment. The second one uses the front surface adjustment method, and the third one is the same network using front perpendicular plane adjustment method. Inlets are located at the top of the graph and outlets are at the bottom. The invasion without any adjustment method is just one spike of invasion inside the network and shows that all the other nodes in the network had very few chances of being invaded.

Three dimensional views of the potentials for these three methods with and without adjustment are shown in figures 5.59 to 5.61 for a comparison.

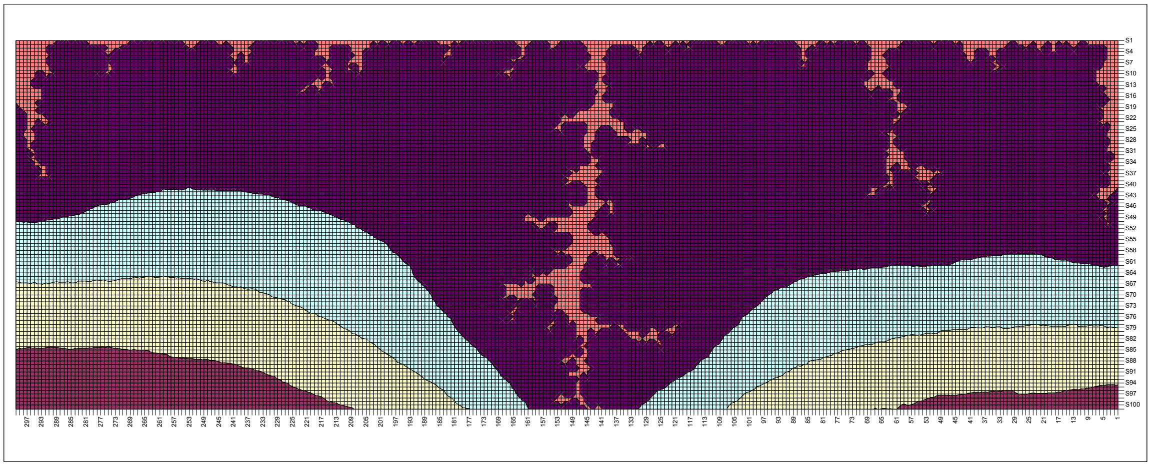

Figure 5.56 Invaded nodes without any adjustment method

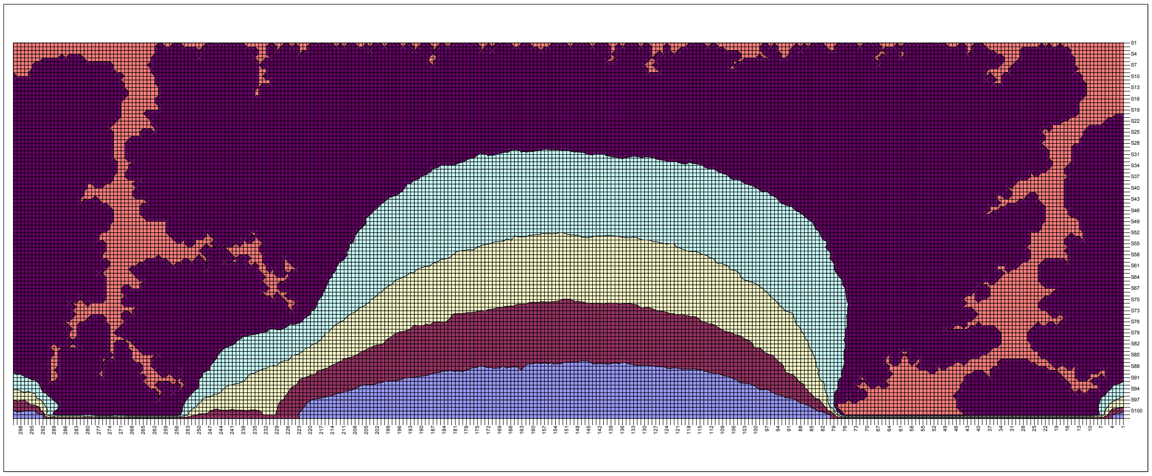

Figure 5.57 Invaded nodes using front surface adjustment method

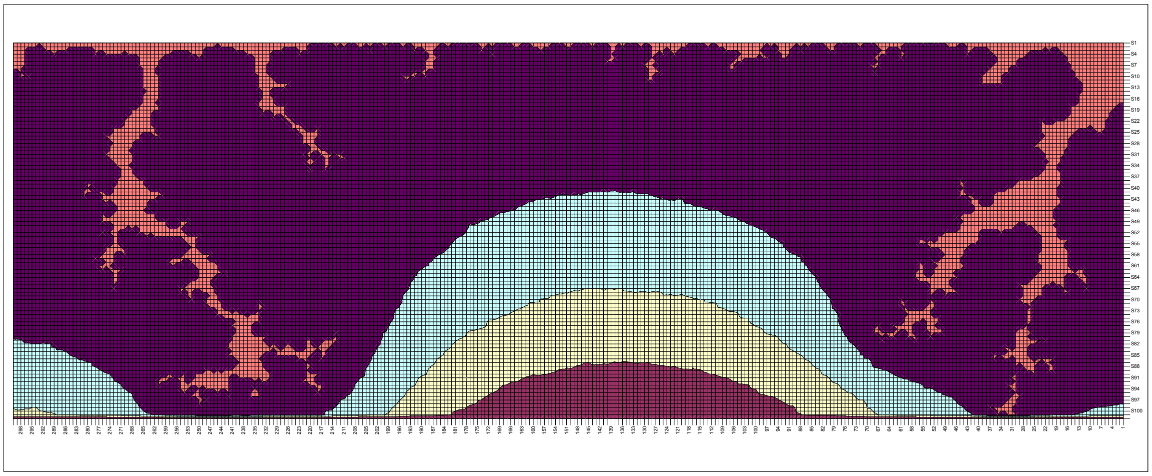

Figure 5.58 Invaded nodes using front perpendicular plane adjustment method

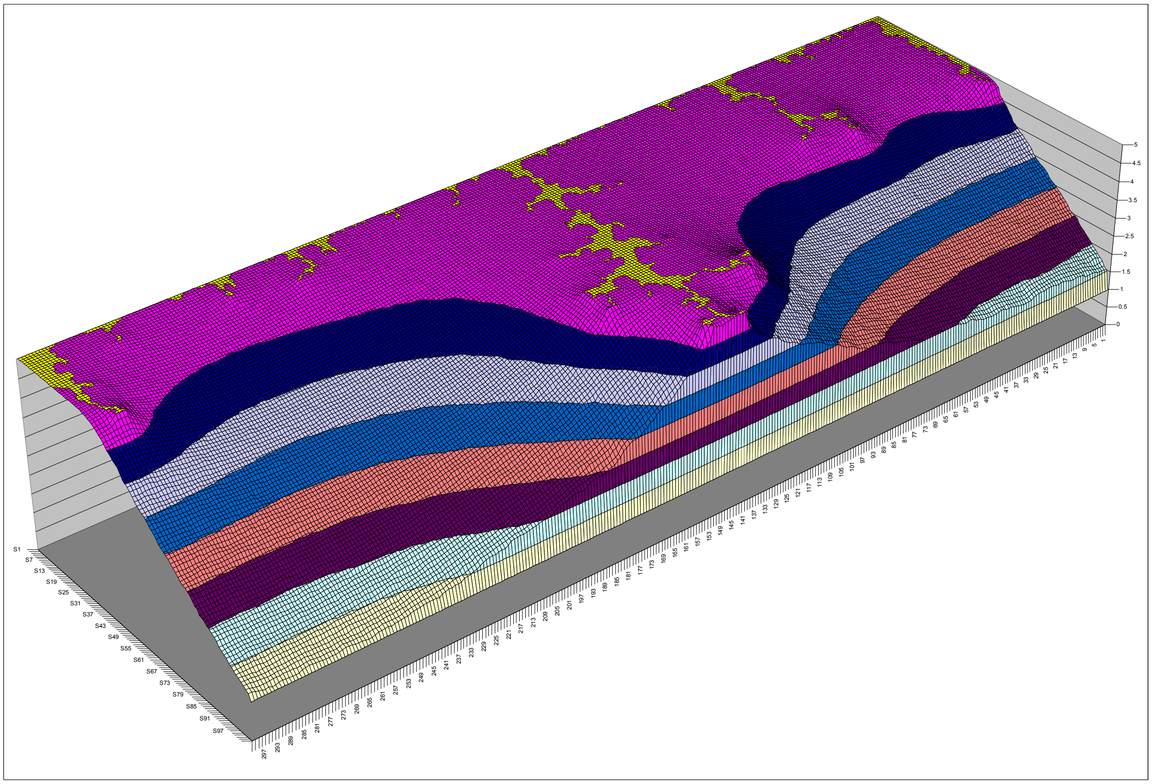

Figure 5.59 3D view of potential distribution in the network at the breakthrough without any adjustment method

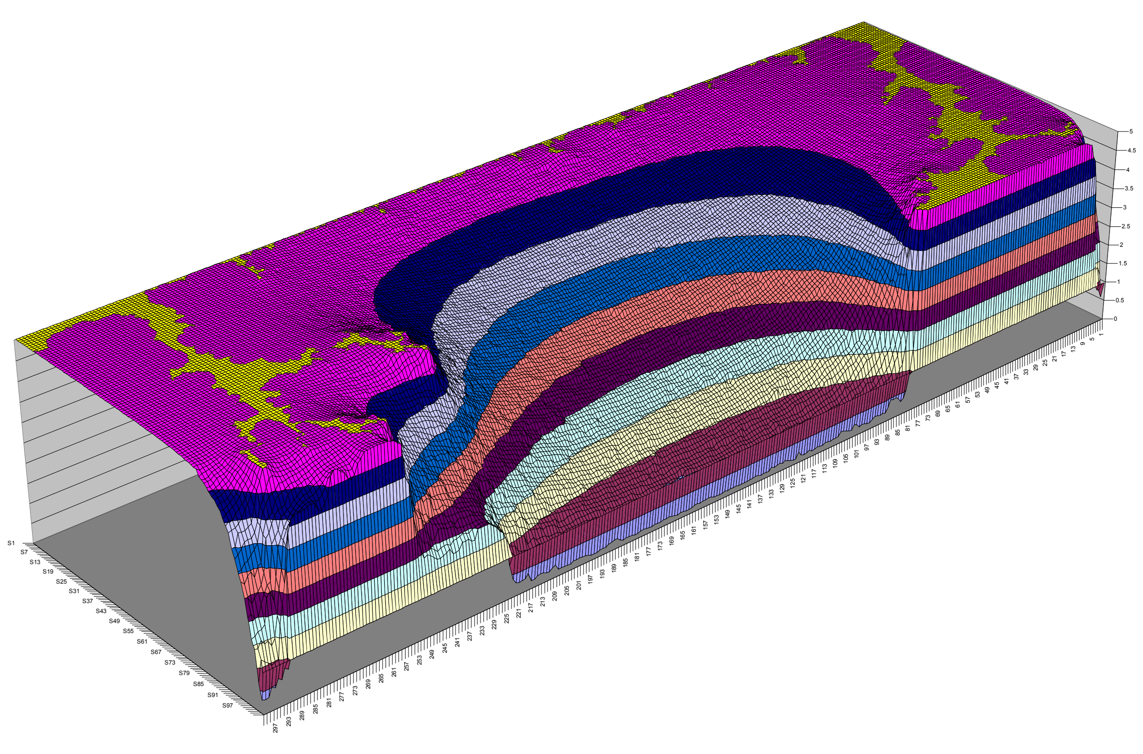

Figure 5.60 3D view of potential distribution in the network at the breakthrough using front surface adjustment method

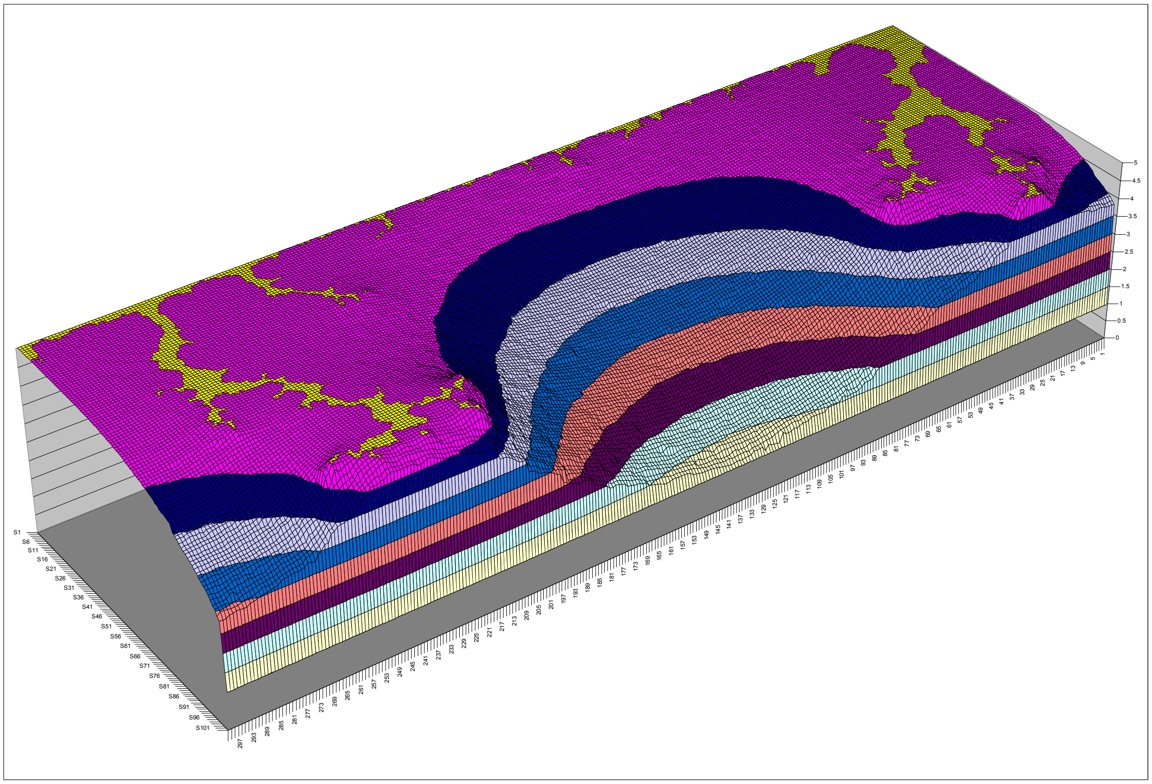

Figure 5.61 3D view of potential distribution in the network at the breakthrough using front perpendicular plane adjustment method

Comparison between these three invasions tests show similar behaviors as before. Again we have 2,703 invaded nodes for the surface adjustment and 2,499 invaded nodes for the case of perpendicular plane adjustment. The case without any adjustment method has only 1,912 invaded nodes which show more than 35% percent fewer invaded nodes than the adjusted case. Therefore, we have to use adjustment methods otherwise the invasion will be less realistic.

5.11. TIMING CORRELATIONS

In this section we examine the duration time for these simulations to present the time expense involved in these modeling. By knowing the trend of elapsed time for different size networks or throat radii distribution we can arrange the largest and most complicated networks that can realistically be simulated by our simulator.

The setup hardware for our simulations is a central processing unit with the frequency of 3 Giga hertz (GHz) and 2 Giga bytes of random access memory (RAM).

The first test is to keep the distance between the injector (inlet) and producer (output) constant and increase the area of fluid flow. To do so, we used a cubic lattice and have set a 3D rectangle with the x and y directions expandable and constant z direction of 2 nodes. Therefore, the distance between inlet and outlet is always constant equal to 20 nodes, but the rectangle is expandable from the area perpendicular to flow (XY) plane. We started with a 7 by 7 node area up to 100 × 100 nodes in X and Y directions. Table 5.7 shows the size of these networks.

X	Y	Z	Total Nodes
7	7	20	980
10	10	20	2,000
16	16	20	5,120
22	22	20	9,680
32	32	20	20,480
32	32	20	20,480
50	50	20	50,000
71	71	20	100,820
100	100	20	200,000

Table 5.7 Total nodes in each network

We use a uniform random distribution for sampling throat radii in the network; inlet nodes have 5 units of potential outlets have 1 unit. All the nodes on z = 1 and z = 20 planes are connected to inlets and outlets respectively. Figure 5.62 illustrates a schematic of these three dimensional rectangles.

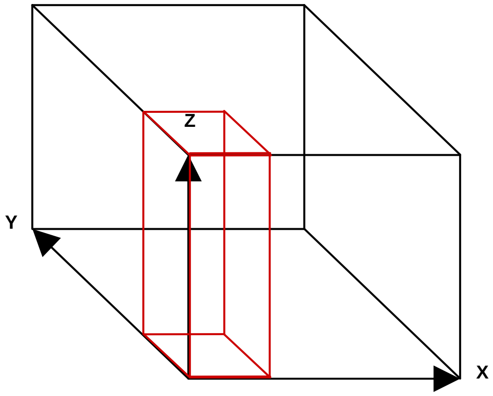

Figure 5.62 Expandable 3D rectangles in X and Y directions

Viscous invasion simulations have been performed on these networks ant the total running time at the breakthrough in seconds for each simulation have been recorded. Table 5.8 reflects the running time for each simulation.

Nodes	Time (sec.)	Time (hr.)
980	10.65	0:00:10
2,000	26.40	0:00:26
5,120	77.59	0:01:17
9,680	154.72	0:02:34
20,480	380.46	0:06:20
50,000	1082.06	0:18:02
100,820	2059.07	0:34:19
200,000	4634.79	1:17:14

Table 5.8 Computer running time at the breakthrough

Figure 5.63, shows the plot of number of nodes in the network vs. the elapsed time in seconds. The best fit to these data points is a straight line with the equation

$$Time(\sec.) = 0.023 * Number\_of\_Nodes - 65.445$$
$$R^2 = 0.997$$

With this best fit equation we can predict the total running for larger networks with 500,000 or 1,000,000 nodes. The predicted running time for couple of larger networks is shown in Table 5.9. Figure 5.63, shows the added graph of the running time for the simulated network and the predicted ones.

Nodes	Time (sec.)	Time (hr.)
500,000	11,500.00	3:10:34
750,000	17,250	4:47:30
1,000,000	23,000	6:23:20

Table 5.9 Predicted running time for larger networks

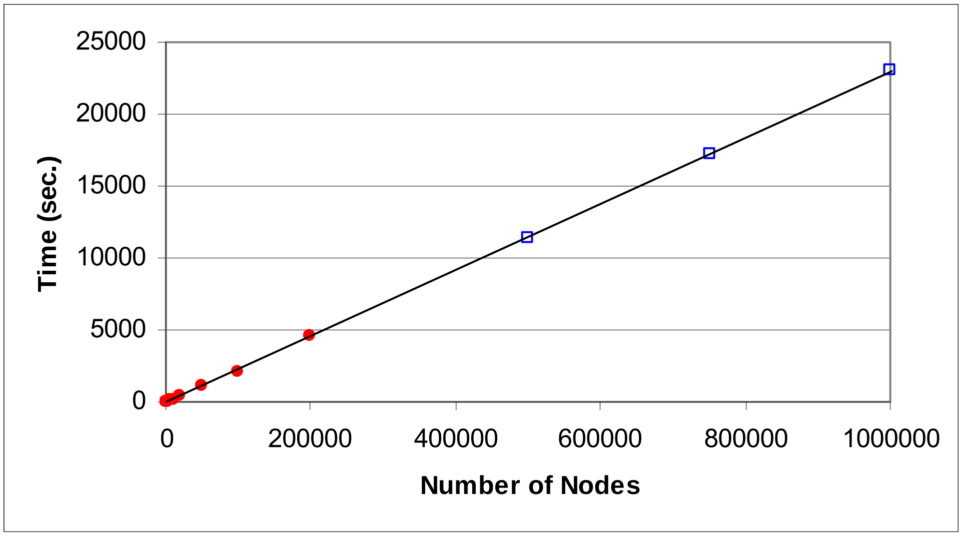

Figure 5.63 Simulated and predicted computer running time for the case of fluid flow area expandable network

The next case is to set the same cubic lattice but this time keep the XY area constant and increase the distance between the injector and producers. XY area is a 20 × 20 node surface and we increase number of nodes in Z direction from 20 to 500 nodes. Table 5.10 shows the network size for such cases.

X	Y	Z	Total Nodes
20	20	5	2,000
20	20	12	4,800
20	20	20	8,000
20	20	25	10,000
20	20	50	20,000
20	20	125	50,000
20	20	250	100,000
20	20	500	200,000

Table 5.10 3D network with increasing number of nodes in Z direction

We do the same procedure as the last case, run the viscous invasion simulations, record the computer running time in seconds, fit the best trend to the results and predict the running time for larger networks. Table 5.11 reflects running time for the simulated values.

Nodes	Time (sec.)	Time (hr.)
2,000	2.469	0:00:02
4,800	18.062	0:00:18
8,000	58.625	0:00:58
10,000	98.546	0:01:38
20,000	615.703	0:10:15
50,000	3,735.89	1:02:15
100,000	13,260.5	3:41:00
200,000	41,716.4	11:35:16

Table 5.11 Computer running time for viscous invasion for the case of increasing Z

The best fitted trend is a second order polynomial to number of nodes vs. running time results as:

$$\text{Time (sec.)} = 8 \times 10^{-7} \times N^2 + 0.0514 \times N - 351.17$$
$$R^2 = 0.9995$$

The predicted running time for networks up to 1,000,000 nodes is shown in table 5.12 and Figure 5.64 shows a plot of simulations, trend line and predicted values.

X	Y	Z	Nodes	Time (sec.)	Time (hr.)
20	20	250	500,000	225,348.83	3:10:34
20	20	500	750,000	488,198.83	4:47:30
20	20	1,000	1,000,000	851,048.83	6:23:20

Table 5.12 Predicted running time for case of increasing Z

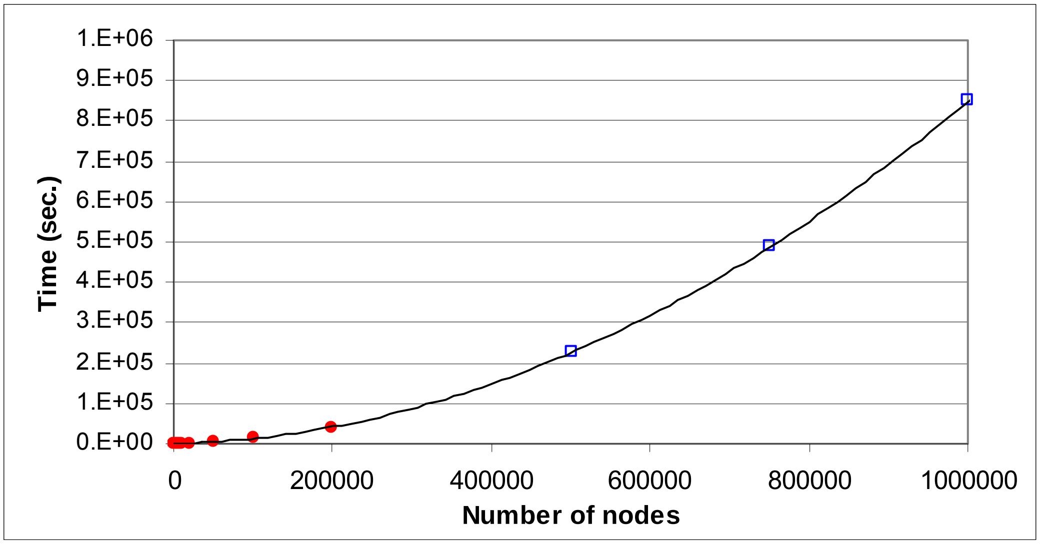

Figure 5.64 Simulated and predicted computer running time for the case of increasing Z direction

As both of these cases show, running simulations for up to one million nodes are easily achievable with in 6 hours but going to higher number of nodes, challenges much more computer memory which is not easily available. Two giga bytes of memory allows for one million nodes system, going to larger networks require more RAM which is not easily accessible and computer has to use hard disk drive (HDD) to compensate for the lack of memory, using HDD makes the computation more physical oriented process (read and write to the physical drive than using the RAM). This effect makes the simulation times at least couple of orders of magnitude longer, which is not recommended. Therefore, we will keep the networks sizes lower than one million nodes for the purpose of practicality.

CHAPTER 6

Results Discussion

This chapter consists of the key tests on large networks to study, describe, and quantify the viscous dominant displacement. The viscous dominant displacement simulations have been modeled with both artificial and real sample models on 2D and 3D networks.

The tests have been simulated on regular lattices to get the essence of displacement behavior results. Then, some of the tests have been performed on real samples to verify the behavior. The nature of the viscous invasion was the outcome of these simulations and has been explained in details in each section. At the end of this chapter, sweep efficiency and its relation to the viscous invasion has been explained. Specific results have been inferred from each test and further discussed.

It is very important to mention that we have performed too many tests for each of these sections; thus we are only showing one or at most two example test results for each of them. So, if there are only one or two graphs in a test, they were hand-selected graphs to show the behavior or results of each characteristic of viscous displacement. In each series of tests, there have been many realizations that showed identical results.

6.1. NATURE OF VISCOUS INVASION

These are tests that have been performed for studying the nature of viscous displacement. We have inspected the different behaviors of viscous invasion by changing the distribution of conductivities, adding spatial correlations to the distribution of conductivities for different tests, and then quantifying the results of each series of tests.

Characteristics like self-contracting behavior (invading fluid tends to form a single channel instead of spread into the network), average bonds per nodes, finger density and R_Z ratios have been derived from the tests and explained in detail.

6.1.1. SELF CONTRACTING

This test has been performed on a three dimensional square lattice. We have set constant pressures in invaded region, inlets and outlets. Displacing fluid is single phase, low viscosity fluid, such as water or diluted solvent with $\mu \approx 1$ centipoises (cp). The displaced fluid is high viscosity heavy oil with viscosities in the range of 10,000 cp to 100,000 cp. Conductivities have been sampled using a uniform re-sampling of Finney pack distribution on a 100 × 100 × 40 network, which is a total of 400,000 nodes, 1.3 million bonds, and 20,000 inlet and outlet Nodes. The simulated viscous invasion test results are shown in Figure 6.1. Displacement is from bottom to top, which is from lower Z's to higher Z's in the network. We neglect the gravity term and criterion for invading a bond is the 70% of the maximum invading rate.

It is important to mention that this is one of the many simulation results that have been modeled. We have performed many tests on smaller size networks and received the same results, but we only show one of these several test simulations here.

As shown in Figure 6.1, the displacement consists of many individual channels. All of the channels in the network are individual fingers, and although we have much more invaded nodes at the first step of invasion (nodes with lower Z values at the bottom of the graph), displacement forms individual channels that follow through the network. After a very short time (e.g., steps) of invasion, the channeling shows itself. Therefore, the displacement consists of individual channels. The displacement does not show a piston-like displacement; therefore, we can refer to this type of generation of channels or fingers in the network as the self contracting behavior of the viscous displacement.

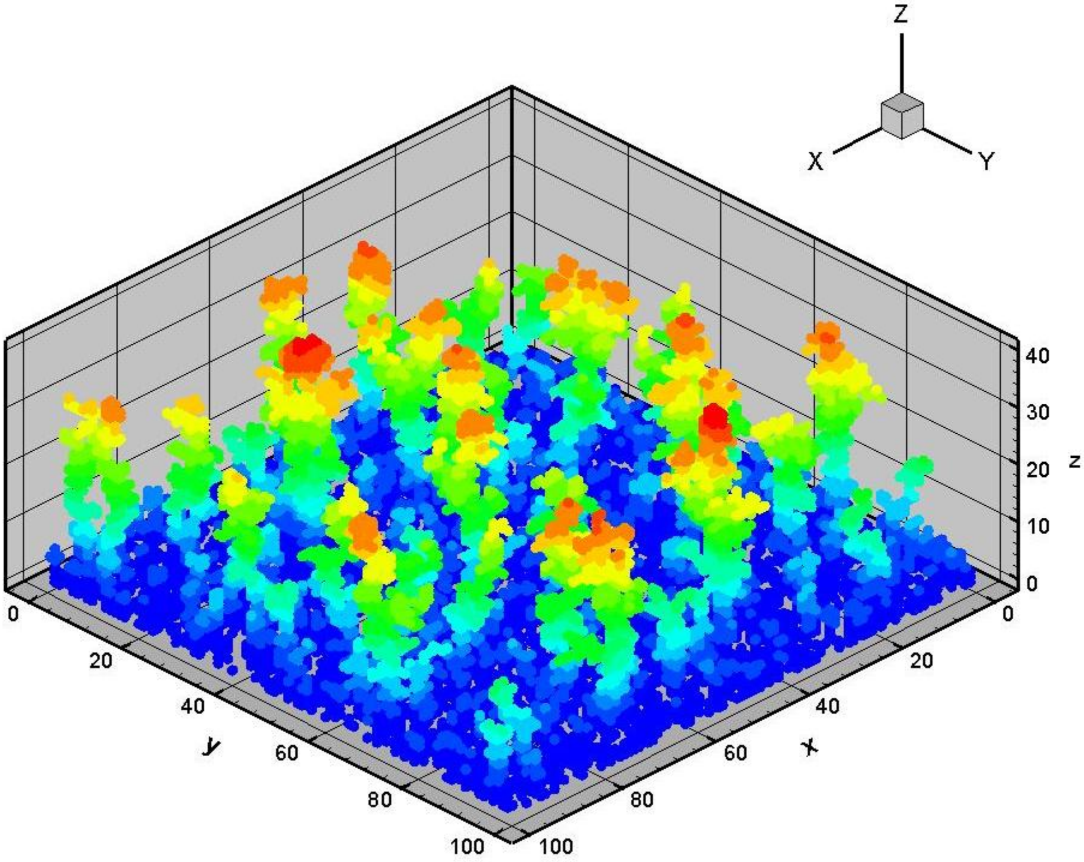

Figure 6.1 Self contracting behavior, viscous dominant invasion

Figures 6.2 to 6.4 show three two-dimensional slices with more details of channels in the displacement graph shown in Figure 6.1. These slices show only one channel and not a cross-section of the whole network. As shown, the displacement does not result in making a sharp piston-like front.

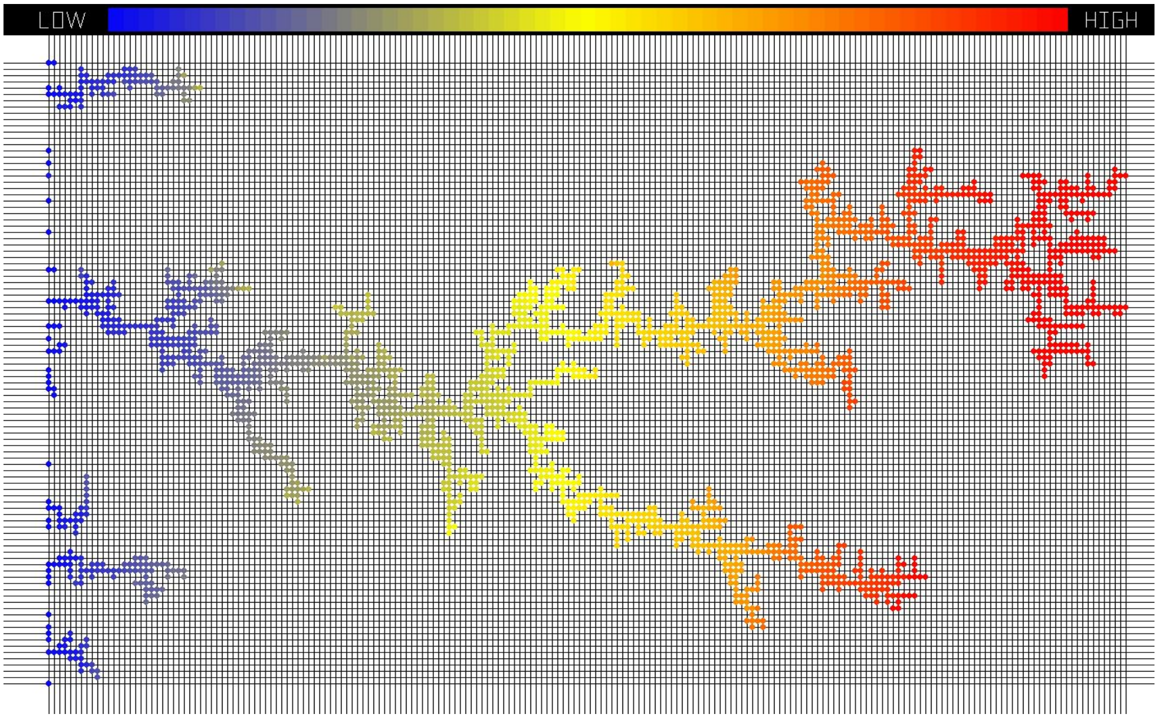

Figure 6.2 Slice 1, self contracting behavior

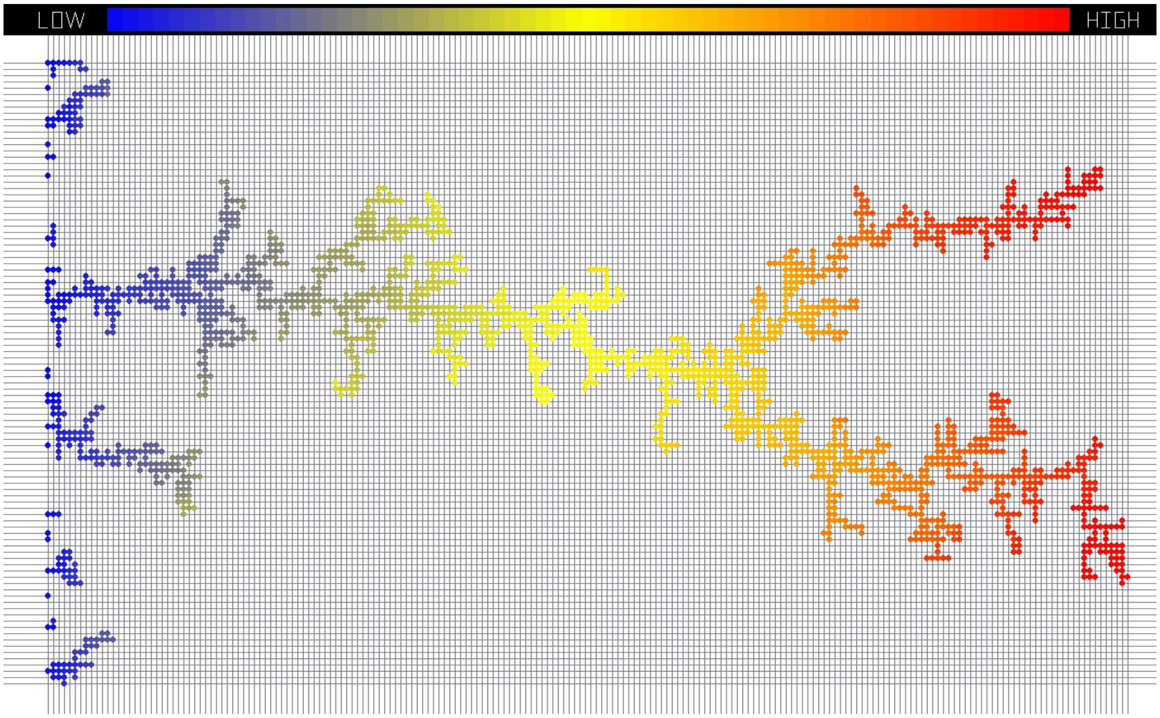

Figure 6.3 Slice 2, self contracting behavior

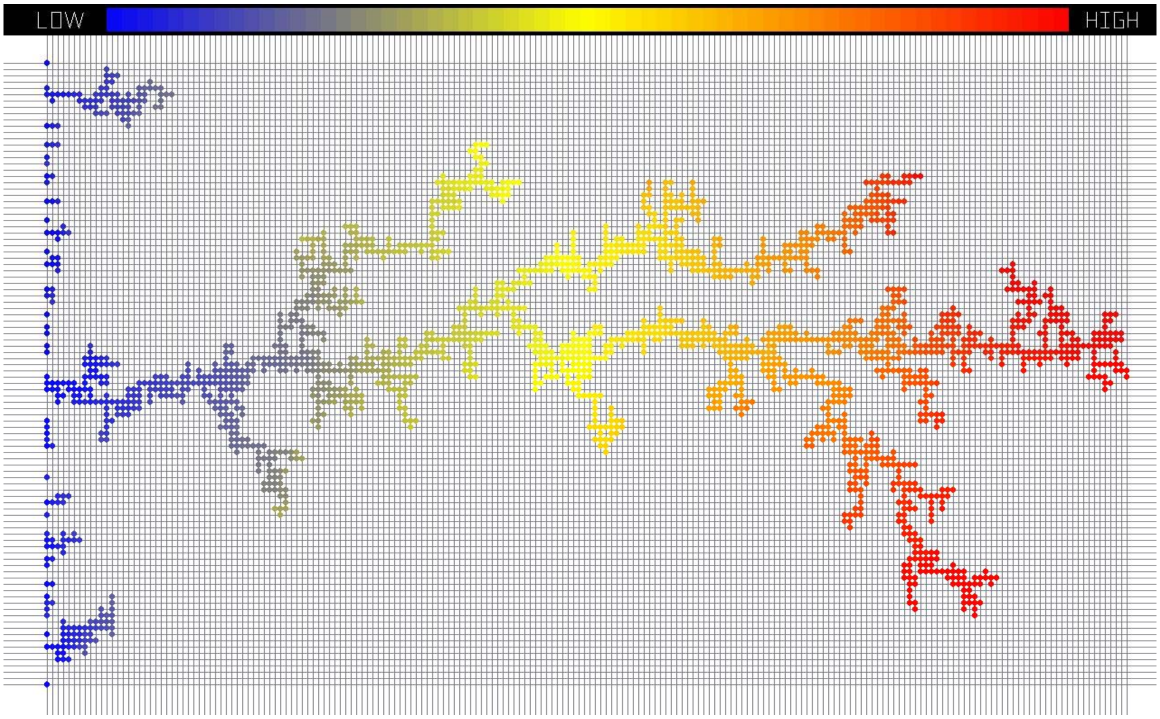

Figure 6.4 Slice 3, self contracting behavior

6.1.2. AVERAGE BONDS PER NODES

In this test, we investigate the number of invaded bonds per nodes; i.e., how many nodes were connected to each single node in the network. For example, we may have two nodes connected to each other, or the nodes maybe connected in a cluster shape so that each node had more than two nodes connected to it.

The selected network for this test is a three dimensional. We also chose a very small network with the dimensions of 30 * 30 * 10 and a total size of 9,000 nodes. This cube has four sides sealed to no flow boundaries, and top and bottom sides connected to inlet and outlet, respectively. Conductivities were arbitrarily sampled from a uniform random distribution. We performed the viscous invasion simulation and counted the number of invaded bonds in the system. Table 6.1 and Figure 6.5 show these values.

Invaded bonds	Number of nodes
1	565
2	690
3	178
4	50
5	14
6	3

Table 6.1 Number of invaded bonds per node (network with 9,000 nodes)

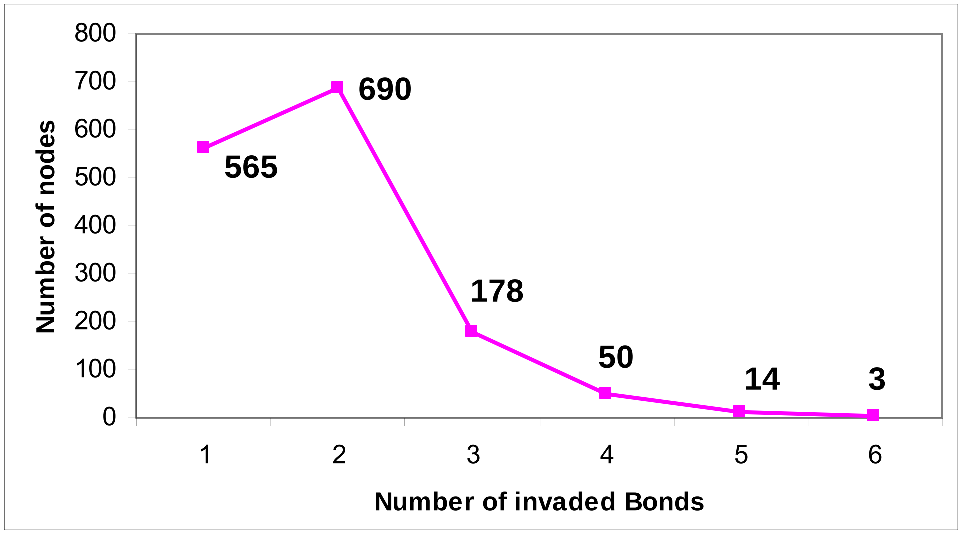

Figure 6.5 Trend of the number of invaded bonds per node for a 9,000 node system

We had approximately 1,500 invaded nodes and 2,760 invaded bonds; therefore, the average number of invaded bonds per invaded nodes was 1.84. This is very close to the linear invasion in which we have an average of two bonds per node, in which each node is connected to the two adjacent nodes in the direction of flow.

We conducted the same test on a larger network consisting of 125,000 nodes. The test network was a 50 * 50 * 30 lattice. Bond conductivities were sampled from a uniform random distribution. There were four sides to no flow boundaries, and top and bottom were connected to inlets and outlets. Table 6.2 reflects the number of invaded bonds per node and Figure 6.6 shows the trend of these values (number and percentage on a different axis).

As shown, the majority of the nodes have one or two bonds invaded and the nodes with more than 3 invaded bonds are a very small percentage of the total invaded nodes (as shown in Figure 6.6). The average value of the bonds per nodes results in a value of 1.88, which is very similar to the value observed in the small 9,000 node system. Again this is very close to linear invasion of two bonds per node.

Invaded bonds	Number of nodes
1	1,944
2	2,266
3	652
4	243
5	66
6	9

Table 6.2 Number of invaded bonds per node, 125,000 nodes network

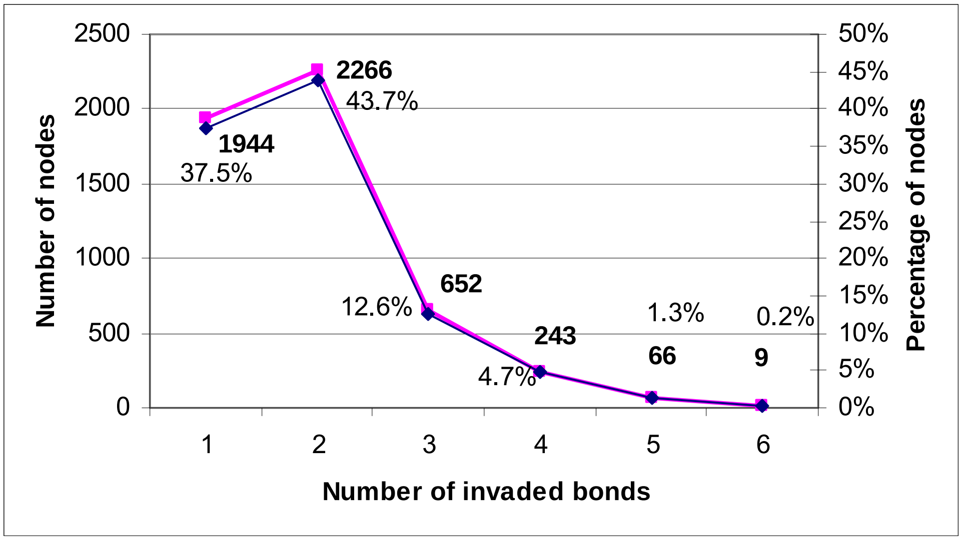

Figure 6.6 Trend of number of invaded bonds per nodes for a 125,000 nodes network system

Figure 6.7 shows a linear invasion when only two bonds of a node are invaded in the imaginary direction of flow from left to right.

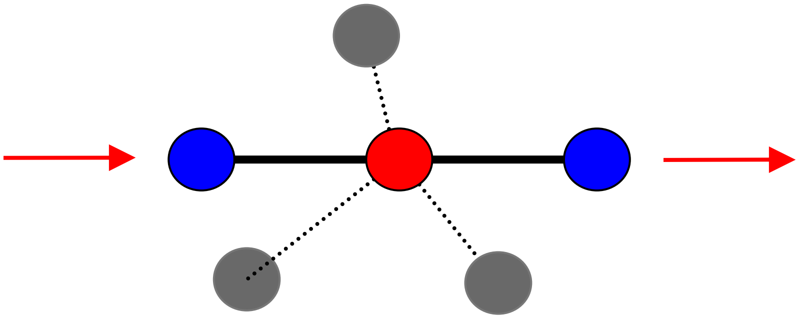

Figure 6.7 Demonstrates two invaded bonds for the invaded node in the middle

It appears that viscous dominant invasion is spike-like in nature. It has the tendency to make channels and fingers in the network as opposed to making a piston-like uniform displacement.

6.1.3. CONDUCTIVITY DISTRIBUTION EFFECTS ON INVADED NODES

In this test, we examined the effect of distribution of bonds hydraulic conductivity on the total number of invaded nodes in the network. We now understand how the homogeneity or heterogeneity can affect the total number of invaded nodes in the viscous dominated invasion and, ultimately, effects on the total sweep in the network.

From the previous test in Section 6.2.2, we discovered that most of the nodes have one or two invaded bonds (linear invasion). To make sure that the viscous invasion confirms this behavior and ensure it is not the effect of size or hydraulic conductivity distribution, we performed a similar test on larger lattices. However, to study the effect of hydraulic conductivity distribution, we performed these tests with three different hydraulic conductivity distributions. The prepared model was a cubic network lattice with 250,000 nodes in it, four no-flow boundaries on the sides, and inlets and outlets at the top and bottom of the network. We sampled the conductivities for these viscous dominant invasion tests with three sets of conductivities:

a. Uniform random re-sampling of hydraulic conductivities between 1 to 10;
b. Uniform random re- sampling of hydraulic conductivities between 1 and 100; and
c. Finney pack distribution.

After performing the viscous dominant invasion tests, the resulting numbers of invaded bonds per nodes for each test are shown in Table 6.3 and Figure 6.8 reflects the comparison of trends for these three different distributions.

Distribution	Random 1-10		Random 1-100		Finney pack	
	No. Nodes	Percentage	No. Nodes	Percentage	No. Nodes	Percentage
	4,119	38.0%	3,463	38.0%	743	38.7%
	4,945	45.6%	4,148	45.6%	916	47.7%
	1,267	11.7%	1,049	11.5%	208	10.8%
	417	3.8%	347	3.8%	46	2.4%
	89	0.8%	83	0.9%	8	0.4%
	13	0.1%	13	0.1%	1	0.0%
Total	10,849		9,102		1,921	

Table 6.3 Number of invaded bonds per nodes for different distributions

Table 6.3 reflects the different number of invaded nodes or bonds for each test. Although these three networks had the same number of nodes in them (250,000 nodes), the invaded nodes in the three tests were completely different and varied from 20% to 90% in the number of invaded nodes, from random values of hydraulic conductivities to Finney pack distributions.

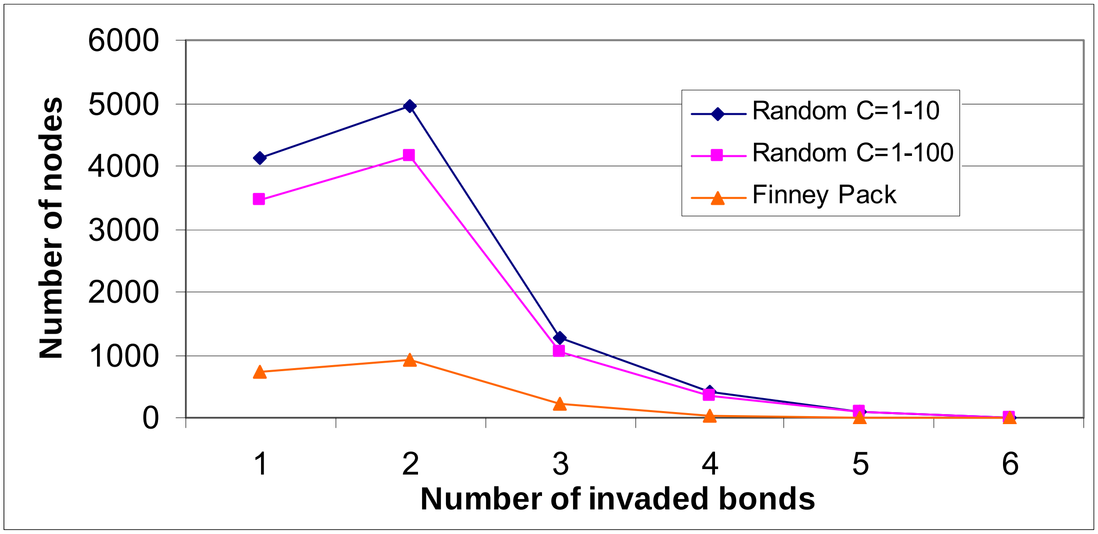

Figure 6.8 Trend comparison of the number of invaded bonds per nodes in a 250,000 node network with three different distributions

From Figure 6.8, it appears we received three different outcomes, but if the percentage of the invaded bonds per invaded nodes is considered, as shown in Figure 6.9, a similar behavior from all of the three distributions is noted.

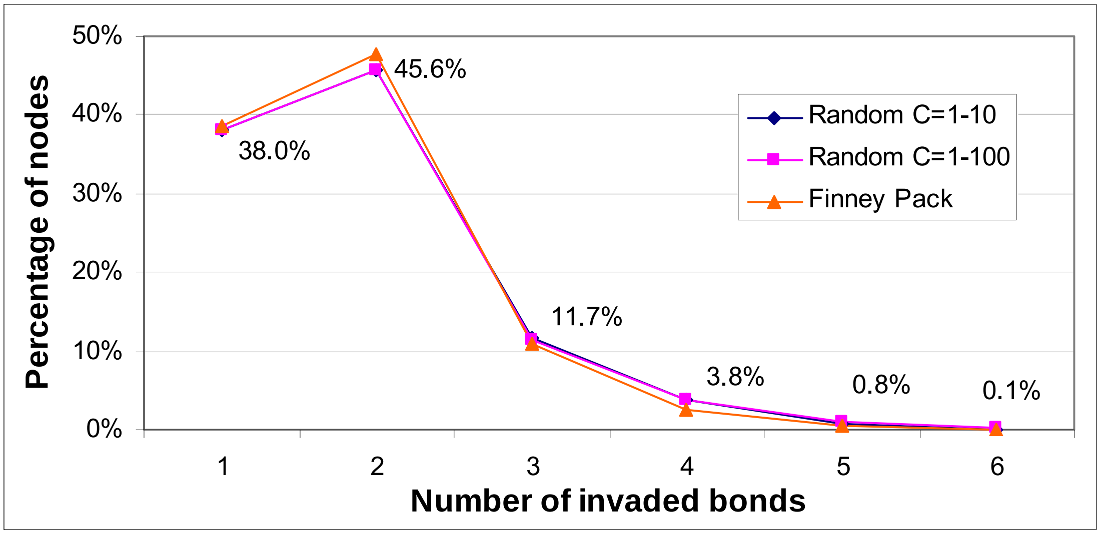

Figure 6.9 Percentage of invaded bonds per nodes

When we calculated the average number of invaded bonds per nodes for each of these distributions, we received a similar value as before. Table 6.4, illustrates these average bonds per nodes values.

	Average Bonds/Node
Random 1-10	1.84
Random 1-100	1.84
Finney pack	1.78

Table 6.4 Average invaded bonds per nodes

Note that these values are the same linear invasion as before, which was two bonds per node, and was proven previously in section 6.2.2.

These tests prove that the distribution of hydraulic conductivity can affect the total number of the invaded bonds or nodes in a network. A more homogeneous distribution leads to a higher number of invaded bonds and nodes, which consequently increases the sweep, similar to the random distribution test using the narrow range of conductivities between 1 and 10. A more heterogeneous distribution such as the random values between 1 and 100 or the more heterogeneous Finney pack distribution has fewer invaded bonds or nodes, but the behavior of the viscous dominant invasion remains the same and is not affected by the hydraulic conductivity distribution. Thus, the value of the average bonds per nodes remains similar for all tests.

Therefore, if the distribution of conductivities becomes more heterogeneous, the number of invaded nodes decreases. Consequently, the sweep efficiency decreases. Although more homogeneous systems have more swept than heterogeneous nodes, the bonds hydraulic conductivity distribution does not affect the ratio of invaded bonds per invaded nodes. Thus, the viscous dominant invasion displacement structure remains the same regardless of what conductivities distribution exists in the model.

6.1.4. FINGER DENSITY

Thus far, we determined that viscous dominant invasion is not a self-stabilizing displacement (does not make a sharp piston like front, instead, makes a denderic finger type front), and it tends to make channels and fingers through the porous media when displacing. But, when we quantify the viscous dominant displacement, we are able to better explain and compare different displacement models or scenarios with each other.

To do this, we use the finger density of viscous displacement as the quantifying value. ***Finger Density*** is defined as:

The number of flow paths (e.g., fingers) divided by the total number of nodes in the surface area perpendicular to the general flow direction from inlet to outlet.

Note that we count the fingers that have advanced 80% (of the distance between inlets and outlets) in the network at the time of breakthrough. All other fingers which are not advanced at least 80% into the network will not be considered in our calculations.

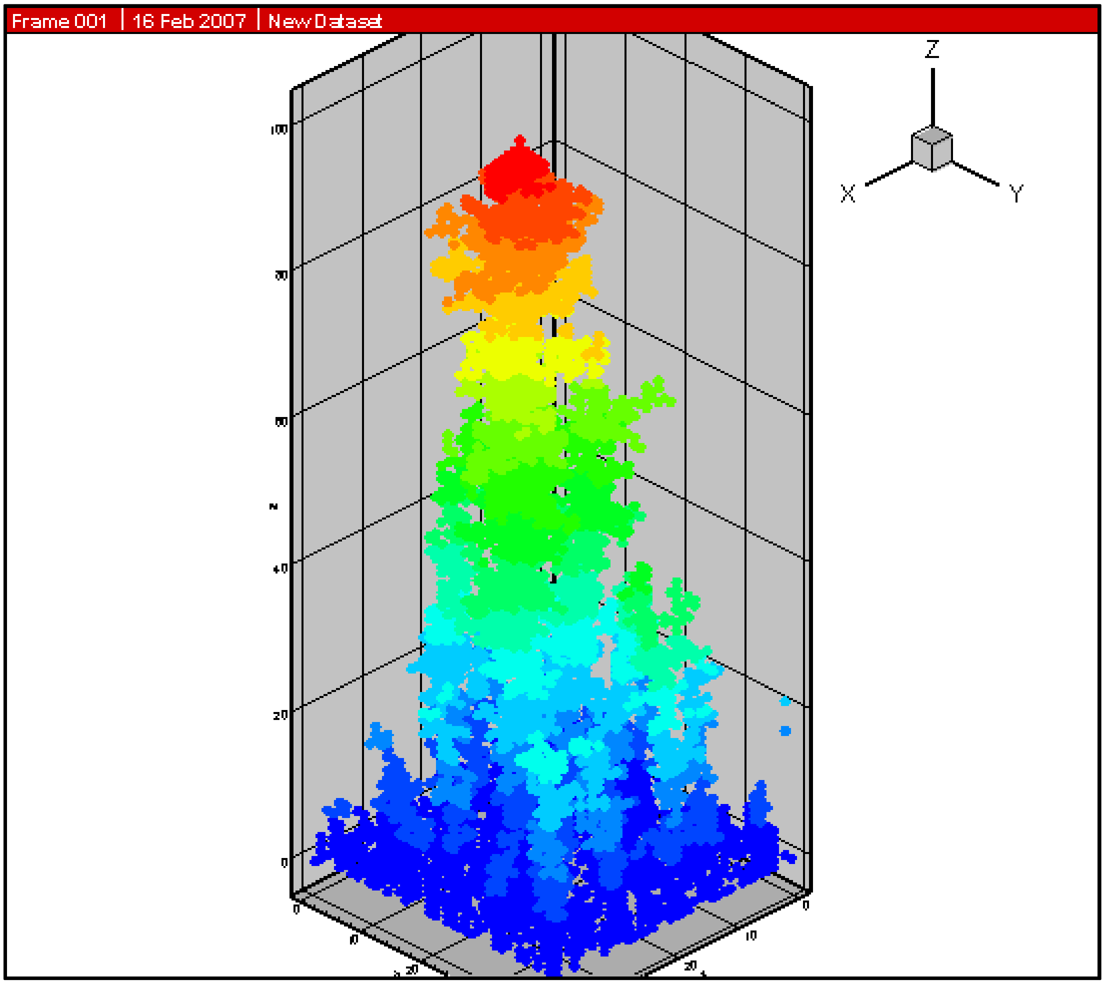

Figure 6.10 One major finger in the 40 × 40 × 100 network, viscous dominant invasion

For example, if the model is a 40 × 40 × 100 node system and the flow is in the Z direction, which has 100 nodes, we have a total of 1,600 nodes in the perpendicular area to the general direction of flow. If Figure 6.10 is the resulting viscous invasion test that has been modeled, then there is only one finger that exists after modeling the viscous dominant invasion test. Therefore, the finger density for the example test in Figure 6.10 will be calculated as follows:

$$\text{Finger Density } = \frac{1}{1600} = 0.000625$$

Another test example, shown in Figure 6.11, is the 100 × 100 × 40 node system. It flows in Z direction, which has 40 nodes. The total number of fingers counted is 24 channels. Therefore, finger density is calculated as:

$$\text{Finger Density } = \frac{24}{10000} = 0.0024$$

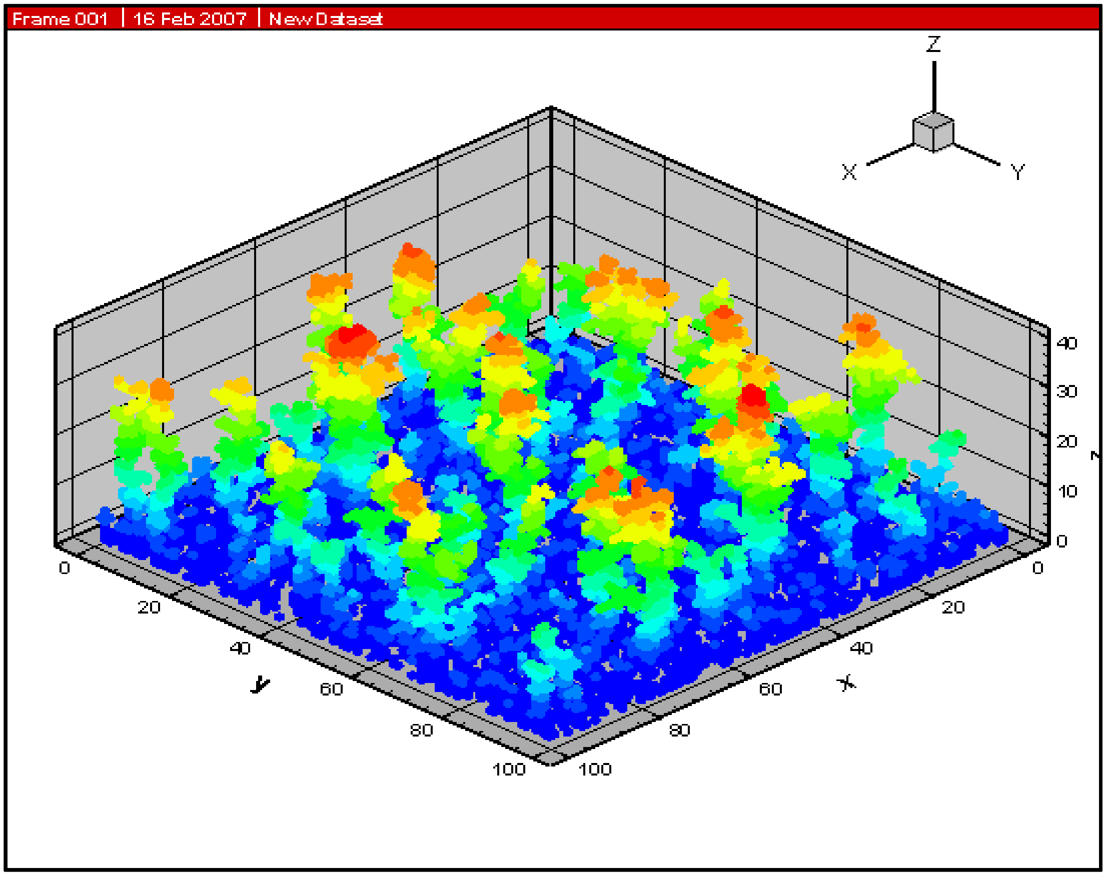

Figure 6.11 Viscous invasion channels in a 100 × 100 × 40 network

Once finger density was defined, we performed different tests with viscous invasion to study the effect of the network geometry on the finger density or the number of swept nodes. To do this, we conducted two series of tests, as follows:

a. The distance between the inlet and outlet were kept constant and the area perpendicular to flow direction was increased; and
b. We simultaneously changed the dimensions in X, Y and Z directions in equal proportion.

For the first series of these tests, we kept the distance between the injector and producer constant at 40 nodes (e.g., Z direction) and simultaneously increased the dimensions size in X and Y directions, as shown in Figure 6.12.

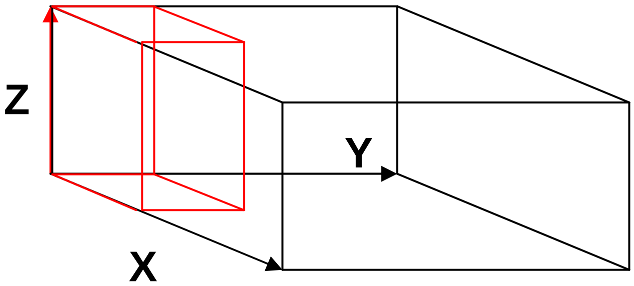

Figure 6.12 Areal expansion of lattice in X and Y dimensions

The first test in this series was conducted on a 10 × 10 × 40 (e.g., 4,000 nodes) cubic lattice and we increased the size to 90 × 90 × 40 (e.g., 324,000 nodes). The sizes and calculated finger densities for this series of tests are shown in Table 6.5.

X	Y	Z	Number of Area Nodes	Total Nodes	Number of Fingers	Density
10	10	40	100	4,000	1	0.01000
20	20	40	400	16,000	3	0.00750
30	30	40	900	36,000	4	0.00444
40	40	40	1,600	64,000	5	0.00313
50	50	40	2,500	100,000	7	0.00280
60	60	40	3,600	144,000	9	0.00250
70	70	40	4,900	196,000	11	0.00224
80	80	40	6,400	256,000	12	0.00188
90	90	40	8,100	324,000	13	0.00160

Table 6.5 Increase of flow surface area

Figure 6.13 demonstrates the plot of finger density versus the total number of nodes in the lattice for the second series of tests. As shown, the graph decreases to a certain density value, approximately 0.002 finger density per node (in area perpendicular to the general flow direction).

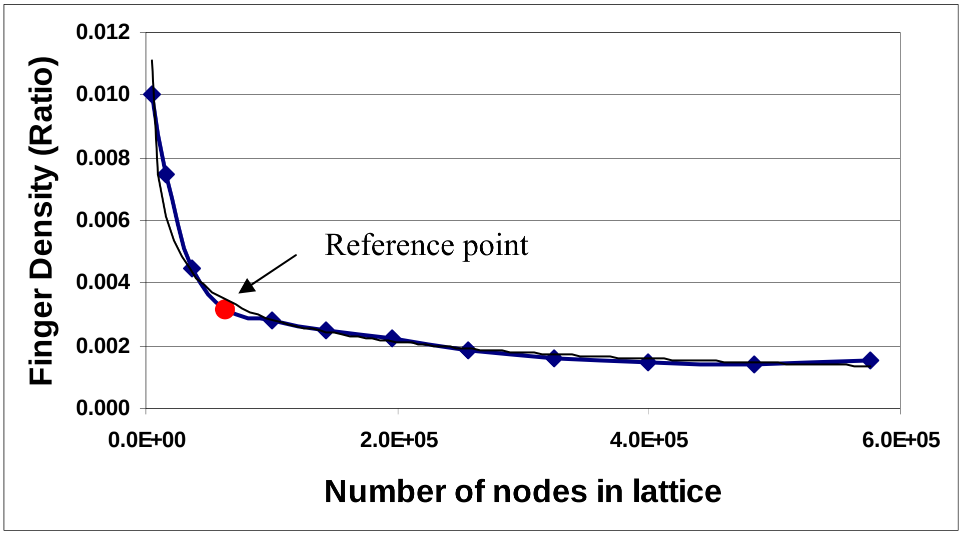

Figure 6.13 Plot of Finger density vs. number of nodes, case of areal expansion

This plot illustrates a power trend. The equation of the fitted plot to the graph is:

$$\text{Density} = 0.0774(Nx.Ny.Nz)^{-0.2816} = 0.0274(Nx.Ny)^{-0.2816}$$
$$R^2 = 0.9813$$

The area perpendicular to the flow in these tests was increased by the power of two, but the distance remained constant. While the breakthrough happened, the number of fingers that could not advance more than 80% of distant (between inlet and outlet) into the network, decreased. This is why finger density dropped to an asymptotic approximately 0.002 finger density.

In the second series of tests, we changed the dimensions of the network simultaneously in all three (X, Y, and Z) directions. Thus, the size of the network grew by the power of three. We began with a 10 × 10 × 10 cubic lattice (e.g., 1,000 nodes) and increased the dimensions up to a 90 × 90 × 90 (e.g., 729,000 nodes) cubic lattice. Figure 6.14 illustrates the expansion of the network model for all three dimensions.

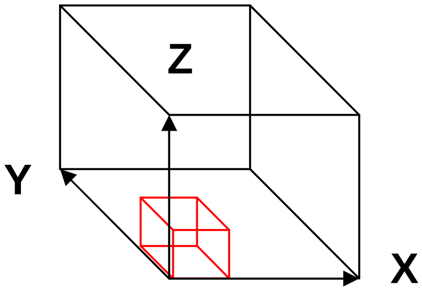

Figure 6.14 Simultaneous expansion of lattice in all three dimensions

We performed the viscous invasion test and calculated the finger density as explained previously in Section 6.2.4. Table 6.6 reflects the size of the modeled network and the resulting density for each invasion test.

X	Y	Z	Number of Area Nodes	Total Nodes	Number of Fingers	Density
10	10	10	100	1,000	3	0.03000
20	20	20	400	8,000	4	0.01000
30	30	30	900	27,000	7	0.00778
40	40	40	1,600	64,000	5	0.00313
50	50	50	2,500	125,000	5	0.00200
60	60	60	3,600	216,000	6	0.00167
70	70	70	4,900	343,000	7	0.00143
80	80	80	6,400	512,000	7	0.00109
90	90	90	8,100	729,000	8	0.00099

Table 6.6 Calculated finger density in a simultaneous expansion of lattice in all directions

When we plotted the finger density versus total number of nodes in the cubic lattice (Figure 6.15), it appeared that after a certain dimension size the decreasing trend of the finger density changed the slope and became almost a flat line, approximately asymptotic to a value less than 0.002, and did not decrease any more.

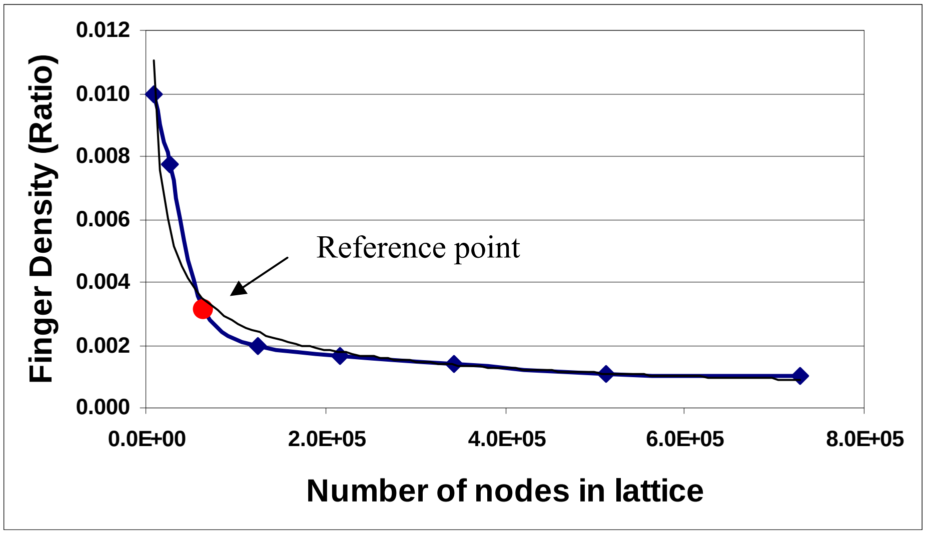

Figure 6.15 Plot of Finger density vs. number of nodes, case of simultaneous expansion in all three dimensions

The best match for our results is a power line fit with following equation:

$$\text{Density } = 1.8008(Nx.Ny.Nz)^{-0.5579} = 1.8N^{2.44}$$
$$R^2 = 0.9807$$

There is a reference point in these two series of tests to verify the accuracy of these tests. The data point reference for the 40 × 40 × 40 node system (shown in larger circle on Figures 6.13 and 6.15) has a similar resulting finger density in both series of tests.

It is clear from Figure 6.15, that when the distance between the injector and producer increases, the density of the fingers reduces. Therefore, we performed another set of tests to verify this behavior. This series of tests are explained in the next section, since they lead to a new calculated ratio.

6.1.5. R_Z RATIO

The ratio of distance between injector and producer to the area perpendicular to flow, denoted as R_Z, can be used to indirectly define the effectiveness of the viscous displacement in terms of sweep efficiency.

In the designed series of tests we used to investigate the inlet and outlet distance effects, we kept the area perpendicular to the general flow direction from injector to producer constant, and also increased the distance (e.g., size of the network) between the injector and producer. In this fashion, we were able to accurately focus on the distance between the injectors and producer, as shown in Figure 6.16.

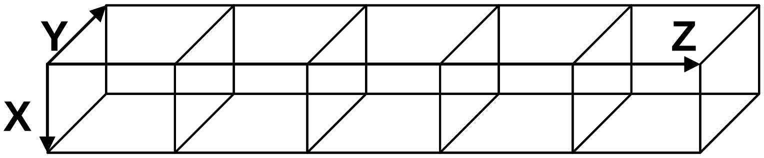

Figure 6.16 The schematic increase of distance between inlet and outlet

The test network had 40 × 40 nodes in the perpendicular flow area. We increased the number of nodes in Z direction (e.g., general flow direction) from 10 to 200. The resulting networks had from 16,000 to 320,000 nodes. We performed the viscous invasion modeling and calculated the finger density as before. Note that in these series of tests we calculated one other variable, the $\mathbf{R_z}$ ratio.

R_z ratio is defined as:

The number of nodes in general flow direction Nz, divided by the number of nodes in the area perpendicular to flow (e.g., Nx multiply by Ny).

$$R_z = \frac{Nz}{Nx * Ny} \qquad \text{Eq. 6.1}$$

In practice, to calculate the R_z ratio we divided the distance between the injector and producer (e.g., well spacing) by the area perpendicular to flow (e.g., sweep area), as follows:

$$R_z = \frac{\text{Well Spacing}}{\text{Area to Flow}} \qquad \text{Eq. 6.2}$$

For every single Z distance, we calculated the R_z ratio, which is the number of nodes in each realization divided by the 1,600 nodes in the area perpendicular to the general flow direction.

We also simulated at least 10 realizations for each of these tests. The conductivities were sampled using the uniform random distributions option in the simulator. We then counted the number of fingers that advanced more than 80% of the distance between the injector and producer in each simulation, and averaged all realizations in each test series.

To calculate the density, we simply divided the average number of fingers in each test by the 1,600 nodes.

The results for these series of tests are shown in Table 6.7 below. Table 6.7, illustrates number of nodes in Z (as distance), total nodes in the simulated network, calculated R_z ratio, calculated average number of fingers for each network size, and the density of fingers that resulted from each series of tests.

Z distance	Total nodes	Rz	No. of Fingers	Density
10	16,000	0.0063	30	0.01875
15	24,000	0.0094	19	0.01188
20	32,000	0.0125	13.5	0.00844
25	40,000	0.0156	10.4	0.00650
30	48,000	0.0188	9.1	0.00569
35	56,000	0.0219	7.8	0.00488
40	64,000	0.0250	6.8	0.00425
45	72,000	0.0281	6.1	0.00381
50	80,000	0.0313	5.7	0.00356
55	88,000	0.0344	4.6	0.00288
60	96,000	0.0375	4.6	0.00288
70	112,000	0.0438	3.8	0.00238
80	128,000	0.0500	3.5	0.00219
90	144,000	0.0563	2.6	0.00163
100	160,000	0.0625	2.4	0.00150
120	192,000	0.0750	2.2	0.00138
160	256,000	0.1000	2.1	0.00131
200	320,000	0.1250	1.9	0.00119

Table 6.7 Calculated R_z ratios

Figure 6.17, illustrates a plot of density of fingers versus the R_z ratio. As shown in this figure, the general trend is the same as before, which was decrease of density by increase of total number of nodes in the network. Figure 6.17 confirms the same decrease versus the increase of R_z ratio. But, since the R_z ratio is a measure of the network geometry (the area to flow versus the distance between the injector and producer), provides a better understanding of the behavior versus the shape of the model (e.g., reservoir).

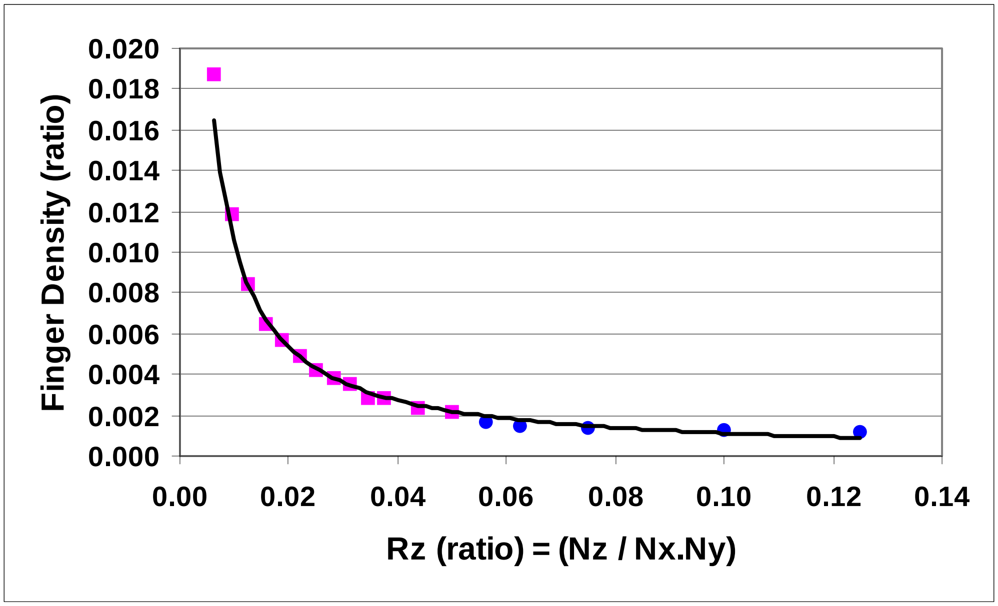

Figure 6.17 Finger density decline versus the R_z ratio

Figure 6.17, demonstrates that as the R_Z ratio increases, the number of fingers that can survive in the viscous dominant invasion displacement, decreases. Fitting a best curve to the data reflects a power behavior for the results, using the following equation:

$$\text{Density} = 0.0001\, R_z^{-1.0327}$$
$$R^2 = 0.9931$$

This results in the same behavior as found in previous tests.

If the number of fingers in a viscous displacement decreases, it is an indication that a fewer number of pores have been invaded. Consequently, less volume has been swept by the invading fluid and lower sweep efficiency is reached. As shown in Figure 6.18, as the R_z increases, then the density decreases. But, after a certain decrease the density remains constant and becomes asymptotic to a value of approximately 0.002. This density indicates that after a certain distance between the injector and producer, there will be only one dominant single channel in the network model of viscous dominant invasion displacement.

This value of finger density (approximately 0.002) corresponds to the R_z ratio of approximately 0.05 (figure 6.18).

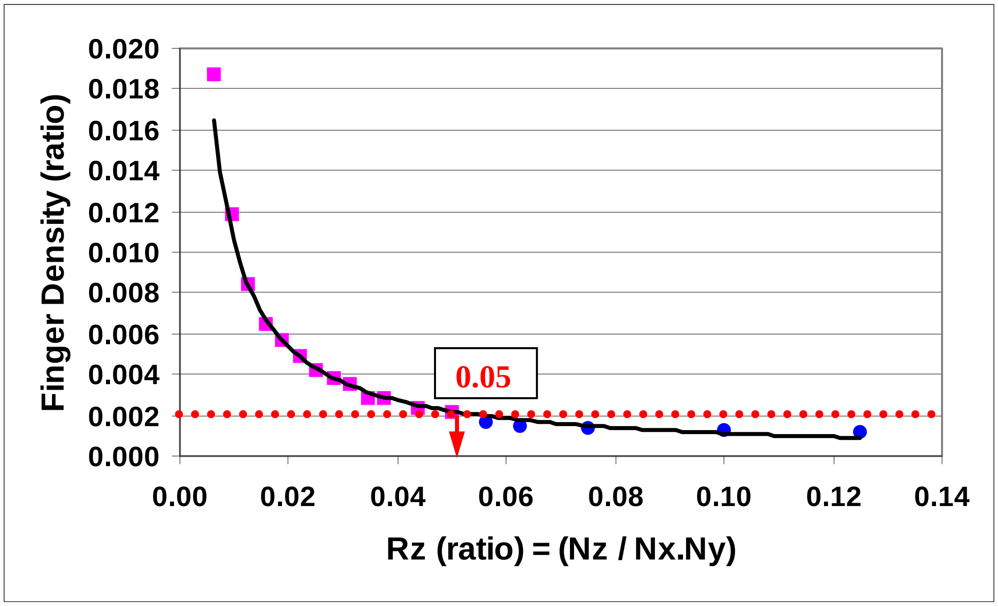

Figure 6.18 Critical value of finger density

As the distance between the injector and producer increases in a viscous dominant displacement, the R_z ratio reaches the critical value of 0.05. After this critical value there will be only one dominant single channel in the network, and the sweep efficiency will not increase. To gain higher sweep efficiency in the viscous dominant displacement, the distance between the injector (inlet) and the producer (outlet) should always remain less than the critical R_z ratio.

Radial flow also increases the average bond per nodes parameter by approximately 15% (Refer to Section 6.6.1). But, the effect of setting wells in a radial form causes the value of R_z to become larger, which has more negative effects on sweep efficiency. The radial flow effectiveness becomes more obvious in the case of steam-assisted gravity drainage (SAGD). In the case of SAGD, injector and producer wells are located parallel to each other and the flow is radial from injector to producer. The distance between the injector and producer in a SAGD system is very small (approximately 10 to 20 feet), in comparison to the swept length of the two parallel wells (hundreds or thousands of feet), which can result in a low R_z ratio.

To verify if the R_z can be a correct representative of the efficiency of a displacement, we can use the dimensions of a Steam Assisted Gravity Displacement (SAGD) example. If the distance between the injector and the producer wells are 20 ft and the length of the two parallel wells are 2,000 ft and the sweep an area of about 30 ft thickness, the R_z ratio can be calculated as follows:

$$R_z = \frac{20}{30 * 2000} = 0.0003 \ll 0.05$$

Since R_z is much less than the critical value, it is an efficient sweep. On the other hand, if vertical wells are used in this system to displace the oil, instead of the SAGD geometry configuration, the efficiency will not be achieved. Consider the wells are 2,000 ft apart, swept area of flow is 200 ft wide and the thickness is the same as before, 30 ft. The calculated R_z will be:

$$R_z = \frac{2000}{30*20} = 3.33 \gg 0.05$$

This R_z ratio is much larger than the critical value of 0.05, and therefore, the system is not efficient at all. Therefore, configuring the well placement in a reservoir to honor the R_z ratio to values less than the critical value, can make a system to be efficient or non efficient.

6.2. SPATIAL CORRELATION EFFECTS

We set up another series of tests to study the behavior of the viscous dominant displacement. These tests are to study the spatial correlation between the conductivities and the effects of spatial correlation.

To generate the spatially correlated hydraulic conductivities, we used a publicly available distribution generator that has been widely used by universities, research labs, and the industry. In general the software used is known as Geostatistical Software Library (G-SLIB), version 9.0.

G-SLIB name was originally used for a collection of geo-statistical programs developed at Stanford University, over the last 15 years. The original G-SLIB inspired the writing of the Geo-statistical Software Library by Clayton Deutsch and André Journel, 1992, 340 pp., during 1990 to 1992. The second edition was completed in 1997. Both editions were published by Oxford University Press. See www.dslib.com the official website of G-SLIB software.

There are many possibilities of spatial correlation in nature, but we only modeled the spatial correlations that were more likely to be a case in the production of oil and gas, as follows:

a. Spikes of high hydraulic conductivity in the direction of the potential gradient;
b. Disks with high hydraulic conductivity in the direction of flow;
c. High hydraulic conductivity disks perpendicular to flow; and
d. Spheres of high hydraulic conductivity.

6.2.1. SPIKES OF HIGH HYDRAULIC CONDUCTIVITY IN THE DIRECTION OF FLOW

In this case, the spatial correlation of hydraulic conductivities, visualizes spikes of high flow paths in the network. The correlation length is only in the direction of general flow or in other words, potential gradient. As a test example, we set the correlation length to be 2-2-10 in X, Y and Z directions, respectively. This meant the spikes of high hydraulic conductivity had a thickness of two in X and Y directions, and provided a ratio of five for the spatial correlations in Z over X, and in Z over Y, directions. Using a random distribution of throats radii, we generated a field of hydraulic conductivities, as shown in Figure 6.19. Also, Figure 6.20 illustrates a closer look into these spikes of high hydraulic conductivity paths. As expected, these spikes are in the Z direction and are shown here.

The modeled network had dimensions of 50 × 50 × 50 nodes, and was a three dimension cubic lattice with 125,000 nodes. The top and bottom nodes were connected to outlets and inlets, and the four sides were no flow boundaries. The general potential direction was from the bottom to the top of the cube.

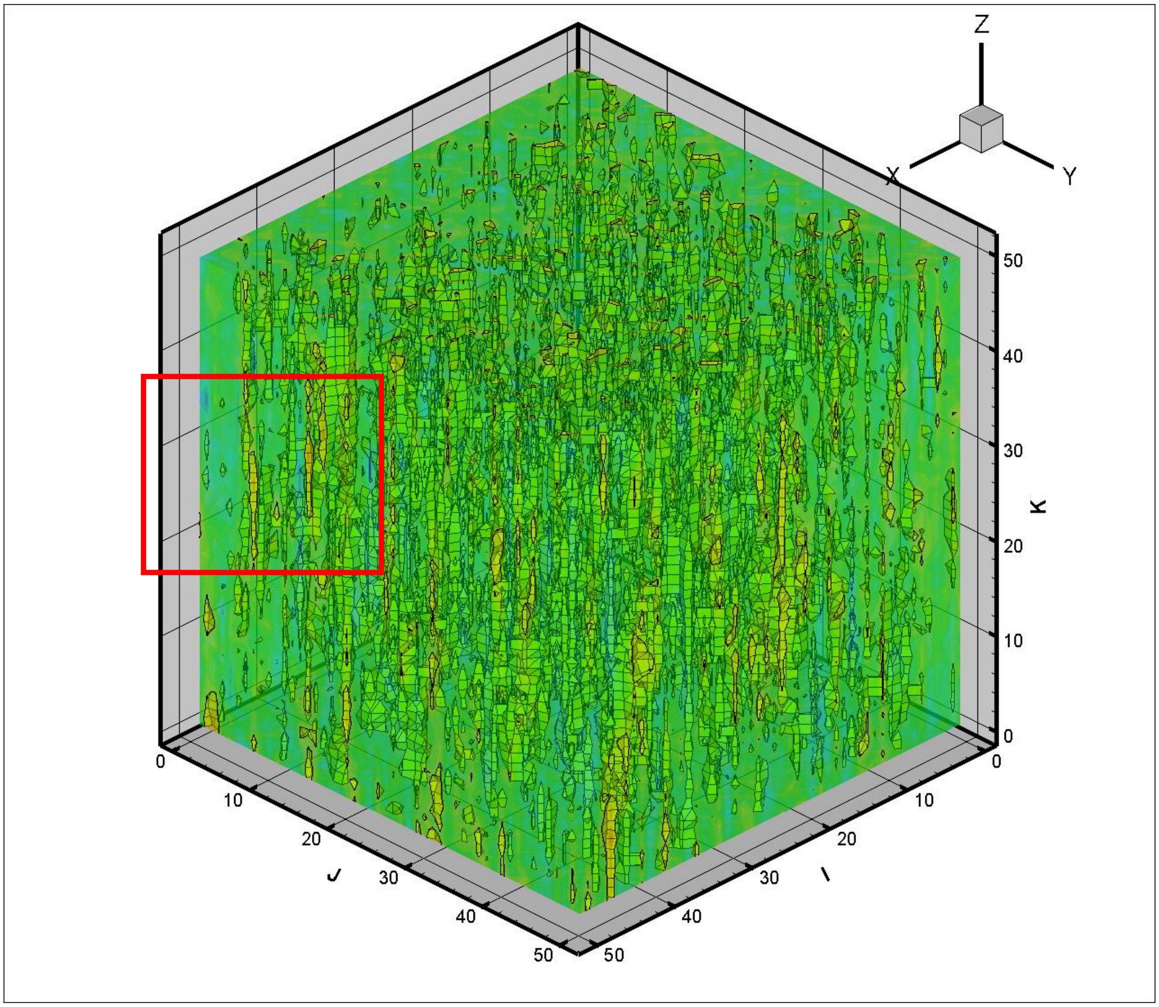

Figure 6.19 Spikes of high hydraulic conductivity

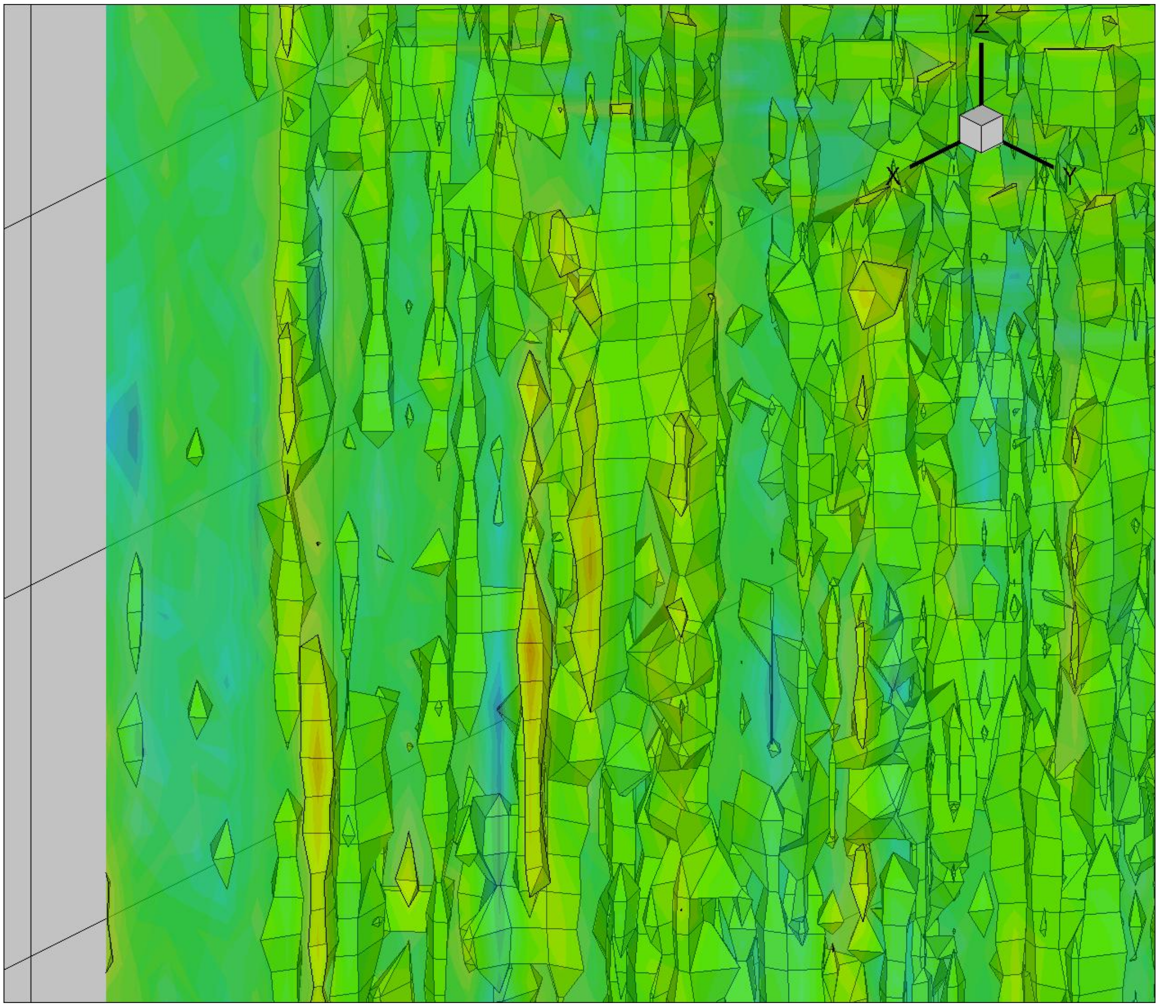

Figure 6.20 Closer look at the spikes of high hydraulic conductivity from the selected square in Figure 6.19

We simulated the viscous dominant invasion on the set system. The resulting invasion is shown in Figure 6.21.

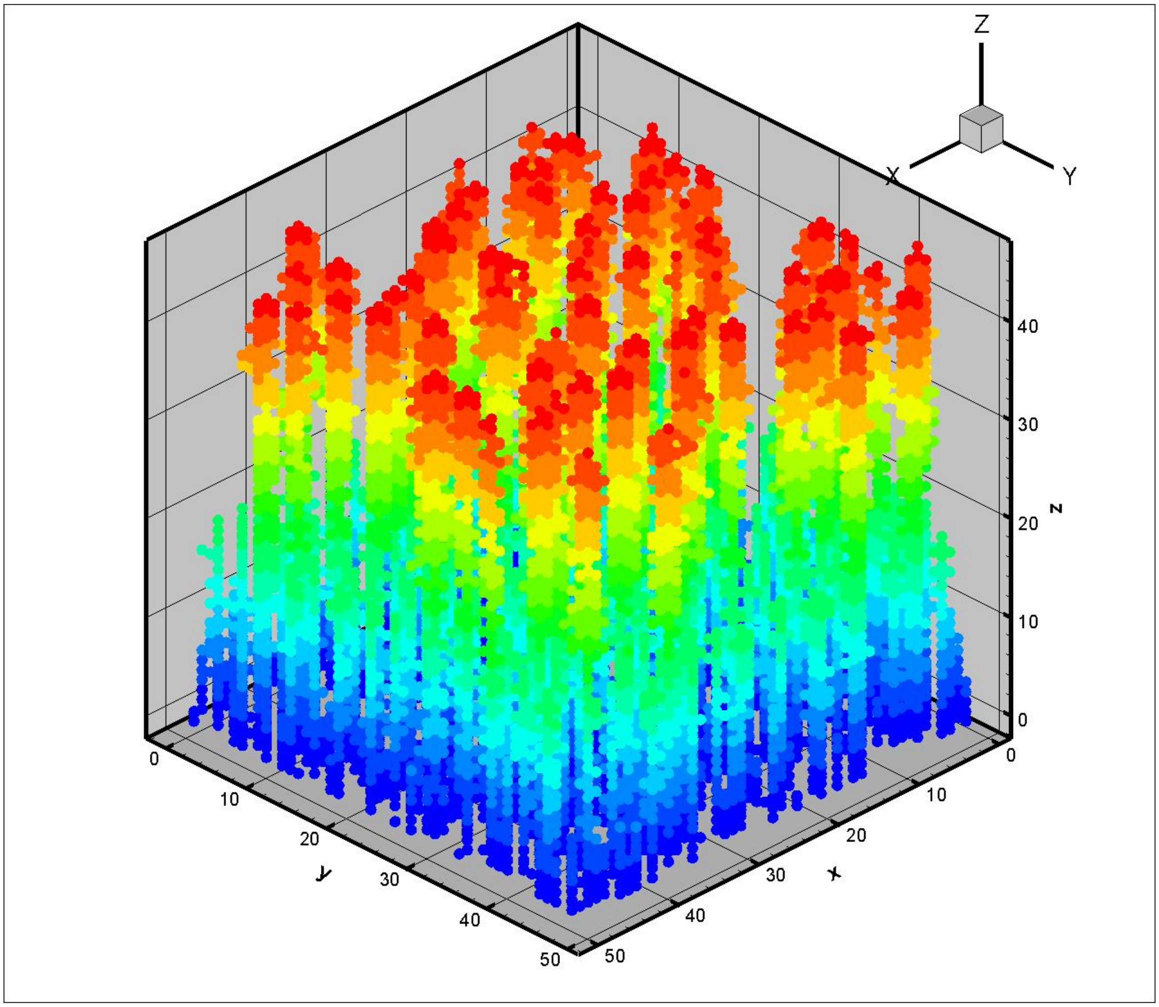

Figure 6.21 Results of viscous displacement on the network with spikes of high hydraulic conductivity

As shown, there is a very close match between the high flow paths and the invaded nodes in the direction of flow. Calculating the finger density in this invasion results in a very high value, as follows:

Number of channels = 71 channels

Number of nodes in the area perpendicular to flow = 2,500 nodes

$$\text{Finger density} = \frac{71}{2500} = 0.0284 \text{ and } R_z = \frac{1}{50} = 0.02$$

This density of fingers is a high density in respect to the calculated R_z for this network system.

6.2.2. HIGH HYDRAULIC CONDUCTIVITY DISKS IN THE DIRECTION OF FLOW

This type of spatial correlation corresponds to the cases of high conductivity disks in the reservoir when the flow between the injector and producer is in the direction of the layering. In this case, the disks simulate higher permeable sand disks in lower permeable matrix.

We used the G-SLIB to reproduce this simulation. We set the parameters of spatial correlation for the hydraulic conductivities to be N units of distance in Y and Z directions, but only one unit of distance in X direction. We set the general flow between the injector and producer to be in Z direction. Therefore, we received disks that were statistically N units of distance in diameter in Y and Z, but only one unit of distance in diameter in X direction.

The network was 50 × 50 × 50 nodes in all 3 dimensions. We chose N to be 10 and 15, respectively, for different realizations to gain possible individual disks of high hydraulic conductivity and low hydraulic conductivities in the lattice. In the three dimensional cubic lattice, the bottom and top nodes were connected to inlets and outlets, respectively, and the general potential for flow in the Z direction was from low to high numbers in Z. All four sides were connected to no flow boundaries.

We chose not to use the 25 or 50 nodes correlation length, because we didn't want to create a high flow path between the injectors and producers.

Figures 6.22 and 6.23 demonstrate a three-dimensional view of a 1-10-10 spatial correlation of hydraulic conductivities. As shown, there are many clusters of higher hydraulic conductivity in the network, and they generally look like disks. The side view of the same frame illustrates that these disks are generally very thin, with almost one node thickness.

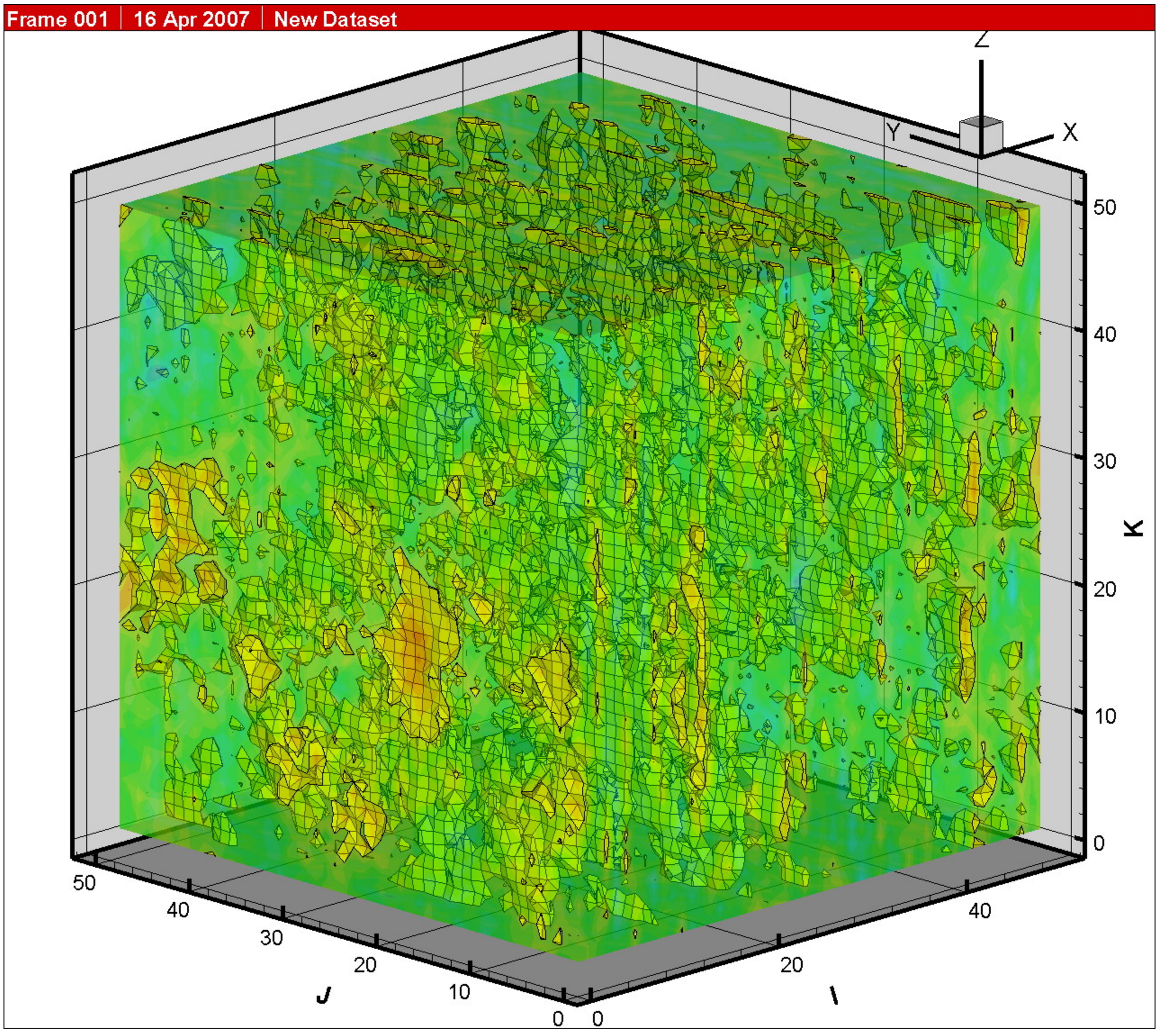

Figure 6.22 Three dimensional 1-10-10 spatial correlation

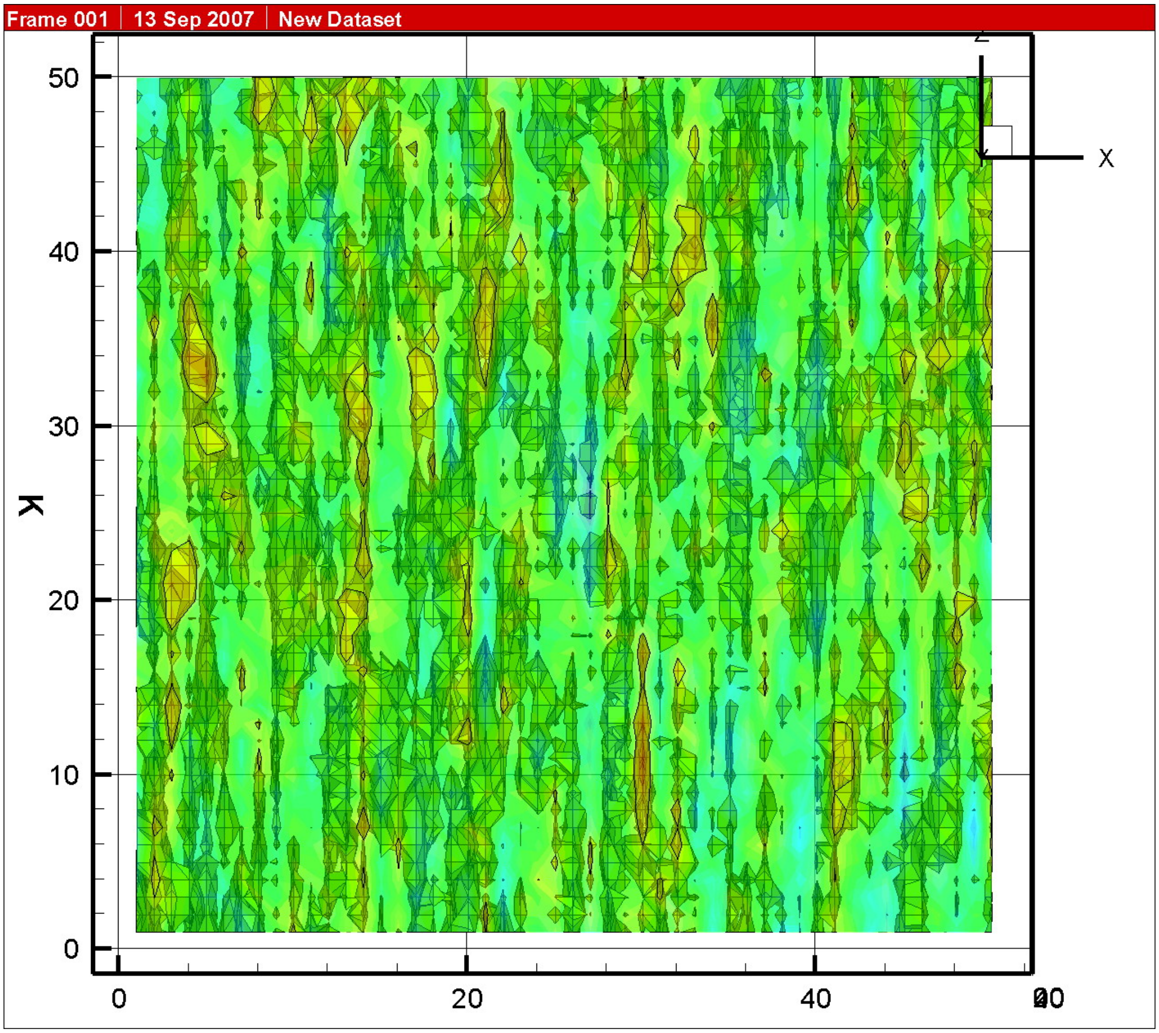

Figure 6.23 Three dimensional 1-10-10 spatial correlations, side view of Figure 6.22

Figures 6.24 and 6.25 also demonstrate the same production of hydraulic conductivities, but with the spatial correlation of 1-15-15 in X, Y and Z directions.

The difference between the spatial correlation of 1-10-10 and 1-15-15 is that in the latter we have wider disks, but the thicknesses of both realizations are the same.

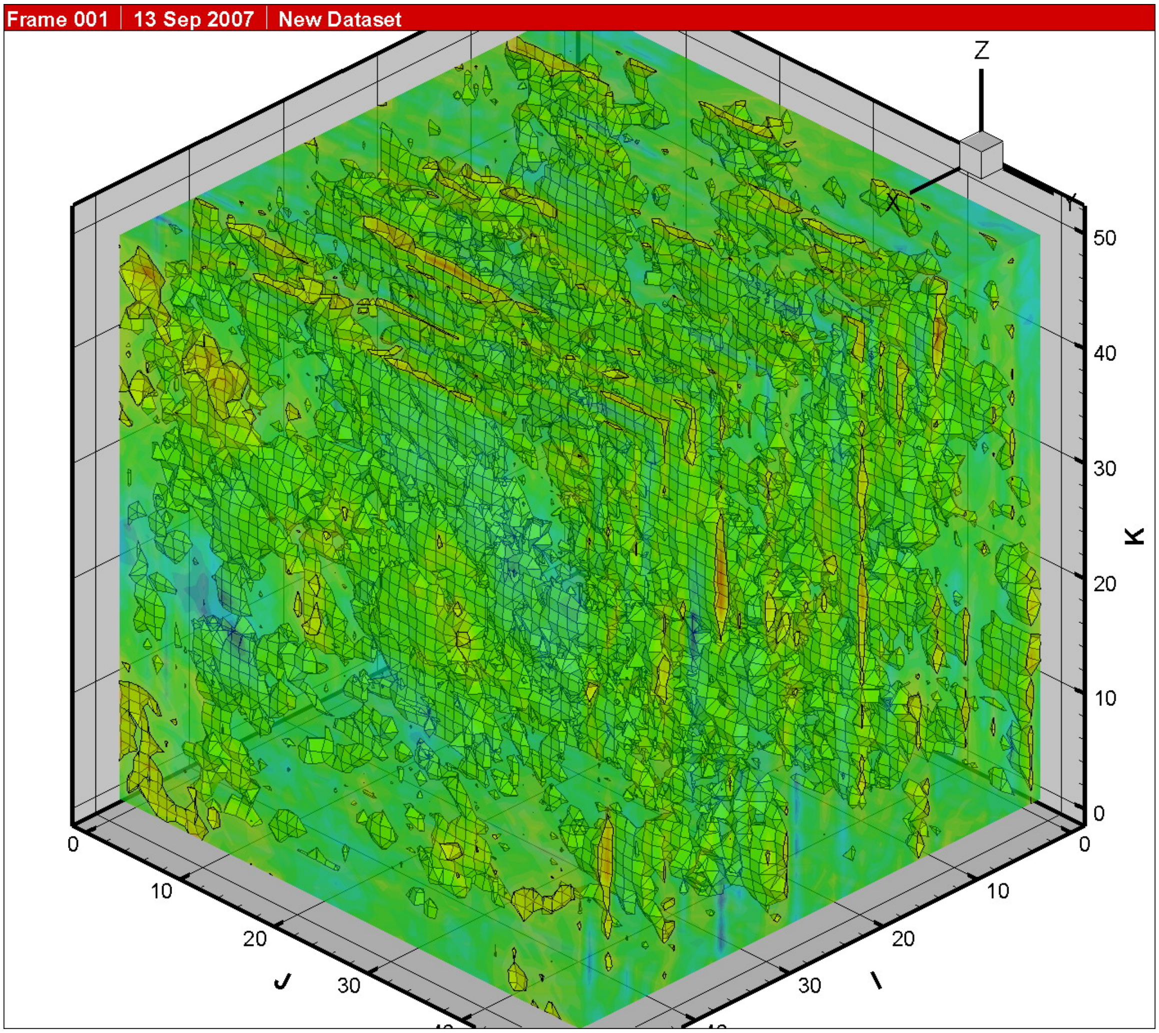

Figure 6.24 Three-dimensional 1-15-15 spatial correlation

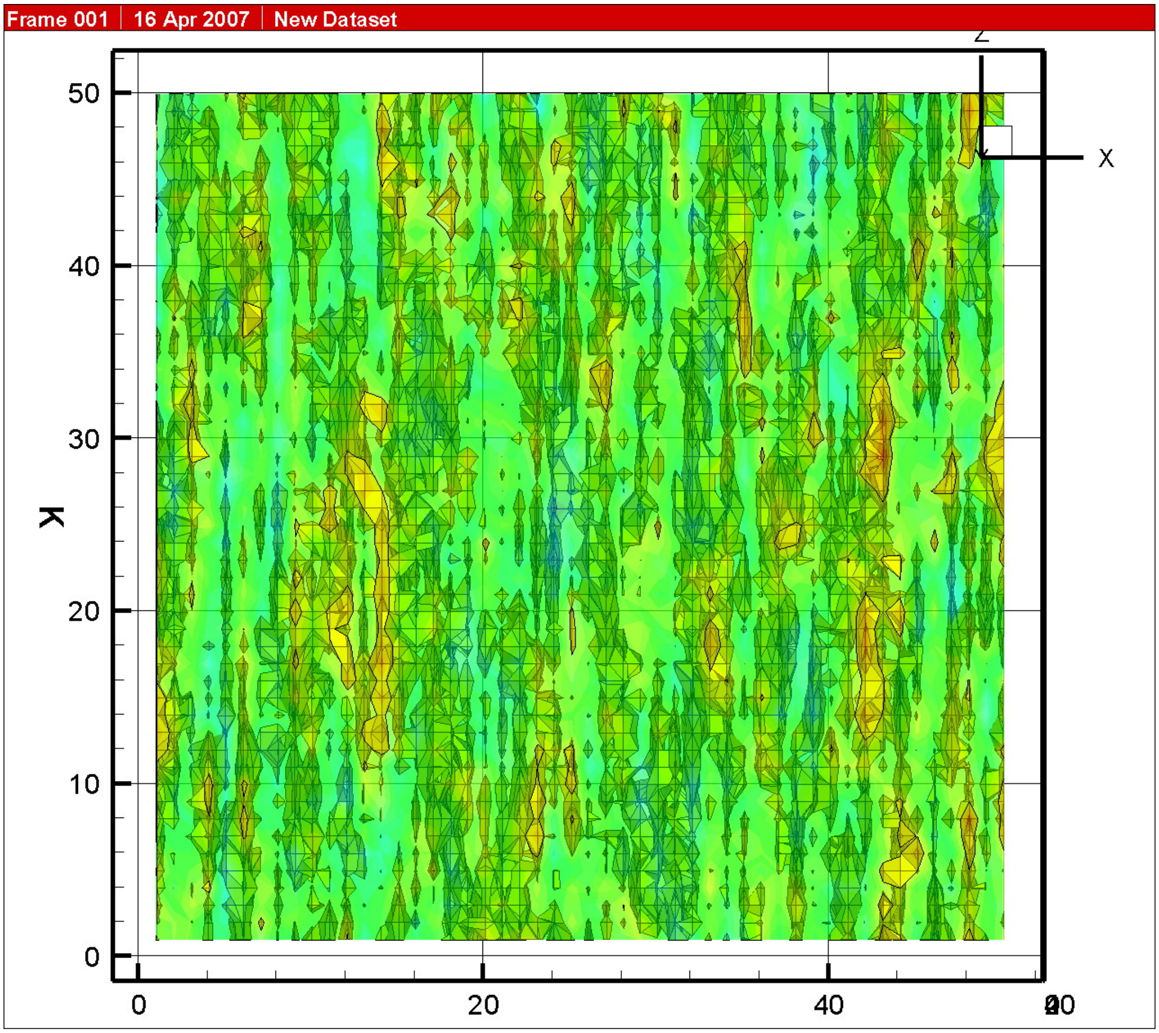

Figure 6.25 Three-dimensional 1-15-15 spatial correlations, side view of Figure 6.24

Viscous invasion was simulated on several realizations of these spatial correlation structures. The modeled networks used were 50 × 50 × 50 cubic lattices and had a total of 125,000 nodes. The inlets and outlets were at the bottom and top of the cube, respectively. The general flow was in Z direction. All of the hydraulic conductivities were read directly from the generated file by G-SLIB, and were assigned to the corresponding bond location in the network.

Figure 6.26 reflects the resulting viscous invasion modeling for the case using the 1-10-10 spatial correlation lengths. As expected, the flow followed the high hydraulic conductivity passes and the disks, filling those in its path.

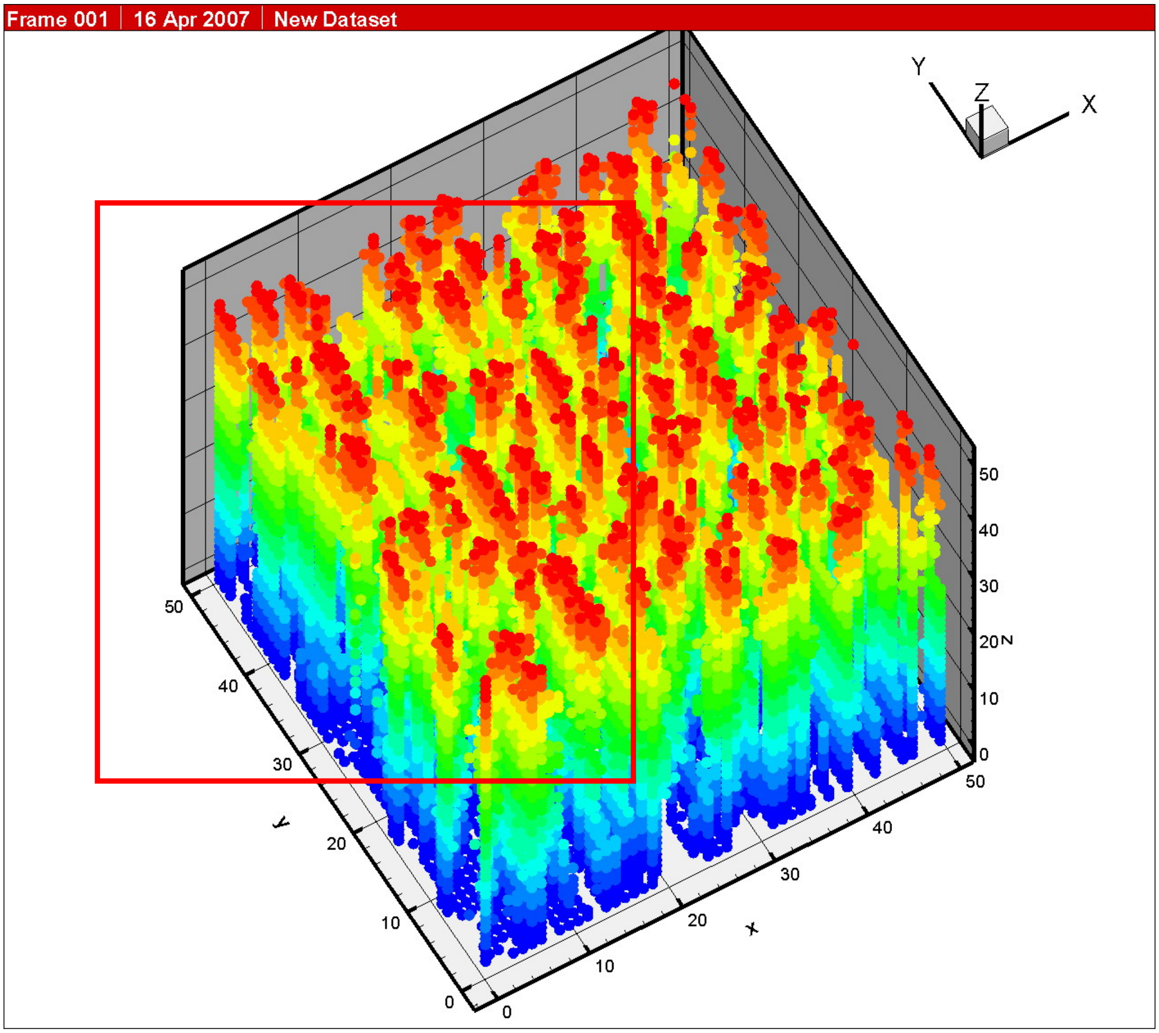

Figure 6.26 Result of viscous invasion on spatially correlated hydraulic conductivities with a 1-10-10 correlation length

A closer examination of these invaded pores reflects that the invasion contained one pore thickness and filled the high hydraulic conductivity disks (Figure 6.27).

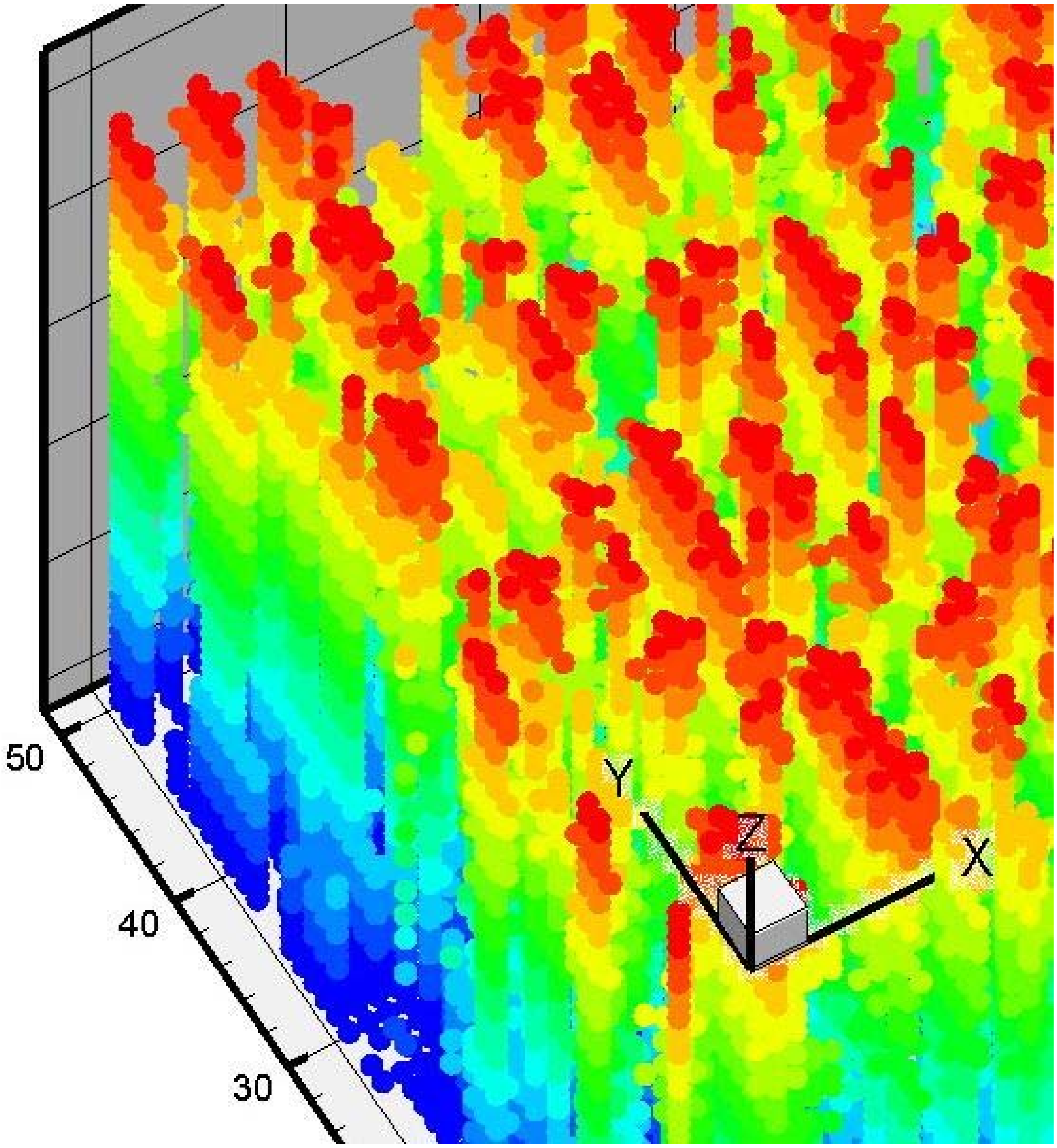

Figure 6.27 A more detailed view of the selected square in Figure 6.26

The same invasion occurred to the disks in the second case using 1-15-15 spatial correlation length for hydraulic conductivities. Again, like the previous case, high hydraulic conductivity disks were filled in the viscous displacement (Figure 6.28).

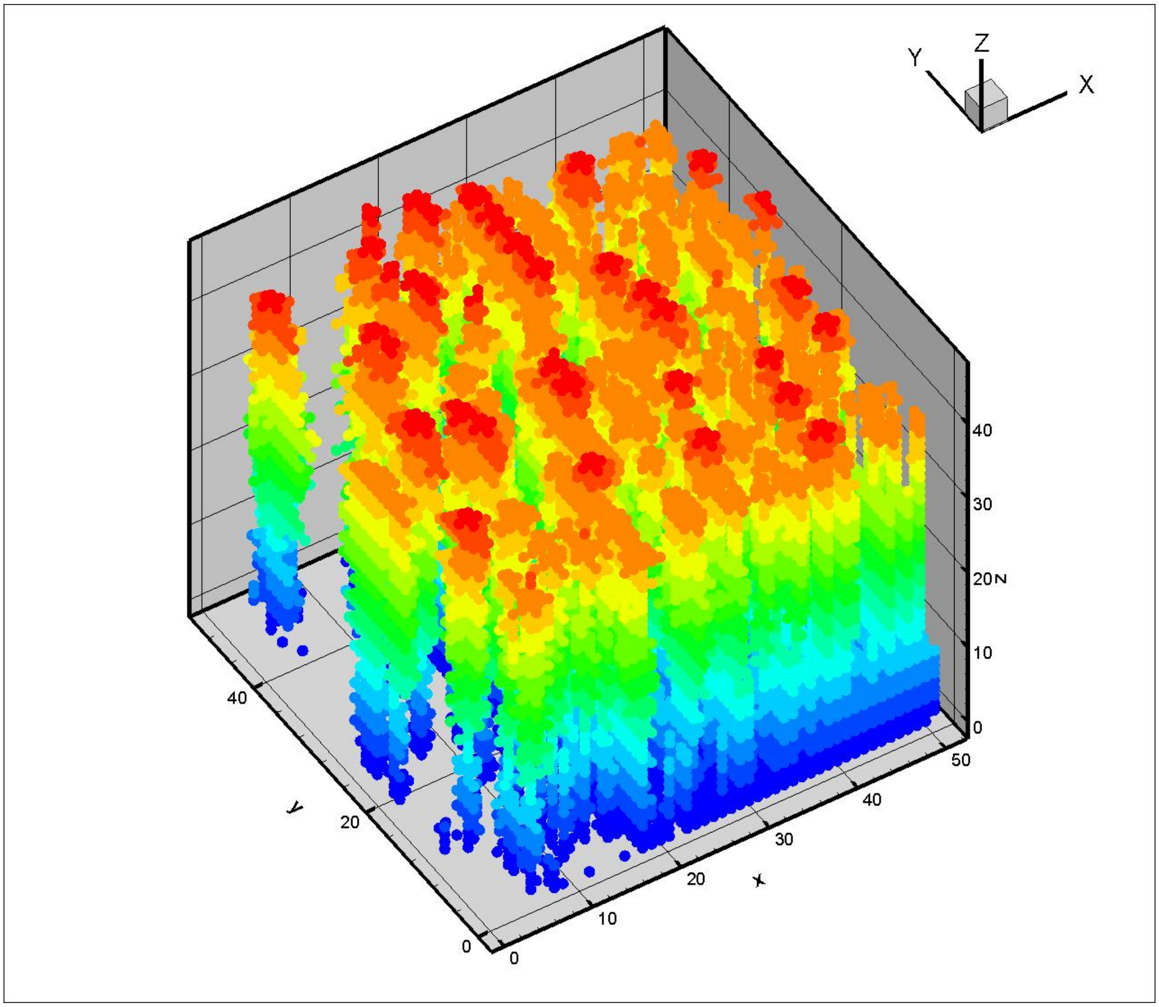

Figure 6.28 Viscous invasion on a 1-10-10 spatially correlated hydraulic conductivities

The viscous invasion still reflects its characteristic behavior of self-contracting. The calculated average bond per node remains approximately two, as previously examined.

6.2.3. HIGH HYDRAULIC CONDUCTIVITY DISKS PERPENDICULAR TO FLOW

The second sets of spatial correlation tests were high hydraulic conductivity disks or layers perpendicular to the general direction of flow. These planes were stretched in the XY plane and had a thickness of one pore or node, as in the previous case.

In these cases, we modeled additional selections, from an individual disk up to a high hydraulic conductivity layer that covered the whole perpendicular path to the general flow direction.

We again used a three dimensional cubic lattice model, where the bottom and top nodes were connected to inlets and outlets, respectively, and the general potential for flow was in the Z direction from low to high numbers in Z. All four sides were connected to no-flow boundaries.

We modeled the spatial correlations for the hydraulic conductivities with the correlation lengths of 10-10-1, 15-15-1, 25-25-1, and 50-50-1 in the format of X-Y-Z. Since the modeled networks were 50 × 50 × 50 nodes in X, Y and Z directions, the case of 10-10-1 spatial correlation reproduced the high hydraulic conductivity disks; the last case of 50-50-1 spatial correlation reproduced the case of high hydraulic conductivity layers in the network model. Cases using 15 and 25 correlation lengths simply resulted in wider disks, but did not cover the whole flow path with high hydraulic conductivity.

Figures 6.29 to 6.32 illustrate samples of high hydraulic conductivity disks or layers for each of the realizations. As shown in these figures, longer correlation lengths cause the disks grow wider until they cover the whole layer or flow path.

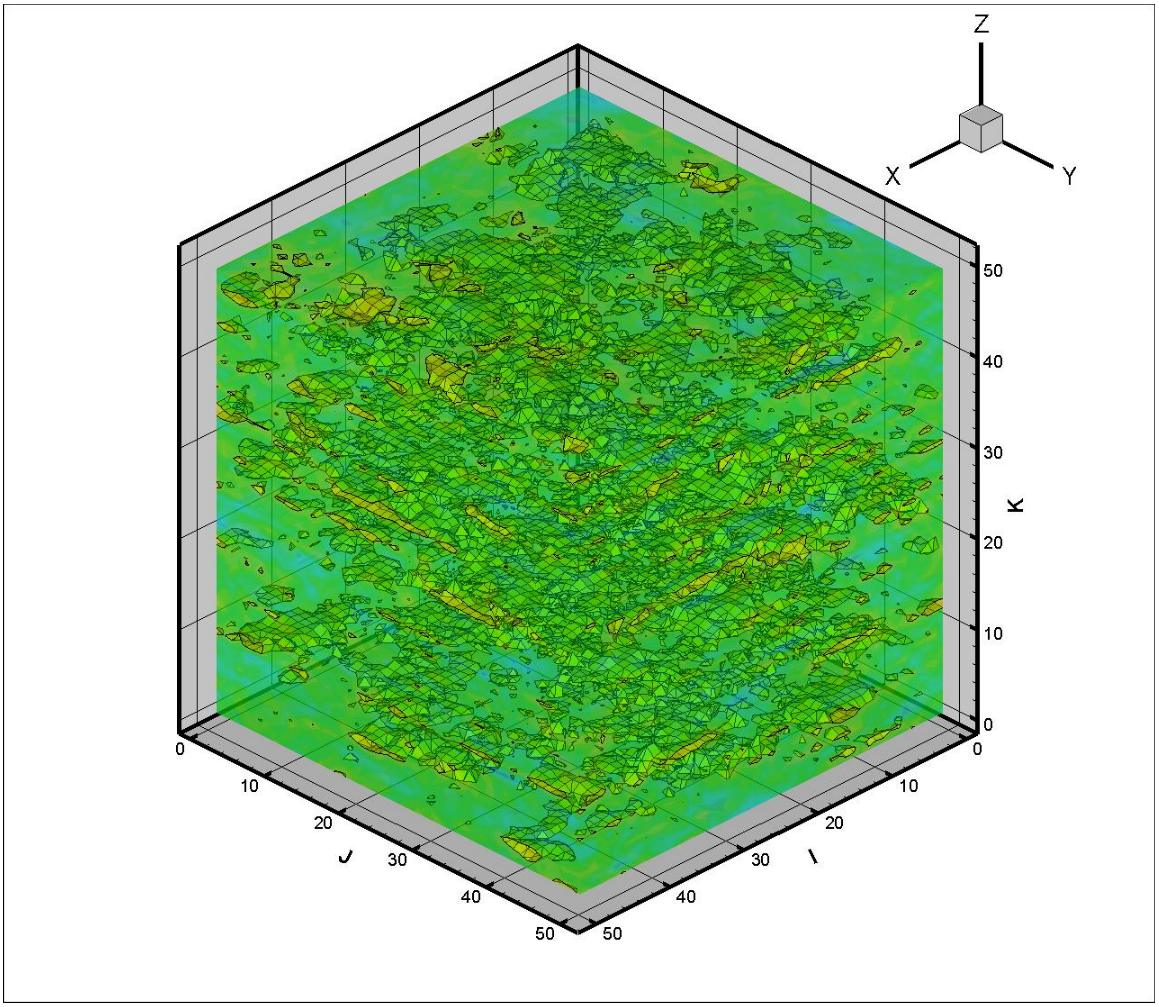

Figure 6.29 High hydraulic conductivity distribution with 10-10-1 spatial correlation

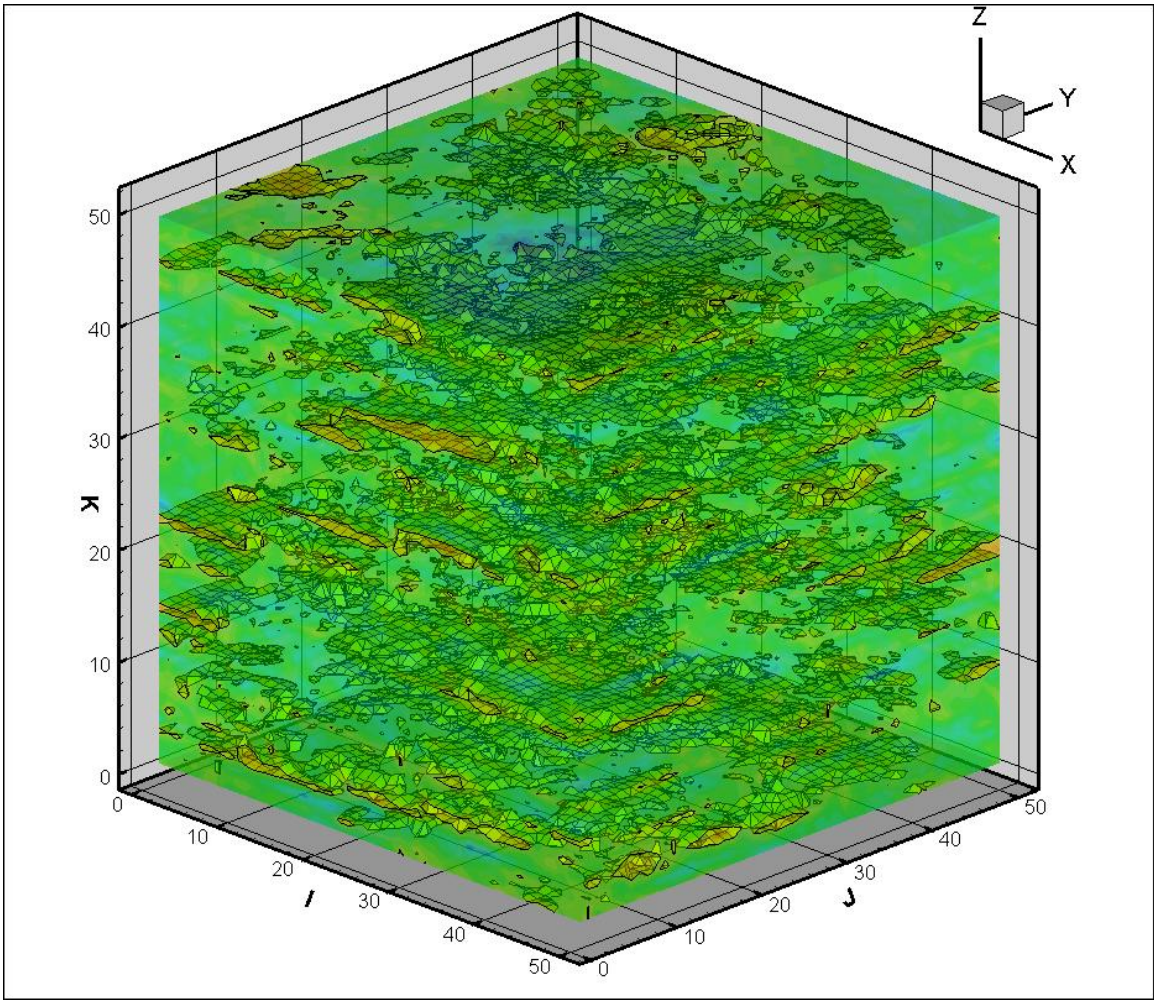

Figure 6.30 High hydraulic conductivity distribution with 15-15-1 spatial correlation

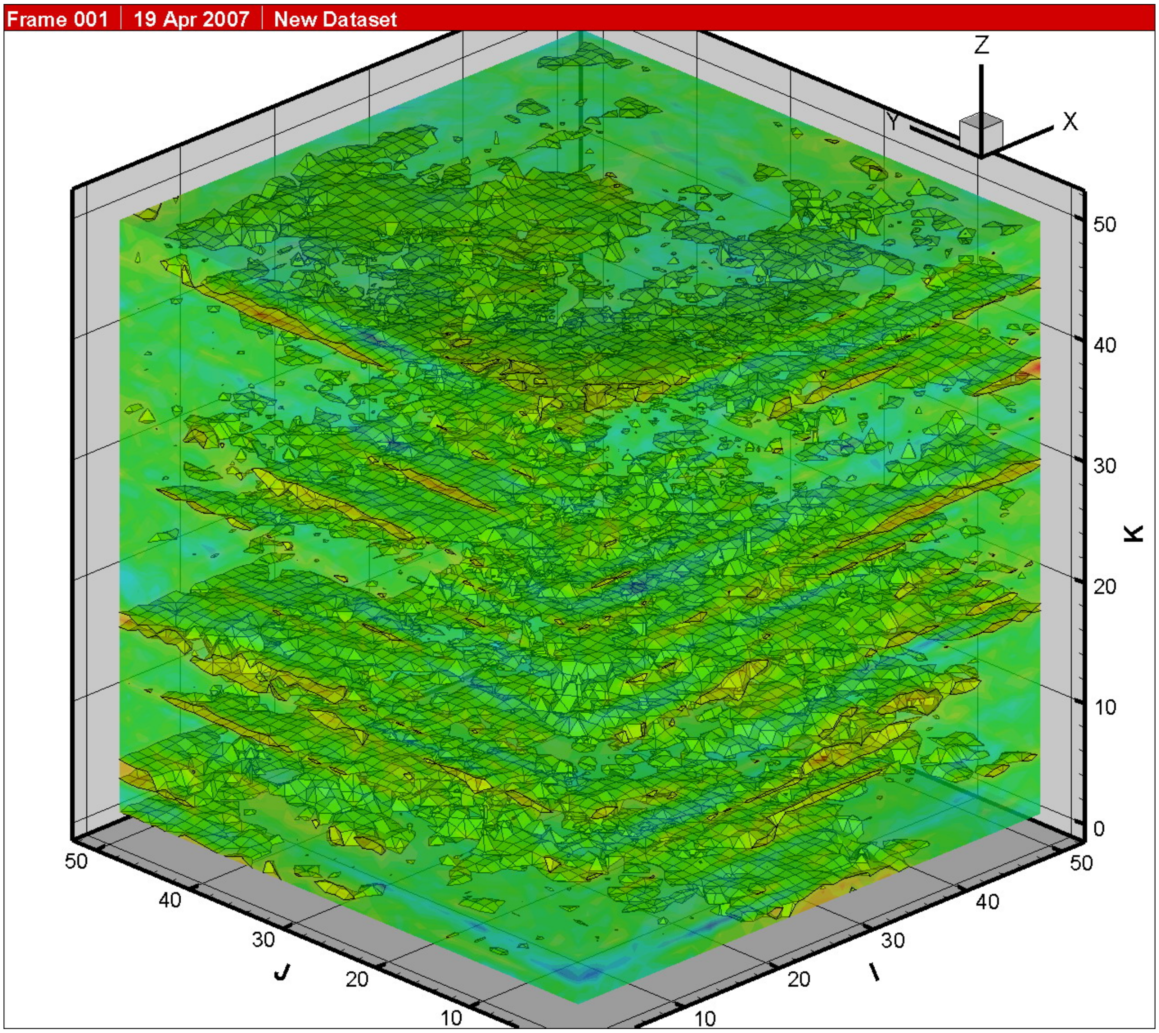

Figure 6.31 High hydraulic conductivity distribution with 25-25-1 spatial correlation

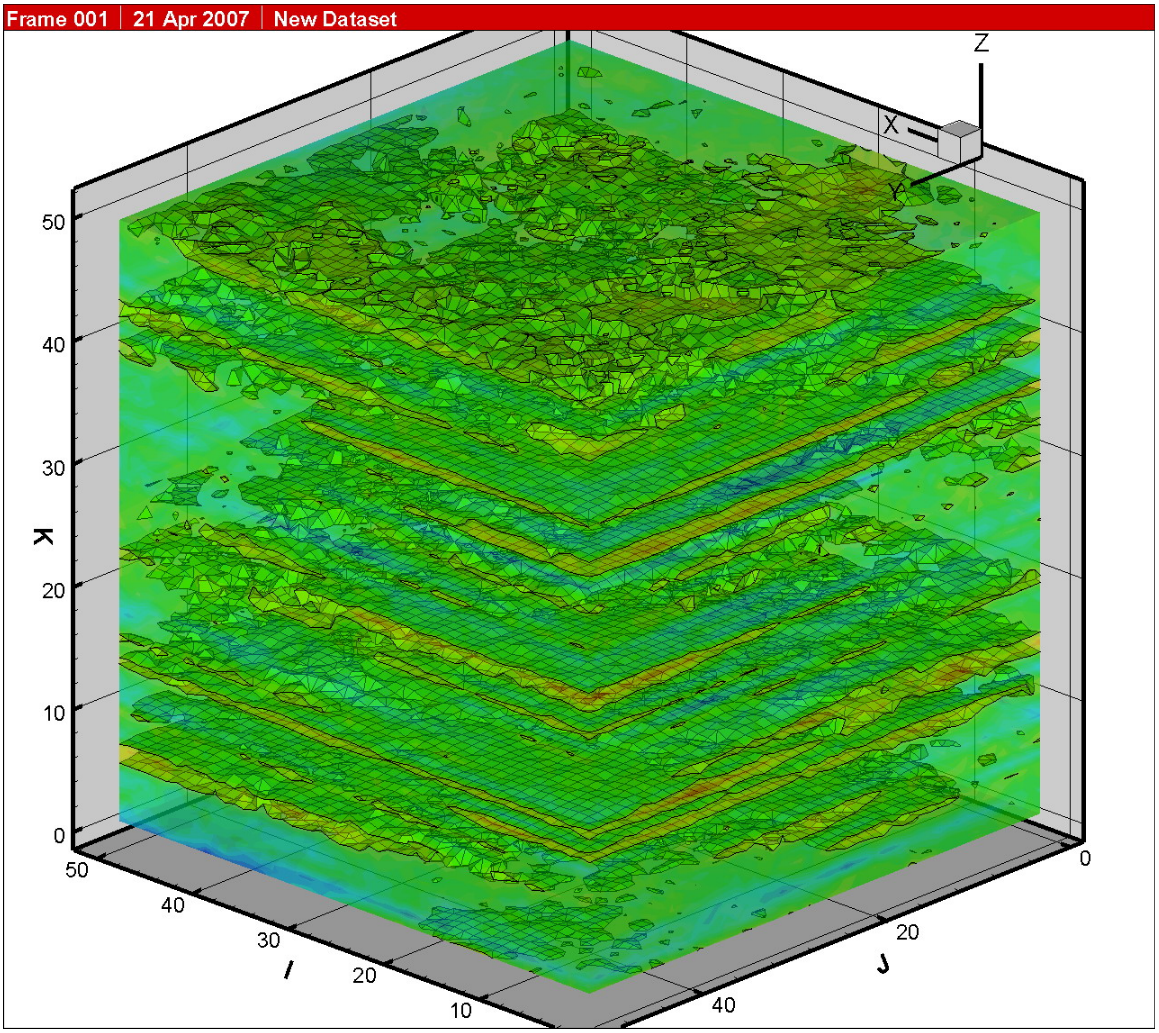

Figure 6.32 High hydraulic conductivity distribution with 50-50-1 spatial correlation

The viscous invasion was simulated for these structured hydraulic conductivities with spatial correlations. The resulting viscous invasions are shown in figure 6.33 for the case of 10-10-1 spatial correlation of hydraulic conductivity. In this figure, even though the viscous invasion attempted to reach the producers, it also clearly spread into the high hydraulic conductivity disks at every possible stage of invasion. Most of the channels in Figure 6.33 look like disks stacked on top of each other.

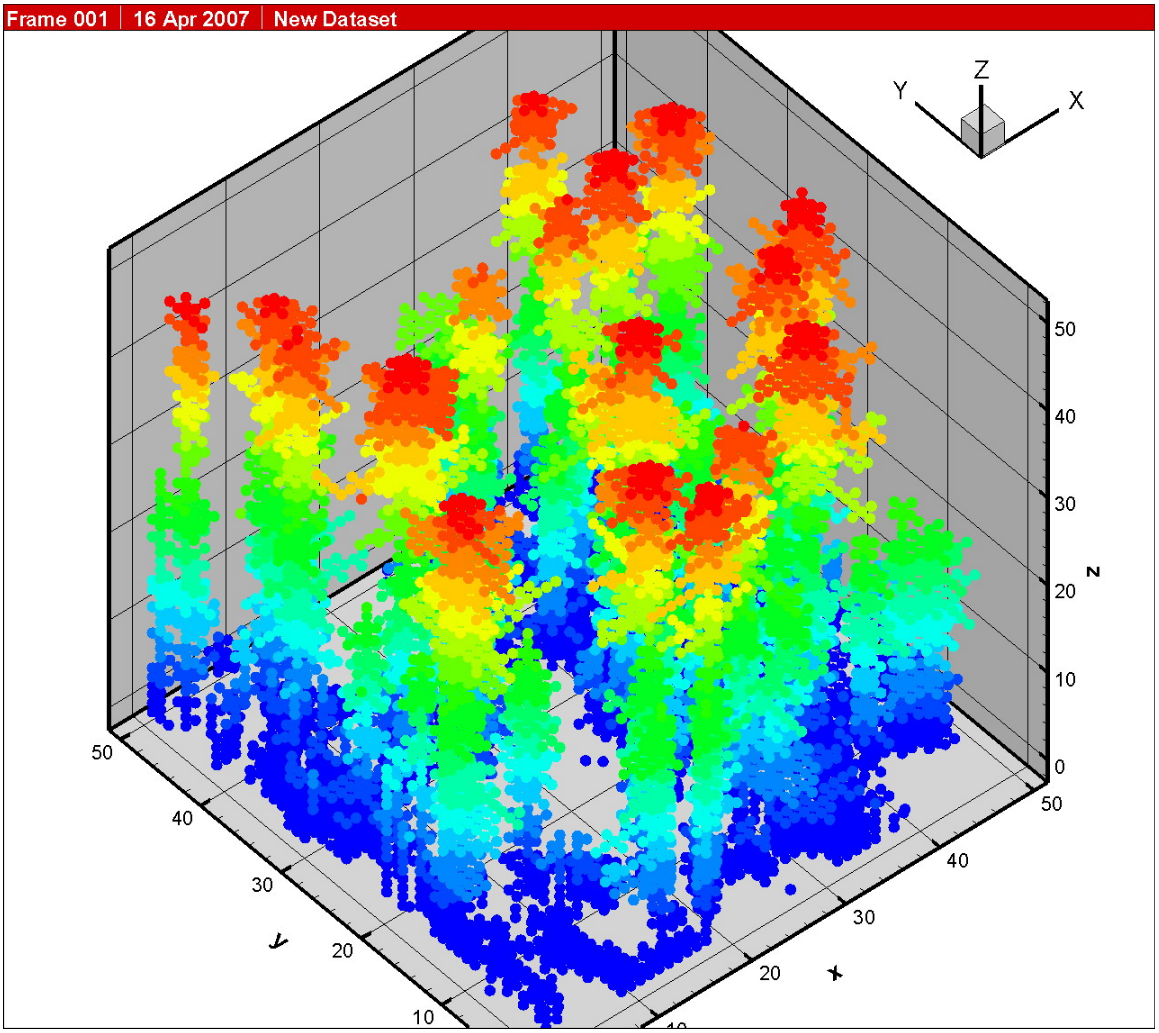

Figure 6.33 Viscous invasion for 10-10-1 spatially correlated hydraulic conductivities

Since the case of 15-15-1 spatially correlated hydraulic conductivities had a similar outcome as the case of 10-10-1 spatial correlation, we show the next test series, which was 25-25-1 pores correlation length. Figure 6.34, illustrates the viscous displacement of this test. The channels were one pore thick in some cases, but at every level we saw that the viscous invasion spread into the larger disks. After invading the disks, the flow continued to a higher level, and when possible, spread into the network. The shape of the invasion was similar to that of a Christmas tree, with a thin central core and wide spreads. We calculated an average bond per node of 2.13. The average bond per nodes value grew more than the value of two because of the spreads, but was still very close to the value of two.

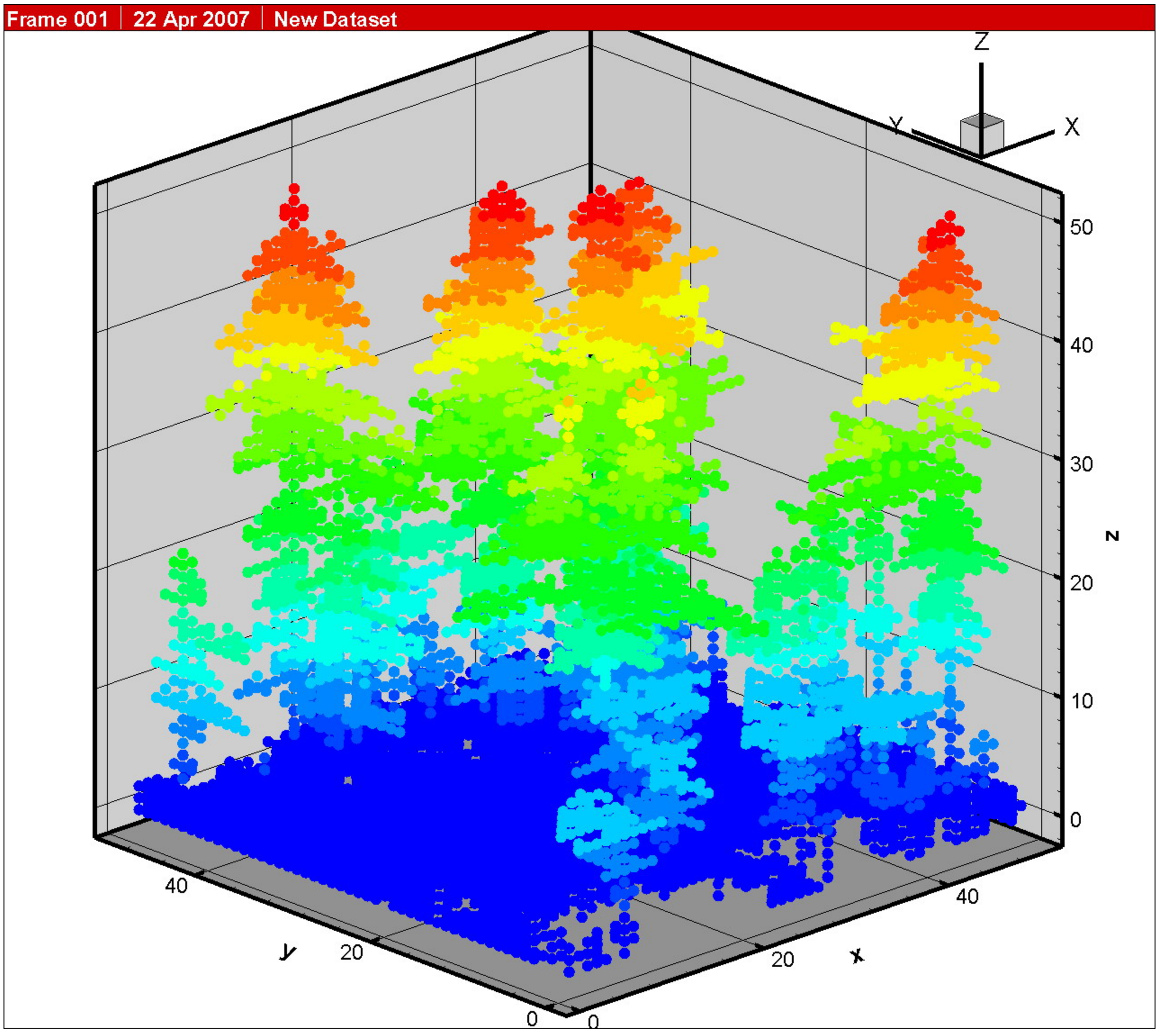

Figure 6.34 Viscous invasion for 25-25-1 spatially correlated hydraulic conductivities

The last simulated case in this group was layers of high hydraulic conductivity. The high length of correlation put a high hydraulic conductivity layer in front of the flow path at several stages in the network. As shown in Figure 6.35, the number of invaded nodes in the viscous displacement dropped in comparison to the previous cases, but the spreads were somewhat larger in size. The spread of fluid into the high hydraulic conductivity layers prevented the underlying pores from getting enough draw potential from producers to get invaded; thus, lots of pore was left behind without being affected. This large number of untouched pores was not suitable in terms of sweep efficiency.

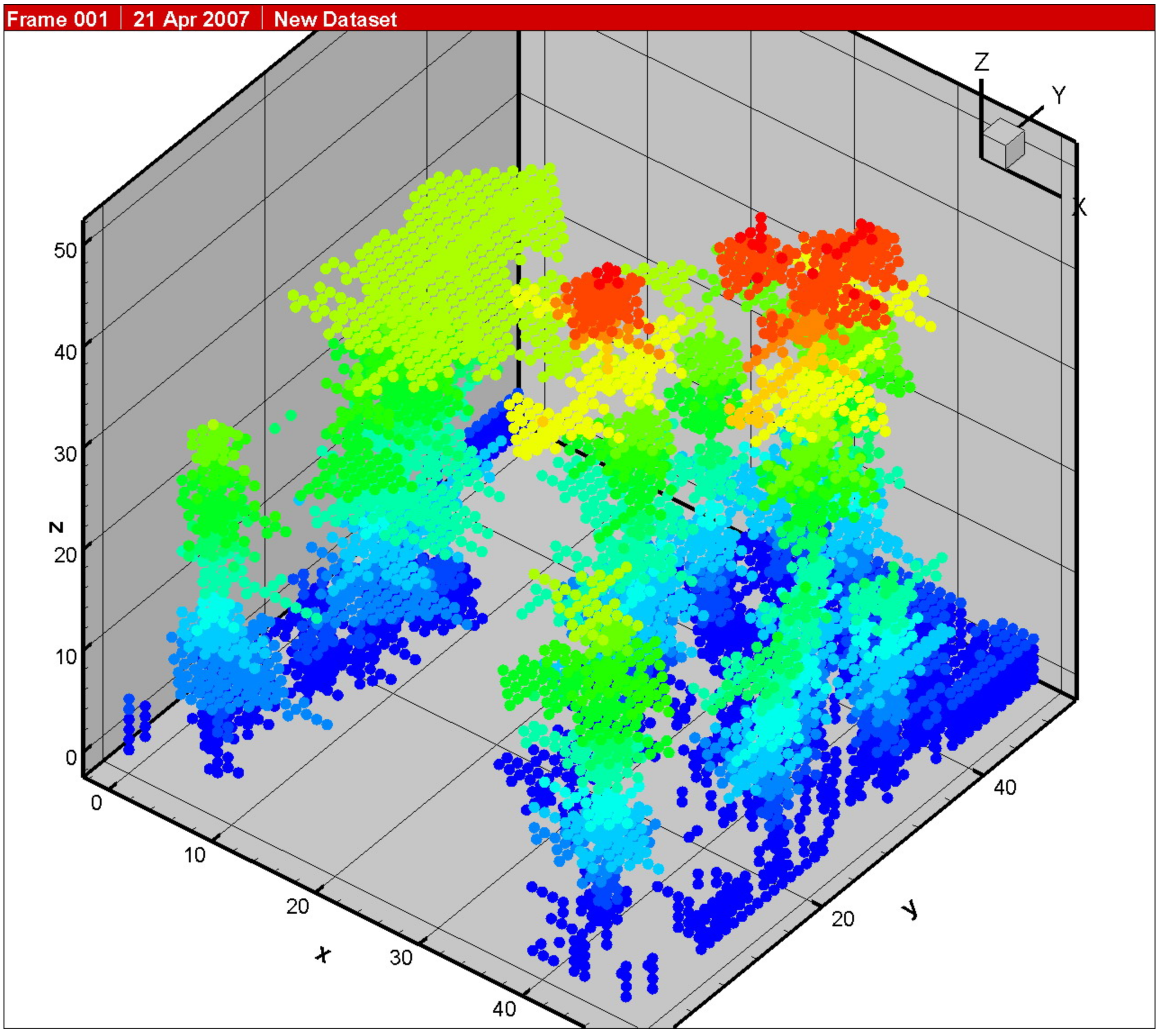

Figure 6.35 Viscous invasion for 50-50-1 spatially correlated hydraulic conductivities

Movement from one layer to another top layer was still controlled in the linear flow behavior, and the average bond per node was less than two for the advancement from one high hydraulic conductivity layer to another.

Table 6.8 reflects a comparison between the total numbers of invaded nodes in two cases of disks with high hydraulic conductivity in the direction of and perpendicular to the direction of flow. Note that there was a drop in the total number of invaded pores.

Disks' direction	Spatial correlation	Invaded pores	% of total nodes
Parallel to flow	1-10-10	38,981	31.18%
Perpendicular to flow	10-10-1	8,702	6.96%
Parallel to flow	1-15-15	45,056	36.04%
Perpendicular to flow	15-15-1	9,886	7.91%

Table 6.8 Comparison of the total number of invaded nodes in cases where disks were in the direction of or perpendicular to the direction of flow.

So, if the reservoir has layers of high hydraulic conductivity and low hydraulic conductivities at the same time, it is important to keep the general direction of flow (moving potential) in the direction of the layers or disk to increase the total number of invaded pores, and ultimately, increase the sweep efficiency. To do this, we must make the correct alignment by placing the injector and producing wells in the correct locations and directions. Otherwise, keeping the general direction of flow, perpendicular to the spread of layers in a viscous dominant displacement will decrease the sweep efficiency.

6.2.4. SPHERES OF HIGH HYDRAULIC CONDUCTIVITY

In the last set of spatial correlations, we made the high hydraulic conductivity bonds in the network to form clusters of high hydraulic conductivities. These clusters were set to have a similar correlation length in all directions in three dimensions. Therefore, while we expected to see sphere shape clusters, because of the uniform distribution of conductivity that had to be honored in a Gaussian distribution, they were not exactly spheres. They were clusters spreading into the three dimensional network models, and even though they were not exactly mathematical spheres, they were generated based on an equal correlation length in all directions. The correlation length used for these clusters was a 10-10-10 in X, Y and Z directions.

The network was a three dimensional cubic lattice, similar to that used before, and it had a total of 125,000 nodes in the 50 × 50 × 50 lattice. All four sides were no-flow boundaries, and inlets and outlets were connected to the top and bottom layer of the nodes in the network. The same viscous displacement modeling was used to simulate the effects of high hydraulic conductivity spheres type clusters in the network.

Figures 6.36 to 6.38 reflect some of these high hydraulic conductivity clusters in the network model. We generated many realizations for our study purposes, but only show some of these realizations here. Generally, it appeared that clusters spread inside the network rather than spheres. Figures 6.36 through 6.38 illustrate three different realizations of such spatial correlations with equal length in all directions.

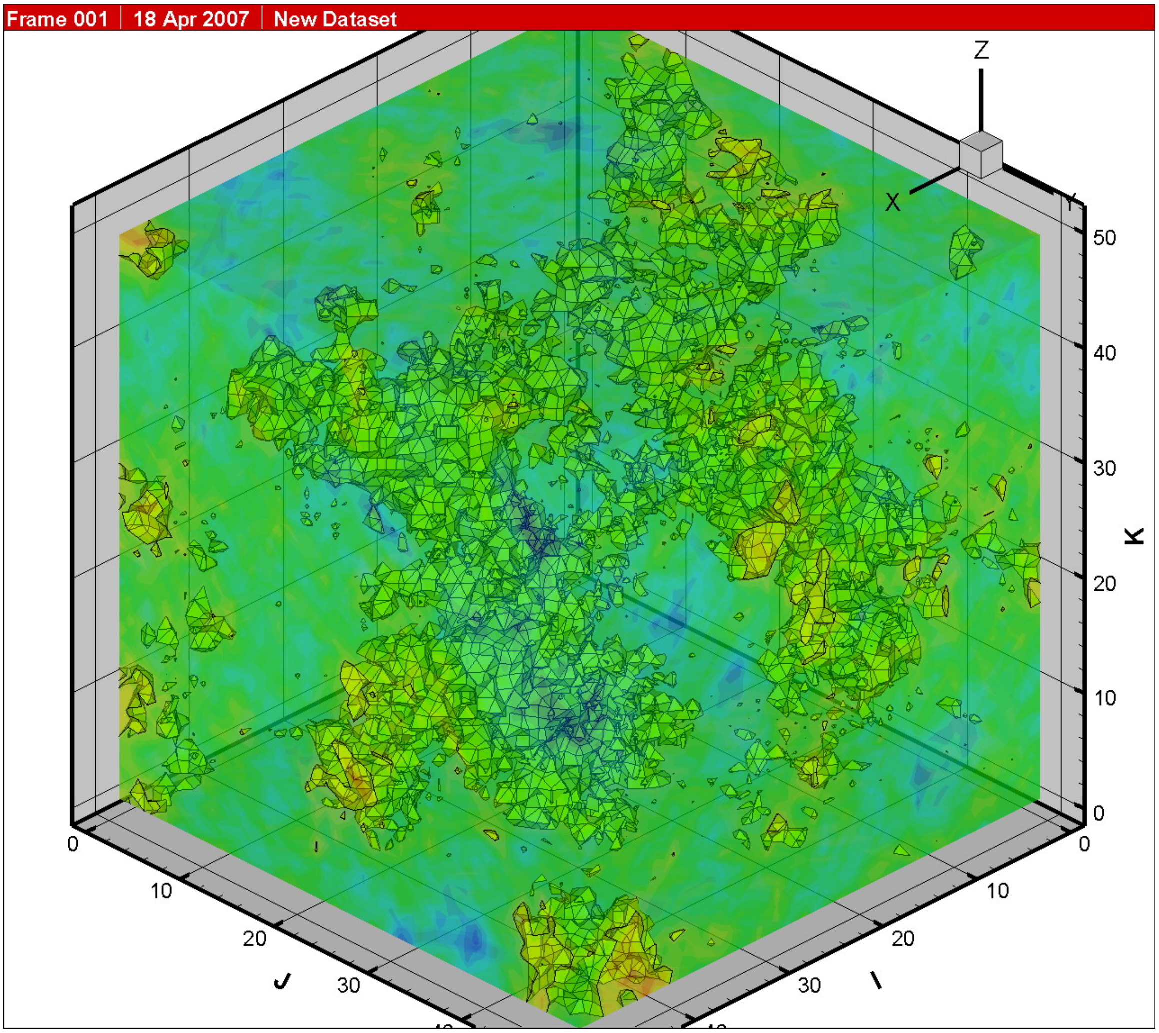

Figure 6.36 Clusters of high hydraulic conductivity, first realization

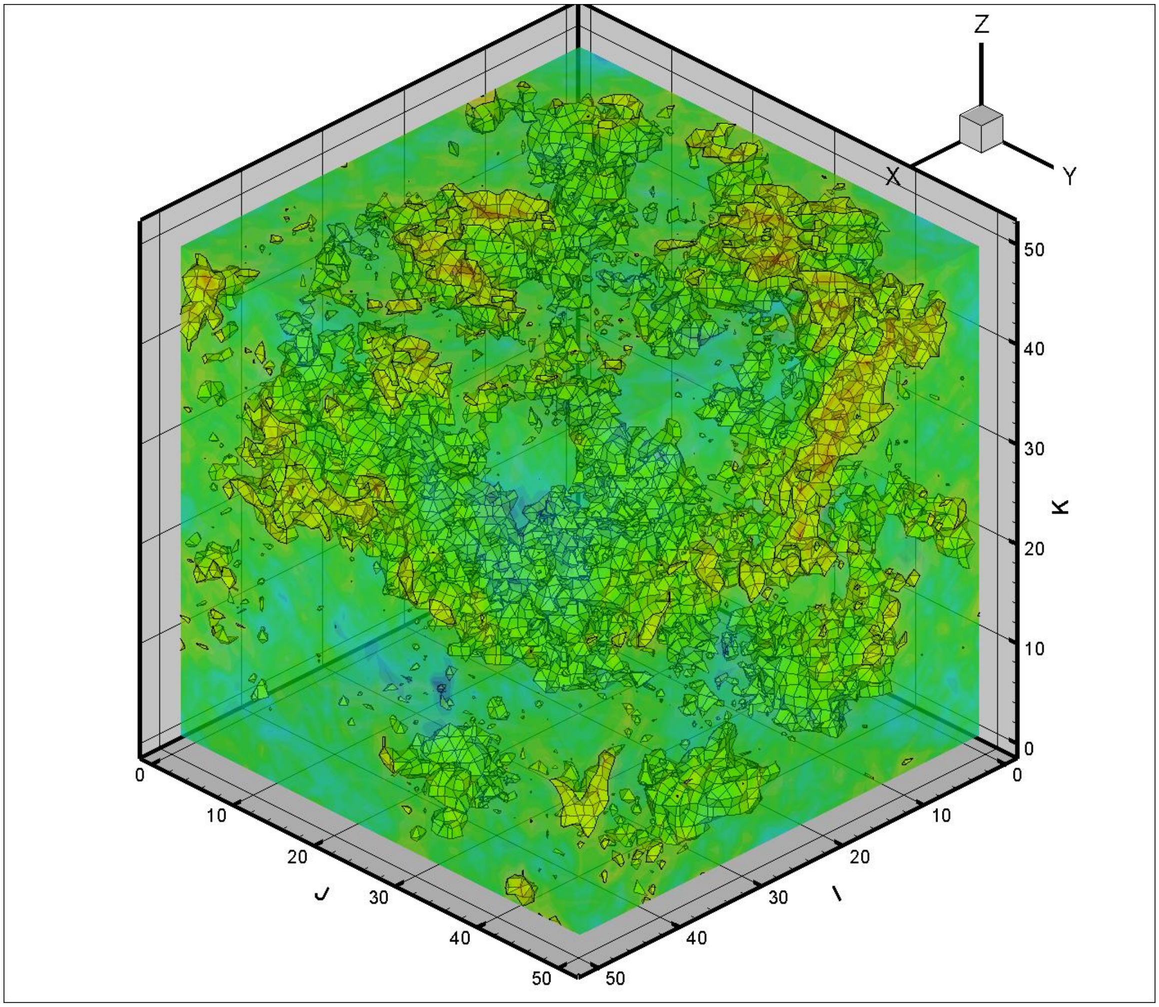

Figure 6.37 Clusters of high hydraulic conductivity, second realization

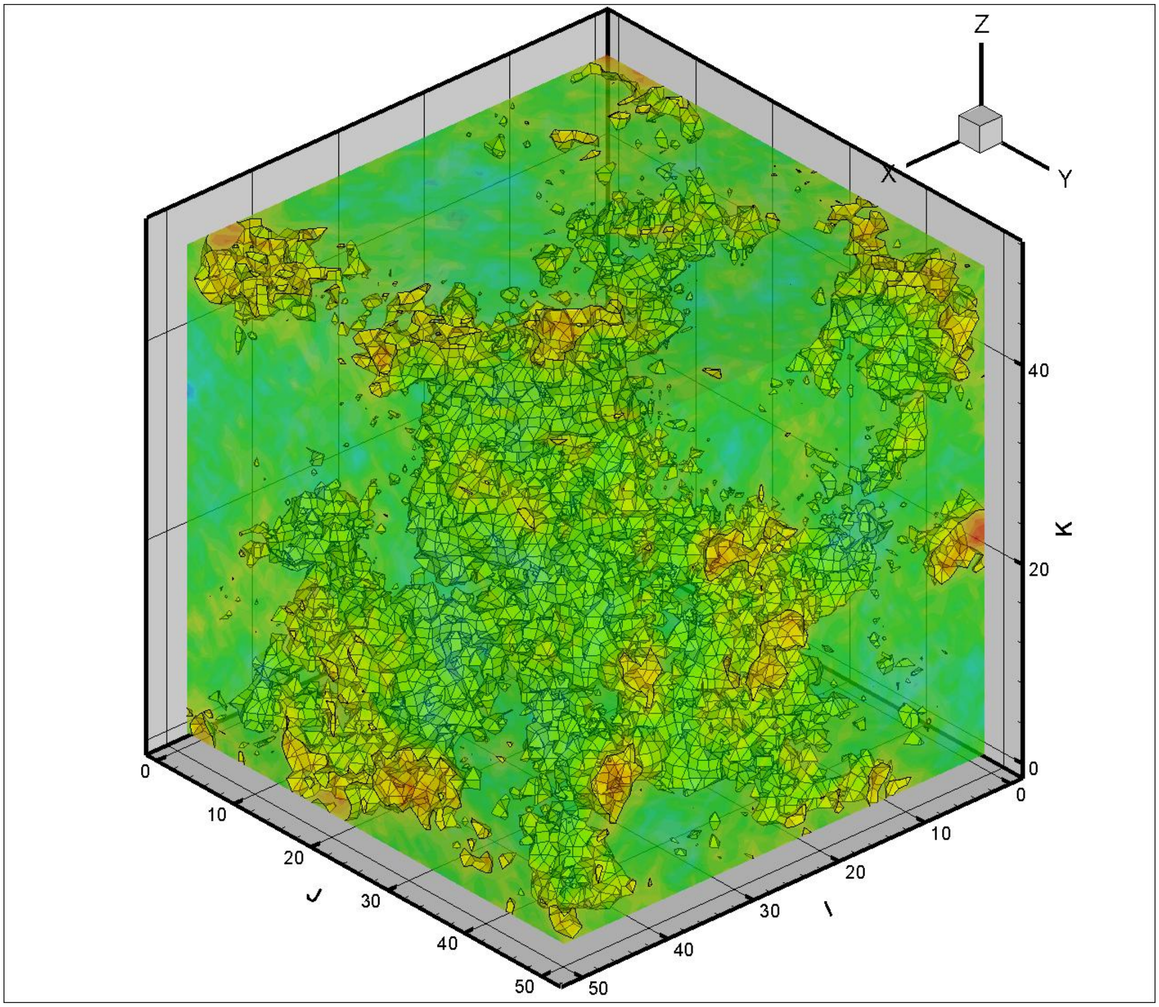

Figure 6.38 Clusters of high hydraulic conductivity, third realization

Figure 6.39 reflects the resulting viscous displacement simulation for the network model shown in Figure 6.38. Invasion paths follow the area that had the highest hydraulic conductivity. As shown in Figure 6.38, high hydraulic conductivity bonds are located more in the center and towards the high index numbers in X; therefore, the invaded nodes are more often located in the same areas.

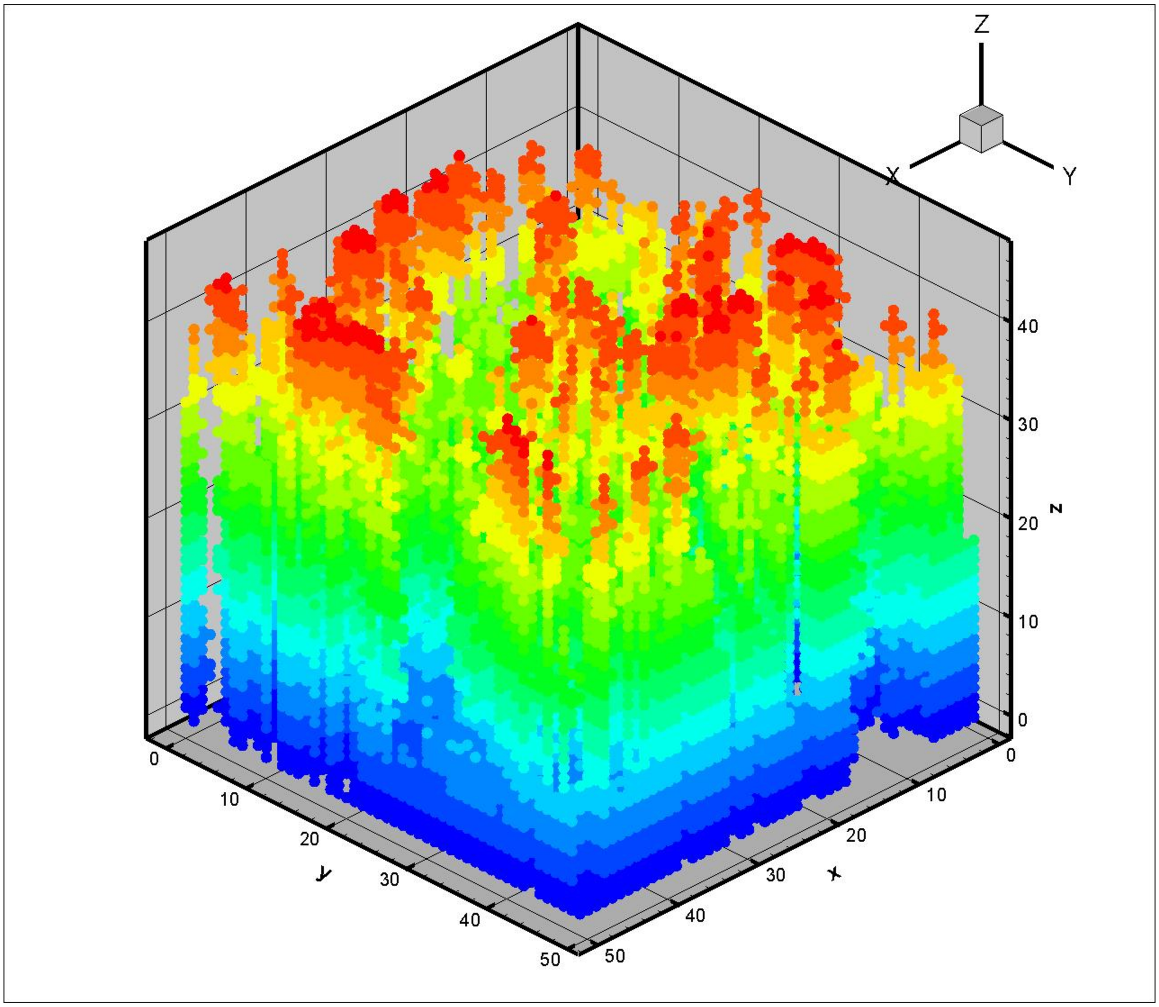

Figure 6.39 Viscous dominant invasion of the network with clusters of high hydraulic conductivity

Another outcome can be realized from the invasion shape. We realized that volumes with higher hydraulic conductivities have a larger number of invaded nodes. Most of the invasion paths were passed through the spaces with higher hydraulic conductivities.

6.3. EFFECT OF SPATIAL CORRELATION ON CHANNELS DENSITY

In order to compare the effects of spatial correlations on the density of channels, we compared all the previously simulated R_z ratios and density, and put them all together on one graph. The next step was to make a more general reference graph of density vs. R_z ratio that would include most of the expected behavior of these types of trends. We started with a random distribution of Hydraulic conductivities, and continued toward the equal distance spatial correlation. We then continued toward the disks in the direction of flow. We modeled several visualizations of viscous displacement for each of these cases to obtain an average value.

The simulated networks were three dimensional cubic lattices of 30 × 30 × 300 nodes, which gave 900 nodes in the area perpendicular to flow. The top and bottom were connected to outlets and inlets, and the four sides of the networks were no-flow boundaries. In each simulation test as the invading viscous fluid reached a certain Z level in the network, we made notations of the number of fingers in order to calculate and generate the plot of finger densities.

Table 6.9 reflects the average results and the corresponding calculated values of each spatial correlation set of simulations. Table 6.10 also reflects the same results for the cases of randomly distributed hydraulic conductivities. These tables contain the average number of fingers and the calculated density of those fingers.

We demonstrate one of these tests here. Hydraulic conductivities were re-sampled from a spatial correlation distribution with correlations length of 1 × 10 × 10 in X, Y, and Z directions, respectively. Therefore, the resulted distribution appeared as disks or patches of high hydraulic conductivity in the direction of flow, as shown in Figure 6.40.

Nz	10	15	30	45	60	75	90	105	120	135	150	165	180
10 - 10 - 10 Spatial Correlation													
R_z	0.011	0.017	0.033	0.050	0.067	0.083	0.100	0.117	0.133	0.150	0.167	0.183	0.200
No. of Channels	39	30	22	14	10	8	8	7	7	6	5	4	4
Density	0.043	0.033	0.024	0.016	0.011	0.009	0.009	0.008	0.008	0.007	0.006	0.004	0.004
1 - 10 - 10 Spatial correlation													
R_z		0.017	0.033	0.050	0.067	0.083	0.100	0.117	0.133	0.150	0.167	0.183	0.200
No. of Channels		150	44	30	19	13	9	6	6	5	3	2	2
Density		0.167	0.049	0.033	0.021	0.014	0.010	0.007	0.007	0.006	0.003	0.002	0.002
3 - 1 - 3 Spatial correlation													
R_z	0.011	0.017	0.033	0.050	0.067	0.083	0.100	0.117	0.133	0.150	0.167	0.183	0.200
No. of Channels	39	28	18	10	10	10	9	7	7	6	5	5	5
Density	0.043	0.031	0.020	0.011	0.011	0.011	0.010	0.008	0.008	0.007	0.006	0.006	0.006

Table 6.9 Finger density and R_z results for several cases of spatially correlated hydraulic conductivities

Random Distribution of Hydraulic Conductivities			
Nz	**R_z**	**Number of Channels**	**Density**
10	0.00625	31	0.01938
15	0.00938	15	0.00938
20	0.01250	12	0.00750
25	0.01563	11	0.00688
30	0.01875	10	0.00625
35	0.02188	9	0.00563
40	0.02500	8	0.00500
45	0.02813	6	0.00375
50	0.03125	5	0.00313
55	0.03438	4	0.00250
60	0.03750	4	0.00250
70	0.04375	4	0.00250
80	0.05000	3	0.00188
90	0.05625	3	0.00188
100	0.06250	3	0.00188
120	0.07500	3	0.00188
160	0.10000	3	0.00188
200	0.12500	1	0.00063

Table 6.10 Finger density and R_z results for random distribution of hydraulic conductivities

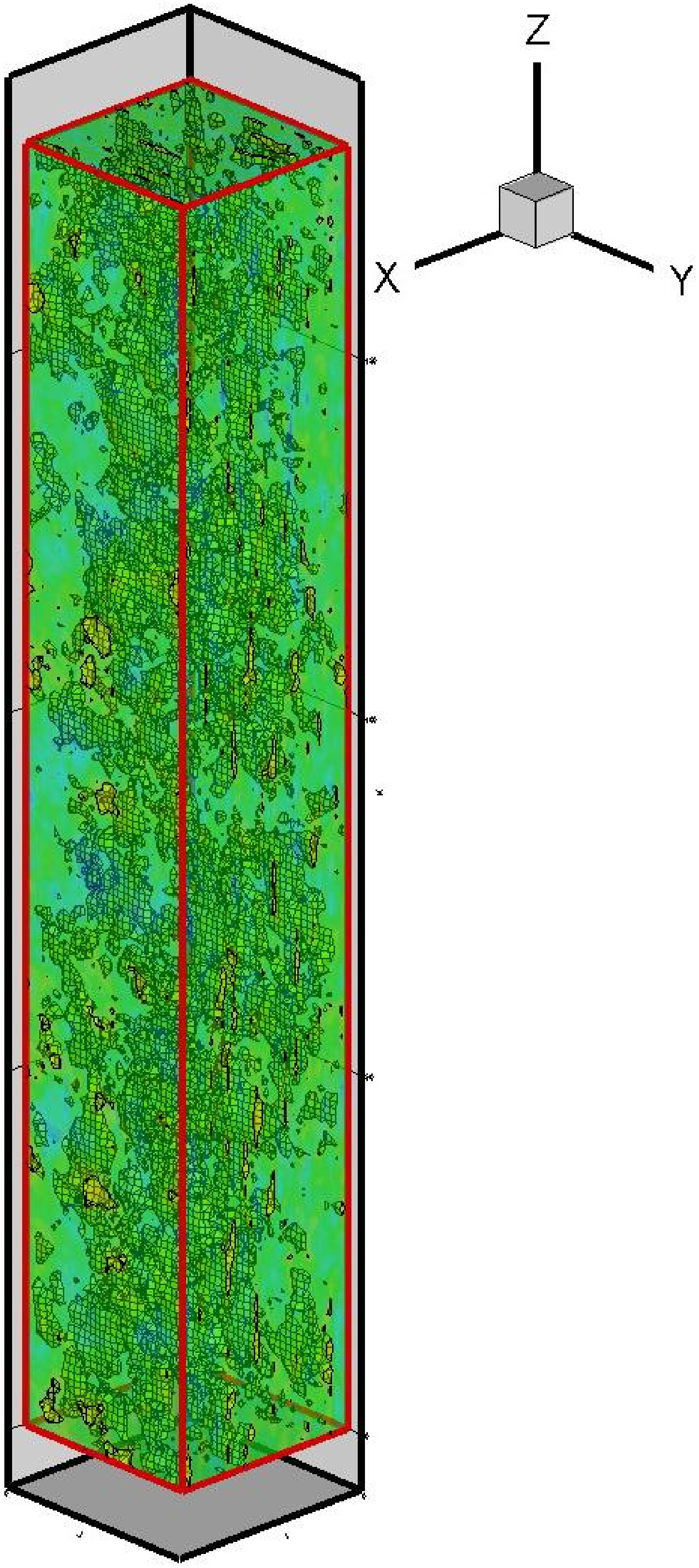

Figure 6.40 A three dimensional cubic lattice with 30 × 30 × 180 dimensions and correlation lengths of 1-10-10 in X, Y, and Z directions

The viscous dominant invasion results are illustrated in Figures 6.41 through 6.52. In this example, we used a 30 × 30 × 180 node system network. The network size in Z direction was 6 times larger than the X and Y directions, which enabled us to capture the larger R_z ratios effects. The top and bottom of this three dimensional cubic lattice was connected to outlets and inlets, and the four sides were no-flow boundaries. The general potential gradient was in the Z direction.

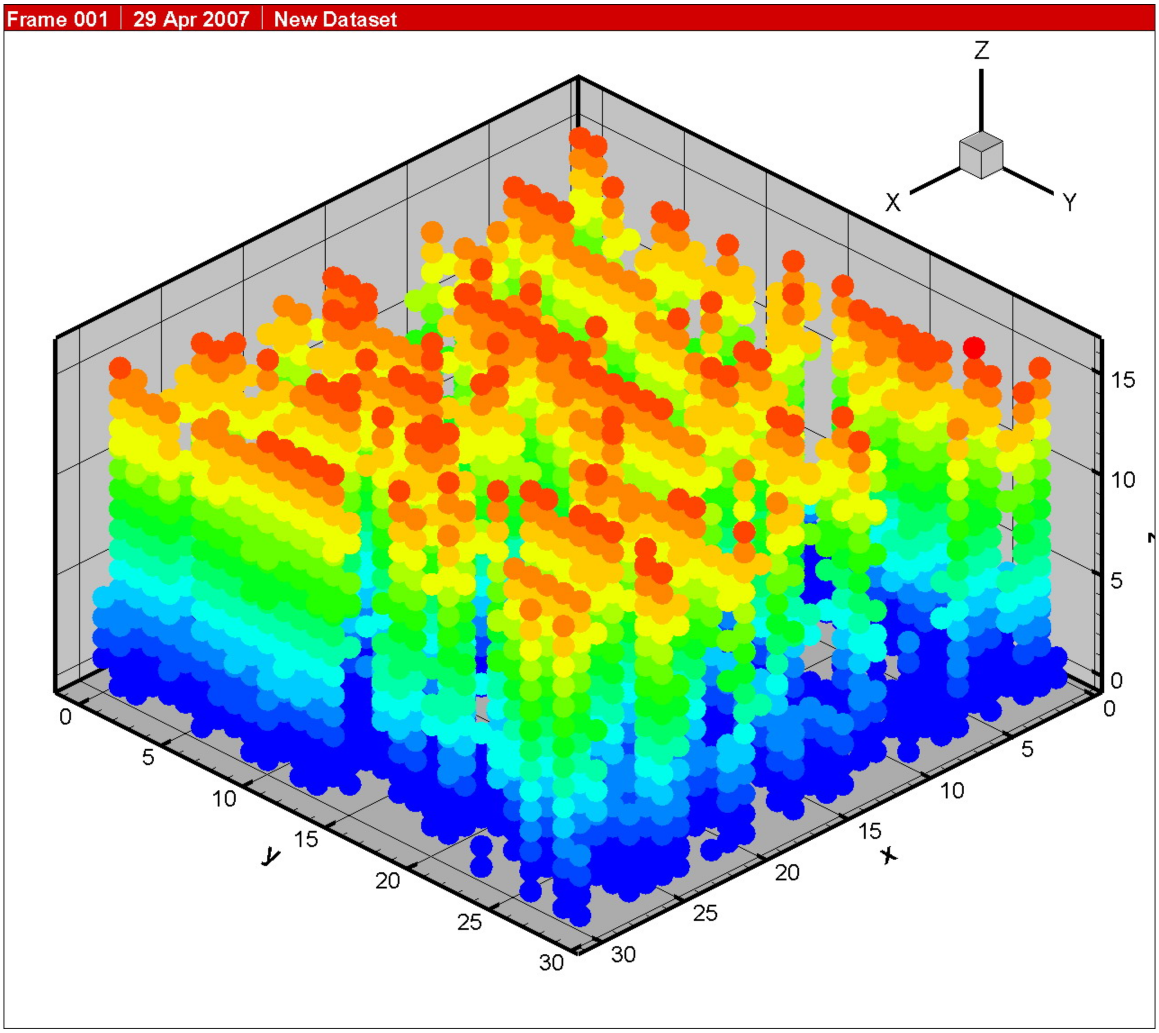

Figure 6.41 Viscous invasion at Z=15

In each step of invasion we took pictures of viscous invasion. The resulting viscous invasion in these example networks are shown in figures 6.41 to 6.52. These figures illustrate the viscous dominant invasion simulation; every time that the invading fluid reached a specific level in the Z direction (e.g., every 15 nodes of high), we took a slide, until viscous invasion reached the outlets and the invading fluid made the breakthrough. Channels counted only if they passed the 80% of length in each Z set.

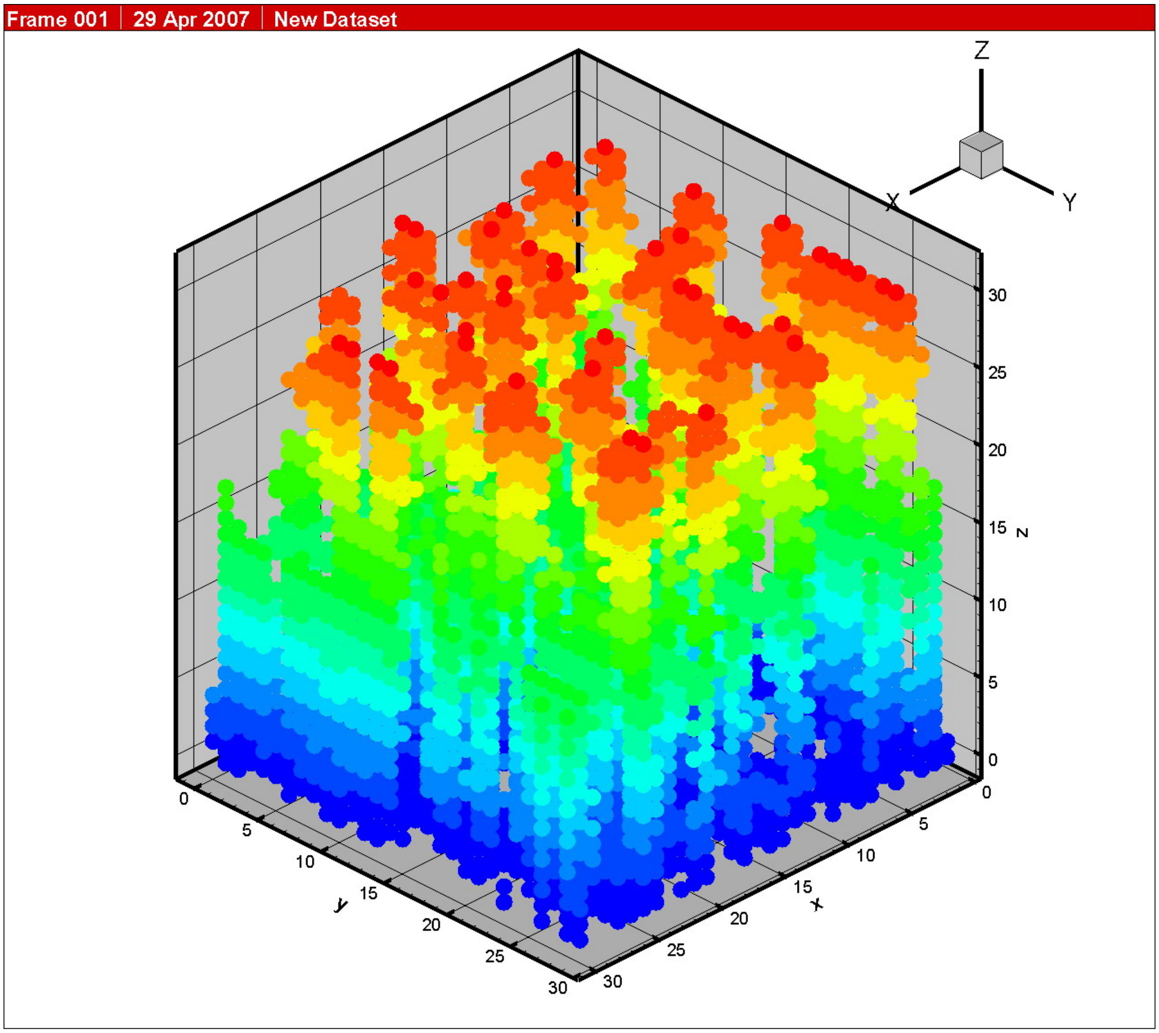

Figure 6.42 Viscous invasion at Z=30

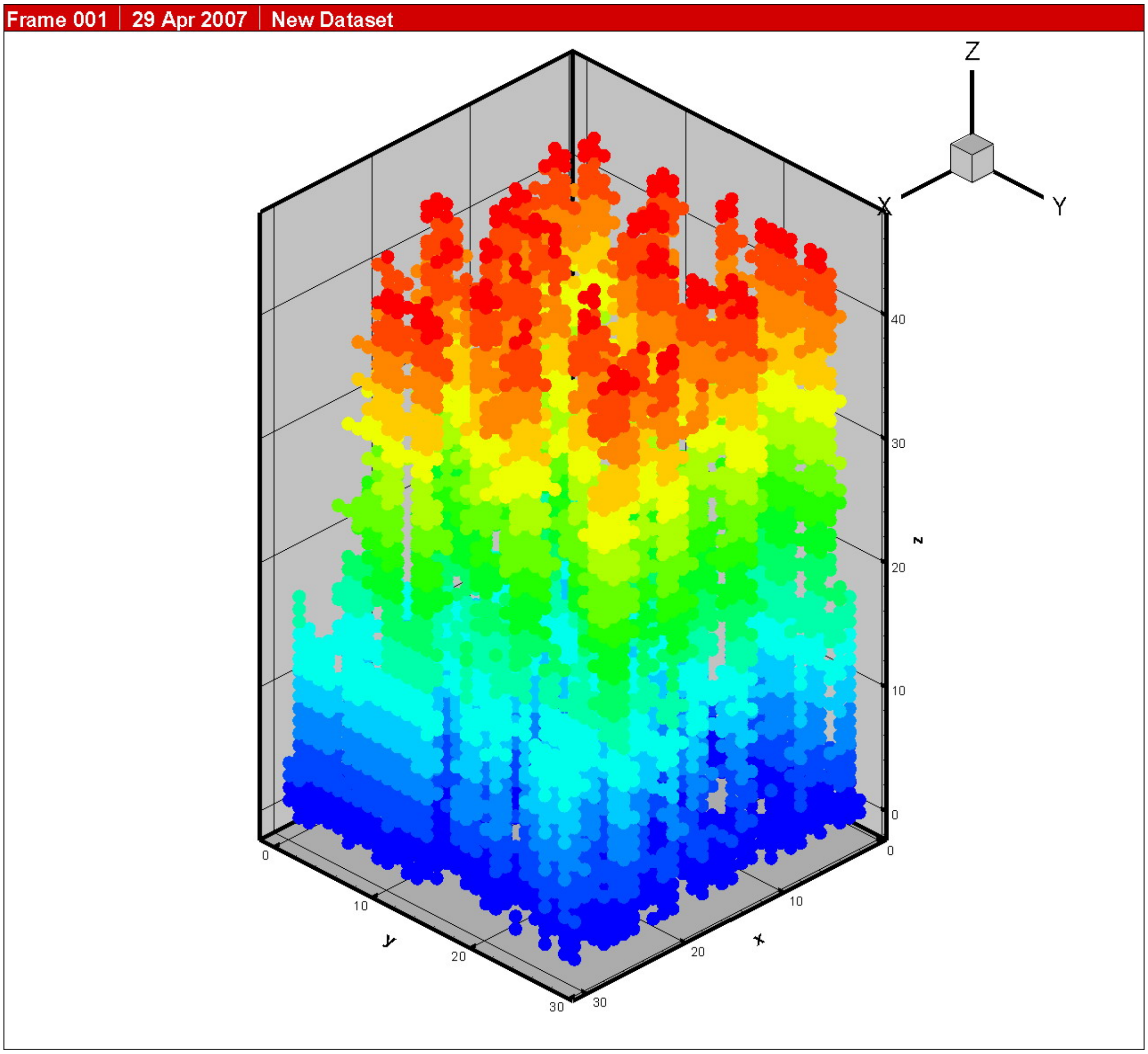

Figure 6.43 Viscous invasion at Z=45

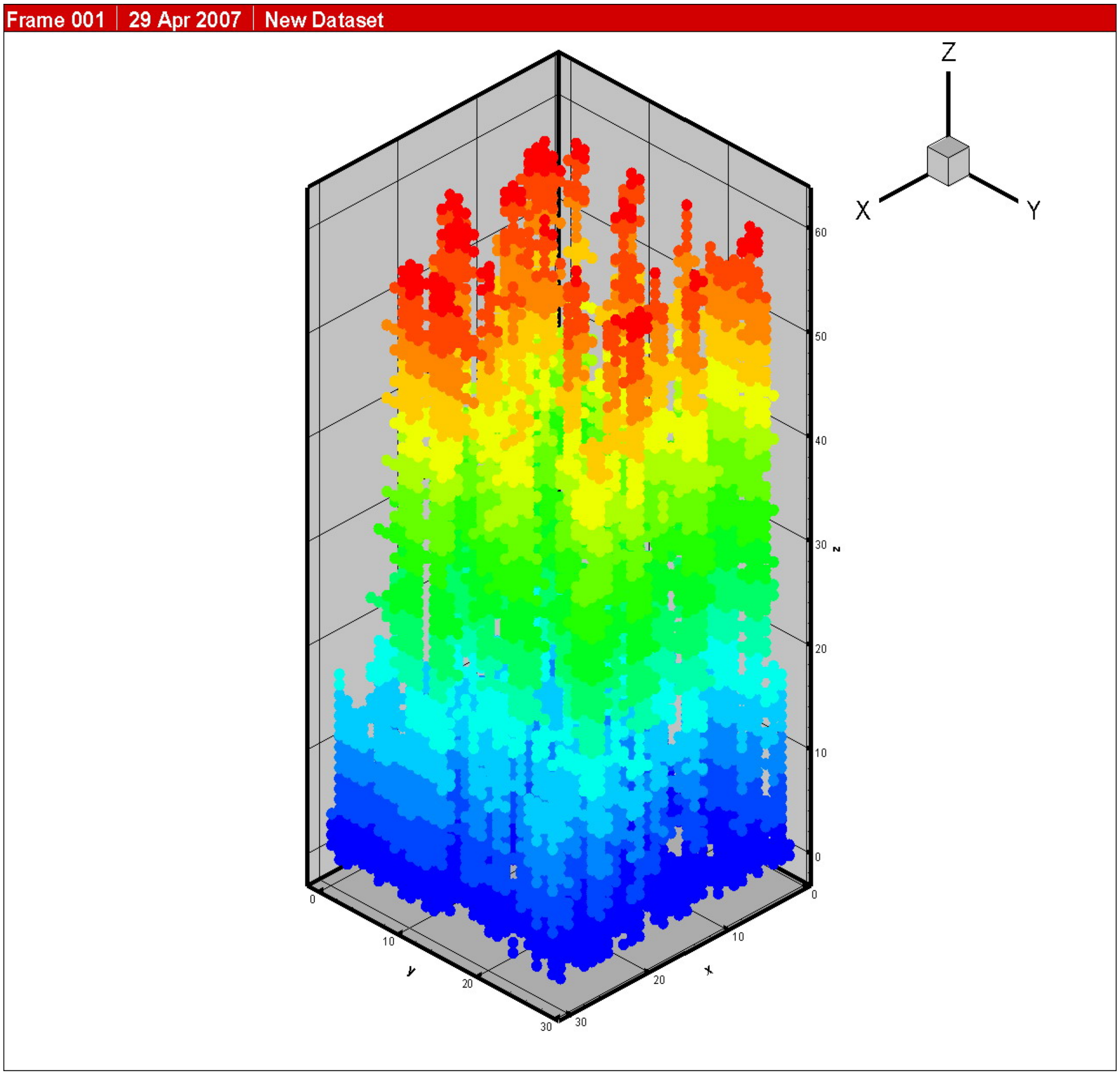

Figure 6.44 Viscous invasion at Z=60

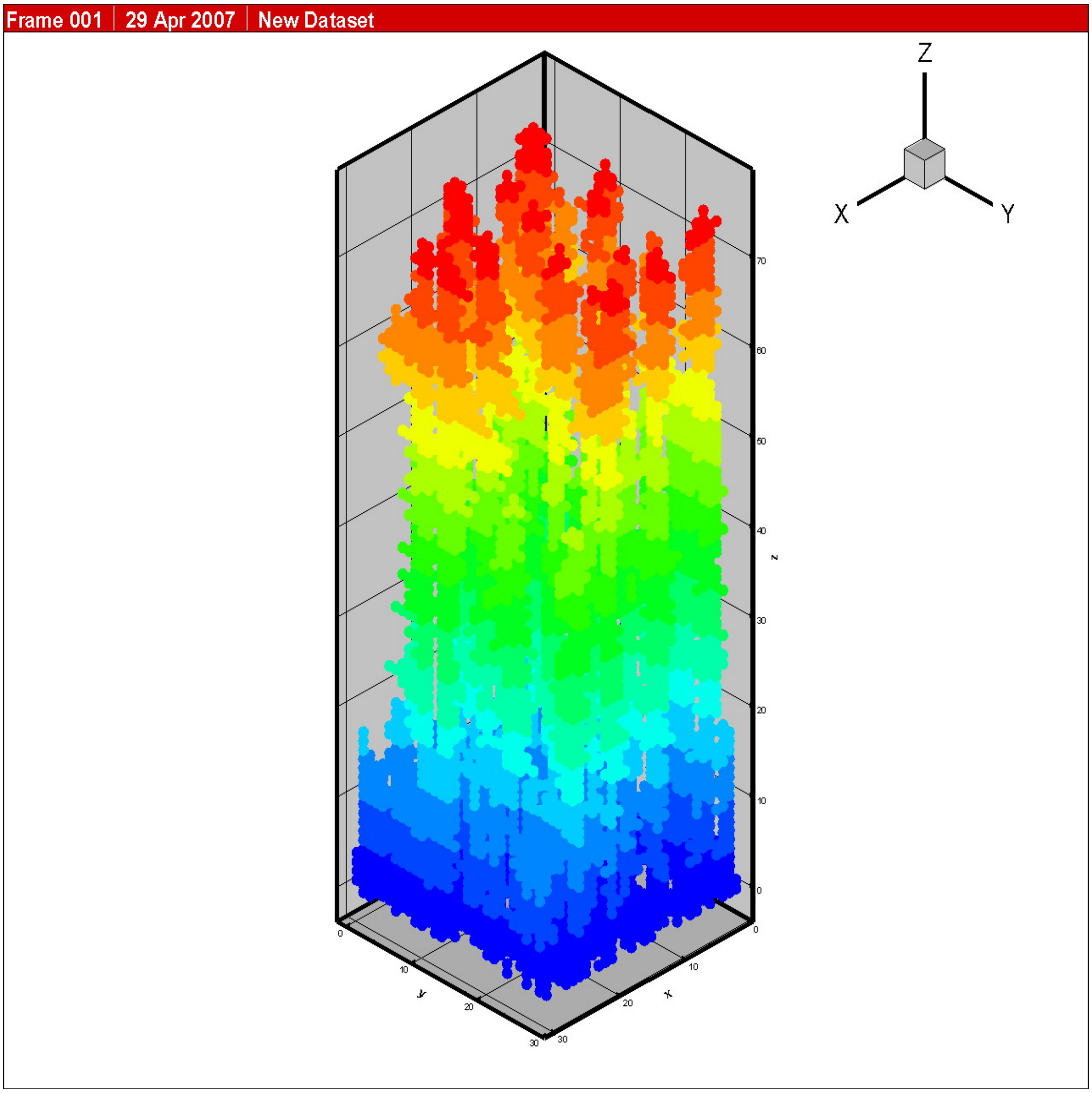

Figure 6.45 Viscous invasion at Z=75

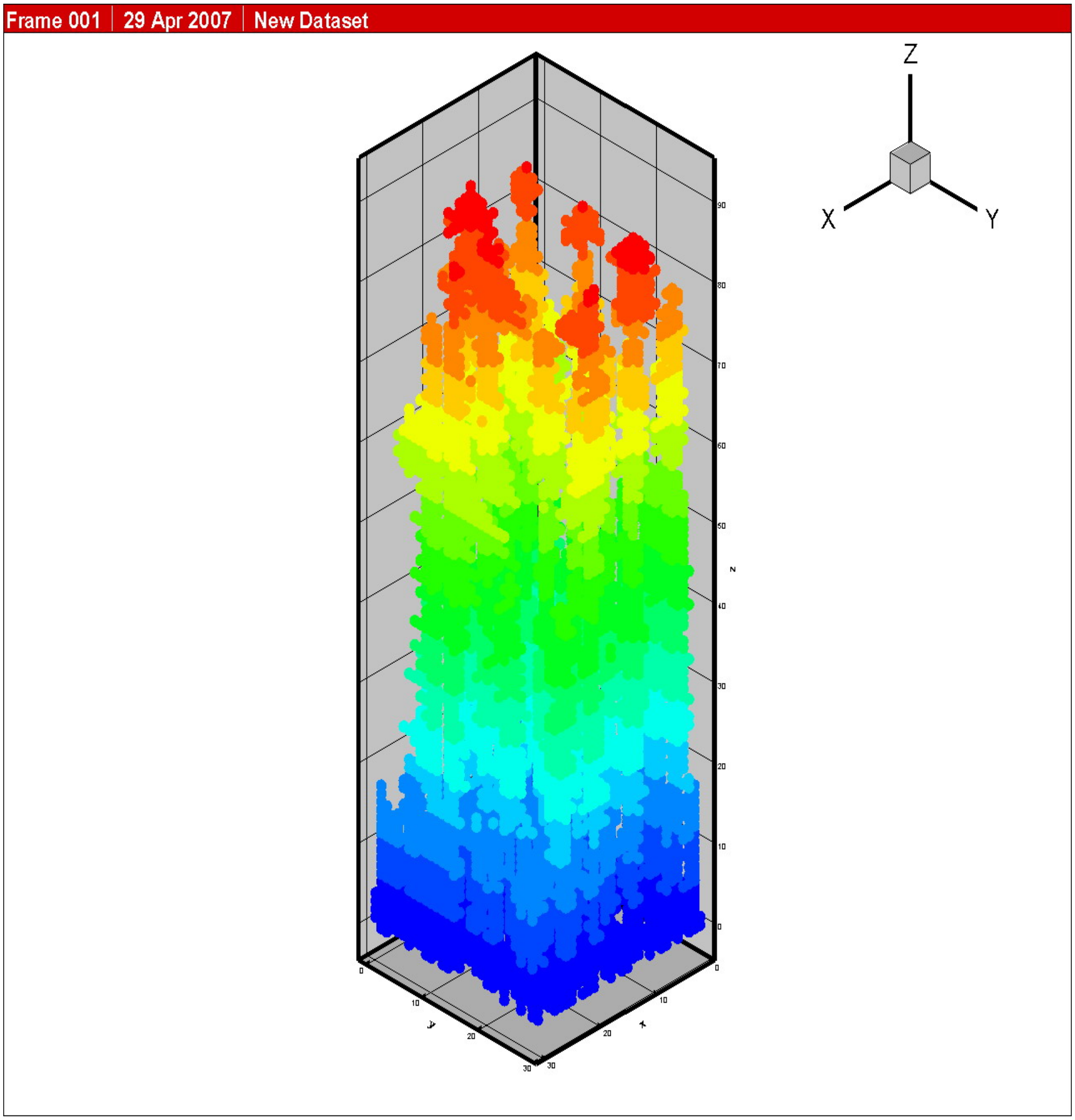

Figure 6.46 Viscous invasion at Z=90

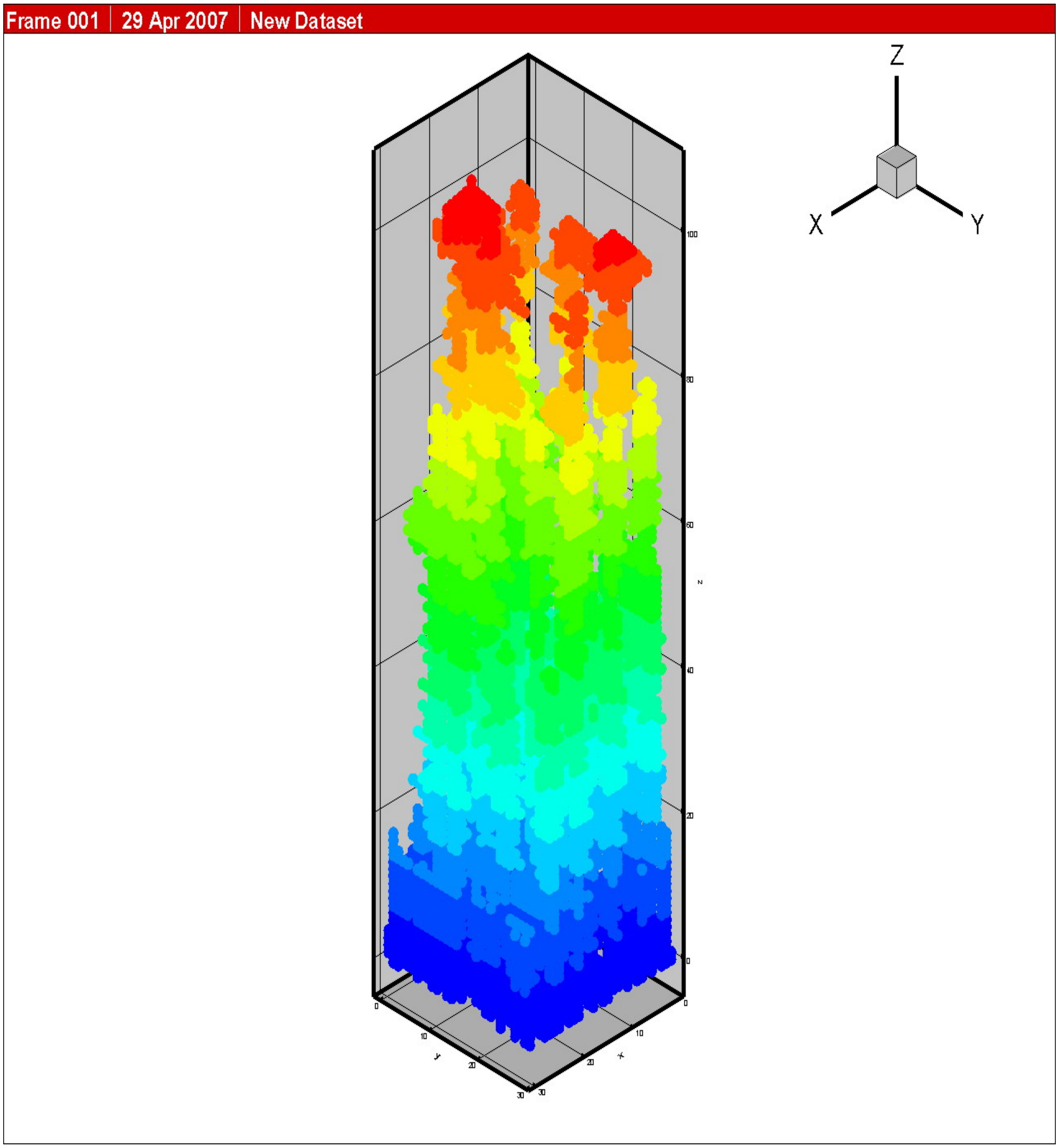

Figure 6.47 Viscous invasion at Z=105

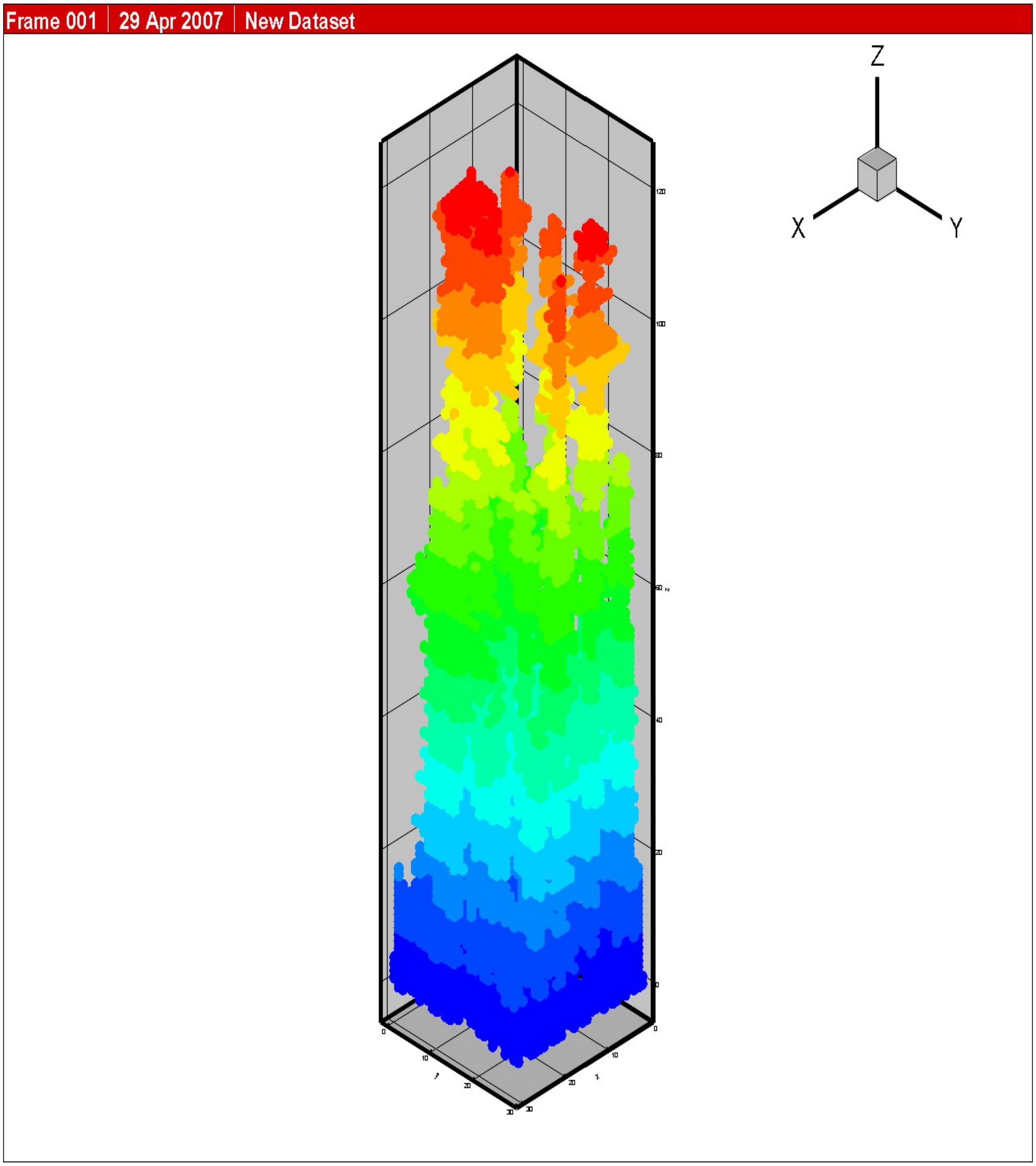

Figure 6.48 Viscous invasion at Z=120

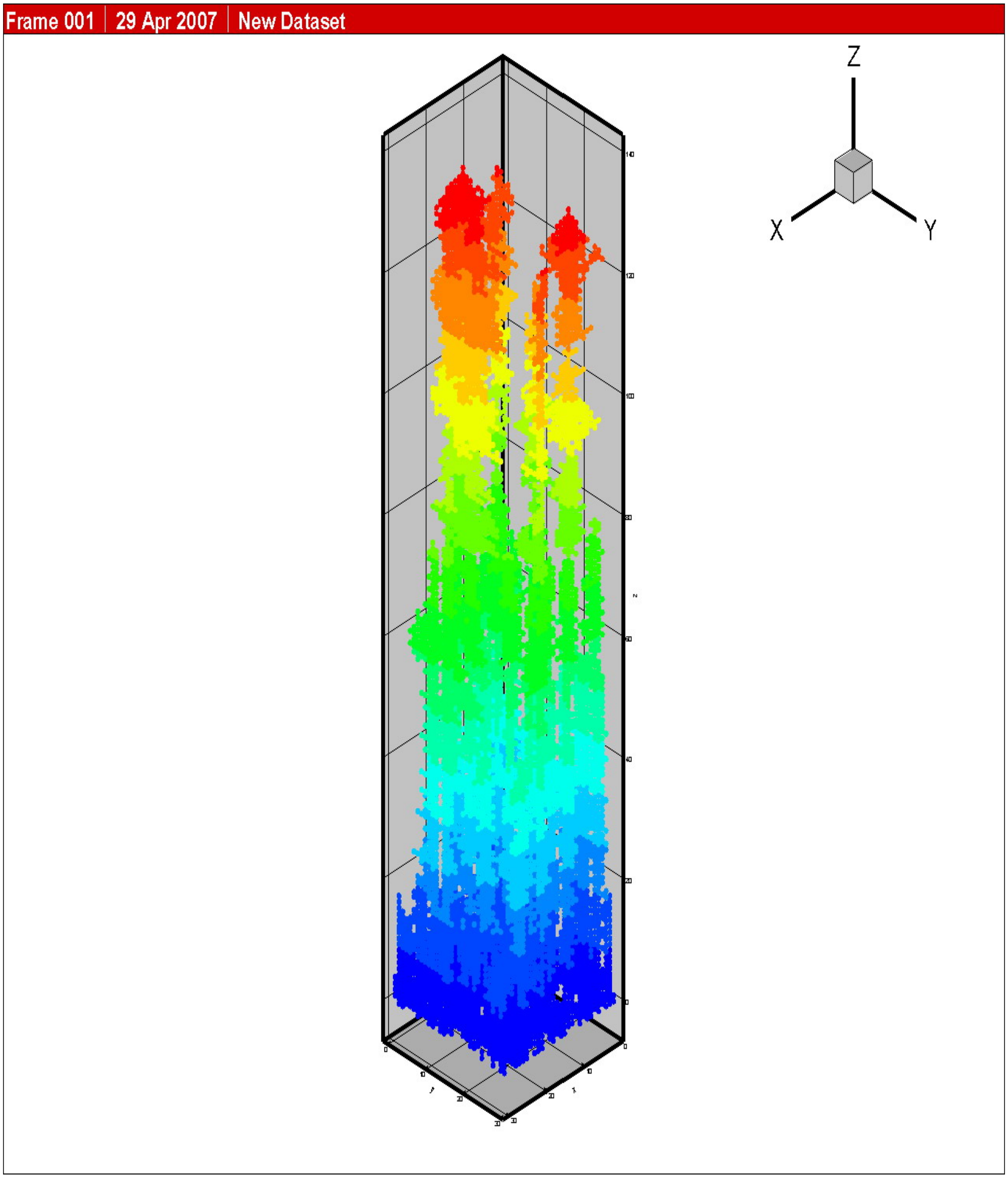

Figure 6.49 Viscous invasion at Z=135

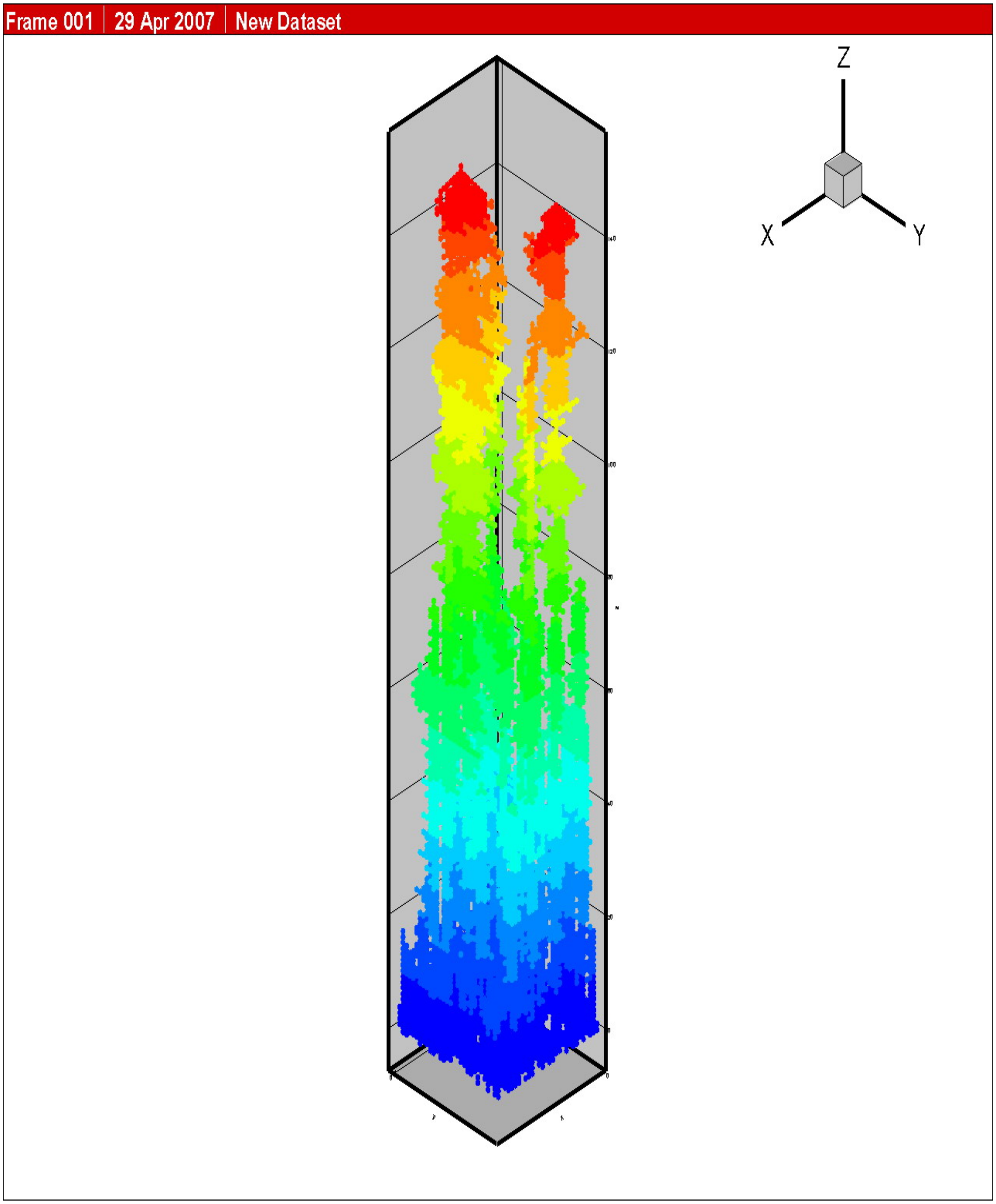

Figure 6.50 Viscous invasion at Z=150

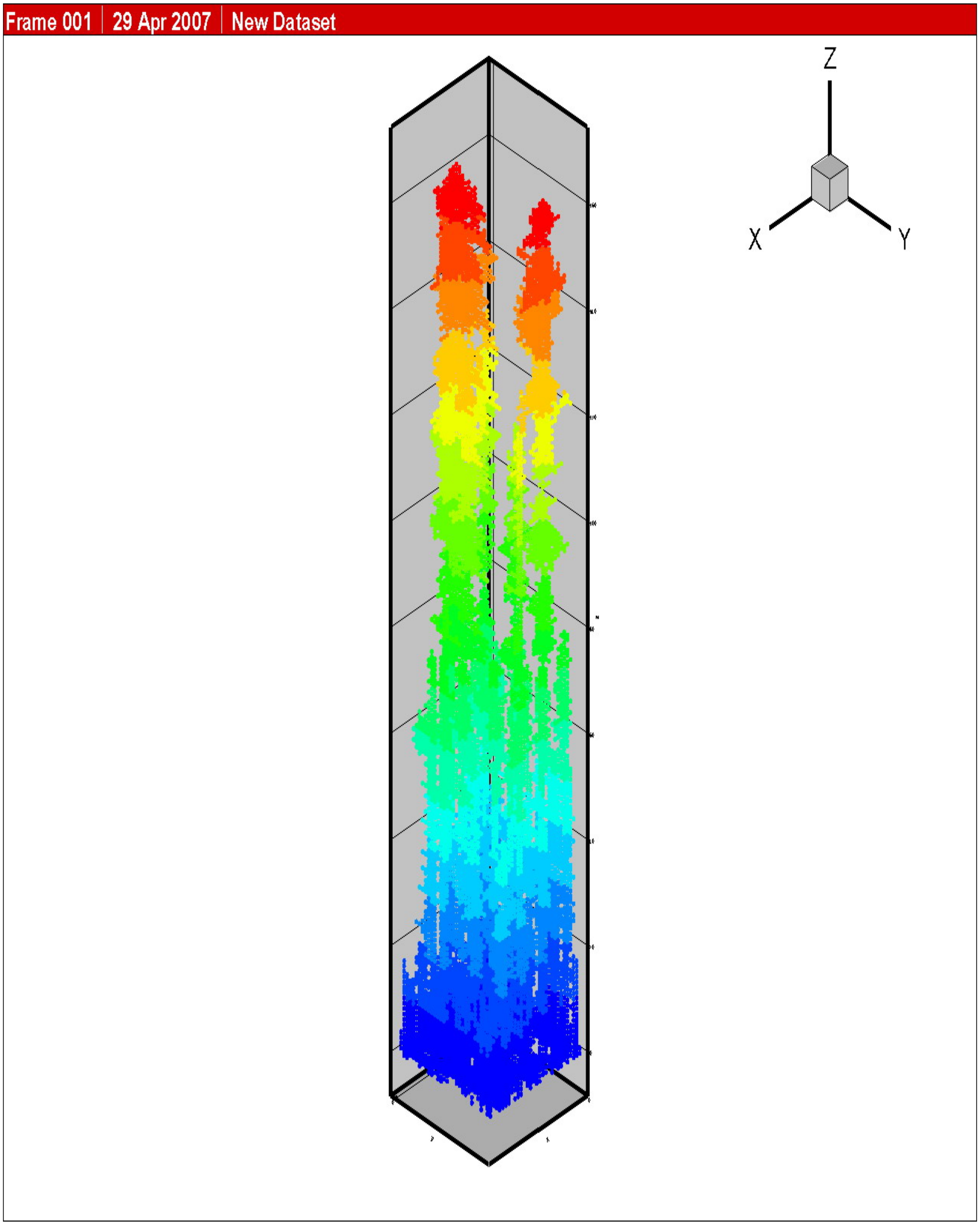

Figure 6.51 Viscous invasion at Z=165

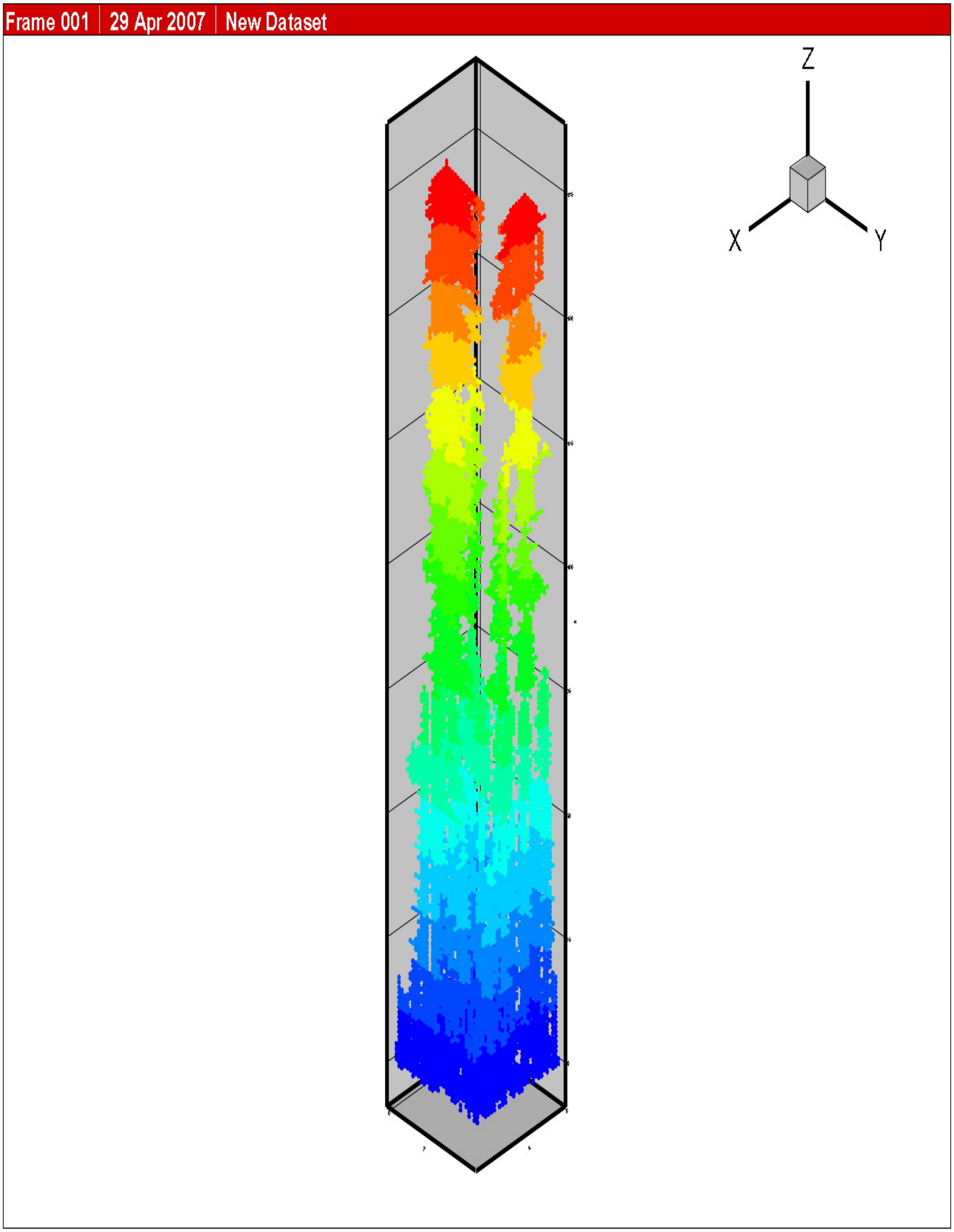

Figure 6.52 Viscous invasion at Z=180

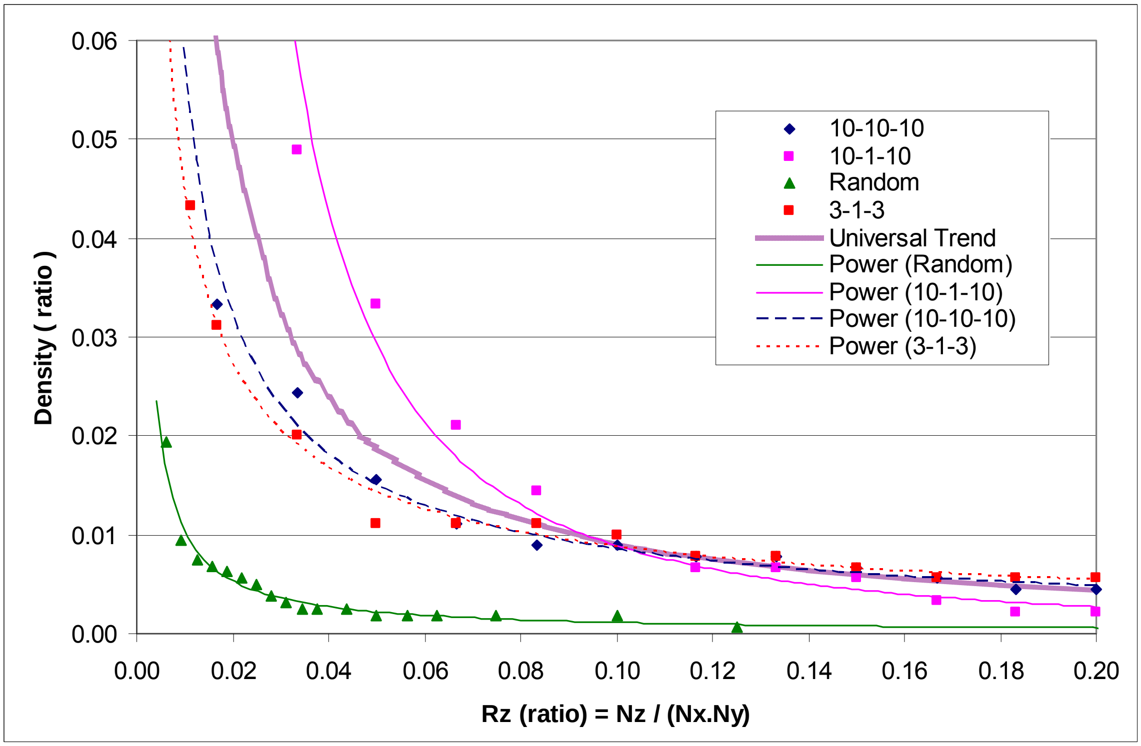

Figure 6.53 Plot of the finger density vs. R_z ratio

As shown in the above Figure 6.53, we fitted power trend lines to each set of results. The general trend was a decline to an asymptotic value, similar to the case of random distribution of hydraulic conductivities. But, when comparing these trend lines to the one for the random values of hydraulic conductivities, the density drops in later times of invasion because of spatial correlation between the values. This behavior is because we artificially created some fast and slow paths for the viscous flow; therefore, more channels were able to move simultaneously inside the network. Consequently it took more time for one channel to outperform and pass the other fingers.

Equations of fitted power trend lines for the above results, by set, and a calculated universal value base on these trends, are shown in table 6.11.

Spatial Correlation Length	**Density Trend Line**	**R^2**
10-10-10	$0.0013\ R_z^{-0.8251}$	0.9742
10-1-10	$0.0002\ R_z^{-1.7136}$	0.9785
3-1-3	$0.0017\ R_z^{-0.7052}$	0.9774
Random values	$0.0001\ R_z^{-0.9606}$	0.9364
Average Fitted Trend Line	$0.0008\ R_z^{-1.0451}$	1.0

Table 6.11 Equations of the fitted trend line to the calculated density for viscous invasion simulation of spatially correlated hydraulic conductivities

As shown in Figure 6.53 when a pure random distribution used to re-sample the hydraulic conductivities, there is no spatial correlation length in any specific direction. Viscous invasion shows the fewest invasion channels at the same distance between the injector and producers, among the tests, this means less density. From a long spatial correlation length in all directions to a high correlations length in the general direction of flow gradient, the viscous invasion again shows more finger density.

We have concluded that, as the ratio of correlation length in the direction of potential gradient for the hydraulic conductivity distributions (in respect to other directions) grows, the density of fingers will grow.

6.4. MILLION NODES TESTS AGREEMENT

We were not able to perform all the previously mentioned tests on large networks due to the lack of computational capacity and the extensive time required for simulating large networks in the scales of 1,000,000 nodes or more. Therefore, after performing all previous tests in smaller networks with a maximum number of approximately 400,000 nodes, we modeled some of the previously mentioned simulations on networks larger than 400,000 nodes to verify the observed behavior and results.

Please note that some of the simulations were so time consuming that we had to terminate them to re-allocate the computational capacity resources to the simulations that were performing faster with the available capacity.

Some of the simulation results for these large networks with more than 500,000 nodes were given as an example. The numbers resulted of the simulations were studied and calculated to verify the previously observed results. Some of them have been shown in figures and tables in this section.

We performed tests for viscous invasions on a set of large networks ranging from 500,000 to 1,000,000 nodes. The networks were cubic three dimensional lattices with 100 × 100 × 50, 100 × 100 × 75 and 100 × 100 × 100 nodes in X, Y, and Z directions, respectively. The hydraulic conductivities were sampled from a Finney pack distribution using a uniform re-sampling. Just as with all the cubic lattices in these series of tests, we put no-flow boundaries on the sides and connected the inlets and outlets to the tops and bottoms of the networks. The resulted viscous invasion for the case of 500,000 nodes is shown in Figure 6.54.

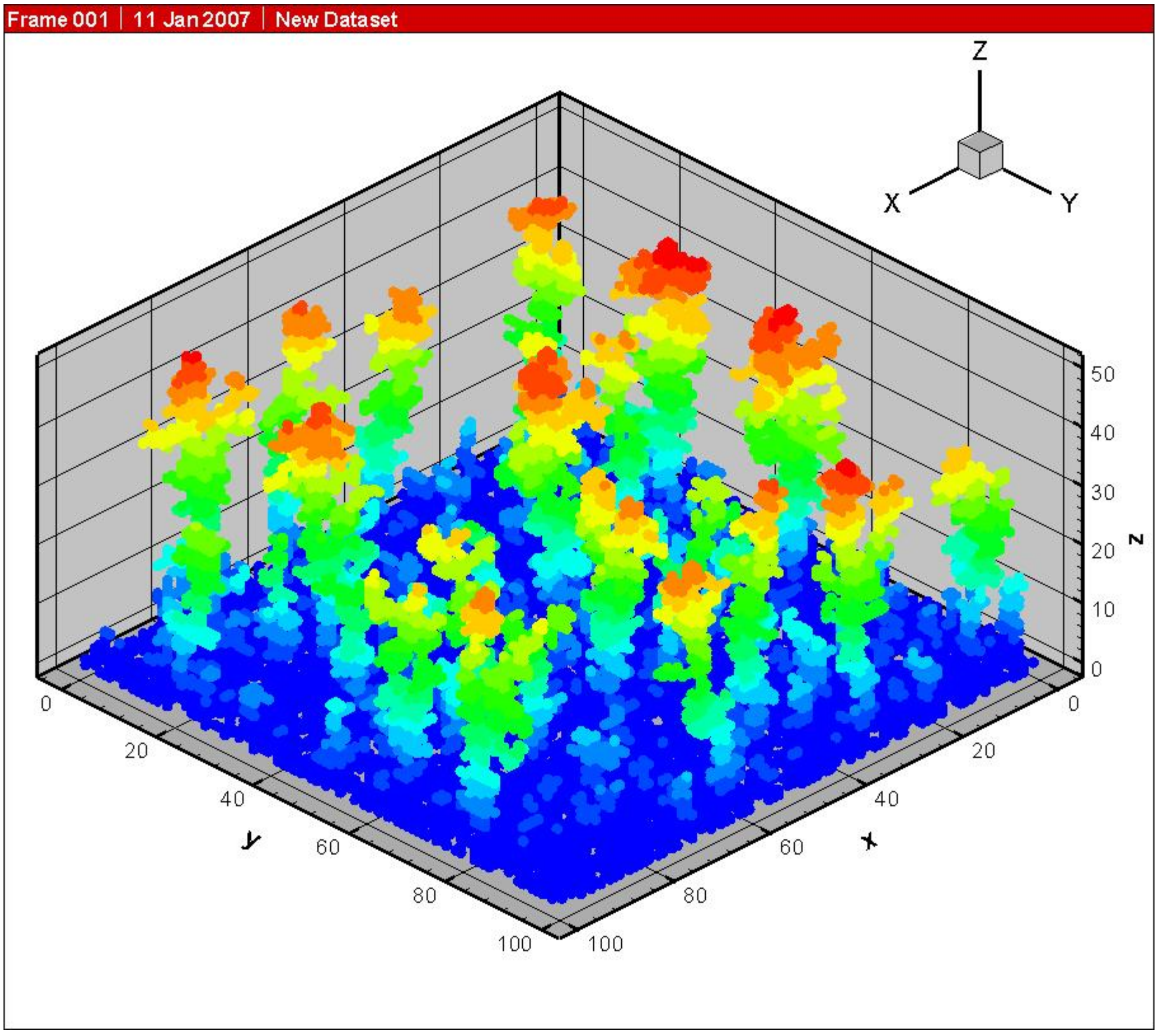

Figure 6.54 Viscous dominant invasion results on a 500,000 node system

As shown in Figure 6.54, the viscous invasion reflects the same self-contracting behavior as seen previously in the smaller networks.

The total number of invaded nodes was 51,076 nodes. Table 6.12 reflects the nodes and corresponding invaded bonds for each category. The average bond per nodes value was 1.99, and did not show any significant deviation from the expected value of 2.0. The channels were the major structure for the viscous dominant invasion.

Invaded Bonds	Number of Nodes
1	13,665
2	25,930
3	7,771
4	3,049
5	614
6	47

Table 6.12 Number of nodes with the corresponding invaded bonds, case of 500,000 nodes network.

The same behavior was observed in both the 750,000 and 1,000,000 nodes system cases, with no noticeable changes.

For the cases of spatial correlation, we observed the same behavior as that received for the cases of smaller networks. Figure 6.55 illustrates the hydraulic conductivity distribution of bonds with a spatial correlation length of 100-100-1 in X, Y, and Z directions. This is equivalent to disks or layers of high hydraulic conductivity perpendicular to the general direction of potential gradient. Figure 6.56 illustrates a side view of hydraulic conductivities shown in Figure 6.55.

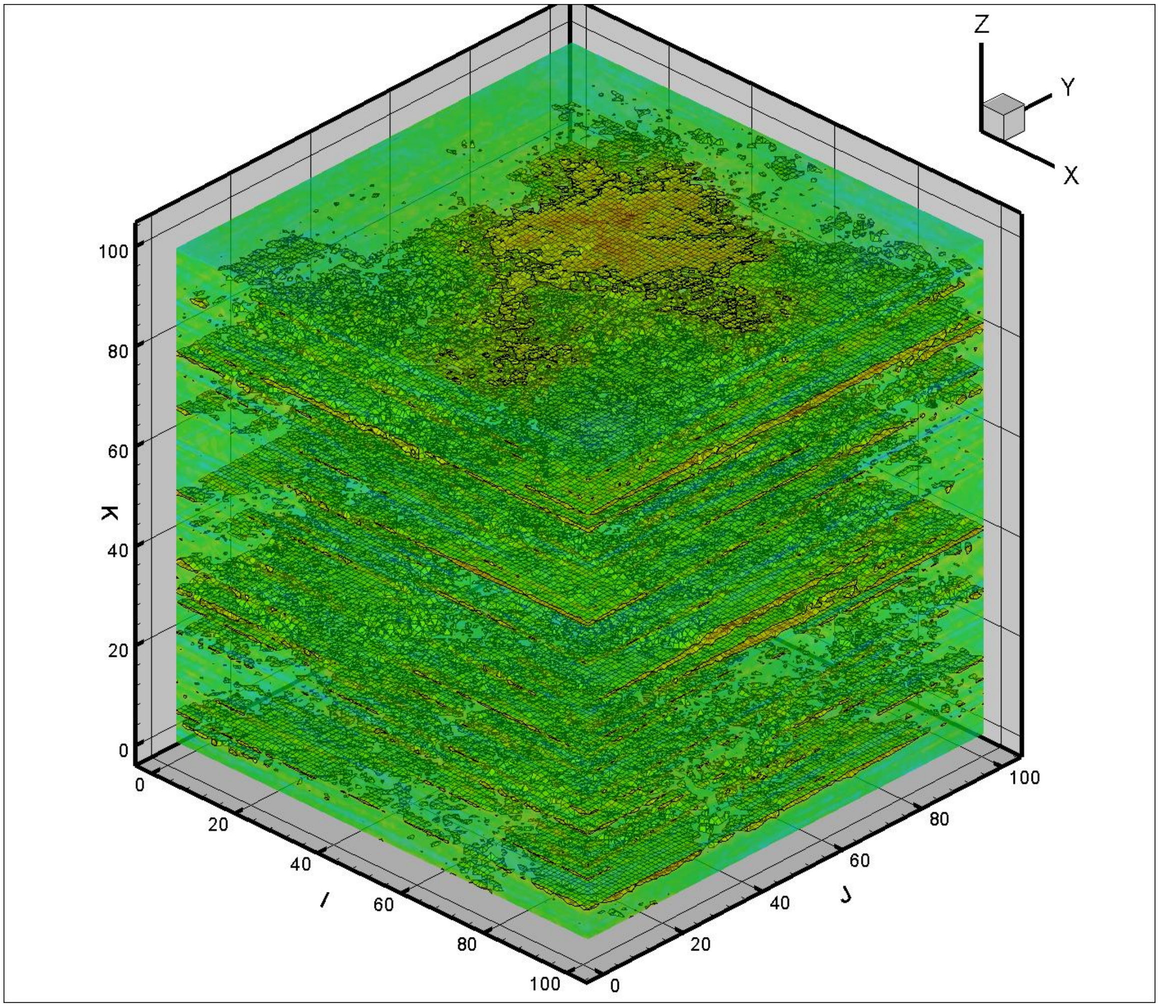

Figure 6.55 High hydraulic conductivity layers in a one million node network

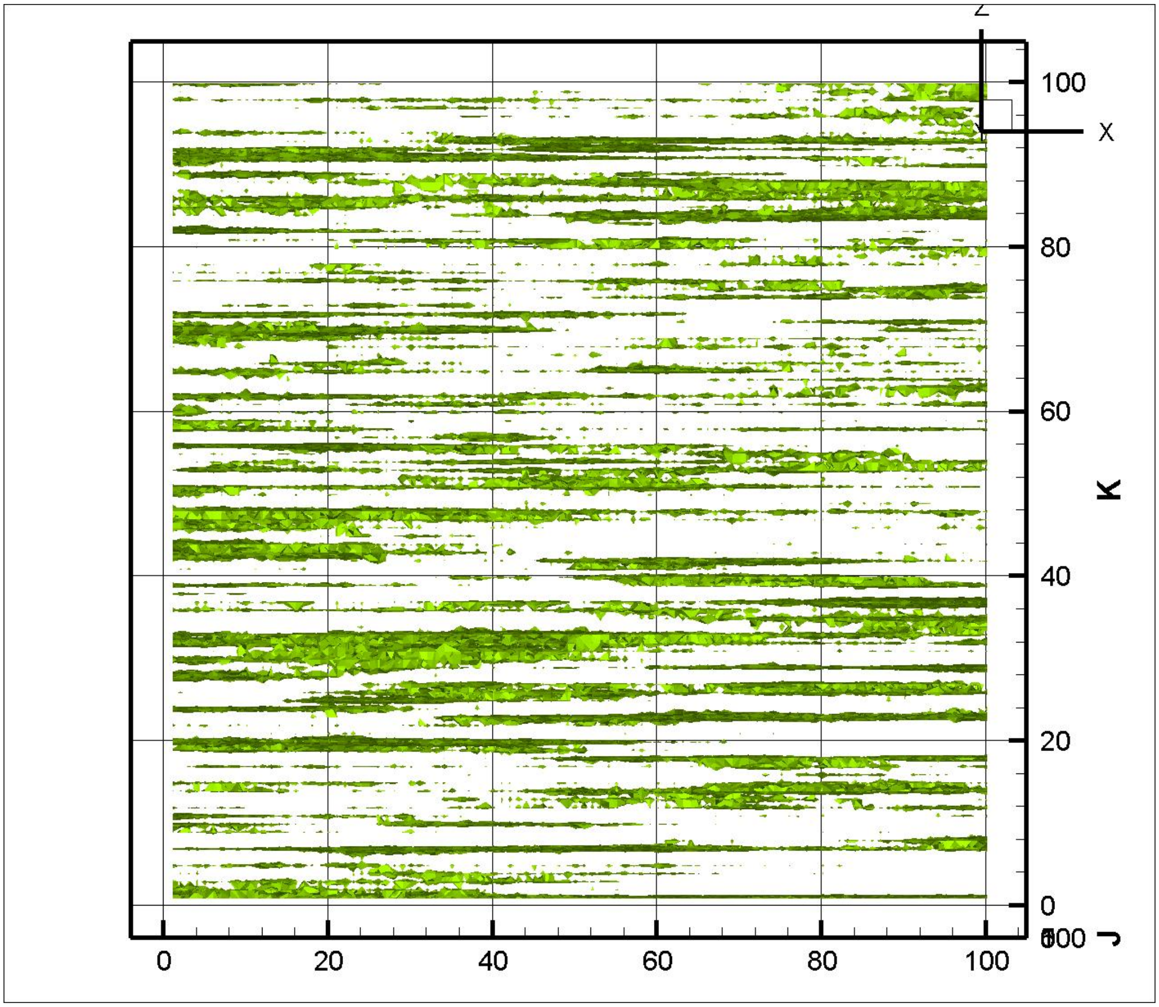

Figure 6.56 High hydraulic conductivity layers in a one million node network, side view

The same network properties for the 500,000 nodes network were applied to simulate the viscous invasion. After the breakthrough, we compared the results to the ones from the smaller networks, and found that they were very similar. The resulting viscous invasion for the case of a one million nodes system is shown in Figure 6.57.

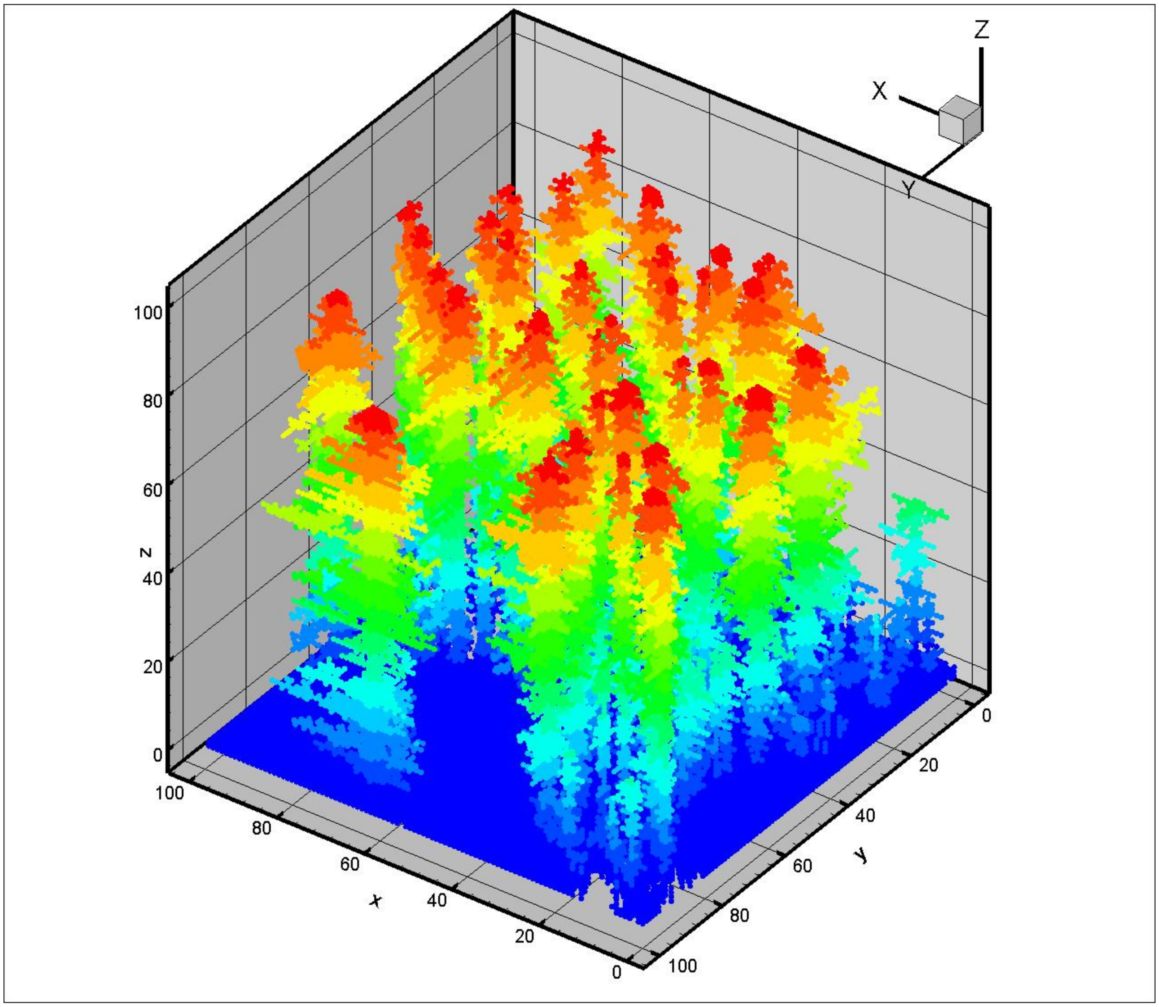

Figure 6.57 Viscous invasion on a one million node system

As shown in Figure 6.57, every time that the invasion had the opportunity to spread into the layers with a higher hydraulic conductivity this occurred, even though the general trend is in the direction of potential gradient. This is the same behavior we observed for the smaller networks.

The total number of invaded nodes was 74,097 nodes, with the average bonds per nodes value of 1.95. Table 6.13 reflects the number of invaded nodes and the number of invaded bonds associated with them. In the case of the one million node network, the number of nodes with all of the six bonds invaded is 868, which resulted in a higher local cluster invasion than the smaller 500,000 nodes network with smaller size layers. Therefore, we concluded that if the layers of high hydraulic conductivity are large enough to force the spread of viscous invasion in the perpendicular direction to the general flow direction, more clusters of invaded pores will form locally. This ultimately increases the sweep efficiency.

Invaded Bonds	Number of Nodes
1	29,570
2	29,170
3	7,965
4	4,718
5	1,806
6	868

Table 6.13 Number of nodes with its corresponding invaded bonds, case of one million nodes network

The structure of viscous dominant invasion remains the same for all sizes of networks modeling. Whether modeling a small sample or a large one, viscous invasion behaves similarly.

6.5. ELAPSED TIME CORRELATIONS

The elapsed time for the simulations was in the predicted range. Also as predicted previously in Figures 5.64 and Table 5.12 in chapter 5, the system obeys a second order polynomial trend as the networks' size increases. We have simulated several larger networks to ensure elapsed time. These results are shown in Table 6.14.

Nodes	Time (seconds)
500,000	215,348
750,000	498,492
1,000,000	870,061

Table 6.14 Elapsed time for networks larger than 500,000 nodes

Figure 6.58 reflects these new results with the previous results. As observed, the trend of elapsed time has not changed from the small networks to the larger ones. The fitted trend lines to these two sets are the same for small and large networks. Even though the hardware capacity on larger network systems (ranges above 750,000 nodes), does not completely allow for electronic calculations in the computer memory, elapsed time still obeys the second order polynomial trend line. In larger networks, the computations need larger memory and the physical exchange of data becomes necessary for calculations (using HDD), which will increase the elapsed time for the viscous invasion simulations.

The equation of the second order polynomial fitted trend is $Time(\text{sec.}) = 8E-07N\_Nodes^2 + 0.0317N\_Nodes + 14.466$ with $R^2 = 0.999$, which is very similar to the previously predicted values.

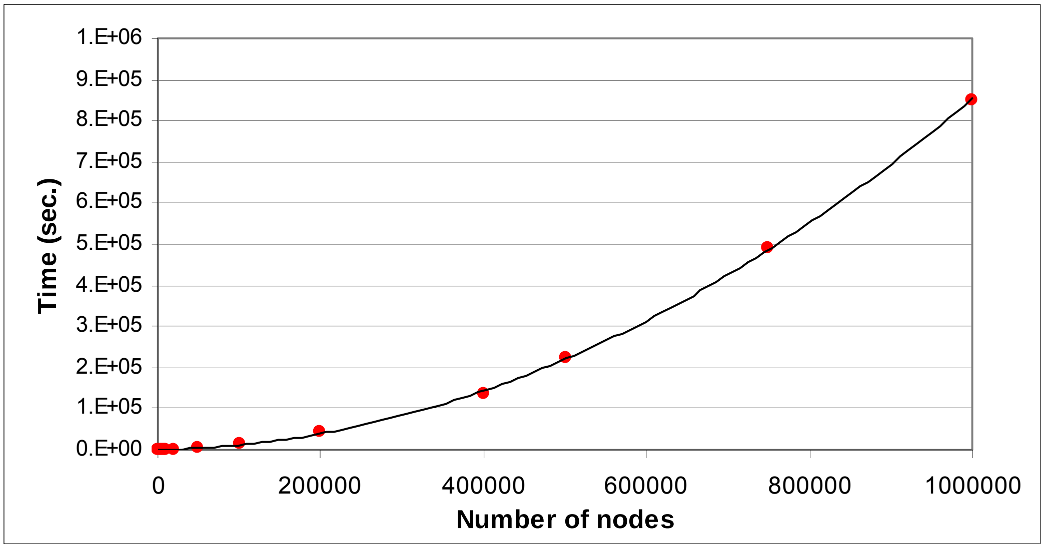

Figure 6.58 Second order polynomial fitted trend line for both small and large networks, computation time

If we theorize that these two sets of small and large networks obey a linear trend and fit a separate line to each set, the trend line equations for both sets of observed data in Figure 6.59 will be:

$Time(\text{sec.}) = 0.2033 * N\_Nodes - 2333.7$ with $R^2 = 0.9592$ for networks smaller than 400,000 nodes; and

$Time(\text{sec.}) = 1.3094 * N\_Nodes - 454103$ with $R^2 = 0.994$ for the larger networks But, the R^2 is still more accurate (closer to 1.0), if we use a second order equation and treat all data as one entity.

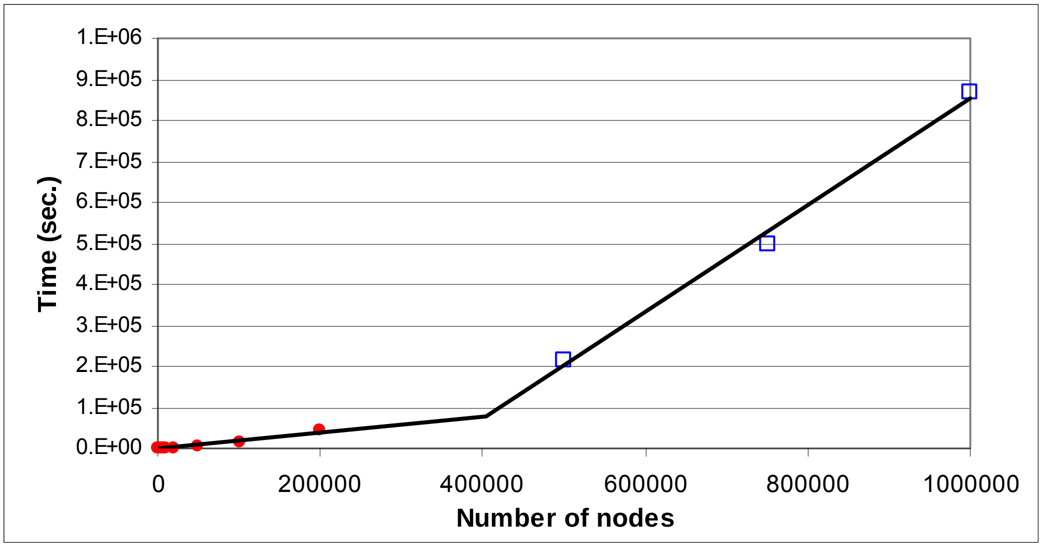

Figure 6.59 Fitting an independent line to each set of simulation times

6.6. PHYSICALLY REPRESENTATIVE LATTICES

Thus far we have used artificially generated regular network samples with computer generated hydraulic conductivities, or re-sampling of a real hydraulic conductivity distribution. But what if we use a real sample with real properties? Will we get similar results, or will we receive a completely different behavior for viscous displacement?

We used two different structures to study the behavior of viscous displacement in real samples. These two are:

a. Finney real sample
b. Compact granular spheres

The first one is a geometrically spherical sample and the second one is a compact dense packing of spheres in a periodic cube. We used both of these samples to simulate viscous invasion.

The outcome of the simulation of these two samples will verify the correctness of results from the previous artificial regular networks.

6.6.1. FINNEY REAL SAMPLE

In this section, we used a Finney pack real sample with three dimensional locations of pores and throats and real values of the throats' radii. The sample was previously scanned as a sphere. Nodes had different numbers of connectivity and conductivities. Figure 6.60 illustrates the topology of this three dimensional sphere sample.

To simulate the viscous displacement for this sample, we treated a few of the central nodes (nodes located in the center of the Finney sphere sample) as the inlets and most of the surrounding nodes, at the maximum radial distance to the center of the sphere as the outlet nodes. Theoretically, the general flow direction would be a radial flow from the center to the surface of sphere.

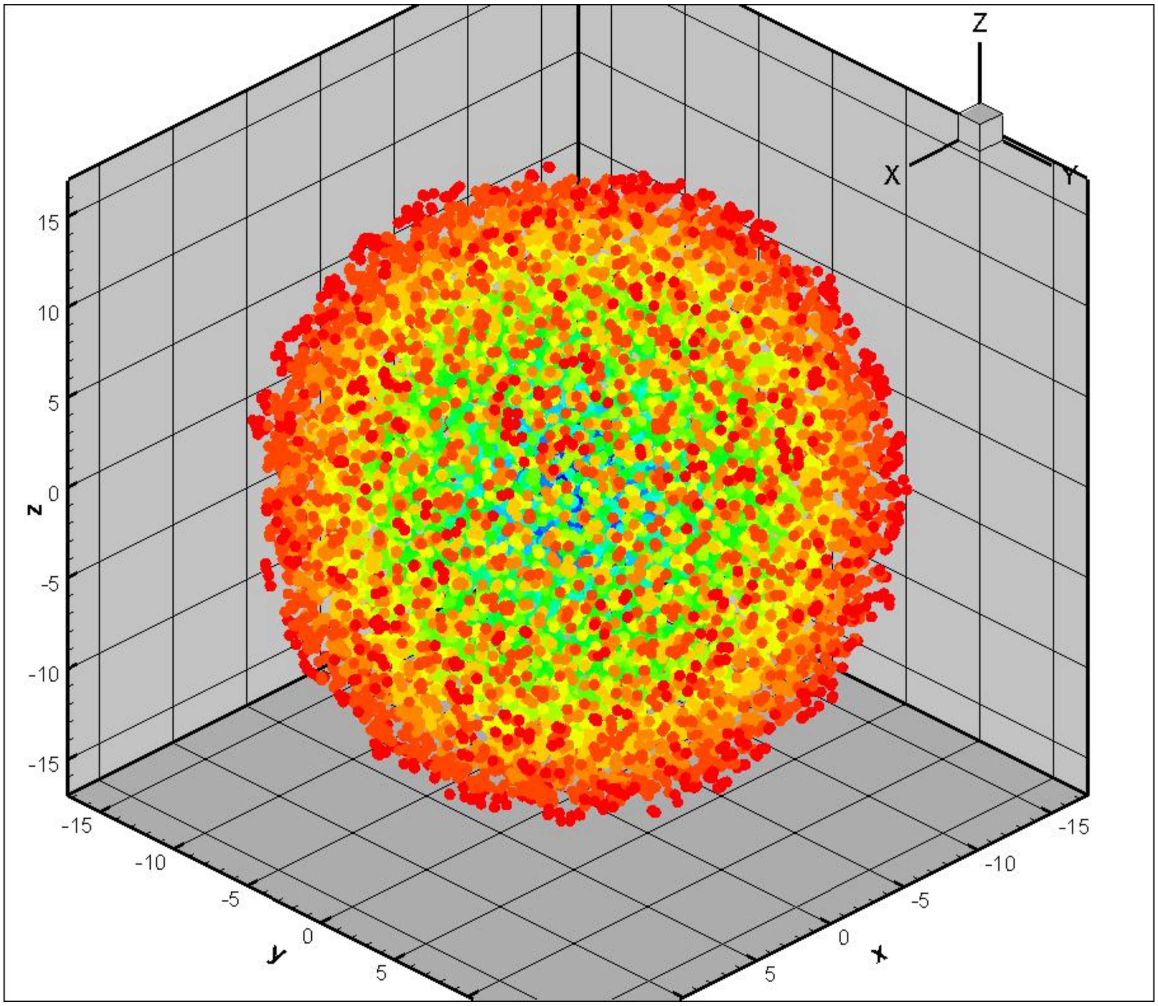

Figure 6.60 Finney spherical sample

One of the advantages of simulating viscous invasion in this sample is that we did not put a no-flow boundary around the sample. The flow had equal opportunity to move in all directions.

The other advantage of simulating this spherical sample was that flow had multiple choices for advancement in each node. Sometimes there are multiple adjacent nodes in similar directions (outward from the center of sphere) and at other times there is only one node from which to choose. Depending on the potential gradient at each node and stage, the advancement flow can either advance radially or move to adjacent nodes in the same level. So, the flow has complete freedom of any type of movement in this spherical sample.

We modeled the viscous displacement on this real Finney sample in the same way as the previous artificially generated regular networks. Figures 6.61 and 6.62 reflect the resulted invasion of such a viscous displacement on this three dimensional sphere sample. These figures represent two views of this radial invasion.

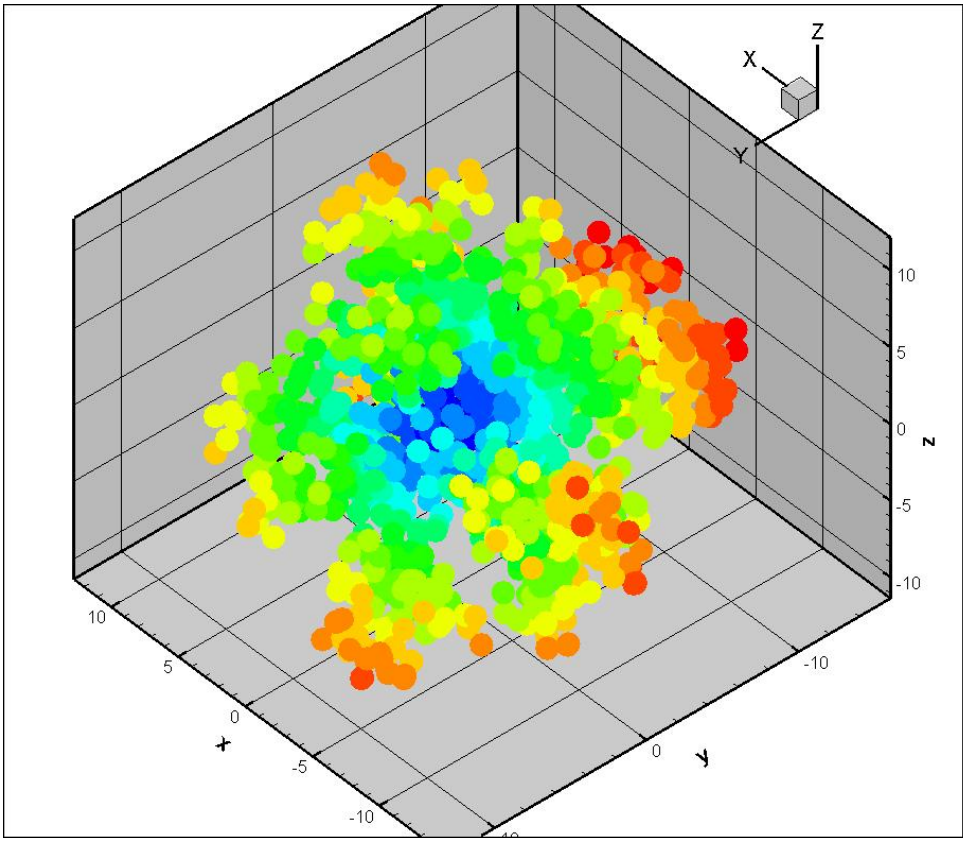

Figure 6.61 Viscous invasion on a three dimensional Finney sphere sample, view 1

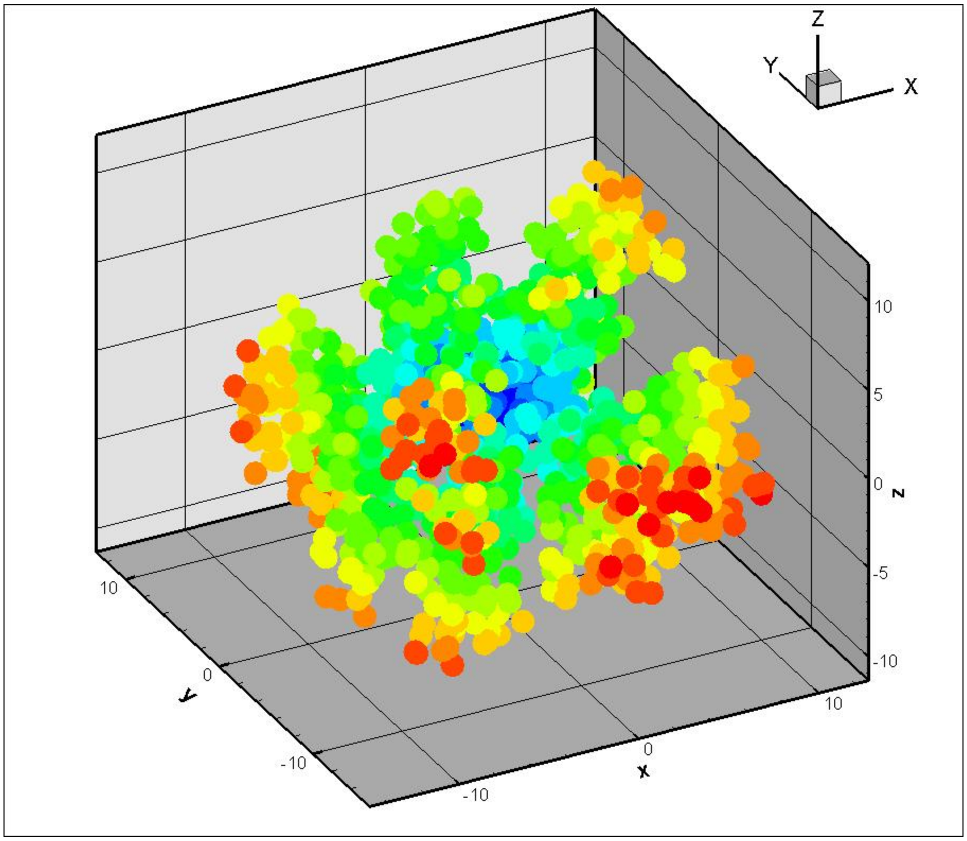

Figure 6.62 Viscous invasion on a three dimensional Finney sphere sample, view 2

The general characteristics of the viscous invasion on this sphere were the same as the previous artificially generated lattices. The viscous invasion still reflects a self-contracting behavior. Invasion channels originated from the inlet nodes and advanced towards the outlet nodes. Even though we had more branching of channels towards the surface, this was only because the total number of nodes in each radial distance from the center increased as we got further from the center of sphere. However, the calculated value of average bond per nodes did not change significantly and still reflected the linear flow. Table 6.15 contains some information about the Finney sphere sample and the simulated viscous invasion results.

Total nodes in Sphere	14,871
Maximum Throat Radius	0.693482
Minimum Throat Radius	0.148854
Total Invaded Bonds	3,841
Total Invaded Nodes	1,658
Average Bonds per Node	2.32

Table 6.15 Spherical sample invasion results

Please not that the Finney sphere sample was a homogeneous sample with a bimodal distribution of throat radii. We used a relative error of 10^{-15} in our simulation as the stopping criterion of the iterative method mathematical solver.

The results reflect that the numerical value of average bond per nodes do not have a significant difference from the previously modeled artificial samples. However, they do show an increase of almost 15%. This is because, as the flow expands towards the surface of the sphere, the area in front of the invasion channels expands and the invasion channels have more opportunity to find new paths towards the surface (outlets). Thus, they expand and divide into new channels as they move toward the surface.

6.6.2. COMPACT GRANULAR SPHERES

The second test of physically representative models was done on a compact granular packing of spheres using Delaunay tessellation. The model was generated by one of the M.Sc. students in the Department of Petroleum and Geosystems engineering in The University of Texas at Austin [Behseresht, 2007].

The model is a 12,000 compact granular packing of spheres in a three dimensional cubic shape with the dimensions of 0.7 centimeter. Table 6.16 reflects some of the characteristics of the spheres and the throats in this compact packing. Figure 6.63 illustrates a three dimensional view to this compact packing of spheres.

	Millimeter
Maximum Throats radius	1.4112
Minimum Throats radius	0.1424

Table 6.16 Dimensions and characteristics of spheres in the compact granular packing

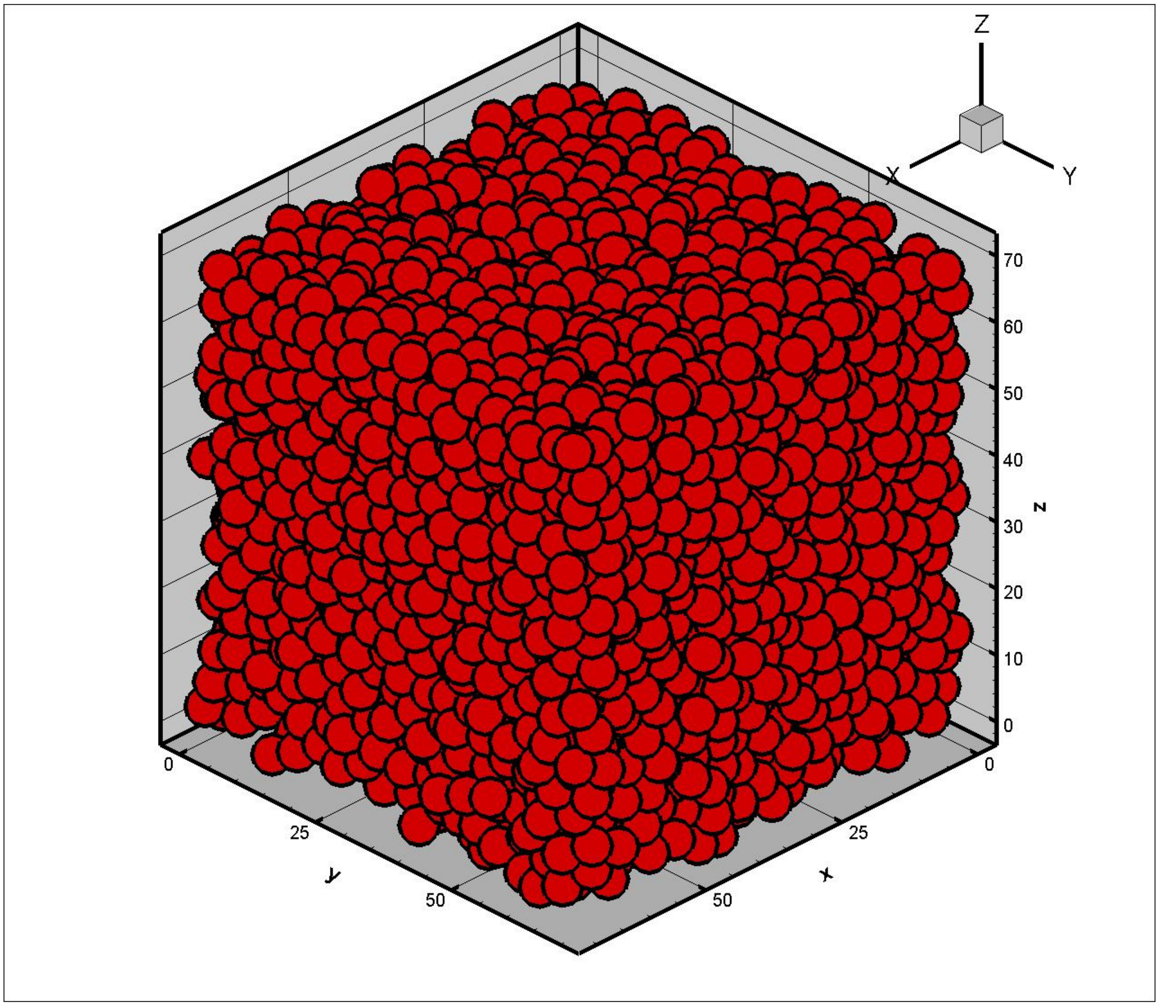

Figure 6.63 Compact granular packing of spheres

To perform viscous invasion on this model, we set the top and bottom parts of the cube to outlets and inlets, respectively. All four sides are considered no-flow boundaries and the general direction of flow potential gradient is from bottom to top of the cube. We performed viscous invasion on this physically representative model. The resulted invasion is shown in Figure 6.64.

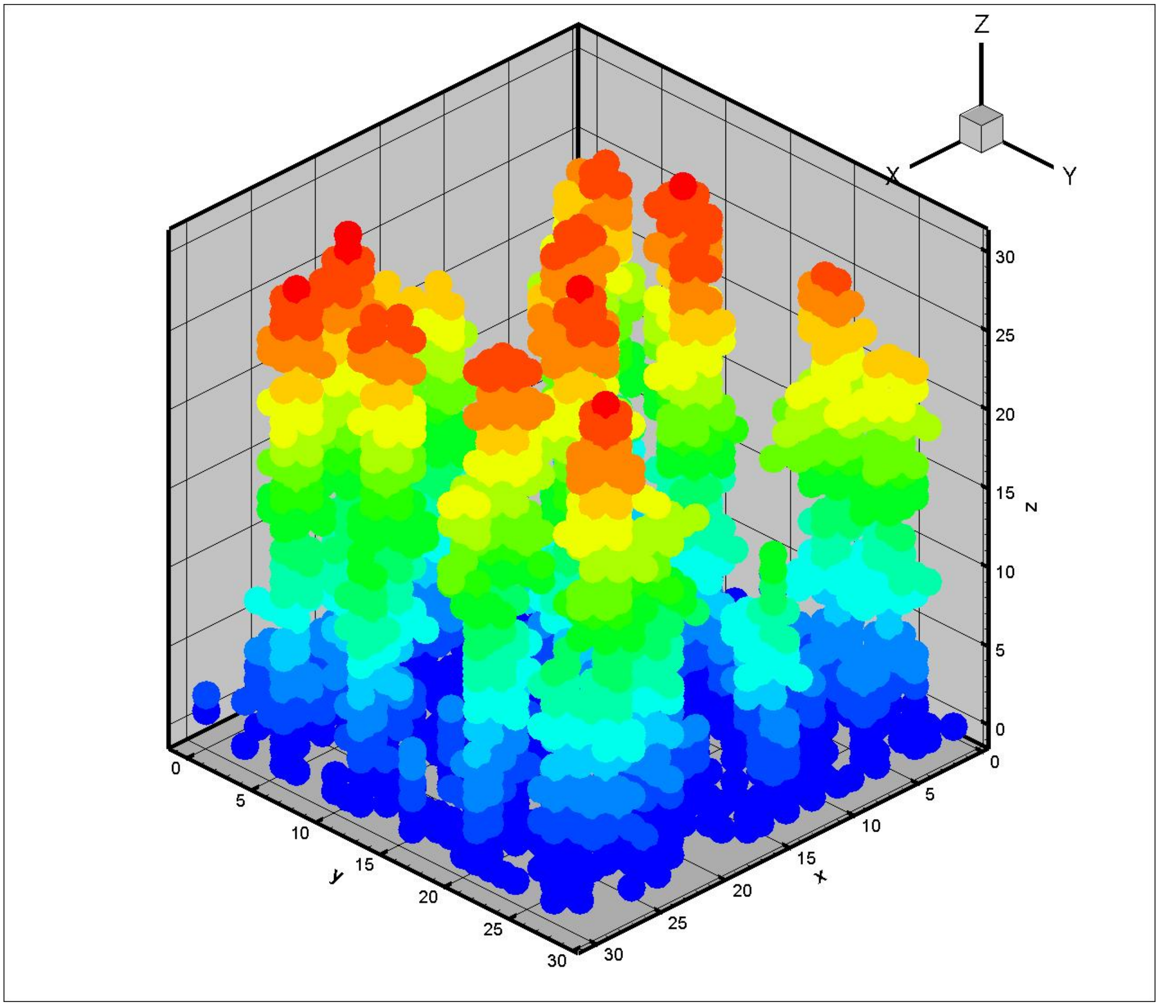

Figure 6.64 Viscous invasion on a dense packing of spheres model

The total number of invaded nodes in this system was 1,472 nodes and the calculated average bonds per nodes value was 1.95, which is very close to the previously calculated values on the regular lattices.

The calculated sweep efficiency was 12.27%, which is higher than the regular lattices. Notice that, even though the system might visually look similar to a regular cubic lattice, the spheres or resulting pores are not located in a regular lattice network.

Pore throats radii distribution is shown in Figure 6.65 for the packing of spheres using Delaunay tessellation. As demonstrated, the pore throats radii distribution is not uniform. The distribution indicates that there are many pore throats with high radius (in the top 30% of distribution) in comparison to a Gaussian normal distribution (which was uniformly re-sampled for random cases), which can allow the invasion to pass through them. Therefore, the resulted invasion sweep efficiency was higher than regular lattice simulations.

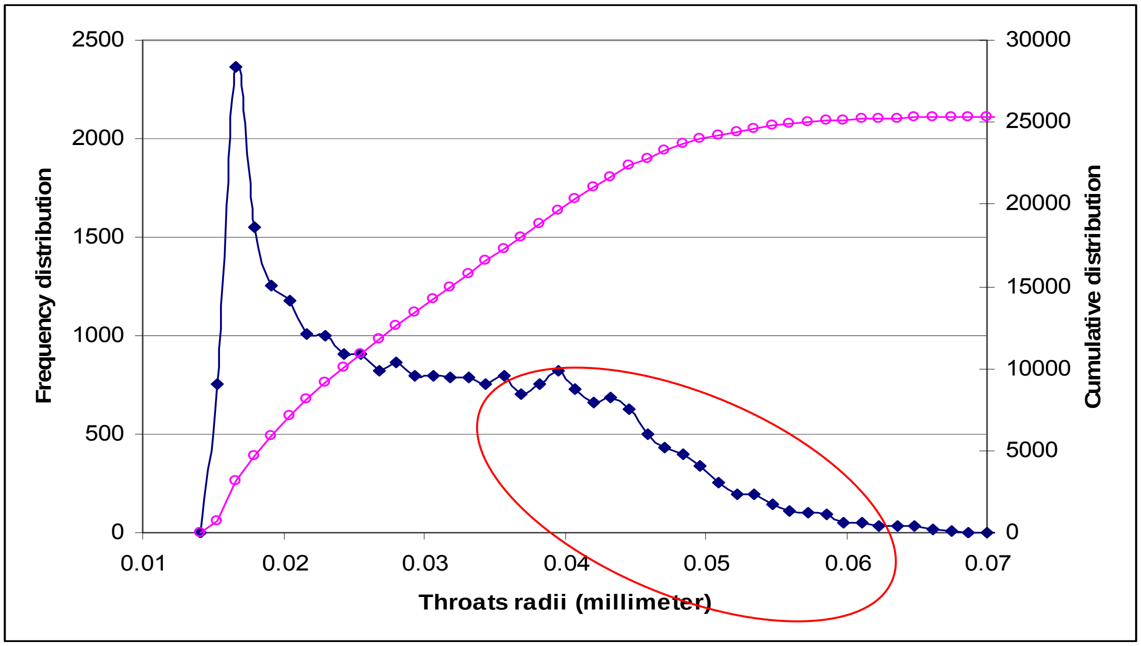

Figure 6.65 Pore throats radii distribution in the dense packing of spheres

6.7. SWEEP EFFICIENCY

Sweep efficiency is a direct ratio of the number of invaded or swept pores in relation to the total number of pores in a sample. In an invasion strategy, the higher the number of invaded pores, the better sweep results. So, sweep efficiency will be a fraction between 0 and 1.

Calculating the sweep efficiency in network modeling is simple. In a network invasion model, we know most of the information about pores in a network, such as the total number of pores existing in a sample, volume of pores, surface area, locations, and the total number of invaded nodes and bonds after the invasion. Therefore, calculating the total porous volume and the swept volume is not a problem for evaluating the sweep efficiency.

We have gathered the invasion results of the previously simulated viscous dominant invasion models in Table 6.17 and calculated the sweep efficiency of each simulation.

Conductivities characteristics	Total Nodes	Invaded nodes	Sweep Efficiency
Finney Pack Distribution	250,000	1,921	0.77%
Random 1-100	250,000	9,102	3.64%
Random 1-10	125,000	5,180	4.14%
Random 1-10	250,000	10,849	4.34%
Spatial Correlation 10-10-1	125,000	8,702	6.96%
Spatial Correlation 100-100-1	1,000,000	74,097	7.41%
Spatial Correlation 50-50-1	1,000,000	76,189	7.62%
Spatial Correlation 15-15-1	125,000	9,886	7.91%
Granular Dense packing	12,000	1,472	12.27%
Finney Sphere	14,871	3,841	25.83%
Spatial Correlation 1-10-10	125,000	38,981	31.18%
Spatial Correlation 1-15-15	125,000	45,056	36.04%

Table 6.17 Calculated weep efficiency for different viscous invasions

The results from Table 6.17 indicate that, as the distribution of hydraulic conductivities makes more alignment towards the general direction of the flow potential gradient, more nodes will be invaded in the network, and consequently sweep efficiency will increase.

At the same coordination of hydraulic conductivities towards the general direction of flow potential gradient, if the hydraulic conductivities show more homogeneous distribution, sweep efficiency will increase as well (refer to Section 6.1.3.). Therefore, homogeneity of hydraulic conductivity distribution increases the sweep efficiency.

The previously simulated invasion models' results reflected in Section 6.1.3 indicate that as the heterogeneity of the hydraulic conductivity distribution increases, the total number of invaded pores decreases. As shown, in Table 6.3, a random distribution of hydraulic conductivities with smaller ranges of distribution has more invaded pores than the larger spread of conductivity. Both homogeneous distributions in this table have a larger number of invaded pores in comparison to the non homogeneous Finney pack distribution. Therefore, homogeneity increases the total number of invaded nodes in a viscous invasion, and ultimately increases the sweep efficiency.

The critical value of R_z ratio, in a viscous dominant displacement, indicates that if the distance between the injector and producer increases beyond this critical value, there will be only one dominant single channel in the network, and sweep efficiency will not improve. To get higher sweep efficiency in the viscous dominant displacement, the distance between the injector (inlet) and the producer (outlet) should always be kept less than the critical R_z ratio.

In Section 6.4, the one million nodes tests, Table 6.13 illustrates that if the layers of high hydraulic conductivity are large enough to force the viscous invasion to spread in a perpendicular direction to the general potential or flow gradient, more clusters of invaded pores will form locally, which increases the sweep efficiency.

6.7.1. SURFACE AREA CONTROLS THE MASS TRANSFER

Increasing the surface area of contact is the key controller of concept of injecting high temperature steam or dilute solvent into heavy oil reservoirs. Larger contact surface will increase either transfer of heat into the heavy viscous in place oil and make it moveable or dissolve it into the solvent mixture or any other easily flow-able liquid form to force it to flow through the pores and pore throats. To increase the efficiency of these systems, one should increase the contact area between the injected fluids and the displaced ones.

As shown in this document, viscous displacement resulted in the formation of large numbers of channels in the network or sample. As the number of channels in the system increases, the total surface area between the injected and displaced fluids increases. This is a suitable condition for making contact between the injected and displaced fluids. Consequently, the increased surface area results in a better environment for mass and heat transfer between the fluids.

We modeled many cases of orientation and distribution of hydraulic conductivities in homogeneous and heterogeneous networks. From all those realizations, cases in which the general potential gradient of flow was in the direction of the high hydraulic conductivity disks, or spikes, showed a higher number of channels or invaded pores. Therefore, these cases make the largest surface area of contact between the injected and displaced fluids. This will result in a better heat or mass transfer.

To achieve a higher surface area, more channels or fingers has to be created in the network. As Figure 6.53 illustrates, spikes of high hydraulic conductivity are the best environment to create maximum contact surface area between the injected and displaced fluids. As the homogeneity of distribution of conductivities in the network increases or the distribution looses its coordination towards the general direction of the potential gradient, invasion tends to make less and less fingers in the network. When finger density decreases, the contact surface area will decrease too.

CHAPTER 7

Conclusions and recommendations for future work

7.1 CONCLUSIONS

- Homogeneity of hydraulic conductivity distribution increases sweep efficiency in a viscous invasion. Any deviation from homogeneous distribution of hydraulic conductivities in a network forces the viscous invasion to make a dominant single channel in shorter distance between the injector and producer.
- It appears that viscous dominant invasion is spike-like in nature. Viscous displacement forms individual channels throughout the network. Channeling reveals itself just after the first steps of invasion. Viscous dominant displacement does not show a piston-like displacement in any stage of invasion. We refer to this type of generation of channels or fingers in the network as the self-contracting behavior of the viscous displacement.
- The average bond per nodes value in most of the viscous displacement simulations was approximately 2, which is an indication of channeling type invasion with less branching.

Hydraulic conductivity distribution can affect the total number of invaded pores in a porous medium. Homogeneous hydraulic conductivity or pore throats radii distributions have more invaded pores than the heterogeneous ones. The hydraulic conductivity distribution does not affect the ratio of invaded bonds per invaded nodes. The number of invaded nodes is the direct controller of the viscous dominant displacement.

- In viscous displacement, involving a long distance between the injector and the producers, with a narrow swept area, only one channel will dominate and will breakthrough.
- Distance between the injector and producer plays an important role in the efficiency of the displacement. Longer distances between two points of potential in a viscous-dominant displacement, increases the geometry ratio (which is the distance between the potential points divided by the area perpendicular to flow), above the critical value of 0.05. Beyond this critical value, there will be only one dominant single channel in the porous medium that advances in the direction of potential gradient. For any geometry ratio above the critical R_z, sweep efficiency will not increase. To gain higher sweep efficiency in the viscous dominant displacement, the distance between the injector and the producer should remain less than the critical R_z ratio.
- Spatial correlation between hydraulic conductivities can change the density of channels and ultimately affect the sweep efficiency. Spikes of high-hydraulic conductivity in the direction of flow are favorable in the viscous displacement. Higher density of spikes results in higher density of channels in the porous medium. Disks of high hydraulic conductivities, in the general direction of flow, have a similar effect as the spikes. We can therefore, conclude that as the ratio of correlation length in the direction of potential gradient for the hydraulic conductivity distributions (in respect to other directions) grows the density of fingers will grow. However, disks or layers of high-hydraulic conductivity perpendicular to flow, reduce the density of channels in the porous medium. If the disks are large enough to act as layers and completely cover the flow path, they might, however, increase the total number of invaded pores by letting the invading fluid spread into the high-hydraulic conductivity layers, in the perpendicular direction of

flow. This will result in higher sweep efficiency; even though fewer channels may be created during the invasion.

- Without spatial correlation between the hydraulic conductivities in any specific direction, viscous invasion creates fewer invasion channels at the same distance between the injector and producers, as compared to the cases with spatial correlation between the hydraulic conductivity values. This means less channel or finger density. Note here that the structure of viscous dominant invasion does not change, whether modeling a small sample or a large one.
- The numerical value of average bond per nodes for radial flow does not have a significant difference from the parallel flow in cubic lattices. However, the 15% increase occurs because, as the flow expands radially, the area in front of the invasion channels expands, and the invasion channels have more opportunity to find new paths as they move further from the center. Thus, they expand and divide into new channels as they move toward the surface of sphere.
- Even though the sweep efficiency was higher for the compact dense packing of spheres in comparison to the three-dimensional cubic lattices, viscous invasions still behaved similarly in the artificial cubic lattices. The non-uniformity of the pore throats radii distribution can be a cause of higher-sweep efficiency. More pore throats with large radii (e.g., in the top 30% of distribution) in comparison to a Gaussian distribution, allows the resulting invasion sweep efficiencies to be higher than regular lattice simulations.
- If the reservoir has layers of high-hydraulic conductivity and low hydraulic conductivity, it is important to keep the general direction of flow potential in the direction of the layers or disk to increase the total number of invaded pores and, ultimately, increase the sweep efficiency.

- In order to increase the sweep efficiency, the alignment of wells in a reservoir (e.g., injector and producing wells) has to be in correct locations and directions, to reduce the R_z ratio below the critical value. If the injector and producer wells alignment is such that the general flow direction stays in the same direction as the alignment of the high hydraulic conductivity clusters, sweep efficiency will be higher in comparison to other alignment of flow and high hydraulic conductivity clusters. Keeping the general direction of flow perpendicular to the spread of layers in a viscous dominant displacement will decrease the sweep efficiency.
- Large layers of high-hydraulic conductivity, perpendicular to general flow potential, can force the spread of viscous invasion in the perpendicular direction to the general flow direction. This, in turn, can make more clusters of invaded pores form locally and, ultimately, increase the sweep efficiency. Reservoirs with layers of high hydraulic conductivity have a better sweep of pores and get a higher number of invaded pores.
- The high density of spike with high hydraulic conductivity in the direction of flow is the best environment to achieve maximum contact surface area between the injected and displaced fluids. As the homogeneity of distribution of conductivities in the network increases, or the distribution loses its coordination towards the general direction of the potential gradient, invasion tends to make less and less fingers in the network. When finger density decreases, the contact surface area will decrease, also.
- We have shown that, in the case of extreme viscosity ratios, many fingers or channels develop in the network as we invade the heavy viscous fluid already in place. Therefore, more heavy oil will be left intact in the porous medium. This is consistent with the findings of J. Wang et al. [Wang, 2006]. They indicated that, for strongly water-wet systems such as sand packs, the displacing water phase preferentially invades the small

pores or narrow flow channels. The higher the oil viscosity, the more viscous fingering, and the more oil will be left in pores in the process of water flooding. In our research, which considered the viscosity ratios of the in-place oil to the invading fluid in four or more orders of magnitude, we observed similar behavior. In most of our simulations, the invasion made an early breakthrough and there were many fingers accompanying the simultaneous invasion of the sample at different parts in the sample networks.

7.2 RECOMMENDATIONS FOR FUTURE WORK

Finally, we showed that sweep efficiency is strongly dependent on the value of the R_z indicator.

The developed model in this dissertation can be used as a foundation for examining additional physical processes, such as:

a. Mass transfer between phases;

b. Gravity-driven drainage of oil;

c. Geo-mechanics (e.g., relative motion of grains); and

d. Surface tension and wettability.

Implementing more physics in the developed model will require more computational resources, which is currently beyond single processor computers. Implementing parallel processing in calculations for several million nodes networks is necessary; otherwise, single processor computers will not have the capability to simulate porous medium models consisting of several million pores.

Sufficient understanding of viscous dominant displacement can also help to formulate a macroscopic model for reservoir simulation. Therefore, up-scaling from microscopic models to reservoir modeling can be an important capability, which has not yet been achieved.

APPENDIX

A. SOFTWARE DATA ENTRY

Input parameters are being read from an input file named “input.txt.” It is an ASCII standard format text file which can be edited with any text editor from the oldest version of DOS to recent Windows, Mac, and UNIX operating systems.

The file contains numbers and text for different choices and approaches to the problems. The only important factor to consider when preparing the input file is to keep the sequence of the input parameters. One can also enter space between the lines of data and even make comments, but the sequence of the data should be kept intact. Also, to enter comments, one should indicate that the line is a comment, by placing an asterisk “*” at the beginning of the line. More information about the parameters and the ideas behind them can be found in chapters 3 to 5.

These parameters are as follows:

1. Using a **dimensional** or **dimensionless** approach. ‘0’ signifies a dimensionless system. Any other value signifies a dimensional approach. A dimensionless structure is that which only searches for the connectivity between nodes and not the location of nodes in the network. For example, a regular search for the neighbors is to check the location of i-1 and i+1 node in X, Y or Z directions, but in a dimensionless system the search is conducted by using the neighbors’ ID. Note that the neighbors can be any other node and not necessarily the adjusting topological neighbors in the network.

2. Second parameter is the name of the **Connectivity file** that should be read by the program. This file is automatically generated by the software, depending on the Nx, Ny, and Nz values. It can also be prepared manually for virtual cases, but since manual preparation is a very time-consuming process, we do not recommend generating the Connectivity file in this manner. This file is an ASCII text file format with the “txt” extension and can be read or edited by any operating system.

The first column identifies the number of connected nodes to the current node. The current node is simply the row number of the current editing line. This means if you are on line 123 you are, therefore, editing node number 123. The other columns identify the ID number of connected nodes to the node in first column.

At the end of this file, the boundary nodes are reported, with the same format. These nodes usually have a connectivity of one and the connected node. No comments or spaces are allowed in this file.

3. **Generating the Conductivity file** is automated, also. Like the others, this file is a text format file with an extension of “txt.” It does not have the same first column as the connectivity.txt file. The other columns correspond one to one with column two all the way to the last column in the connectivity file, and they hold the bonds’ connectivity information. Again, no comments or spaces are allowed in this file.

4. The **Invasion model** indicates whether a simulator should use capillary-dominated percolation or viscous-dominant invasion. Numbers one and two corresponds to these models, respectively.

5. The **Node Output Counter** parameter indicates when an output should be generated and after how many invaded nodes (which is considered as a step). This output file contains the potential of the nodes for each middle step of the invasion. For example, if you enter 25 then after each 25-node invasion the program writes a potential distribution of the system to the output file. These data are the nodes potential at cumulative invasion of 25, 50, 75, and etc., nodes until the end of invasion simulation. If it is not being defined, then the program generates one potential distribution at the end of invasion, which is at the breakthrough time.

6. The **Constant potential** file, “cPVfile.txt,” is a file which holds information about the nodes with a specific potential. This feature can be used to generate objects like fractures, extra inlet and outlet nodes, or intrusions in the system. It behaves like a fracture information data box, or any other special experiments, in which one may need a couple of nodes to have a specific constant pressure (e.g., potential) at the start of invasion, and that will hold these values through the simulation. For example: A case in which you need to simulate a fractured sample.

The parameter in line one should bee the number of nodes for this file. The node’s number, with the specific potentials, is defined in columns one and two from the second line.

The program does not require connectivity between these constant potential nodes. It is the user’s responsibility to decide if he needs connectivity or not. The program automatically retrieves the nodes and assigns the corresponding potentials to them.

7. The next parameter determines whether you want the simulation to **use the constant potential nodes** or not. If this value is equal to zero (e.g., “0”), the simulation does not use the constant potential node structure developed within the code. If you use any other value, the constant potential nodes will force the simulator to read the cPVfile.txt file. In this file, you must define the number of nodes or data lines which this file contains. For example, if you have 27 nodes with constant potential values, you should first enter 27 on the first line, then, for each additional line, enter the node number and its corresponding potential.

8. A **Cumulative Distribution File** (CDF) can be used to generate the bond conductivities. The simulator reads this file and generates a condense CDF file if necessary. This file is called “CumulativeDist.txt,” and it re-samples the bond conductivities from this newly condensed distribution file.

The first line of the input file contains the number of samples. From the second line forward, column one is the value of the distribution and column two contains the cumulative distribution value. Note that this file also has an ASCII text format.

9. A **Parameter type** is used to define the conductive bond, which is generally type ‘R’, which means the radius. This parameter is important because of the four components that change the conductivity properties of the porous media. These components are as follows:

- **a.** ‘r’ power;
- **b.** constant;
- **c.** exponent; and
- **d.** cement Thickness.

These components will be defined later in the realization parameters.

10. As is obvious from its name, **maximum error tolerance** defines the maximum acceptable relative error for the iterative method. When the iterative solver solution converges, the error drops. When it reaches a value less than this tolerance for each individual node, the iterative method stops and exports the solution back to the called location of the function. Note that the lower the error tolerance, the more iterations are needed for the solver to get to the desired relative error. This is more expensive for larger sized networks. It usually exhibits an exponential behavior as the network grows.

11. The **Mass Balance** parameter indicates the necessity for a mass balance calculation. If you need to study the mass balance error in the simulation, you can trigger this parameter to call the appropriate function in the simulator, and it will perform a mass balance calculation. It can also be used to check the accuracy of the simulation for any unexpected errors. There are only two parameters: ‘Y’ means “yes,” and instructs the program to calculate the mass balance; and ‘N’ means “no,” and instructs the program not to perform the mass balance calculation(s).

12. The “**Print on screen**” option is used to output the results to the screen. It reports the potential for each node in each step on the screen and outputs for all nodes. For larger networks, we recommended you not to use this parameter, because it takes a long time to output all of the nodes information to the screen. Also, doing this may cause a delay in calculation.

Same as for the previous parameter, it only accepts two parameters: ‘Y’ (e.g., yes), to output to the screen and ‘N’ (e.g., no), to not output to the screen.

13. If you need all parameters, calculations, and results for each step to be exported to output files, then should trigger **Output all Information** parameter. If you enter ‘Y’, then the “output_Information.txt” file will be generated. It contains all of the results and calculations for each step. If you select this parameter, you will get the mass balance, potentials, invasion candidates, invaded nodes, and all corresponding values in each step for each realization. It was important for the purposes of this research to follow the behavior of the flow channels in the interim situations before the final breakthrough. So, this logic was developed in the code to give users an extra edge.

Please note that if you choose to generate output for all of the steps for larger networks, the resulting file might be larger than many software capabilities to read. For example, a file larger than 65,536 (2^{16}) lines cannot be imported to Microsoft office XP professional Excel versions. So, you might lose some of the benefits by having unnecessary information in your output file.

14. The **Simulations** parameter identifies the number of different simulations you want to perform. Each simulation is followed by a line of parameters. For example, if you have three different networks with different parameters, then you must set this value to 3 and then set up three lines of parameters for each value.

These lines of parameters hold the specific data for each simulation, such as network size, inlet and outlet potentials, etc.

15. The **Simulations parameter line** consists of several parameters that define a series of realizations.

- The first parameter is the number of realizations you want the simulator to execute with this line of values. For example, a value of 5 will provide 5 realizations. The maximum number of realizations for each line is 100. If you want more similar realizations, you will need to repeat this line.
- The next three parameters are Nx, Ny, and Nz. These values define the size of the network in each direction in space for a regular cubic lattice.
- The fifth parameter is the input method. This can have 5 values as, follows:
  - **(1).** A value of ‘1’ indicates that conductance has to be read from a file. So, the defined file for the “InputCDF_File” will be used to assign the conductivity of the bonds.
  - **(2).** A value of ‘2’ indicates that a Cumulative Distribution File will be used to re-sample the values. One should consider that the number of the data lines in the CDF table can not be more than 100. However, program will generate a denser table if needed.
  - **(3).** A value of ‘3’ indicates similar values of conductivity to the minimum parameter. The minimum values for these realizations will be defined further in the same line for each realization.
  - **(4).** A value of ‘4’ indicates random values between the minimum and maximum defined parameters in the realization line will be used for the conductivities.
  - **(5).** A value of ‘5’ indicates both conductivity and connectivity data have to be read from a file.

d. Update is the 6th element in this line. If this value is set to ‘1’ then conductance for each realization will be regenerated. But if this value is ‘0,’ then the old conductance samples will be used. This becomes useful if one needs to perform a comparison on the same samples but with different physics.

- **e.** **Percentage** indicates what portion of the potentials that are away from the maximum potential (e.g., invasion rate) have to be invaded along with the maximum invasion node. For example, if this value is set to ‘0,’ only the maximum invasion rate will invade a node. All other rates and potentials cannot invade a node, even with 99% of the maximum value. Another example is if the value is set to 10. When this occurs it means that all the invasion rates or potentials within 10% from the maximum rate will also invade the corresponding invasion candidate node. This is a very useful parameter to use to control the invasion into the porous media.
- **f.** Parameters 8 and 9 are the **inlet and outlet potentials**, respectively. They can be any values. We do suggest however, that you choose a higher value for the inlet and a lower value for the outlet. Additionally, you may also use negative values which, in this case, can reverse the invasion process.
- **g.** Parameters 10 and 11 are the **minimum and maximum parameters** which have been used by the previous sections. These values indicate the minimum and maximum conductance that will be assigned to each bond. If the input method value of 3 is selected, then the minimum parameter used will be this (minimum) value.
- **h.** The next two parameters are the **constant and** the **exponent** for the equation ($C = a\ r^{b}$). These are called the proportionality constant between the conductance and the radius or length. The first parameter is the constant multiplier and the second parameter is the power of the conductance

equation. These two values can be used to generate the equivalent conductivities in different calculations, such as ($c = r^4$) or ($c = 1/r$).

- **i.** The **Cement thickness** parameter indicates the thickness of the flow path that will be occupied by the cement. This thickness will reduce the conductivity of each bond as a length parameter. It can only be used if the input parameter selected is ‘2.’ A value of ‘0’ indicates no cement thickness.
- **j.** The **Adjusting boundary** parameter is used to set the flag to either run the outlet potential adjustments or not. You may enter a value of ‘Y’ or ‘N,’ indicating ‘Yes’ or ‘No,’ respectively.
- **k.** The **Adjustment type** parameter is the indicator that either adjusts the boundary according to the front perpendicular surface invasion or the actual front surface.

B. INPUT FILE EXAMPLES

Two input files are shown here to give you a general idea about how to input the parameters to run the simulations to your satisfaction.

The first example is a 30×30×30 three-dimensional cubic network system. Conductivities are imported from the “FinneyDrnCDF.txt” file. Also, we use the dimensionless viscous dominant invasion modeling to simulate the invasion. The relative error criterion is 10^{-12}. Note that blank lines and lines beginning with an asterisk will not be read or imported by the developed software. The software will automatically generate the conductivity and conductance files with the internal file generators. We also use front adjustment for the outlet potentials, as follows:

```
Start of input file -------------------------------------------------------------------------
* Using dimension-less system; any other value indicates dimensional system.
0

Connectivity.txt
Conductivity.txt

FinneyGeometryRadius.txt

* Invasion Model 1: Percolation; and
* Model 2: Viscous Dominant Invasion
2

* Expected output after this number of node invasions
1000

* Constant Potential File.
cPVfile.txt

* CDF table for re-sampling. This name is used to read the conductance from
FinneyDrnCDF.txt

* Parameter type.
R
```

```
* Max Error Tolerance
1.0e-12

* Mass Balance Calculation
Y

* Output to Screen
N

* Output all steps.
Y

* Make potential output in each Z direction.
N

* Number of Simulations.
1
1  30  30  30   2  1  70   5  1  1  100   1  100  2  0.0  15  Y  F

End of input file ---------------------------------------------------------------------------
```

The second example is a 100×100×100 three-dimensional network system. All parameters, such as connectivity or conductivities values are imported from other files. In this example, the spatially correlated conductivities with the G-SLIB software (“sgsim.out”) are imported to the simulator. Dimensionless viscous dominant invasion modeling is used to simulate the invasion. The relative error criterion is 10^{-7}. And with no adjustment to the outlet potentials.

```
Start of input file --------------------------------------------------------------------------
* Using dimension-less system; any other value indicates dimensional system.
0

Connectivity.txt
Conductivity.txt

FinneyGeometryRadius.txt
```

```
* Invasion model 1: Percolation; and
* Invasion model 2: Viscous Dominant Invasion.
2

* Expected output after this number of node invasions.
1000

* Constant Potential File.
cPVfile.txt

* Conductance to be imported directly from a file.
sgsim.out

* Parameter type.
R

* Max Error Tolerance.
1.e-7

* Mass Balance Calculation.
Y

* Output to Screen.
N

* Output all steps.
Y

* Make potential output in each Z direction.
N

* Number of Simulations.
1
1  100  100  100   1  1  70   5  1  1  100   1  100  2  0.0  15  N  F

End of input file --------------------------------------------------------------------------
```

C. OUTPUT FILES

There are many output files generated by this software, essentially cover all necessary results that might be needed to study the behavior of the viscous displacement. A brief description of each of these output files are as follows:

1. "**CumulativeDist.txt**": re-generated output of the original hydraulic conductivity distribution that has been used for the re-sampling.
2. "**RadiusSample.txt**": contains all the pore throats radii that has been generated for each simulation.
3. "**Cvector.txt**": contains all the conductivities for each bond or pore throat in node IDs order.
4. "**NodeConductances.txt**": a file consisting of all the nodes with their IDs and all bonds conductivities or pore throats sizes that are connected to that specific node or pore, in the same order as connectivity file.
5. "**CDM_table_for_LU.txt**": the compressed dimensionless matrix that has been generated for use by the LU decomposition solver.
6. "**CSM.txt**": includes the resulting compressed dimensionless matrix after the LU solver has finished. Each row number belongs to the associated node ID in the network. Connected nodes to the node with a row ID are shown after that, with the corresponding solution.
7. "**Connectivity.txt**": contains the nodes connectivity information.
8. "**Conductivity.txt**": contains the bonds conductivity information.
9. "**BC_RHS.txt**": includes the potential at each boundary outlet node.

10. "**CDM_for_LU.txt**": similar to the "CDM_table_for_LU.txt" file, but is generated in the constant potential function in the software.
11. "**CDM_and_BC_after_setRHB.txt**": this file is created if the adjusting boundary function is used in the simulation. It contains the boundary potentials after the adjustment.
12. "**Solution_Normal_LU.txt**": this file is created if the normal LU decomposition solver is used instead of the compressed one. It contains the solution to the matrix.
13. "**MassBalance.txt**": contains the mass balance error calculated for each node, after the execution of the LU solver.
14. "**HistCumDist.txt**": contains the histogram of the conductivities or pore throats radii data that was used for this simulation. It generates 100 bins of imported data for the histogram, between the minimum and maximum value of the imported data.
15. "**Percolation.txt**": contains the information of the invaded pores in the order of invasion after simulating the percolation.
16. "**Output_Information.txt**": altogether this file consists of all of the potentials of each node at each step of invasion, the calculated mass balance error, and the adjusted boundaries potential.
17. "**StepbyStep_Potential.txt**": an output file of all the nodes potentials at each step of invasion. This file is primarily used to study the behavior of potential changes in a network.
18. "**Invaded_Nodes.txt**": contains the invaded nodes, in order of invasion at the end of the simulation,.

19. "**AdjustedBoundaries.txt**": contains all adjustments to the boundary potentials in each step.
20. "**CumDist.txt**": consists of the cumulative distribution of bonds for each node, if conductivities are being imported from a file.
21. "**InvadedBonds.txt**": reflects the number of invaded bonds for each node in the network after the end of invasion.
22. "**BondsHist.txt**": the histogram of all the invaded bonds and the calculated values of the average bonds per nodes, according to the invasion results.
23. "**TimeTable.txt**": contains the elapsed time for each simulation in seconds or in HH:MM:SS format.
24. "**IterationInfo.txt**": holds the running time, number of invaded nodes, and invaded bonds for each realization, if more than one realization is simulated at each run.
25. "**Plot3D.txt**": generates three-dimensional information set to verify that the generated file topology is similar to the imported one.
26. "**ZPotential.txt**": generates a database of the top view of the three-dimensional shape of the network. At each step of invasion, it can be used to get a top view of the invasion front.

D. OUTPUT FILES EXAMPLES

Examples of output files can be found in the supplied CD-ROM of this dissertation.

E. C++ CODE

The C++ program code was 6,463 lines long not including the graphical user interface, so, the program code is not included here. However, you may refer to the supplied CD-ROM to obtain the C++ code with the necessary input files to start making the viscous dominant or capillary dominant invasion simulations.

To obtain an executable program, you can also send an email to okhtay@hotmail.com or admin@okhtay.com. I will then provide you with an executable file with the necessary input files.

F. SURFACTANT INJECTION

When a surfactant is added to the injecting fluid, the interfacial tension (IFT) between water and oil decreases drastically. This drop ranges from 5 to 6 orders of magnitude. For example, we used a sulfate base surfactant called N67-7POS (commercial name). Figure Aa-1 illustrates the calculated drop in the interfacial tension between an oil/micro emulsions vs. an oil solubililization ratio when this surfactant is added to injecting water using Chun Huh's relationship [Huh, 1979]. The solubilization ratio was about 20 cc/cc, for this test.

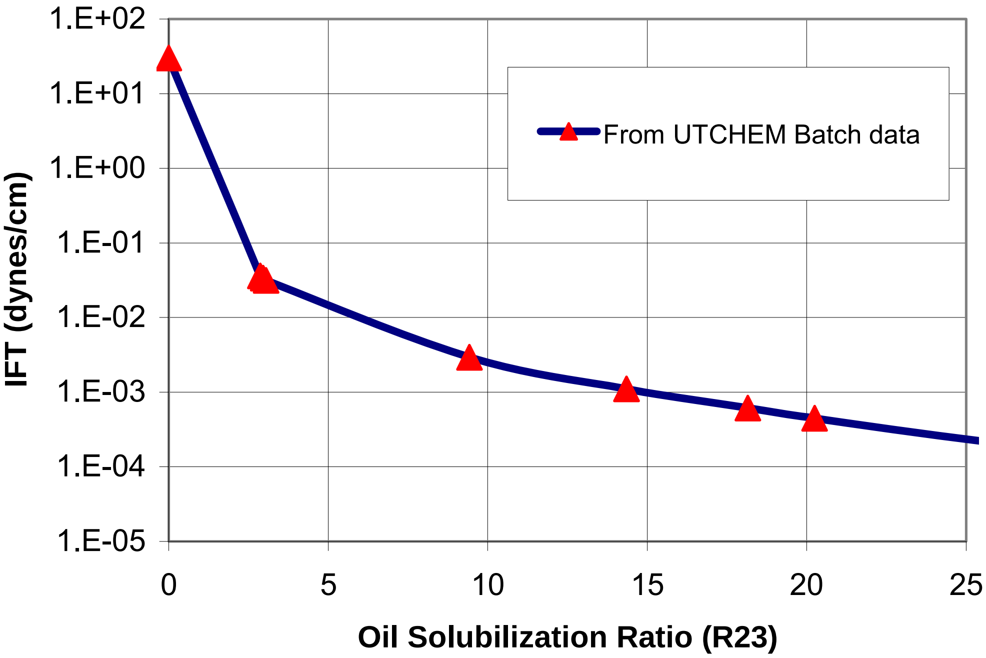

Figure A.1 N76-7POS Surfactant interfacial tension.

These interfacial tension calculations were done using Chun Huh's relationship [Huh, 1979], Equation 2.47 (UTCHEM technical documentation). As shown in Figure

A.1, the IFT between water and oil (σ_{wo}) dropped from a value of 24 to 2.4e10-4, which is 5 orders of magnitude lower than the interfacial tension between water and oil without surfactant.

References

Ambegaokar V., V. Ambegaokar, B.I. Halperin, and J.S. Langer: Physical Review B, Volume 4, 2612 (1971).

Andrade J.S., Jr. S.V. Buldyrev, N.V. Dokholyan, S. Halvin, P.R. King, Y. Lee, G. Paul and H.E. Stanley: Physical Review, Volume E 62, 8270, (2000).

Andrade J.S., J.S. Andrade, Jr., A.D. Araujo, S.V. Buldyrev, S. Havlin, and H.E. Stanley: "Dynamics of Viscous Penetration in Percolation Porous Media," Physical Review E, Volume 63, 051403, 25 April 2001.

Baigorria R., YPF S.A., J.L. Pousa, Conicet-UNLP, F. Di Leo, UTN, J. Maranon Conicet-PROFIMO_UNLP: "Flow in Porous Media," (26971 – MS) SPE Latin America/Caribbean Petroleum Engineering Conference, 27-29 April, Buenos Aires, Argentina, Society of petroleum Engineers

Bakke S., P.E. Oren: "3D Pore-Scale Modeling of Sandstones and Flow Simulations in Pore Networks," SPE Journal 136, (June 1997).

Blunt M.J., Stanford U.; J.W. Barker, Elf U.K. Geosciences research; Barry Rubin, Mark Mansfield, BP Exploration; I. D. Culverwell, Elf U.K. Geosciences Research; M.A. Christie, BP Exploration: "Predictive Theory for Viscous Fingering in Compositional Displacement," SPE Reservoir Engineering Vol. 9, Number 1, February, 73-80, (1994).

Blunt M.J., M.A. Christie: "How to predict Viscous Fingering in Three Phase Media, Transport in Porous media," (1993).

Brock D.C. and F.M. Orr, D.C. Brock: "Flow Visualization of Viscous Fingering in Heterogeneous Porous Media," (SPE 22614) SPE Technical Conference and Exhibition, Dallas, Oct 6-9 (1991).

Bryant S.L. and M.J. Blunt: "Prediction of Relative Permeability in Simple Porous Media," Physical Review A (August 1992).

Bryant S.L. et al., Peter R. King, BP Chemicals; David W. Mellor, Kerr-Mellor Associates: "Network model evaluation of permeability and spatial correlation in a real random sphere packing," (1993).

Buldyrev S.V., P.R. King, Department of Earth Science & Engineering, Imperial College, London, UK, N.V. Dokholyan, E. Lopez, G. Paul, H.E. Stanley, Department of Engineering, Cambridge University, Cambridge, UK, S. Halvin, Minerva Center & Department of Physics, Bar-llan University, Ramat Gan, Israel: "Percolation Theory,", (2001).

Chen J.D., D. Wilkinson: "Physical Review," Lett. Volume 55, (1892).

Chen J.-D. and D. Wilkinson: "Pore-scale viscous fingering in porous media," Phys. Rev. Lett., (1895).

Christie M.A.: "High resolution Simulation of Unstable Flows in Porous Media" (SPERE AUG. 1989) 297 Trans., AIME, 287.

Coniglio A.: "Hydrodynamics of Dispersed Media," edited by J.P. Hulin, A.M. Cazabat, E. Guyon and F. Carmona, Elsevier, Amsterdam, , p. 193, (1990).

Devarajan S., E. Toumelin, and C. Torres-Verdín, The University of Texas at Austin, E.C. Thomas, Bayou Petrophysics: "Pore-Scale Analysis of the Waxman-Smits Shaly Sand Conductivity Model," SPWLA 47th Annual Logging Symposium, June 4-7, (2006).

Dullien F.A.L.: "Porous Media – Fluid Transport and Pore Structure," Academic Press, New York, 1979.

Fayers F.J., M.J. Blunt and M.A. Christie: "Accurate Calibration of Empirical Viscous Fingering Models," Rev. Inst. Francais du Petrole, 46, 311, (1991).

Fayers F.J.: "An Approximate model with Physically Interpretable Parameters for representing Miscible Viscous Fingering," SPERE 551, (May 1988).

Fenwick D.H., SPE, M.J. Blunt, SPE, Stanford U.: "Network Modeling of Three Phase Flow in Porous Media," SPE Journal (38881-PA), Vol. 3, No. 1, Pages 86-96, Society of Petroleum Engineers, (March 1998).

Helfferich F.G., 1981: "Theory of Multicomponent Multiphase Displacement in Porous Media," SPEJ 51, (Feb. 1981).

Huh, C., J. Colloid: "Interfacial Tension and Solubilizing Ability of a Microemulsion Phase That Coexists With Oil and Brine," Interface Sci., 71, 408-428, (1979).

Klov T., P.E. Oren, SPE, J.A. Stensen, SPE, T.R. Lerdahl, SPE, L.I. Berge, SPE, S. Blake, T. Boassen, Statoil, ASA, and G. Virnoveskey, SPE, Rogaland Research, SPE: "Pore to field Scale modeling of WAG," (SPE 84549) SPE, ATCE Denver, Colorado, 5-8, (2003).

Lee Y., J.S. Aharony, Jr. S.V. Buldyrev, N.V. Dokholyan, S. Halvin, P.R. King, G. Paul and H.E. Stanley, Physical Review, Volume E 60, 3425, (1999).

Måløy K. J., J. Feder, and T. Jøssang,: "Viscous fingering fractals in porous media," Phys. Rev. Lett., :26881-2691, (1985).

Murat M. and A. Aharony, Physical Review Lett., Volume 57, (1986).

Nilsen L.S. et. al.: "Prediction of Relative Permeability and Capillary Pressure from a Pore Model," (SPE 35531), European 3D Reservoir Modeling Conference, Stavanger, 16-17 (April 1996).

Oren P.E., S. Bakke, O.J. Arntzen: "Extending Predictive Capabilities to Network Models," (SPE 38880) SPE annual Technical Conference and Exhibition, San Antonio, Texas, 5-8 (October 1997).

Oren P.E. et. al.: "Prediction of Relative Permeability and Capillary Pressure from Pore-Scale Modeling Proc.," Fifth European Conference on the Mathematics of Oil Recovery, Leoben, Ausrtia.

Oxaal U., F. Boger, J. Feder, T. Jossang, P. Meakin and A. Aharony: Physical Review, Volume A 44, 6564, (1991).

Paterson L.: "Diffusion-limited aggregation and two-fluid displacements in porous media," Phys. Rev. Lett., (1984).

Polyanin A.D., A.M. Kutepov, A.V. Vyazmin, and D.A. Kazenin: "Hydrodynamics, Mass and Heat Transfer in Chemical Engineering," Taylor & Francis, London (2002).

Rhyming Inge L.: "Dynamique des fluides," PPUR, (1991).

Saffman P. G. and G. Taylor: "The penetration of a fluid into a medium of hele-shaw cell containing a more viscous liquid," Proc. Soc. London, Ser A, :312-329, (1958).

Sahimi M.: "Flow and Transport in Porous Media and Fractured Rock," VCH, Boston, (1995).

Stauffer D., Aharony: "Introduction to Percolation Theory," Taylor & Francis, London (1994).

Thompson A.H., A.J. Katz and R.A. Raschke, Physical Review Lett. Volume 57, 29 (1987).

Vortsos Y.C., C. Satik, U. of Southern California; D. Salin, J.C. Bacri, U. Pierre & Marie Curie,: "Large Scale Averaging of Drainage at Local Capillary Control," (22592 –

MS) Society of Petroleum Engineers (SPE) Annual Technical Conference and Exhibition, 6-9 October, Dallas, Texas (1991).

Wang J., M. Dong, SPE, and K. Asghari, SPE, U. of Regina: “Effect of Oil Viscosity on Heavy-Oil / Water Relative Permeability Curves,” (SPE 99763) SPE/ODE, Tulsa, Oklahoma, 22-26, (April, 2006).

Wilkinson D. and J. F. Willemsen: “Invasion percolation: a new form of percolation theory,” Journal of Physics A, 3365-3376, (1983).

Wikipedia, Online dictionary.

Witten T. A. Jr., L. M. Sanderz: “Diffusion-limited aggregation, a kinetic critical phenomenon,” Phys. Rev. Lett., :1400-1403, (1981).

Vita

Okhtay Taghizadeh Dizaj Cheraghi was born on April 10, 1974, son of Gholam-Ali Taghizadeh Dizaj Cheraghi and Zahra Firouzi Dashtestani, in Shiraz, Iran. He received his Bachelor and Masters degrees in Mining Engineering, with an emphasis on Exploration, from Faculty of Engineering at The University of Tehran, Iran in 1996 and 1998, respectively, with the First Rank in both B.S. and M.S. levels. While studying at the university he worked part time for Tehran Padir Consulting Engineers and Oil Industries Engineering and Construction (OIEC) of Iran. From 1994 to 2001, he was involved in various mining and hydrocarbon engineering projects in Iran, such as Geophysical and Geochemical projects, Ore Production and Mineral Processing design, Geographical Information Systems (GIS) and Digital Maps, Economical Evaluations of Reserves, feasibility studies, and supervising Buyback projects in Iranian Oil fields. In 2002, he began his Ph.D. program at the Department of Petroleum and Geosystems Engineering at The University of Texas at Austin. He developed a pore scale simulator for his dissertation to model the displacement of extremely viscous fluid with a low viscosity fluid. His experience in the United States of America included Compositional Modeling, Simulation of Offshore Gas Condensate Reservoirs, Intelligent Well Completion and Production Strategy Design for Reservoirs, and Optimization of Oil and Gas Production to Maximize the Net Present Value (NPV).

Permanent address: 17103 Simsbrook Drive, Pflugerville, Texas, 78660, USA

This dissertation was typed by the author.